Alma Mater Studiorum - Università di Bologna

DOTTORATO DI RICERCA IN
INGEGNERIA CIVILE, CHIMICA, AMBIENTALE E DEI MATERIALI

Ciclo 34

Settore Concorsuale: 08/B3 - TECNICA DELLE COSTRUZIONI

Settore Scientifico Disciplinare: ICAR/09 - TECNICA DELLE COSTRUZIONI

Exploiting the environment for structural health monitoring

Strategies, algorithms, and technologies

Presentata da:
Said Quqa

Supervisore:
Prof. Luca Landi

Coordinatore Dottorato:
Prof. Alessandro Tugnoli

Co-Supervisori:
Prof. Pier Paolo Diotallevi
Prof. Maria Pina Limongelli
Prof. Kenneth J. Loh

Esame finale anno 2022

Exploiting the environment for structural health monitoring

Strategies, algorithms, and technologies

A dissertation submitted for the degree of
Doctor of Philosophy

To my three moms

Abstract

A densely built environment is a complex system of structures, infrastructure, nature, and people closely interconnected and interacting. Vehicles, public transport, weather action, and sports activities constitute a manifold set of excitation and degradation sources for civil structures. In this context, operators should consider different factors in a holistic approach for assessing the structural health state. Vibration-based Structural Health Monitoring (SHM) has demonstrated great potential as a decision-supporting tool to schedule maintenance interventions or manage emergencies. However, the mentioned excitation sources are considered an issue for most practical SHM applications since traditional methods are typically based on strict assumptions on input stationarity. Last-generation low-cost sensors present several limitations related to a modest sensitivity and high noise floor compared to traditional and expensive instrumentation. If these devices are used for SHM in common urban scenarios, short vibration recordings collected during high-intensity events and vehicle passage may be the only available datasets with a sufficient signal-to-noise ratio. While researchers have spent considerable efforts to mitigate the effects of short-term phenomena in vibration-based SHM, the ultimate goal of this thesis is to exploit them and obtain valuable information on the structural health state. First, this thesis proposes strategies and algorithms for smart sensors operating individually or in a distributed computing framework to identify damage-sensitive features based on instantaneous modal parameters and influence lines of instrumented structures. Ordinary traffic and people activities become essential sources of excitation, while human-powered vehicles, instrumented with smartphones, take the role of roving sensors in crowd-sourced monitoring strategies. In this context, the technical and computational apparatus is optimized using in-memory computing technologies. Moreover, identifying additional local features can be particularly useful to support the damage assessment of complex structures. Thereby, smart coatings are also studied in this thesis to enable the self-sensing properties of ordinary structural elements. In this context, a machine-learning-aided tomography method is proposed to interpret the data provided by a nanocomposite paint interrogated electrically.

Incorporated publications

Part of the text, figures, and tables in this thesis is published in the following papers:

- **Quqa S.**, Landi L., Diotallevi P.P. (2021). Modal assurance distribution of multivariate signals for modal identification of time-varying dynamic systems, Mechanical Systems and Signal Processing, 148, 107136. DOI: 10.1016/j.ymssp.2020.107136
- **Quqa S.**, Bernagozzi G., Landi L., Diotallevi P.P. (2021). A novel time-frequency distribution for real-time monitoring of civil infrastructures, in: Special collection of papers of the European Workshop on Structural Health Monitoring, pp. 335-345. DOI: 10.1007/978-3-030-64594-6_34
- **Quqa S.**, Landi L., Diotallevi P.P. (2021). Seismic structural health monitoring using the modal assurance distribution, Earthquake Engineering and Structural Dynamics, 50, pp. 2379-2397. DOI: 10.1002/eqe.3451
- **Quqa S.**, Bernagozzi G., Landi L., Diotallevi P.P. (2020). Dynamic identification of a reinforced concrete structure by means of modal assurance distribution, in: Proceedings of the 17th World Conference on Earthquake Engineering (17WCEE), 6g-006. September 27 October 2, 2021, Sendai, JP.
- **Quqa S.**, Landi L., Diotallevi P.P. (2020). Instantaneous modal identification under varying structural characteristics: a decentralized algorithm, Mechanical Systems and Signal Processing, 142, 106750. DOI: 10.1016/j.ymssp.2020.106750
- **Quqa S.**, Landi L., Diotallevi P.P. (2022). Instantaneous identification of densely instrumented structures using line topology sensor networks, Structural Control and Health Monitoring, 29(3), e2891. DOI: 10.1002/stc.2891
- **Quqa S.**, Landi L., Diotallevi P.P. (2021). Automatic identification of dense damage-sensitive features in civil infrastructure using sparse sensor networks, Automation in Construction, 128, 103740. DOI: 10.1016/j.autcon.2021.103740
- **Quqa S.**, Giordano P.F., Limongelli M.P. (2022). Shared micromobility-

driven modal identification of urban bridges, Automation in Construction, 134, 104048.
DOI: 10.1016/j.autcon.2021.104048

- **Quqa S.**, Antolini A., Franchi Scarselli E., Gnudi A., Lico A., Carissimi M., Pasotti M., Canegallo R., Landi L., Diotallevi P.P. (2022). Phase change memories in smart sensing solutions for structural health monitoring, Journal of Computing in Civil Engineering, 36(4), 04022013.
DOI: 10.1061/(ASCE)CP.1943-5487.0001027
- **Quqa S.**, Shu Y., Li S., Loh K.J. (2022). Pressure mapping using nanocomposite-enhanced foam and machine learning, Frontiers in Materials.
DOI: 10.3389/fmats.2022.862796

Acknowledgements

First and foremost, I would like to express my sincere gratitude to my Advisor and Co-Advisors, for introducing and supporting me in my research activities, constantly interfacing with me professionally and friendly. Prof. Pier Paolo Diotallevi first gave me the opportunity of approaching research, fueling my interest with inspiring talks. With his insights and valuable suggestions, Prof. Luca Landi always gave me freedom, an essential ingredient to loving what we do. Prof. Maria Pina Limongelli has broadened my scientific and personal vision, opening a stimulating and fruitful collaboration network. Prof. Kenneth J. Loh gave me the opportunity of spending a research period at the University of California, San Diego, and in one of the most beautiful places on Earth, offering stimulating challenges and highly-experienced support.

I would also like to express gratitude to the reviewers of this thesis.

Affectionate thanks go to my family, small only in size, and especially to my mom. Without her sacrifices, I would not be here.

Special thanks go to my friends and colleagues, who always supported me. Pier Francesco: working (and running on the A13 bridge) had never been that funny and constructive. Alessio: philosophy talks gave me recreation and nerve. Vittoria, Clementina, and Lidia: I believe that our connection will last forever.

I also thank my failures.

Said Quqa

Contents

List of Figures

List of Tables

1 Introduction

Civil structures vibrate when subject to phenomena such as traffic, human activities, and weather actions. Based on the assumption that dynamic structural properties reflect their mechanical characteristics, the analysis of micro-vibration induced by these phenomena may provide valuable information on the structural properties. Vibration-based Structural Health Monitoring (SHM) is a tool to assess the state of a structure based on information retrieved from its vibration response. Specifically, structural parameters are identified using structural identification techniques and employed to define a Damage-Sensitive Feature (DSF). These features are then monitored over time to identify changes in the structural behavior, which are possibly connected with ongoing damage.

However, micro-vibration can only be collected using specific – and often expensive – sensing instruments, especially when the structure is not artificially excited. Indeed, devices with high-sensitivity and low-noise floor, such as particular accelerometers, are needed to collect low-amplitude structural vibration. This is why SHM is generally perceived as expensive, if not directly related to the benefit it brings in terms of decision support, for instance for emergency management or maintenance planning.

Structural vibration is a superposition of the effects of several phenomena merged without any straightforward way to separate them. These phenomena include multiple exciting factors, inherent structural nonlinearities, and environmental influences (such as temperature and humidity). Besides, the measurements are affected by instrumentation inaccuracies. This last aspect gains particular relevance with the use of recent low-cost sensing devices based on

Micro-ElectroMechanical System (MEMS) coupled with wireless transmission technologies. Given the complexity of the structural identification problem, the first studies in this field were based on strict assumptions on the nature of excitation. Indeed, well-known algorithms used to identify structural parameters from vibration responses assume stationary input excitation (with a wide frequency range) and linear structural behavior, as it will be discussed in Chapter 2. Some solutions were also proposed to process the unavoidable nonidealities of collected data (such as short-term nonstationarities due to varying excitation) simply by considering a sufficiently long dataset to minimize the contribution of these flaws to the outcome.

For decades, SHM applications were devised to compare two "static" conditions of the structure, namely, a baseline condition and a "possibly damaged" condition, having plenty of time to record and process the data in the two situations separately. However, traditional identification methods may be improper in particularly complex scenarios, such as the urban environment, where human activity is intense and traffic is a continuously varying excitation source. Also, in the aftermath of an earthquake, having a timely and complete picture of the structural state is of fundamental importance to promptly take decisions for emergency management. Besides, in these cases, accurate analysis of what happens during the seismic motion can help understand the state of health of a structure and schedule targeted inspections.

External phenomena that may lead to nonstationary and short-term excitation to the structural system were traditionally considered detrimental and represented limitations in practical applications. Thereby, research efforts were spent to mitigate their effects.

Unlike traditional approaches, this thesis studies strategies, algorithms, and technologies to take advantage of those scenarios where the structural response considerably deviates from the simplified assumptions of linear time-invariant systems, highlighting the structural characteristics under particular loading conditions. Thus, this thesis aims to provide efficient tools to enable low-cost SHM of minor structures and infrastructure in the challenging scenarios of the urban and extra-urban environment. The main focus is on exploiting conditions that are typically overlooked in

traditional approaches for identifying DSFs from vibration measurements. Moreover, a new device is proposed to determine the strain distribution of specific structural elements, which becomes particularly useful to support damage identification when structural systems are particularly complex, or the vibration level is too low for low-cost sensing instruments.

1.1 Novel contributions

This thesis aims to build on the rich body of work in SHM and propose original strategies, algorithms, and technologies to obtain information about structural damage from vibration data and "enhanced" structural components. Specifically, the main novelties of this study are listed below:

- A new method is proposed to identify modal parameters in the presence of nonstationary excitation, vanishing components, and narrowband disturbances, typical of the urban environment, where the primary excitation sources are traffic, means of transport, and people activities. Identified modal parameters are instantaneous and can describe variations of the dynamic behavior for time-varying structures. Moreover, the definition of instantaneous nonlinear normal modes allows analyzing nonlinear systems and identifying particular damage conditions, such as breathing cracks, hardly identifiable using other algorithms in the current state of the art.
- In addition to modal parameters, the curvature influence line of bridges is identified using acceleration data collected under moving loads. Curvature is a well-established DSF, and the main advantage of the method proposed in this thesis is that dense curvature estimates can be obtained simply by filtering the structural response, without introducing computational errors due to common techniques to obtain curvature from sparse measurements (*e.g.*, modal amplitudes). Moreover, a novel damage index based on this feature can be used for damage quantification. Unlike other methods employed for damage quantification, the knowledge of structural masses is unnecessary in the proposed algorithm.

- A new strategy is proposed to identify dense modal parameters by fusing the data collected by smartphones deployed on moving light vehicles, such as bicycles and kick scooters. To the author's knowledge, these vehicles were never used for SHM, and this thesis includes a proof of concept carried out using a real case study. The strategy is promising and low-cost, as no sensors are needed on the structure, thus being particularly suitable for minor infrastructure and footbridges.
- Analog in-memory computing is first exploited for SHM, allowing the application of the algorithms presented in this thesis in a computationally efficient way. This aspect is fundamental when dealing with low-cost wireless sensing devices, as it enables efficient edge computing and data compression, thus reducing transmission, which is the most power-consuming part of a wireless sensor network. Compared to other technologies based on microcontrollers, the devices proposed in this study can calculate vector-matrix multiplications in one clock cycle and do not need extensive reading/writing processes that increase runtime and power consumption.
- A new device for local strain mapping is presented, based on a nanocomposite paint that can be easily spayed on a structural element and interrogated electrically to provide a tomographic image representative of the health state of the substrate. Compared to other devices traditionally used to monitor the strain distribution, this solution is easily scalable and provides dense measurements with a single interrogation process.

1.2 Thesis overview

This study investigates common scenarios in the built environment where monitoring could be challenging due to several aspects, including particular excitation sources, the effects generated by moving vehicles, and the limited economic availability for monitoring minor infrastructure. In particular, three main scenarios are considered:

Scenario 1: Civil structures instrumented with dense low-cost sensor networks subjected to nonstationary excitation

induced by nearby traffic, earthquakes, and weather-related sources.

Scenario 2: Bridges instrumented with sparse sensor networks subjected to direct vehicular traffic.

Scenario 3: Light bridges and footbridges, without any specific monitoring instrumentation, crossed by micromobility vehicles, such as bicycles, instrumented with smartphones that operate as moving sensors.

These scenarios are closely interconnected and, therefore, they will not be investigated separately. Instead, the thesis is organized as follows:

Chapter 2, *State of the art*, describes the context of SHM in challenging scenarios, highlighting the major issues related to the analysis of short and nonstationary signals collected during high-intensity vibration events. This section also surveys the latest technologies and algorithms to enable edge computing and exploit the capabilities of low-cost smart sensing systems. Moreover, the last developments in self-sensing structural elements are reported.

Chapter 3, *Filtering vibration*, provides an idea of how structural features and, in particular, modal parameters can be identified in multivariate acceleration recordings and extracted using mainly filtering operations. In this chapter, structural vibration response is studied to extract instantaneous modal parameters. To this aim, a new Time-Frequency Representation (TFR) for multivariate signals is proposed based on the Modal Assurance Criterion (MAC), called "Modal Assurance Distribution" (MAD). This TFR provides an intuitive representation of the modal features of multivariate signals in the time-frequency plane. Moreover, the method proposed provides a TFR that is not directly dependent on the amplitude of signal components, making it particularly suitable for nonstationary signals, even with vanishing components. Based on this TFR, an original signal decomposition algorithm is proposed to extract decoupled modal contributions, which can thus be employed to identify modal parameters. The modal identification algorithm is also applied to nonlinear dynamic responses, considering the Rosenberg definition of Nonlinear Normal Mode (NNM). The instantaneous identification of NNMs allows calculating structural features before, during, and

after strong seismic motions to understand if particular damage conditions are only visible during high-amplitude excitation, *e.g.*, breathing cracks. Two original decentralized procedures are also presented for distributed implementation of the modal identification algorithm, one for star-topology sensor networks (easily applicable to tree topologies by organizing the network in separate clusters) and one for line-topology dense sensor networks. In the second procedure, a novel data compression strategy is proposed to enable the real-time identification of natural frequencies and mode shapes of the structure while minimizing transmitted data. In this case, the power consumption and the computational effort that compete with each node of the sensing system are unrelated to the network size, making the proposed scheme easily scalable. Application examples are presented to show the potential of the proposed identification algorithm to calculate the modal parameters of time-varying systems subjected to nonstationary input excitation, such as those in Scenario 1, even with nonlinear structural behavior. Identified parameters are also employed for damage identification, showing that near real-time damage identification is pursuable even using wireless sensor networks.

Chapter 4, *Exploiting traffic*, based on the concept of filtering, investigates the low-frequency (*i.e.*, quasi-static) effects of moving loads on bridges and viaducts. First, an original algorithm is proposed in this context to identify influence lines using sparse instrumentation, simply by filtering the recorded acceleration during the passage of a vehicle through a particular low-pass filter. In contrast to traditional identification strategies relying on multiple sensors, in this case, spatial information is acquired by considering a moving load that excites all the structural points in time. Identified quasi-static structural features are then employed for damage localization and quantification: due to the physical meaning of the extracted quasi-static feature, a curvature-based DSF is proposed, removing the complex procedures (and thus approximations) which are generally necessary for traditional methods to calculate curvature from identified mode shapes. This novel approach brings considerable advantages, as it enables accurate localization of structural anomalies using limited (and thus low-cost) instrumentation, suitable for widespread monitoring, and removes the need for data synchronization. Unlike

most literature methods [1, 2], damage entities can be quantified without any knowledge of the structural masses and avoid using finite element models. Data extracted from numerical and real case studies representative of Scenario 2 are used to support the findings of this chapter. Second, the applicability of the MAD is tested for civil infrastructures subjected to moving loads. Although the MAD-based identification algorithm has several benefits over other literature methods in many application scenarios, moving loads and short datasets pose a further challenge. A unified and automatic identification strategy usable for Scenarios 1 and 2 is thus proposed for estimating both dense quasi-static structural features and modal parameters using sparse sensor networks (consisting of down to just one sensing device). The procedure relies only on acceleration recordings, without additional devices to track the vehicle location. Moreover, the algorithm proposed for automatically selecting and processing signal windows related to the vehicle passage makes this method particularly suitable for crowdsourced cloud computing applications. Third, this chapter extends the available knowledge on Indirect Structural Health Monitoring (ISHM), exploring the possibility of using unconventional vehicles, *i.e.*, Human-Powered Vehicle (HPV)s, for infrastructure monitoring (Scenario 3). Specifically, the feasibility of using bicycles to extract modal or operational parameters commonly employed by vibration-based SHM methods, *i.e.*, natural frequencies mode shapes or operating deflection shapes, is demonstrated. This research lays the foundations for a human-centered monitoring approach of urban bridges based on shared micromobility vehicles and smartphones. In this scenario, citizens acquire a crucial role in structural health monitoring, becoming a part of the sensing network themselves. It is shown that dense estimates of the fundamental mode shapes can be identified by fusing the data collected by the accelerometer, gyroscope, magnetometer, and Global Positioning System (GPS) embedded in common smartphones. These features can be further employed for damage assessment. Applications to a real case study show that the identified estimates acquire robustness when different users collect multiple recordings in a crowdsensing monitoring strategy.

Chapter 5, *Improving efficiency*, focuses on new technologies to improve the efficiency of the proposed monitoring solutions in

real-world implementation. Filtering is the main computing core of the procedures investigated in Chapter 3 and Chapter 4. Therefore, in this thesis, new solutions are studied to reduce computational time and enable edge computing, *i.e.*, performing filtering tasks directly onboard the sensing devices. Phase Change Memory (PCM) allows performing vector-matrix multiplication (and thus filtering) in a single clock cycle, saving both time and energy. The benefits of PCM technology have never been employed for signal filtering or SHM purposes. Although this tool may be highly convenient, issues related to the accuracy of computations are topical in related research. In this study, the workflow of the structural identification algorithm developed for Scenarios 1 and 2 is adapted for efficient distributed implementation using PCMs. The proposed identification method is mainly based on signal filtering and allows the extraction of both dynamic and quasi-static structural parameters, namely, mode shapes and curvature influence lines of the instrumented structure employing sparse sensor networks. Specifically, an iterative version of the algorithm makes filtering particularly suitable for practical implementation in PCM-based smart nodes for civil infrastructure monitoring under traffic loads. Real acceleration data, processed using a laboratory prototype of PCM show promising results for field applications.

Chapter 6, *Integrating information*, deals with situations where vibration-based SHM is not sufficient for simplifying the decision-making process or when Signal-to-Noise Ratio (SNR) of collected vibration is not high enough to allow identifying accurate structural features, such as at the base of bridge piles. In this chapter, a non-invasive static monitoring technique based on self-sensing structural components is investigated. Since introducing self-sensing elements in existing structures is not straightforward, smart paints were considered. Specifically, two sprayable conductive paints based on graphene nanosheets and carbon nanotubes are studied. The smart paint can be sprayed on structural elements and interrogated to provide an estimate of the strain state and health condition of the substrate, or evaluate the presence of dangerous chemical agents that may accelerate material degradation. The use of smart coatings on regular structural elements enables self-sensing properties, which provide valuable information to identify the causes of iden-

tified anomalies and better understand how to schedule targeted interventions. Electrical Impedance Tomography is employed in this study to obtain dense information on the inspected elements simply by (remotely) interrogating the boundaries of self-sensing components with electrical pulses. Supervised Machine Learning (ML) is exploited to simplify the complex inverse EIT problem and enable edge computing. Since the construction of a reliable training dataset is fundamental for supervised applications, this thesis also proposes a new strategy to generate a potentially unlimited dataset for end-to-end machine learning tools that enables high-resolution crack localization. Besides, a method to assess the suitability of the training set for the desired application is proposed, based on self-organizing maps, an unsupervised ML tool generally employed for data visualization.

Chapter 7, *Conclusions and future research*, reports the concluding remarks and future developments of the studies included in this thesis.

State of the art 2

This chapter provides a general idea of the common issues of vibration-based SHM and the most relevant contributions in this field. Particular attention is posed to the challenges that characterize the built environment, considering nonstationary input excitation, traffic load, and human activities that represent the dynamic society of nowadays. Technical aspects and the latest trends adopted for sensing are also mentioned since they have a crucial role in developing monitoring systems.

2.1 Common issues in monitoring the built environment

Dynamic identification of vibrating systems is a fundamental aspect in different engineering areas, such as civil [3–5], mechanical [6, 7], and aerospace [8, 9], as it enables assessing the structural state of health even for structures that do not show an evident state of degradation[10].

In the last decades, an increasing number of techniques have been proposed for dynamic identification, attempting to broaden the field of applicability and release the assumptions that may limit practical applications. Some types of structures are time-varying, and traditional identification algorithms based on the assumption of stationarity may be unsuitable. This is generally the case for bridges with vehicular traffic [11], time-periodic systems [12], and

robotic or aerospace structures with time-varying geometry [13, 14], to name a few. Besides, some research [15–17] has been recently conducted on methods that refer to short-term recordings obtained during strong events (*e.g.*, seismic events) to study the short-term variation of structural parameters due to nonlinearities. In these cases, identifying instantaneous parameters is of the utmost importance. Indeed, features identified on long time intervals result from an average process that accounts for all the short-term phenomena included in the analyzed time window. Therefore, short-term effects observable during high-amplitude vibration (*e.g.*, due to breathing cracks or other structural nonlinearities) and moving loads (*e.g.*, due to the quasi-static displacements of a bridge deck under passing vehicles) would be lost using long-term features.

Dynamic identification with nonstationary excitation

Several methods have been proposed for the modeling and analysis of nonstationary signals, which can be classified into parametric and non-parametric methods. The first group is mainly based on parametrized time series representations, namely, the time-dependent extensions of autoregressive moving average [11, 18, 19]. On the other hand, the majority of non-parametric methods are based upon TFRs of the vibration energy and allow more intuitive extraction of modal parameters (*i.e.*, natural frequencies, mode shapes, and damping ratios), which are the most used for damage identification of civil structures due to their explicit physical interpretation [3]. Herein, a brief survey of the most used TFRs for dynamic identification of time-varying systems subjected to nonstationary excitation is reported.

Due to the interconnections born in the last few decades between the fields of linear algebra and subband coding [20], a considerable number of transforms leading to different TFRs were proposed. The Short-Time Fourier Transform (STFT) [21] and the Wavelet Transform (WT) [22] are among the most used linear transforms; the first employs a fixed complex exponential windowing function for the analysis, while the second relies on a family of more flexible functions. More recently, the S-transform [23] has received extensive interest due to its versatility since its windowing function is a

Gaussian-windowed complex exponential, the dimensions of which scale as a function of frequency, resulting in a frequency-dependent resolution analysis.

The Wigner-Ville Decomposition (WVD) [24, 25] was also widely studied because of its paramount importance in TFR theory since it does not use any other windowing function except for the signal itself (autocorrelated in the transform definition). On the other hand, practical applications on multicomponent signals are challenging for this transform because of its bilinear structure that creates cross-terms that undermine the distribution readability.

Most identification methods based on the analysis of TFRs may suffer from problems related to closely-spaced, vanishing, and crossing modes. Furthermore, energy concentrations in the time-frequency (or time-scale) plane could also be due to narrow-band disturbances in the excitation, which would be identified, in most cases, as structural modes.

Two classes of methods for improving the readability of TFRs are the reassignment (or reallocation) and synchrosqueezing, shown to be the second a special case of the first [26]. Highly localized TFRs have been derived from STFT and WT by using these post-processing techniques. In particular, the SynchroSqueezed Transform (SST) was formalized as the application of synchrosqueezing on scalograms obtained through continuous wavelet transform. This method received significant interest as an alternative to the Empirical Mode Decomposition (EMD) [27], which is a different technique used to extract signal components associated with different frequencies, *i.e.*, Intrinsic Mode Function (IMF), without relying on any basis function [28]. EMD is mainly used together with the Hilbert Transform (HT), resulting in the Hilbert-Huang Transform (HHT). However, in its original form, this method is affected by several problems, including mode mixing, one of the most important issues for applications aimed at SHM [29]. For this reason, several variants have been proposed. One of the most used is the Ensemble Empirical Mode Decomposition (EEMD), which consists of sifting an ensemble of signals obtained by adding different white noise sequences to the original data and computing the final result as the mean of IMFs

obtained [30]. This method still presents issues related to crossing and vanishing modes.

Recently, the concept of modulated multivariate oscillations was introduced [31, 32], together with analysis methods capable of extracting TFRs from multichannel signals, exploiting the inter-channel dependencies of multivariate data. Namely, extensions to the WVD [33], SST [34], and EMD [35] were proposed.

In particular, the purpose of Multivariate Empirical Mode Decomposition (MEMD) is to extract common IMFs from all data sets by analyzing different projections of the multivariate signal to calculate its envelopes and local mean. Furthermore, some techniques merge noise-assisted and multivariate approaches into increasingly complex methods [36]. The main disadvantage of these techniques is the high computational burden, given by the high number of ensembles necessary to remove the traces of noise introduced in the noise-assisted methods and the number of projections considered in the case of multivariate analysis using MEMD [37].

Except for EMD and its extensions that directly provide IMFs from raw data, non-parametric methods require post-processing procedures to extract the modal parameters from TFRs, generally involving the preliminary decomposition into different modal responses [38, 39]. To this aim, in several applications, a ridge extraction is directly performed on the TFR by finding the local maxima of the distribution over time [40, 41]. However, this procedure may suffer from problems related to components with nonstationary amplitudes and noisy signals [42]. Wang et al. [43] proposed a dynamic optimization method by introducing a penalty function for noisy signals. Other authors investigated the use of Singular Value Decomposition (SVD) for ridge detection [44, 45]. Ditommaso et al. [15] proposed an algorithm based on the manual selection of the areas of the TFR associated with the modal response of interest, facilitated by the good readability obtained through the S-transform.

After detecting and extracting the ridges, modal parameters can be estimated from the skeleton of the TFR (*i.e.*, the sequence of transform coefficients associated with the ridge) [39]. However, the mere extraction of coefficients associated with the frequency peaks may lead to problems related to the complete reconstruction

of decoupled modal responses. In order to limit these issues, more sophisticated techniques based on image processing applied to TFRs are taking a step into system identification. Some researchers first employed image processing to de-noise TFRs [46] and attenuate cross-terms of WVD [47]. Successively, they used image processing to separate modal components. In [48], the regions of the time-frequency plane associated with the energy peaks of different modes are extracted by means of the watershed transform, which is a morphological-based segmentation algorithm [49] previously used by Roueff et al. [50] on scalograms to separate seismic waves. Zhuang et al. [51] used a simpler 4-connected-component labeling algorithm to decompose the signal in the time-frequency domain [52]. One of the major problems related to these procedures concerns the difficulty of effectively separating closely-spaced modes. Indeed, close resonant frequencies may be merged into the same region of the time-frequency distribution by the pre-processing mathematical morphology operations performed to obtain a proper segmentation (*e.g.*, dilation and closing) [53]. Other issues may arise in the case of noisy signals, for which the energy is spread throughout the time-frequency plane, and spurious peaks may be detected.

Dynamic identification of structures with nonlinear behavior

An element that introduces further difficulties in identifying modal parameters is structural nonlinearity. In nature, the dynamic behavior of structures generally follows nonlinear laws [54]. In civil engineering, there are several sources of nonlinearity, mostly related to material behavior (*i.e.*, constitutive laws), geometry (whenever the magnitude of the displacements affects the structural response), and boundary conditions [55, 56]. Several studies also show how nonlinearities usually increase in damaged structures, for which cracks and loosening of connections may occur [56, 57].

In the context of vibration-based SHM, linearity is a necessary assumption for using classical modal analysis methods. Thus, nonlinearities are usually overlooked during the application of Operational Modal Analysis (OMA), relating to the fact that ambient vibration is modest, and the effects of nonlinearities are noticeable only under high-energy excitation [58].

One of the latest trends in SHM is known as "Seismic Structural Health Monitoring" S^2HM [59], for which recordings obtained during seismic events are used for dynamic identification and model updating. This approach allows assessing damage in the aftermath of an earthquake, using short datasets collected immediately before, during, and after the seismic event. In this way, the effects of temperature or variable environmental conditions which may alter the parameters identified in the long term are avoided [16].

Improvements in the hardware apparatus of sensor networks, which lead to increased energy efficiency and the possibility of collecting high-fidelity data, have recently enabled the development of event-triggered sensing systems [60]. These systems are designed to collect data (usually consisting of acceleration recordings) only when a certain amplitude threshold is exceeded. The transmission of a short dataset to the monitoring station is far more efficient than continuous transmission during the monitoring process. Furthermore, recordings obtained during strong events usually have a high SNR, allowing structural characterization even with short data series. However, in the case of strong events, many systems, such as Reinforced Concrete (RC) structures, may manifest strong nonlinearities that can no longer be assimilated to a linear behavior. In fact, according to current codes, civil structures are designed with specific ductility requirements to take advantage of the excursion in the nonlinear field during earthquakes [56].

Since nonlinear structural elements are increasingly used in engineering applications, several studies have been conducted recently on modeling and identifying nonlinear structures [61]. The basic principles usually assumed for modal identification of linear systems (such as the superposition principle) may be no longer usable in the presence of nonlinearities. In this case, modal responses cannot be studied by separating space and time information, and the traditional concept of vibration modes is no longer applicable. Rosenberg [62] first extended this concept by defining a Nonlinear Normal Mode (NNM) of an undamped system as a synchronous (vibration in-unison) periodic oscillation where all material points of the system reach their extreme values and pass through zero simultaneously. This definition is also usable in the case of weakly

damped systems and enables the description of nonlinear structures employing a (nonlinear) modal curve in the configuration space [56].

Several identification algorithms for nonlinear systems operating in time [63, 64], frequency [57], and time-frequency [65] domain were proposed in the last decades. Also, model-based [66, 67] and black-box [68] techniques are taking steps into SHM applications based upon finite element model updating and artificial neural networks.

Recursive approaches for estimating time-varying structural features were largely investigated in the time domain. Loh and Lin [69] identified time-varying natural frequencies and damping ratios employing single-input and single-output pairs consisting of the ground excitation and the structural response, respectively. More recently, Bhowmik et al. [70] used the recursive canonical correlation analysis to implement a reference-free damage identification method for online applications. However, recursive approaches generally need a convergence interval, making them unsuitable for short-term event-triggered applications.

The HHT [28] is currently one of the most largely used time-domain techniques for nonlinear systems, as it allows the instantaneous description of structural resonant frequencies and modal amplitudes [63, 64, 71]. The WT also found application in studies concerning nonlinear dynamic systems [65], as well as the S-transform. In particular, Ditommaso et al. [15] analyzed the dynamic behavior of structures under seismic excitation, considering the mode shape related to the minimum frequency recorded during the maximum excursion in the plastic field as a DSF. Other developments of this method gave rise to reliable damage localization algorithms [17].

2.2 Smart sensors

Some SHM applications may involve limited space for sensor installation, obstacles that may hinder cable deployment, and continuous movement of the workforce, which could damage parts of the monitoring system. Wireless transmission technologies are preferable in

these cases, and when the deployment of long cables may increase the overall costs considerably [72]. However, continuous high-rate data streaming is impractical through wireless systems, especially for dense sensor networks.

Recently, technologically innovative wireless sensing systems have been introduced [73–75] with new MEMS sensors connected to microcontrollers capable of performing simple onboard operations. Their limited computational capacity can be exploited for edge computing, which has recently proven to be an attractive solution in the SHM field [76–78]. Lately, several researchers focused on the development of decentralized algorithms [79] in which part of the signal processing procedures (*e.g.*, filtering and downsampling) is performed at the node level. In this way, the data transferred to the monitoring station is lighter, and the computational burden is significantly reduced, making possible an online monitoring process.

Battery life is one of the most critical issues for wireless monitoring systems, especially when continuous onboard procedures are implemented. Nevertheless, processing and transmissions can be optimized [80], considering an acceptable latency in parameter identification and gaining in network efficiency. To this aim, new algorithms and technologies have been proposed recently.

Latest trends in algorithm development

In the last decades, several studies have been conducted to adapt traditional identification techniques in distributed computing schemes (*e.g.*, the frequency domain decomposition [81], the natural excitation technique [79], and the random decrement method [82]), involving smart sensors organized in tree-type computational models. Besides, Long and Büyüköztürk [78] proposed a novel implementation of the frequency domain decomposition, together with an optimal task allocation algorithm to maximize the efficiency of wireless sensor networks.

More recently, tailored identification algorithms were proposed to exploit the potential of edge computing. Yun et al. [83] implemented a new method suitable for wireless smart sensor nodes

employing wavelet entropy analysis. In this study, the excitation has been assumed as band-limited white noise. Sadhu and Narasimhan [84] proposed a static filtering method based on the Stationary Wavelet Packet Transform (SWPT) for signal decomposition and Fourier transform to identify modal parameters. Other authors presented methods based on the HHT that, however, is not suitable for online applications in the traditional form because of its global rather than local nature [85]. Wang and Chen [86] proposed a method for online identification of time-varying properties of structures employing a recursive HHT-based procedure. Bao et al. [87] applied the HHT on cross-correlated data windows to improve the robustness to noise contamination. To avoid the difficulties related to the Hilbert transform, such as the computation of analytical signals during online applications, some authors experimented with other techniques to extract instantaneous parameters. Ghazali et al. [88] presented a comparative study illustrating the performance of Hilbert transform and other methods, namely, cepstrum analysis, direct quadrature, and Teager Energy Operator (TEO), showing how the last one is simple and suitable for online applications but very sensitive to noise. Moreover, this method can only be applied to mono-component signals and requires prior decomposition.

Goulet and Smith established that largely redundant instrumentation can hinder the ability to interpret data [89]. Indeed, several authors investigated optimal sensor placement to limit instrumented locations and find a compromise between monitoring costs and expected identification performance. For example, Zhou et al. [90] proposed a tool to find the optimal sensor placement using genetic algorithms. On the other hand, due to the accessible cost of the components employed in Wireless Sensor Network (WSN) s and the development of power-optimized systems [78] and advanced synchronization strategies [91, 92], dense distributions of smart nodes are increasingly used for SHM applications [93]. Jang et al. [94] developed an event-triggered system using 70 sensor nodes and two base stations. Real-time implementation has generally demonstrated unfeasible at this scale, making the use of a proprietary wireless network protocol necessary. Whelan et al. [95] developed a network with 40 nodes using a proprietary protocol that supports high-rate acquisition with minimal data loss for real-time applications.

A recent branch of research is oriented towards applying SHM algorithms to large structures and infrastructures using wireless sensing systems, facing the issues that may arise when dealing with complex network topologies [93, 94, 96]. While the tree topology is the most used for practical use, the line topology is particularly suitable for densely distributed structures having a one-dimensional development [97]. However, in traditional applications, the weight of the data packets increases along the transmission path, becoming demanding in the final portion of the network, where the nodes consume a significant amount of energy in forwarding all the data packets collected throughout the sensing system.

Decentralized sensor networks are still rarely implemented for real-time monitoring. However, distributed solutions supported by efficient algorithms for data management may have a key role when online decision making must be achieved for densely instrumented structures, such as for civil buildings and infrastructures in emergency situations.

Latest trends in technology development

One of the most well-known hardware solutions employed to build smart sensing nodes in scientific literature is the Single-Board Computer (SBC). The Imote2 platform, developed by Intel Research, was largely used for laboratory tests and then employed for bridge monitoring [94, 98, 99]. In order to make this system suitable for SHM applications of civil infrastructure and accessible to users without expertise on TinyOS, several sensor boards were designed and a simplified software framework was developed afterwards. In particular, Rice and Spencer [100] proposed the SHM-A sensor board, which was employed in the monitoring campaign of the 2nd Jindo Bridge [94], while Jo et al. [79] proposed the SHM-H board with a high-sensitivity accelerometer used to perform the decentralized stochastic modal identification of a steel truss. Moreover, a service-oriented toolsuite was developed to allow researchers and engineers to easily implement SHM applications [98]. More recently, the Xnode has been presented by Spencer et al. [101], which uses a Real-Time Operating System (RTOS) and a high-resolution

Analog-to-Digital Converter (ADC) to address some of the limitations of the Imote2 devices emerged from the long-term monitoring experience of the 2nd Jindo Bridge. Furthermore, Sabato et al. [102] developed the Acceleration Evaluator, a wireless sensor prototype able to detect microvibrations thanks to the implementation of a voltage-to-frequency converter instead of conventional ADC.

Different computing solutions able to generate a higher throughput were also explored to facilitate high-frequency and real-time applications. Liu and Yuan [103] proposed a dual-controller based architecture that comprises a Field Programmable Gate Array (FPGA) supporting a much higher sampling rate compared to traditional SBC-based solutions. Cigada et al. [104] used an FPGA to perform filtering and downsampling operations in a system used for monitoring the San Siro Meazza Stadium in Milan, Italy. This solution guaranteed durability and the possibility of using high-resolution ADC modules. On the other hand, Varadan [105] proposed to use an Application-Specific Integrated Circuit (ASIC) to further increase durability and processing speed, while reducing size.

Whereas several algorithms have low computational complexity, their implementation in digital systems (*i.e.*, microcontrollers, SBCs, and FPGAs) typically employs many computing steps and extensive memory units to store intermediate results in signal processing operations, thus considerably affecting the overall energy performance. Furthermore, ASICs do not offer versatility since they should be programmed for each specific application.

Phase Change Memory (PCM) has recently emerged as an attractive tool for in-memory computing, which overcomes the conventional computation model by performing operations directly in a memory device [106]. Concerning industrial and commercial applications, PCMs are manufactured only for digital storage at the date [107]. However, recent results highlight their potential for edge computing applications [108], as their features allow accelerating the computation of basic operations, thus reducing power consumption and latency [109, 110]. Specifically, the PCM technology has been successfully employed for image recognition implementing machine learning tools [111–113], and it demonstrated particularly performant for the development of low-power computing architectures [114],

as well as hardware accelerators for data-centric frameworks [115]. Nevertheless, PCM was never employed for smart sensors and edge computing applications in SHM.

2.3 The role of traffic

Failure in road infrastructure leads to immediate direct losses due to the costs of repair or demolition/reconstruction, as well as long-term indirect effects, involving the costs of temporary measures for emergency management, traffic delays, deviations, and accidents, which may also entail longer journeys for emergency vehicles. Economic losses on industry and local business, together with the consequent decrease of demand for work, complete the framework of a catastrophic event, which can also involve the most severe loss concerning human life. Due to the aging of bridges and viaducts and the evolution of traffic demand, structural degradation is becoming a serious concern. Due to the general lack of resources, the recent trend is to migrate from the traditional planned maintenance to condition-based maintenance, performed when certain indicators show signs of decreasing performance or upcoming failure. In this way, the uneconomical "fail and fix" approach would be replaced by a more efficient "prevent and predict" strategy. In the last decades, SHM systems have proven to provide a valuable tool to decision-makers in order to optimize maintenance or interrupt the ordinary use of crumbling infrastructure. Although "information never hurts" [116], the high cost of traditional monitoring systems makes the infrastructure owners skeptical about the investment [117]. Indeed, the age of most civil infrastructure would require the widespread deployment of monitoring systems to manage interventions at a territorial scale, thus involving considerable expenses, which are generally unjustified for minor infrastructures.

Vehicular traffic is an essential source of excitation that allows collecting recordings with a high SNR ratio compared to ambient vibration. However, as aforementioned, the time-variability of the load may not comply with the assumption of stationary vibration at the base of most operational modal analysis OMA [58]. The passage of loads may also modify the short-time behavior of the structure,

opening breathing cracks in RC elements and producing dynamic effects when vehicles hit the expansion joints. Thereby, recordings containing such effects are generally discarded in OMA procedures. However, the spatial information inherent in the structural response collected under moving loads may disclose valuable structural features for SHM purposes.

Aloisio et al. [118] recently studied RC viaducts using signals collected under moving loads to identify their elastic moduli. Khan et al. [119] recently used traffic-induced vibration to identify scour in a decentralized fashion. Besides, recent studies have been devoted to identifying dense structural features (*i.e.*, describing the structural behavior at many locations) by analyzing the quasi-static effects of moving loads. He et al. [51] proposed a damage identification approach that can quantify damage using displacement data collected by a sensor moving at low speed, thus only collecting the quasi-static response of the specimen. Cavedas et al. [120] assessed the performances of moving Principal Component Analysis (PCA) and Robust Regression Analysis (RRA) for this purpose using both displacement and rotation measurements. Other techniques attempt to obtain similar results by analyzing recordings collected by sensors deployed on the bridge rather than on moving vehicles, which are generally less sensitive to vehicle-bridge interaction effects. Frøseth et al. [121] proposed an efficient formulation to calculate the displacement influence line of the structure through deconvolution in the frequency domain. However, in this technique, loads must be known in advance. In the time domain, Zheng et al. [122] presented an efficient regularized least-squares-based method for identifying influence lines using multi-axle vehicle excitation. A review of the most recent methods employing both frequency and time-based models, together with an in-depth comparison, is presented in [123]. Hester et al. [124] employed the rotation measurements collected at the extrema of a beam to identify and localize damage accurately.

Besides rotations and displacement, strain measurements have also been largely employed [125–127]. However, accelerometers, which are still the most widely used sensors in SHM, have rarely been used to identify quasi-static structural features due to problems related to the recording of low-frequency components. Nevertheless,

recent MEMS technologies and more conventional FBA enable the acquisition of low-frequency vibration down to DC and can thus be exploited to investigate the quasi-static structural behavior.

2.4 The role of citizens

The main drawbacks of traditional SHM systems relate to their installation cost, which is strongly influenced by the typology and number of the sensors employed. Moreover, an accessible power source must be available in the proximity of the monitored structure, and the different components require continuous maintenance, involving additional costs during the lifecycle of the SHM system. Besides, SHM systems are not widespread due to the difficulty of estimating their economic benefit over the initial investment [117, 128].

Recent studies conducted on vibration-based Indirect Structural Health Monitoring (ISHM) exploit the dynamic response of instrumented vehicles to identify structural parameters. In principle, the use of passing vehicles simplifies the monitoring process and cuts the cost associated with the installation of SHM systems. The idea of using sensors installed on moving vehicles was initially explored theoretically by Yang et al. [129] in 2004. Specifically, the authors proposed using an instrumented vehicle both as an exciter and a receiver of the structural response. Lin and Yang [130] subsequently demonstrated the possibility of applying this approach in practice. The authors used a tractor-trailer system to identify the first natural frequency of the Da-Wu-Lun Bridge, a prestressed concrete girder bridge in Taiwan. The tractor consisted of a four-wheel commercial light truck, and the trailer was a two-wheel cart. The tractor acted as an exciter while the accelerometers applied to the cart served as receivers. Kim and Kawatani [131] extended this concept to identify structural damage in bridges, introducing the "drive-by bridge inspection". In their work, the authors identified the change in fundamental frequencies due to structural damage in a scaled laboratory model. González et al. [132] managed to identify the damping ratio using a similar approach. A few years later, Cerda et al. [133] called this concept "indirect SHM", in contrast to the "direct

SHM", where measurements are collected directly on the structure. After that, a growing number of scientific papers have proposed several ISHM approaches in terms of different exciter-receiver configurations. For instance, other measuring devices, *e.g.*, video cameras [134] and weigh-in-motion systems [135] were considered to infer information about the moving loads, and advanced SHM strategies exploiting sensors placed both on the structure and on the moving vehicles have been developed to better describe the vehicle-bridge interaction [136]. Kim et al. [137] also suggested using a tractor and two identical instrumented trailers to improve the estimation of the dynamic properties of the bridge. Li et al. [138] developed an ISHM strategy based on two instrumented vehicles in which the first is used as a fixed reference sensor while the other is a moving sensor. Kim et al. [139] proposed a two-stage wireless monitoring strategy relying on vibrational data provided by sensors installed both on a passing vehicle and on the bridge. Matarazzo et al. [140] suggested using crowdsourced data collected by automobiles as the nodes of large-scale sensor networks for bridge monitoring.

In the last fifteen years, several ISHM methods for bridges based on vibration signals were formulated theoretically and tested on numerical models [132, 141, 142] and laboratory-scale experiments [143–145]. Several studies validated ISHM techniques on real structures, such as cable-stayed [146], continuous steel box girder [139], simply-supported box girder [147], simply-supported steel truss [148], and prestressed concrete girder [130, 149] bridges. These studies employed a variety of vehicles for in-situ SHM applications, such as cars [150], vans [147], trucks [139], tractor-trailer systems [130], busses [151], and even hand-drawn carts [146]. References [152–154] provide comprehensive reviews on ISHM methods for bridges. Specifically, Zhu and Law [154] reviewed SHM methods based on vehicle-bridge interaction. Malekjafarian et al. [152] focused on modal identification, observing that mode shapes are the most complex features to identify. Also, they concluded that the main challenges for indirect bridge monitoring are related to the road profile, the limited recording time, and the presence of environmental effects. Shokravi et al. [153] presented a review that includes vision-based, weigh-in-motion, bridge weigh-in-motion, drive-by, and vehicle bridge interaction-based methods.

Very recently, low-cost ISHM strategies based on data collected by smartphones were proposed. Feng et al. [155] investigated the reliability of smartphone accelerometers for vibration-based direct SHM, while, a few years later, McGetrick et al. [156] explored drive-by monitoring systems incorporating smartphones. Both the studies have shown promising results for drive-by and, in general, SHM applications. To address the issue of the low sensitivity and high noise floor of smartphone sensors, Elhattab et al. [157] proposed a stochastic resonance filter that enables identifying the resonant frequencies of weak signals. Their study successfully identified the first four natural frequencies of a bridge using a smartphone. Ozer et al. [158] proposed an approach to extract modal parameters in a similar noisy environment, dealing with synchronous and sampling-deficient measurements.

Recent smartphones include high-performance batteries and have advanced cellular transmission modules that keep them constantly connected to the Internet, generating continuous transmission traffic. The ubiquity of these devices has provided an opportunity to implement crowdsensing strategies [159, 160]. Ozer et al. [161] have shown the possibility of identifying structural modal properties with high accuracy using measurements collected by citizens without expertise. Ozer and Feng [162] explored the potential of using vibration data measured by pedestrians to identify modal parameters of bridges. A few years later, the same authors [163] experimented with a finite element model updating strategy using vibration data obtained from smartphones. Matarazzo et al. [164] gathered data from UBER riders crossing the Golden Gate Bridge in San Francisco, California, to retrieve the main modal parameters of the structure, which in turn can provide valuable information concerning the health state of the structure. Due to the short duration of typical tests conducted in most of the mentioned studies, accurate vehicle-bridge interaction with road roughness modeling is generally necessary to obtain significant results from the collected measurements. This is one of the most critical limitations of heavy vehicles that also affect the structural dynamics and generate nonstationary excitation, which is typically incompliant with the underlying assumptions of traditional SHM algorithms.

Smartphones have several built-in sensors, generally including an Inertial Measurement Unit (IMU) and a Global Positioning System (GPS) module. Some authors proposed approaches for identifying bridges through heterogeneous data fusion [165, 166]. Ozer et al. [167] presented a method to keep track of the orientation changes of the sensor by integrating different measurements collected through gyroscope, accelerometer, and magnetometer.

Applications using data collected by smartphones are not limited to drive-by monitoring of road bridges. For instance, Feng et al. [155] proposed a smartphone-based crowdsensing network for rapid and low-cost post-earthquake damage assessment of structures and infrastructure at a city-scale, while Seraj et al. [168] and Chuang et al. [169] developed methodologies to evaluate the state or road pavements. Other recent applications fused the data collected by other smart wearable devices to estimate crowd flow and load on pedestrian bridges [170].

Bicycles and kick scooters, cathegorized as Human-Powered Vehicle (HPV), has never been considered in the relevant literature for ISHM. The main advantages of these vehicles are their low cost, high sustainability [171], and the environmental benefits they provide in urban areas reducing traffic congestion [172]. Also, light vehicles generally have low speed and negligible mass compared to monitored structures. Thereby, HPVs do not affect the structural dynamic behavior noticeably. Moreover, these vehicles allow monitoring structures not accessible by cars and trucks, such as footbridges. Nevertheless, noise effects introduced by the driver, vehicle dynamics, and inaccurate smartphone built-in sensors may affect the data recorded onboard HPVs. However, the availability of crowdsourcing data could considerably improve the overall quality of the obtained ISHM results, especially if all the users employ standard vehicle types, *i.e.*, if the vehicle properties are known. Shared micromobility vehicles, such as bike and scooter sharing services, could be particularly useful to this purpose since sharing companies generally provide very few vehicle types in a certain urban area.

2.5 When vibration is not enough

Vibration-based SHM techniques provide global structural features and, therefore, global damage indicators, which are affected by several factors, such as variations in stiffness, mass, and boundary conditions. Nowadays, only a minor subset of damage identification techniques can localize or quantify the damage. These methods generally employ dense and expensive sensor networks. However, in the perspective of monitoring complex structures in a territorial scale, *e.g.*, in a urban environment, detailed information on the identified structural anomalies is fundamental to target visual inspections and operator interventions. Moreover, understanding the causes of structural damage and correlating this information for neighboring or similar structures in a given area could guide higher-level maintenance or reparation intervention. In other words, in an informed decision-making and smart maintenance perspective, vibration data could not be enough.

As an alternative or support to sensor-based solutions, self-sensing materials have recently gained enormous interest in different engineering areas, especially in the civil field, due to the local nature – and thus, spatially accurate – of the related features. These materials, forming "smart" structural elements or integrating the ordinary ones to enable the self-sensing capability, can provide information on cracks, strain states, and the presence of chemical elements that may accelerate material degradation. Therefore, fusing these pieces of information with the damage-sensitive features retrieved by vibration-based methods could help identify the cause of damage and schedule targeted interventions.

Some studies were recently conducted on the sensitivity of nanocomposite materials to chlorides [173] and moisture [174]. Besides, several authors [175–178] investigated the influence of cracks and micro-cracks on the electrical response of piezoresistive Engineered Cementitious Composite (ECC) under direct tension, finding that the variability of their mechanical properties is well reflected in the electrical properties of the structural element. For instance, Ranade et al. [178] found that crack patterns significantly affect the composite electrical behaviors of ECCs obtained with different

mixtures. Baoguo et al. [176] and Rana et al. [177] presented reviews on intrinsic self-sensing materials employed for structural health monitoring. The authors highlighted three general issues in the current state of the art of self-sensing materials: the typically high cost of conductive fillers, the challenge in applying smart material-based monitoring to existing structures and large-scale components, and the difficulty of identifying the damage location. A considerable piece of research has been conducted in the last years to further investigate these topics. D'Alessandro et al. [179] tested different fabrication procedures for electrically conductive cement-based materials to investigate the applicability for large-scale self-sensing structural components. Gupta et al. [175] altered the cement-aggregate interface using conductive nano-engineered coatings that reduce the amount – and cost – of dispersed conductive additives, yielding low-cost concrete specimens with electrical properties that varied in response to physical damage. Moreover, in this last study, the authors employed Electrical Impedance Tomography (EIT) to interrogate the self-sensing element and localize concentrated anomalies.

EIT is a well-established imaging technology broadly applied in the medical field and recently employed for anomaly detection in engineering problems [180]. This non-invasive technology uses electrical excitations and measurements on the boundary of a conductive body to estimate its electrical properties, which can be reconducted to its mechanical characteristics. The first use of EIT for SHM was presented by Hou et al. [181]: the authors fabricated a multifunctional Carbon NanoTube (CNT) thin film to localize mechanical and chemical changes by mapping the conductivity distribution in the material. EIT coupled with sensing skins was also employed by Loh et al. [182] for strain monitoring and defect identification in aluminum plates. The sensing material was fabricated in the mentioned study through the layer-by-layer deposition of CNTpolymer thin films. More recently, Loyola et al. [183] applied strain-sensitive CNT-based thin films over Glass FiberReinforced Polymer (GFRP) composites to identify subsurface damage.

In most RC and steel structures, the damage is generally related to superficial cracking. However, cracked elements are typically inaccessible and hardly inspectable. In this case, the application of

smart coatings and thin films on structural components has proven as a valid technique to convert regular structural elements into smart components. Hallaji et al. [184] employed EIT for crack detection in RC beams using a conductive silver coating. Gupta et al. [185] designed a patterned nanocomposite sensing mesh to identify strain in different directions employing EIT. The presented device was effectively employed to localize a cracked region at the base of a reinforced concrete column.

Due to the numerical issues related to the resolution of the inverse EIT problem, which involves the reconstruction of the dense conductivity distribution of the interrogated body from sparse voltage measurements taken on its boundary, most studies employ regularization-based approaches [173, 184, 186, 187]. Although the application of these approaches is generally robust to small variations of the interrogation setup, conductivity images reconstructed using traditional algorithms typically have a low resolution that hardly allows estimating the position and extension of the cracked region.

Very recently, Machine Learning (ML))-based techniques have been applied to solve the strongly nonlinear inverse EIT problem in several application fields. Lin et al. [188] compared two approaches, consisting of an end-to-end Artificial Neural Network (ANN) and a supervised descent method that employs an ANN to calculate the partial results of a traditional iterative procedure. The end-to-end ANN approach was faster and generally provided more accurate results; however, the hybrid procedure showed more robust generalization capability when dealing with different setups. Chen et al. [189] used a Convolutional Neural Network (CNN) to reconstruct the absolute conductivity distribution in the interrogated body from voltage measurements. The authors also employed group sparsity regularization to identify different conductivity levels. Other applications employed ML algorithms to improve the resolution of conductivity distributions obtained using traditional algorithms [190, 191].

One of the main challenges of using supervised machine learning tools is constructing a realistic training dataset suitable for real applications of the trained neural network. However, it is difficult to find

a literature procedure to verify that synthetic data is representative of real measurements.

Filtering vibration 3

The Modal Assurance Criterion (MAC) is one of the most used indicators to check the similarity between two different mode shapes. It was largely employed for identification purposes, in order to compare the results obtained through different techniques [192], to guide the stabilization of stochastic methods [193], and to merge signal components related to the same mode, as in the Enhanced Frequency Domain Decomposition (EFDD) [194]. While in the first examples it was applied to identified mode shapes, in the last case, it was employed to compare the Operating Deflection Shapes (ODS) associated with consecutive frequency values to identify resonant peaks in the frequency spectrum of the structural response. Since EFDD is an identification method in the frequency domain, it does not allow the identification of non-time-varying systems. However, the concept of ODS comparison and clustering is extended in this study taking into account the time dependence of modal features, giving rise to the Modal Assurance Distribution (MAD). This TFR of the structural response allows decoupling modal contributions and identifying instantaneous modal parameters that can be em-

ployed for real-time damage identification. This chapter presents the theoretical framework of MAD after explaining what is meant by "instantaneous ODS". Then, an identification algorithm and related variants are proposed based on distributed computing to identify the parameters of time-varying and nonlinear structures subject to non-stationary excitation.

3.1 Instantaneous operating deflection shapes

The displacement response $u(z,t)$ of a linear structure with distributed mass and elasticity at time t and location z, excited by a generic forcing function, can be represented in general as [195]:

$$u(z,t) = \sum_{j=1}^{\infty} \phi_j(z)\, q_j(t) \tag{3.1}$$

with $\phi_j(z)$ the continuous j-th mode shape and $q_j(t)$ a function of time with narrow (in general, depending on damping) frequency band, the center of which is the damped frequency $\omega_{d,j}$.

Considering a structure with slowly varying features (*i.e.*, with masses and stiffness which are assumable as piece-wise constant), the discrete signal recorded at a given position i by means of a uni-axial accelerometric sensor can be modeled as

$$x_i[t] = \sum_{j=1}^{\infty} \phi_{i,j}^{(t)} \ddot{q}_j[t] + v_i[t] \tag{3.2}$$

where $\phi_{i,j}^{(t)}$ is the piece-wise constant element of the j-th mode shape, $\ddot{q}_j[t]$ is the double derivative in time of $q_j[t]$, and $v_i[t]$ represents a white noise function relevant to the i-th sensor. Applying a band-pass filter with impulse response $b_k[\tau]$ to the recorded signal $x_i[t]$, the filtered structural response can be computed as

$$(x_i * b_k)[t] = \sum_{j=1}^{\infty} \phi_{i,j}^{(t)} \left(\ddot{q}_j * b_k\right)[t] + (v_i * b_k)[t] \tag{3.3}$$

because of the linearity of the convolution operator (here indicated as $*$). It is highlighted that, in this thesis, the tap index of the filter impulse responses is indicated as τ, to differentiate it from the time variable t of the signal.

Since $q_j[t]$ has a narrow band in the frequency domain, the terms of summation which give a result with non-negligible amplitude are only those with $\omega_{d,j}$ close to the frequency band of $b_k[\tau]$. In other words, considering a noise threshold given by the amplitude of v_i, $\left(\ddot{q}_j * b_k\right)[t]$ is higher than this threshold only if $Q_j(\omega) B_k(\omega) > V_i(\omega)$ for some value of ω, where $Q_j(\omega)$, $B_k(\omega)$, and $V_i(\omega)$ denote the Fourier transforms of $\ddot{q}_j[t]$, $b_k[\tau]$, and $v_i[t]$ respectively. Indicating with $q_k[t]$ the time function with central frequency $\omega_{d,k}$ included within the cutoff frequency values of $b_k[\tau]$ and neglecting the contributions of neighboring modes, the filtered response can be rewritten as

$$x_{i,k}[t] \cong \phi_{i,k}^{(t)} \left(\ddot{q}_k * b_k\right)[t] + v_{i,k}[t] \tag{3.4}$$

with $x_{i,k}[t] = (x_i * b_k)[t]$ and $v_{i,k}[t] = (v_i * b_k)[t]$. Moreover, considering the signal $x_r[t]$ collected at a reference instrumented location r, the instantaneous ratio between $x_{i,k}[t]$ and $x_{r,k}[t]$, obtained as indicated in Equation (3.4) through the same filter $b_k[\tau]$, is

$$\frac{x_{i,k}[t]}{x_{r,k}[t]} \cong \frac{\phi_{i,k}^{(t)} \left(\ddot{q}_k * b_k\right)[t] + v_{i,k}[t]}{\phi_{r,k}^{(t)} \left(\ddot{q}_k * b_k\right)[t] + v_{r,k}[t]} \tag{3.5}$$

If the filtered vibration mode is sufficiently excited, the noise terms become negligible, and an estimate of the i-th element of the instantaneous mode shape can be calculated as

$$\phi_{i,k}[t] \cong \gamma_k^{(t)} \frac{x_{i,k}[t]}{x_{r,k}[t]} \tag{3.6}$$

with $\gamma_k^{(t)} = \phi_{r,k}^{(t)}$ representing an instantaneous normalization factor. Considering a multivariate signal consisting of the accelerations collected at different sensor locations, the instantaneous mode shapes can be obtained by normalizing all the estimated values with respect to the same location.

Considering a filter with impulse response $b_{\bar{k}}[\tau]$ such that none of the natural frequencies are included between its cutoff frequencies, all the terms in the summation of Equation (3.3) are close to zero and may thus be neglected, with the filtered signal becoming

$$x_{i,\bar{k}}[t] \cong v_{i,\bar{k}}[t] \tag{3.7}$$

and consisting of a filtered noise component. Therefore, the ratio between $x_{i,\bar{k}}[t]$ and $x_{r,\bar{k}}[t]$ continuously varies over time without reflecting the structural behavior.

ODSs have been traditionally defined as the deflection of a structure at a particular frequency of excitation [58]. Information related to both the forcing input and the resonant structural components is generally fused into ODSs, while mode shapes are inherent properties of the structure. However, it can be assumed that near to the resonance peak of the frequency response spectrum, ODSs are dominated by structural modes. In modal identification, ODSs evaluated at resonant frequencies are, therefore, assumed as fair approximations of the mode shapes. In this thesis, this difference is highlighted using the symbols $\boldsymbol{\varphi}$ and $\boldsymbol{\phi}$ to indicate ODSs and mode shapes, respectively.

Wavelets and filter banks

A filter bank is an array of bandpass filters that separates the input signal into multiple components, each one carrying a single frequency sub-band of the original signal [196].

There are different ways to build bandpass filters. Wavelet transform is a widely used instrument in the field of signal processing, as an alternative to the Fourier transform, especially when dealing with non-stationary signals, since it can capture time and frequency information [197–201].

One of the most used versions of WT is the "non-redundant" Discrete Wavelet Transform (DWT), which entails the recursive application of a basic filter bank, consisting of a low-pass and a high-pass filter [202]. For each subsequent transformation level, only the approximations (obtained from low-pass filtering)

are further filtered. Although this transform is characterized by a low computational effort, it does not possess the time-invariance property and is unsuitable for real-time processing of non-stationary signals [203]. Another widely used version of Wavelet Transform is the Wavelet Packet Transform (WPT), in which both the details and the approximations are decomposed at each level. If the WPT coefficients are not decimated after each filter bank application, the transform is known as Stationary Wavelet Packet Transform (SWPT). In this version, the analyzed signal is transformed into a series of components characterized by a narrow frequency band, each with the same number of samples of the original signal. Given the redundancy, SWPT is characterized by the shift-invariance property, which makes it ideal for estimating dynamic parameters in real time [204].

The recursive implementation of the basic wavelet filter banks can also be represented as an equivalent filter bank with a number of arrays equal to 2^n, where n is the number of iterations in the recursive process, *i.e.*, the transform level.

Wavelet filter banks can be built both to decompose (analysis filters) and reconstruct (synthesis filters) the signal [20]. In order to build such filters, three fundamental parameters have to be determined: the type of function, the order of the associated filter, and the transform level. The first parameter consists of the choice of the function by which the basis of transformation is generated [20]. The second parameter is related to the number of vanishing moments: the higher the number of vanishing moments of the wavelet function, the more the associated wavelet filter is close to an ideal one (with an increase of the support size, *i.e.*, filter length) [205]. The third parameter, as already mentioned, specifies how many times the transform is performed.

In the field of structural health monitoring, several authors use *Daubechies* [205, 206], *Symlet* [207], and *Meyer* [208] functions, selecting the wavelets and their orders to be effective with the implemented algorithms. In Figure 3.1, six different choices of decomposition parameters are compared as an example (the decomposition level is fixed to 4 for each graph). In particular,

the diagrams in the first column show the comparison between the *Fejér-Korovkin* function of order 14 (*fk14*) and the *Daubechies* function of order 7 (*db7*), which have the same filter length. The gray area represents the filter overlap, corresponding to undesired frequency bands included in the designed bandpass filters. The larger this area, the higher is the eventuality of obtaining multi-component responses as an output of the decomposition procedure (*i.e.*, representing more than one modal response). As reported in [209, 210], filter length being equal, the *Fejér-Korovkin* filter is the closest to an ideal sinc (*i.e.*, cardinal sine) bandpass filter. It can also be noted from Figure 3.1 that, even doubling the filter length (see Appendix B for more details on the filter length), *Daubechies* and *Symlet* functions (*db14* and *sym14*) are still characterized by higher error when compared to the *Fejér-Korovkin* function.

Once the decomposition filter bank is built, a convolution of the signal for each generated filter has to be carried out to perform the transform. At the last level (n) of the transform, 2^n series of coefficients are generated by the WPT (or SWPT). The higher the transform level, the narrower is the frequency content for each wavelet component. Given a signal with a sampling frequency F_s, each outcome of the WPT has a principal frequency range of $F_s/2^{n+1}$. Moreover, the higher the order of the wavelet function, the more condensed is the energy in the frequency domain.

The energy computed from the output of the transform can be represented on a time-component plane, the first dependent on the time sample of the input signal and the second represented by the array index k of the filter bank. This representation is known as scalogram [211]. It is also called Time-Frequency Representation, considering implicitly a conversion from the index k to the central frequency of the related bandpass filter.

It is also possible to reconstruct the original signal from the set of wavelet coefficients by performing the sum of convolutions computed between each wavelet component and the corresponding synthesis filter [20].

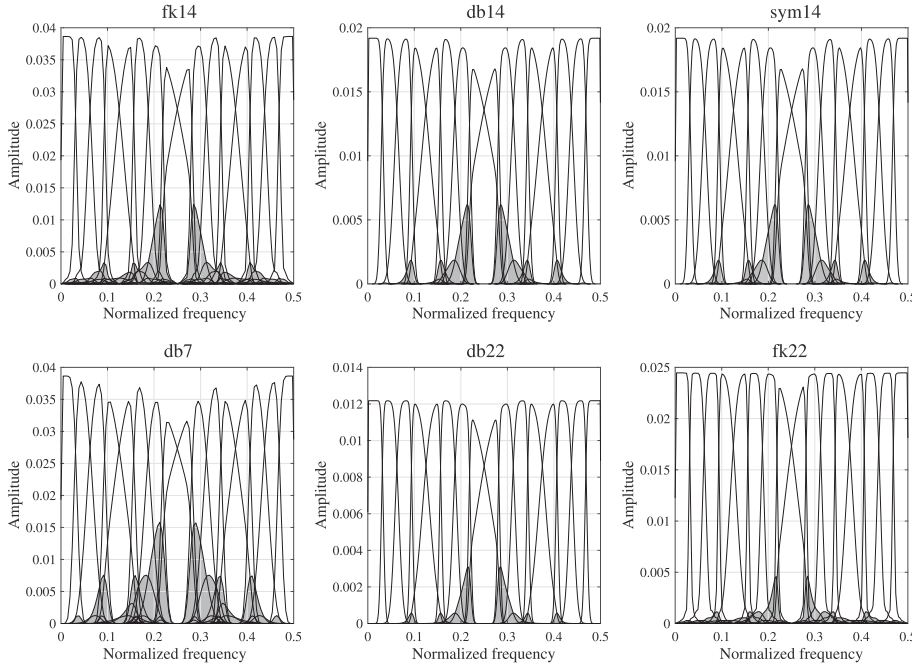

Figure 3.1: Wavelet decomposition filter banks in the frequency domain (decomposition level 4)

3.2 Modal assurance distribution

In the original formulation, the MAC is defined as a normalized scalar product of two vectors $\boldsymbol{\varphi}_a$ and $\boldsymbol{\varphi}_b$ representing two complex mode shapes or ODS:

$$MAC_{a,b} = \frac{\left|\boldsymbol{\varphi}_a^T \boldsymbol{\varphi}_b^*\right|^2}{\left(\boldsymbol{\varphi}_a^T \boldsymbol{\varphi}_a^*\right)\left(\boldsymbol{\varphi}_b^T \boldsymbol{\varphi}_b^*\right)} \tag{3.8}$$

where $\boldsymbol{\varphi}^*$ and $\boldsymbol{\varphi}^T$ represent the complex conjugate and the transpose of $\boldsymbol{\varphi}$, respectively. In this study, the concept of modal assurance is applied to instantaneous estimates of the ODSs, calculated using narrow-frequency components of the signals collected at different locations, obtained by means of the WPT, as schematized in Figure 3.2. Considering a complete decomposition tree, in a recursive implementation, wavelet packet coefficients $d_{i,2k}^{(p+1)}[t]$ and $d_{i,2k+1}^{(p+1)}[t]$ can be obtained by decomposing the coefficients $d_k^{(p)}$ at the level p

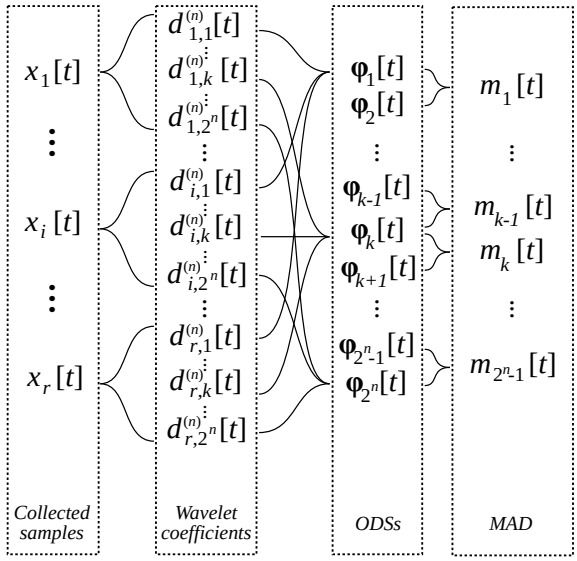

Figure 3.2: Procedure to generate the modal assurance distribution

using the Mallat algorithm [211] as follows:

$$d^{(p+1)}_{i,2k}[t] = d^{(p)}_k * \bar{h}[2t] \tag{3.9a}$$

$$d^{(p+1)}_{i,2k+1}[t] = d^{(p)}_k * \bar{g}[2t] \tag{3.9b}$$

where $k = 0, \ldots, 2^p$ indicates the subband of the obtained coefficients, $*$ denotes the convolution operator, and $h[\tau] = \bar{h}[-\tau]$ and $g[\tau] = \bar{g}[-\tau]$ are the impulse responses of the low-pass and high-pass filters associated with the selected wavelet function, respectively. Considering the discrete signal $x_i[t]$ collected at location i, the root of the tree $d^{(0)}_0[t]$ can be assumed coincident with $x_i[t]$ if the sampling frequency of the collected signal is sufficiently high, committing however a "wavelet crime" [212]. It should be noted that the wavelet decomposition can also be implemented as a filtering procedure using a filter bank the elements of which are 2^n equivalent filters that produce the coefficients of Equations (3.9a) and (3.9b) at the final transformation level, say n [20]. It should be noted that, at a given transform level, a higher sampling frequency determines filters with wider passband range. It is therefore essential, in the case of high sampling frequencies, to select transforms with higher level to obtain a good frequency discretization of the signal. However, the maximum selectable level depends on the length of the signal and on the filter order. In particular, it is equal to the integer number

$n_{max} \leq \log_2(N/N_f)$, where N and N_f are the length of the signal and the selected order of the wavelet filter, respectively.

The terms of vector $\boldsymbol{\varphi}_k[t]$, representing the real normalized instantaneous ODSs associated with a given subband k of the level n can thus be computed through the ratio

$$\varphi_{i,k}[t] = \frac{d_{i,k}^{(n)}[t]}{d_{r,k}^{(n)}[t]} \tag{3.10}$$

with $d_{i,k}^{(n)}[t]$ denoting the t-th sample of the wavelet component related to the subband k obtained by decomposing the signal collected at the location i, and r indicating a reference location. Using these instantaneous estimates, the MAD is defined as the matrix $\mathbf{M} = [\mathbf{m}[0], \mathbf{m}[1], \ldots, \mathbf{m}[T]] \in \mathbb{R}^{(2^n-1\times T)}$ consisting of the $\mathbf{m}[t]$ vectors, related to time instants t, containing the elements

$$m_k[t] = \frac{\left|\boldsymbol{\varphi}_k^{\mathrm{T}}[t]\boldsymbol{\varphi}_{k+1}[t]\right|^2}{\left(\boldsymbol{\varphi}_k^{\mathrm{T}}[t]\boldsymbol{\varphi}_k[t]\right)\left(\boldsymbol{\varphi}_{k+1}^{\mathrm{T}}[t]\boldsymbol{\varphi}_{k+1}[t]\right)} \tag{3.11}$$

with $k = 1, \ldots, 2^n - 1$ and T denoting the length of $d_{i,k}^{(p)}$. Each element of $\mathbf{M}$ is between 0 and 1 and represents the instantaneous similarity of ODSs related to neighboring components k and $k + 1$. The ability to represent the time-varying modal features of the analyzed signal is due to the fact that damped modes have values in the frequency spectrum which are spread around the peak represented by the damped frequency. The spreading is generally dependent on both damping and natural frequency of the selected mode. If a sufficiently high decomposition level n is selected to analyze the response of a damped structure, the part of spectrum related to each mode is divided into a set of narrow-frequency band components. Each of these components is however part of the same mode and, therefore, have similar ODSs (calculated by considering the same components of signals collected at different instrumented locations). This fact leads to high MAD values in the regions of the time-component plane where subbands relevant to the same mode are present. On the other hand, the signal filtered through cutoff frequencies selected far from the damped frequency

values consists of a filtered noise component, as reported in Equation (3.7), thus not characterized by physically meaning features. These components, instead of generating persistently high MAD values in the time-component plane, produce spurious peaks due to random similarities between the "shapes" of filtered noise components.

Readability improvement

As mentioned, far from natural frequencies, high MAD values may be generated by random similarities between neighboring filtered noise components. This phenomenon may compromise the readability of the distribution and prevent a correct application of further procedures for the extraction of modal responses, *e.g.*, ridge extraction. In order to reduce this risk, two techniques are proposed herein to improve the readability of MAD.

The first involves the selection of a forgetting factor α, used to compute the t-th element of a weighted distribution that also takes into account the previous estimates. In particular, each element of the weighted distribution $\bar{m}_k[t]$ can be computed as

$$\overline{m}_k[t] = (1-\alpha)\, m_k[t] + \alpha \overline{m}_k[t-1] \tag{3.12}$$

The higher is α and the more the distribution appears smooth in the time direction, resulting however in a slower updating and a lower sensitivity to sudden variations. This method is particularly effective to remove noise-generated random similarities, which are generally characterized by sharp peaks with short duration.

The second criterion consists of a noise-assisted approach which, similar to the concept used in the EEMD, involves the computation of the final MAD as the mean of an ensemble of L matrices, each consisting of the MAD evaluated on the multivariate signal plus an uncorrelated finite-amplitude white noise matrix. Operating this way, only persistently high values over the ensemble of trials will form the high-similarity areas of the final MAD, canceling out spurious peaks due to noise components which are different for each trial. The ensemble

MAD is computed as

$$\widetilde{m}_k[t] = \frac{1}{L}\sum_{\lambda=1}^{L} m_k^{(\lambda)}[t] \tag{3.13}$$

where $m_k^{(\lambda)}[t]$ is the MAD value obtained using the λ-th noise-added trial $\mathbf{x}[t] + \mathbf{v}_\lambda[t]$, with $\mathbf{x}[t] = [x_1[t], x_2[t], \ldots, x_r[t]]^{\mathrm{T}}$ being the collected signal and $\mathbf{v}_\lambda[t] = [v_{\lambda,1}[t], v_{\lambda,2}[t], \ldots, v_{\lambda,r}[t]]^{\mathrm{T}}$ is a vector of uncorrelated white noise sequences. In order to prevent the added noise from covering the signal parts with low amplitude, the sequences $v_{\lambda,k}[t]$ can be chosen as non-stationary, having an amplitude dependent on the analyzed signal

$$v_{\lambda,k}[t] = \beta\ std\{x_k[t-\xi, t+\xi]\}\ s_{\lambda,k}[t] \tag{3.14}$$

with $std\{x_k[t-\xi, t+\xi]\}$ denoting the standard deviation of x_k in the interval from $t-\xi$ to $t+\xi$, $s_{\lambda,k}[t]$ is a sequence of zero-mean white noise with standard deviation 1, and β, ξ are user-defined parameters that control the amplitude and adaptivity of the added noise, respectively. Considering the wavelet filters as ideal bandpass filters, if β is higher than the standard deviation of the recording noise and the ensemble is formed by a high number of trials, the mean of MAD values in noise-only areas can be estimated as $1/r$, where r is the number of sensors. Indeed, the expected value of the normalized dot product between two vectors $\mathbf{a}, \mathbf{b} \in \mathbb{R}^N$, the elements of which are random variables independently distributed in a given interval, is

$$E\left[\frac{|\mathbf{ab}|^2}{|\mathbf{a}|^2\,|\mathbf{b}|^2}\right] = \frac{1}{N} \tag{3.15}$$

Since wavelet filters with limited order cannot be considered as ideal bandpass filters, the filtered noise components cannot be assumed as independent. Especially for high transform levels, the expectation of MAC tends, in fact, to a value higher than $1/r$. This value becomes the minimum of MAD, canceling out the effects of recording noise.

3.3 Modal identification of time-varying systems

The MAD can be used as a TFR for visualizing the distribution of modal features through the time-component plane (from now on, referred to as time-frequency plane). Moreover, it can also be exploited for separating modal responses. Indeed, it is possible to define a set of adaptive bandpass filters with cutoff frequencies defined by low-valued MAD areas, as explained in the following.

In this section, watershed segmentation and MAC-based cluster analysis are used to automatize the recognition of different modal contributions in the MAD, which is interpreted as a grey-scale image obtained by assigning the color white to 1 and black to 0 values (and different shades of gray in between). A mask $\mathbf{Z} \in \mathbb{R}^{(2^n-1\times T)}$ is created to select the MAD values above a user-defined threshold η. Specifically, the elements of $\mathbf{Z} \in \mathbb{R}^{(2^n-1\times T)}$, $\zeta_k[t]$, are zeros where $m_k[t] < \eta$ and ones where $m_k[t] \geq \eta$. Opening and filling morphological operations are applied to $\mathbf{Z} \in \mathbb{R}^{(2^n-1\times T)}$ to remove spurious white areas and black regions generated by noise. Then, the mask is applied to $\mathbf{M}$, generating $\widehat{\mathbf{M}} = \mathbf{Z} \bullet \mathbf{M}$, with $\bullet$ denoting the point-wise multiplication.

A Gaussian filter with low standard deviation is then applied to the masked matrix to further smoothen the distribution. The local maxima can thus be identified. Finally, the watershed transform is applied to segment the masked distribution into different areas, each containing a single identified maximum, which are then converted into different matrices $\mathbf{Z}_a \in \mathbb{R}^{(2^n-1\times T)}$, each with the same size as $\widehat{\mathbf{M}}$, consisting of ones in the identified region and zeros elsewhere.

For each identified area, the a-th signal (localized both in frequency and time) can be extracted by means of a reconstruction matrix $\mathbf{R}_a \in \mathbb{R}^{(2^n\times T)}$, the elements of which are obtained as

$$\rho_{a,k}[t] = \begin{cases} 1 & if\ \zeta_{a,k}[t] = 1 \ \vee\ \zeta_{a,k-1}[t] = 1 \\ 0 & \text{otherwise} \end{cases} \tag{3.16}$$

where $\zeta_{a,k}[t]$ are the elements of $\mathbf{Z}_a$. The partial multivariate signal component $\mathbf{w}_a[t]$ extracted by $\mathbf{R}_a$ can thus be computed as the

inverse Inverse Wavelet Packet Transform (IWPT) applied to the masked wavelet coefficients $r_{i,k}^{(n)}[t] = d_{i,k}^{(n)}[t]\rho_{a,k}[t]$. By means of the Mallat algorithm [211], the coefficients $r_{i,k}^{(p)}[t]$ at level p can be calculated recursively as

$$r_{i,k}^{(p)}[t] = \check{r}_{i,2k}^{(p+1)} * h[t] + \check{r}_{i,2k+1}^{(p+1)} * g[t] \tag{3.17}$$

where $\check{r}[t]$ indicates the sequence obtained by inserting a zero between each sample of $r[t]$. Therefore, $w_{i,a}[t] = r_{i,0}^{(0)}[t]$ represents the i-th element of $\mathbf{w}_a[t]$ (*i.e.*, referring to the i-th sensor location).

After reconstructing the partial components, each of them can be associated with a vibration mode by performing a MAC-based clustering procedure. The average mode shape of the a-th partial component can be computed as

$$\boldsymbol{\varphi}_a = \frac{1}{s}\sum_{t=1}^{s}\frac{\mathbf{w}_a[t]}{w_{1,a}[t]} \tag{3.18}$$

with s denoting the number of non-zero time samples in $w_{1,a}[t]$. Then, the clustering can be performed with the following rule:

$$\boldsymbol{\varphi}_a, \boldsymbol{\varphi}_b \in C_l \Leftrightarrow MAC_{a,b} \geq 1 - \theta \tag{3.19}$$

where C_l represents the l-th cluster (related to the l-th identified mode), $MAC_{a,b}$ is the modal assurance between the shapes ϕ_a and ϕ_b, obtained using two partial components w_a and w_b, respectively, while θ is a user-defined sensitivity parameter. The complete decoupled modal responses can thus be obtained by merging (*i.e.*, summing up) all the partial components classified within the same cluster. Moreover, instantaneous modal parameters can be identified from the extracted mono-component responses using, for example, the HT or the TEO, as it will be shown later. It should be noted that, while modal amplitudes obtained at different instrumented locations need to be combined to obtain mode shapes, natural frequencies can be identified using a single recording channel. The responses extracted in locations far from the nodes of the mode shapes should be used to retrieve instantaneous frequencies in order to limit the influence of noise.

Parameter selection and residual analysis

The selection of different values for η and θ may lead to different decompositions. In particular, η is responsible for signal segmentation: the higher this threshold, the smaller the masked areas, which could be eroded during the morphological operations, reducing however the noise included in the reconstructed partial components. On the other hand, θ concerns the final clustering procedure: high values of this parameter lead to more clusters, which could nevertheless belong to the same mode if slight variations affect the mode shapes over time (*e.g.*, due to ongoing damage).

A method for verifying the proper selection of the first parameter consists of the residual analysis. The residual of the DAMA can be obtained as

$$\varepsilon[t] = \mathbf{x}[t] - \sum_{a} \mathbf{w}_a[t] \tag{3.20}$$

The variance of this sequence should be similar to the variance of the recording noise, therefore, low compared to the variance of the original signal. It is worth noting that, even by applying the noise-assisted method, the signal is not affected by added noise since it is only used to select the masking matrix, which is then applied to the decomposed original signal.

A criterion for selecting the optimal value of η in offline implementations is applying the DAMA with multiple thresholds, and selecting the parameter after observing the curve of residual variance as a function of η. As the threshold increases, the variance of the residual should increase steeply for low and high values of η, presenting a lower slope in the central part. The first interval with a high slope is due to the overcoming of the recording noise, while the second part represents the inclusion of significant signal components into residuals. Therefore, the optimal value of η should be selected in the part contained between these two high-slope intervals, for example immediately after the first one or where the slope of the curve is minimum.

The θ parameter should be selected in order to obtain a small

number of clusters that generate mono-component decoupled responses, *i.e.*, containing information related to a single modal response. A Principal Component Analysis (PCA) can thus be performed on the modal responses extracted at different sensor locations to evaluate the variance explained by each Principal Component (PC). In order to be mono-component, the percentage of variance explained by the first PC should be much higher than the variance explained by the others [213]. High variance explained in the other principal directions may denote multi-component responses or high noise in the recordings. The first involves errors in the estimation of modal parameters for all sensor locations, except for those near to a node of the mode shape of the disturbing mode. On the other hand, if only a subset of recordings has a low SNR (due for example to the deployment of sensors close to nodes of the mode shapes), only the responses extracted at those locations will provide noisy parameters. If multi-component responses are identified, the analysis should be repeated upon increasing the θ parameter.

It is worth underlining that the Decomposition Algorithm based on Modal Assurance (DAMA) proposed in this section is equivalent to a band-variable filter bank the parameters of which are signal-adaptive and estimated upon the MAD. This generalized filter bank with a variable number of components and cutoff frequencies enables the automatic extraction of modal responses even at the occurrence of strong variations in the dynamic behavior of the monitored system and in presence of vanishing components. Some practical examples of using the MAD and the DAMA will be illustrated in the following sections, considering numerical and real case studies.

Modal identification of a linear time-varying beam

The first case study is a numerical model of a simply-supported RC beam with a rectangular section (40 cm wide and 85 cm high) and a length of 10 m. The simulated instrumentation consists of four uni-axial accelerometers deployed in the vertical direction, as represented in Figure 3.3. Damping with a ratio of 0.02 was selected for each mode to solve the equation of motion and obtain

the structural response through the Newmark method. In order to simulate localized time-varying damage, a segment of the structure is modeled with varying Young modulus, as reported in Figure 3.4. In particular, the damage is modeled as slowly increasing up to 1400 s, when an instantaneous retrofit is simulated.

The acceleration dataset consists of a multivariate signal of 2000 s, obtained by collecting acceleration at the instrumented locations shown in Figure 3.3 with a sampling frequency of 250 Hz. The input excitation used to compute the structural response is a synthetic acceleration obtained by adding a white noise sequence with a standard deviation of 1 m/s^2 to a harmonic component with amplitude 0.3 m/s^2 and frequency of 50 Hz, which simulates a narrow-band disturbance, as reported in Figure 3.5. The exciting input was applied to 11 nodes, equally spaced of 1 m, in the vertical direction. Before using the signals, each collected acceleration sequence was corrupted by introducing a zero-mean white noise component with a standard deviation of 10% with respect to that of the original response, to simulate instumentation noise.

Figure 3.6 plots the power spectrum of the signal collected at sensor location S3 computed through the STFT. The narrow-band disturbance generates a high-amplitude component that intersects the modal responses in the time-frequency plane. Using most traditional structural identification procedures, this persistent peak in

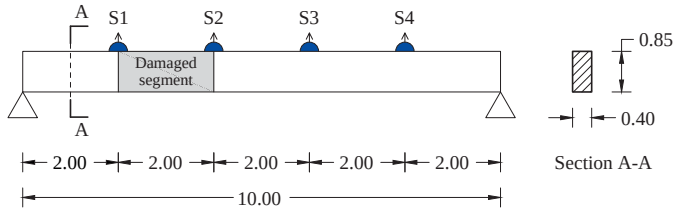

Figure 3.3: Scheme of the simply-supported beam

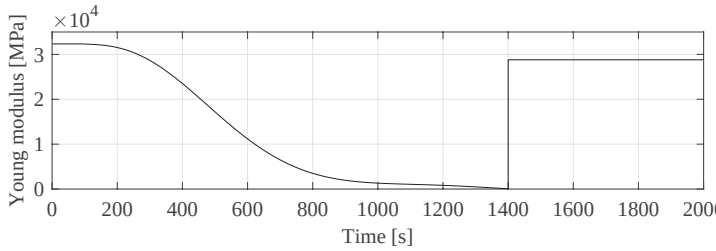

Figure 3.4: Simulated damage over time

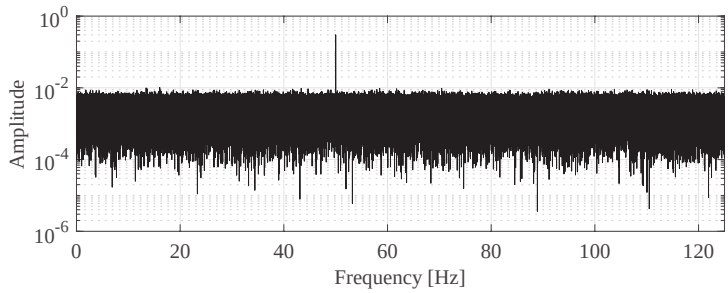

Figure 3.5: Frequency spectrum of the input excitation

the frequency spectrum could be interpreted as a modal component. Moreover, it could induce mode-mixing issues related to crossing modes if processed using the HHT.

The MAD was calculated using the *Fejér-Korovkin 22* wavelet function with a decomposition level 8 and represented in Figure 3.7a. In this case, the decomposition bank consists of 256 filters with a passband range of 0.49 Hz. It is possible to observe that regions in the time-frequency plane with high values (in white) are present along the entire distribution, following the trend of damage and also reflecting the abrupt variation that occurs at 1400 s. However, the disturbance component is completely overlooked, resulting in low MAD values around 50 Hz, since the ODSs associated with neighboring subbands are different.

Due to the random similarities in noise-generated ODSs, there is a considerable number of spurious peaks which could undermine

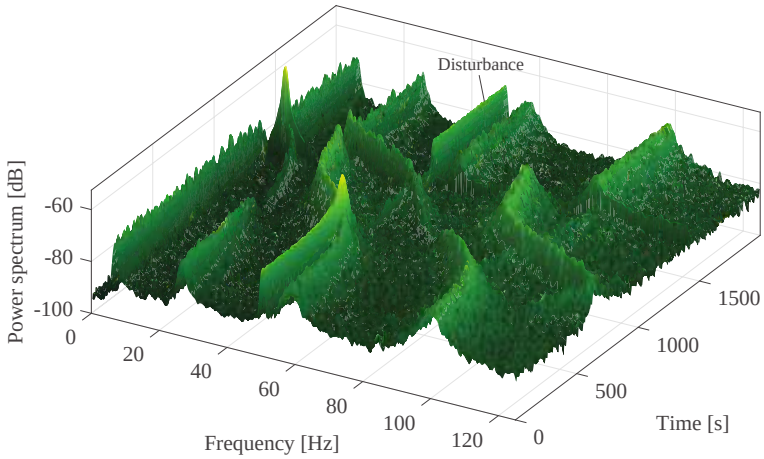

Figure 3.6: Power spectrum of the analyzed signal

the application of DAMA or any other ridge extraction procedure. To smoothen the distribution before further analyses, a forgetting factor of 0.9 is adopted (see Equation (3.12)), which leaves the frequency resolution unchanged but removes abrupt variations on the time axis, introducing a slight delay in the updating of the equivalent band-variable filters (Figure 3.7b). Afterward, a mask is applied to the distribution selecting the areas with MAD value higher than $\eta = 0.50$. In (Figure 3.8), the variance of residual is reported in logarithmic scale as a function of η. It is possible to notice that the first interval with a high slope is for η values between 0.10-0.30, while other steep increments are observable around 0.70 and 0.85. The optimal value was chosen between these two intervals, where the slope of the average curve is minimum.

In order to apply the watershed segmentation, a Gaussian filter with standard deviation 1 is used before extracting the local maxima and obtaining the areas reported in Figure 3.7c. MAC-based clustering with sensitivity $\theta = 0.05$ is then applied to associate the components obtained by reconstructing the partial signals related to each area to a different vibration mode. In this way, the areas shown in Figure 3.7d are obtained. In this experiment, a total number of 6 vibration modes is identified, one of which consisting of the orange area located around 1400 s, which should be a part of the fourth mode. The missing association with the appropriate cluster is due to the substantial change in the mode shape of mode 4 caused by the highly damaged state at the time interval close to 1400 s. In the clustering process, the mode shape of that region is recognized as considerably different from that of mode 4.

Figure 3.9 shows the frequency spectrum of the original signal collected at S4 compared with that of the sum of identified modal contributions at the same location and with the spectrum of the DAMA residual (computed using Equation (3.20)). It is possible to observe that the spectrum of the residual is very similar to that of the input (Figure 3.5), *i.e.*, the residual is almost white, except for the narrowband disturbance at 50 Hz. On the other hand, the spectrum of the reconstructed signal approximates well the spectrum of the original structural response, confirming the fact that all the significant information is extracted through the DAMA.

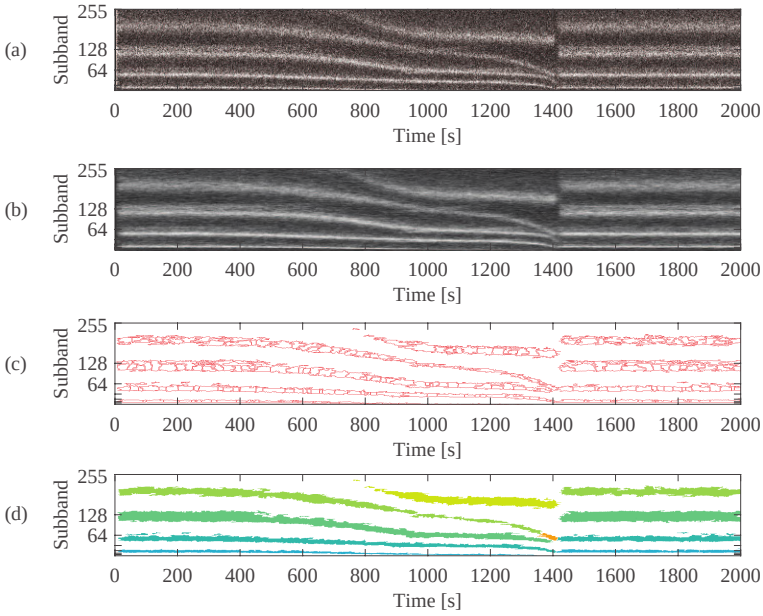

Figure 3.7: MAD (a), smoothed MAD (b), watershed segmentation (c), and DAMA application (d)

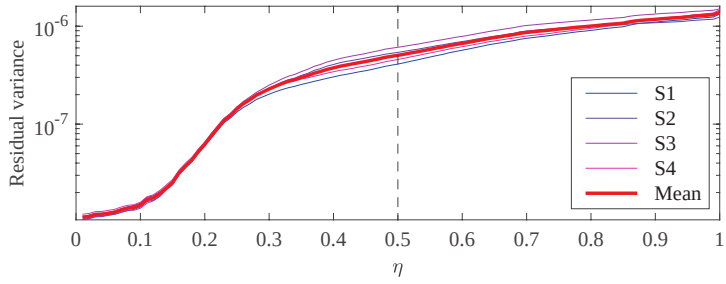

Figure 3.8: Parameter selection procedure: residual variance for different values of the threshold

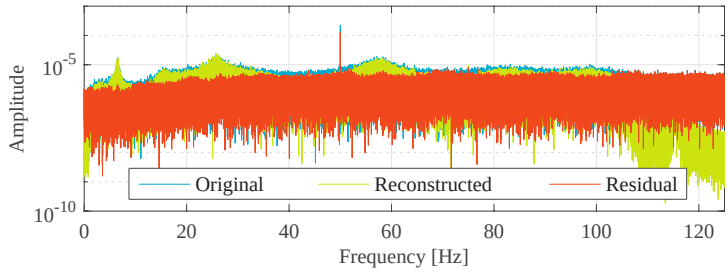

Figure 3.9: Frequency spectrum of the extracted components and of the noise residual

The instantaneous frequencies identified by applying the HT to the decoupled modal responses extracted by means of the DAMA to the signal collected in location S4 are reported in Figure 3.10, superimposed to the theoretical values and to the disturbance component. A median filter with a window size of 1000 samples

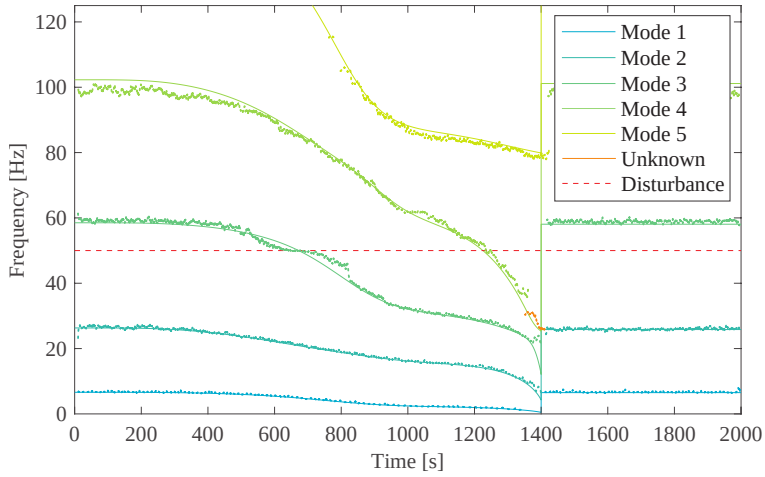

Figure 3.10: Theoretical (solid lines) and estimated (dots) instantaneous natural frequencies of the numerical model

was applied to the time sequence of identified frequencies before plotting, in order to improve the readability of the figure.

The estimated values for the first two modes are almost coincident with the theoretical curves. The third natural frequency is well-identified except for the time interval in which the disturbance intersects the natural frequency curve. On the other hand, the fourth frequency is not influenced by the disturbance, presenting however a slight underestimation for higher frequencies. The fifth mode is vanishing, since it is only visible in the interval between 700 s and 1400 s due to the selected sampling frequency. However, a good estimation for the instantaneous frequency values is achieved, without leading to mode-mixing issues.

The EMD and its multivariate extension, the MEMD, were considered to compare the obtained results with well-known literature methods for adaptive signal decomposition. In particular, the EMD was applied to the time history collected at location S4 (see Figure 3.3), while the MEMD was used to decompose the multivariate signal into four sets of IMFs (one for each sensor location). The instantaneous frequencies obtained by applying the HT on the IMFs related to location S4 obtained by means of traditional and multivariate EMD are reported in Figure 3.11. Here, the same median filter used to obtain the identified values reported in Figure 3.10 is employed. It is possible to notice that the IMFs extracted by EMD are saturated with noise, showing scattered frequencies with a slightly variable

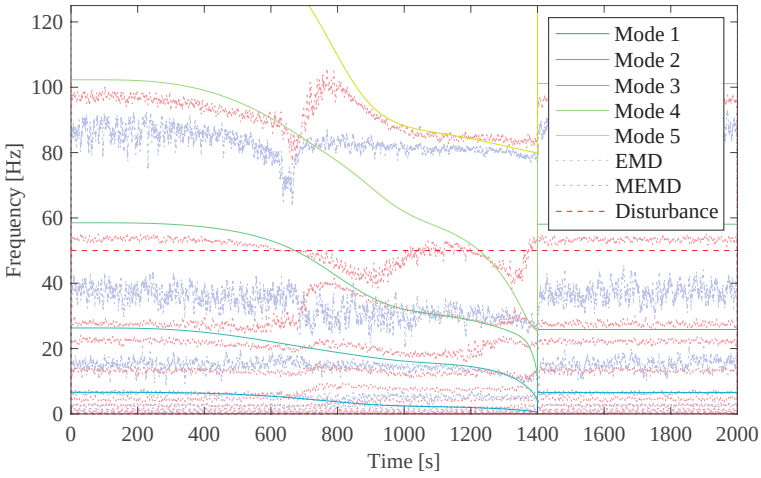

Figure 3.11: Instantaneous frequencies estimated through the EMD and its multivariate variant

mean trend, which are however not able to follow the theoretical curves. On the other hand, MEMD shows to be less sensitive to noise, exhibiting however strong mode-mixing issues. It is indeed clearly noticeable that the instantaneous frequencies of all IMFs jump to the upper mode at 700 s and back to the lower at 1400 s.

The modal amplitudes obtained as simple ratios between the modal responses extracted through the DAMA are reported in Figure 3.12 (the same median filter used for natural frequencies was employed on instantaneous ratios). Here, the normalization was performed selecting the modal responses of sensor S1 as a reference. In this plot, the set of modal amplitudes in a given time instant is an instantaneous mode shape. It is possible to notice that the third mode, which already showed slightly corrupted frequency values close to the intersection with the narrowband disturbance (Figure 3.10), is also influenced in the mode shape, which exhibits an oscillation across the theoretical curve around 700 s. Moreover, the fifth mode shows reliable estimates only around 800 s, with an underestimation of the ratio elsewhere. A slight underestimation is also noticeable for mode 4. However, the general and constant shift in the values identified at locations S2, S3, and S4 suggests that the error is only related to the curve of sensor S1. Therefore, a different normalization would shown more accurate results. On the other hand, modes 1 and 2 are identified almost perfectly, regardless of the noise and narrowband disturbance.

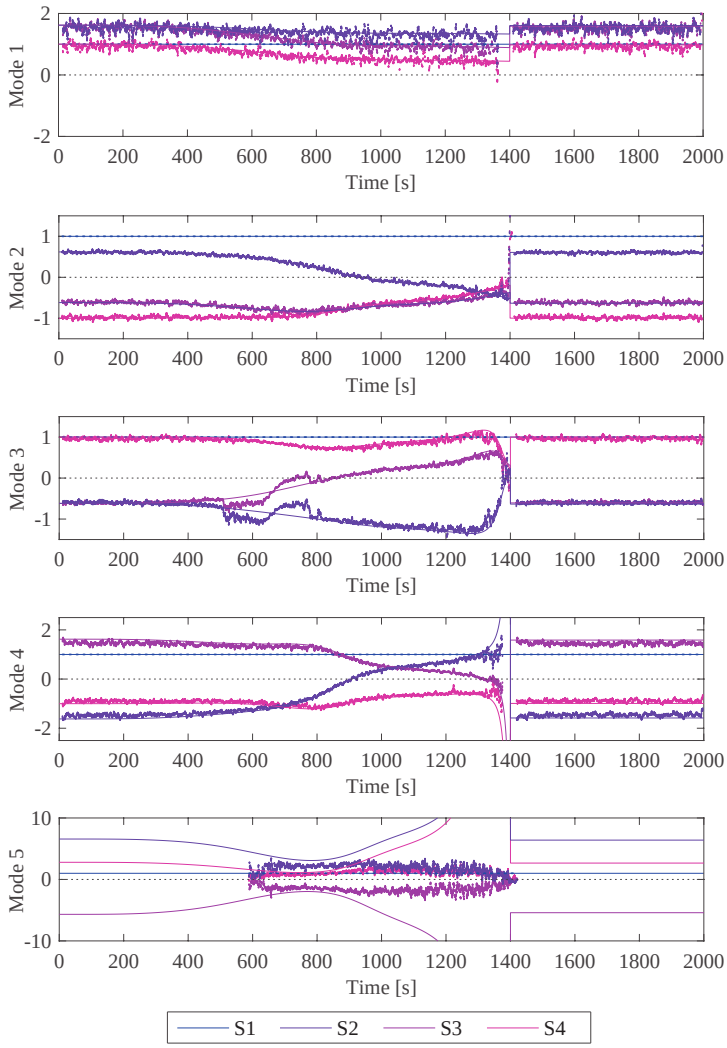

Figure 3.12: Theoretical (solid lines) and estimated (dots) instantaneous amplitudes of mode shapes (normalized over the amplitude of S1)

Modal identification of a time-varying RC building

The second case study is a slice of a full-scale 7-story RC building with cantilever structural walls acting as a lateral force resisting system (Figure 3.13). The structure is 20 m high and consists of two perpendicular walls in elevation (*i.e.*, web and flange walls) with a horizontal RC slab at each level. In addition, an auxiliary post-tensioned column provides torsional stability and 4 gravity columns support the slabs, as schematized in Figure 3.13a. The test structure was tested on a shaking table at the University of California, San

Diego, through the George E. Brown Jr. Network for Earthquake Engineering Simulation program [214–216] under seismic and white noise base-impressed excitation, the second with 0.03 g Root Mean Square (RMS) amplitude, as well as under ambient vibration (*i.e.*, with the shaking table locked).

The forced vibration tests were designed to progressively damage the building through the simulation of four historical earthquakes of increasing intensity recorded in Southern California. Before and after each test with seismic excitation, the building was subjected to intervals of white noise excitation and ambient vibration. In this application, only the acceleration collected during the "inspection" intervals after the application of each seismic motion were used. In particular, for the "undamaged" (U) and for each damaged condition (A, B, C, and D), 480 s of white noise excitation and 120 s of ambient vibration data are considered and merged together in a single set of data with a total duration of 3000 s (as shown in Figure 3.14). Therefore, the first 600 s of the data set refer to the reference condition U, after which the first seismic excitation (EQ1) of low intensity was applied, consisting of the longitudinal component recorded from the Van Nuys station during the San Fernando earthquake of 1971. Afterward, another inspection interval of 600 s is considered, referring to the damaged condition A. The third interval (B) is collected after applying the first medium-intensity seismic excitation EQ2, selected as the transverse component recorded during the San

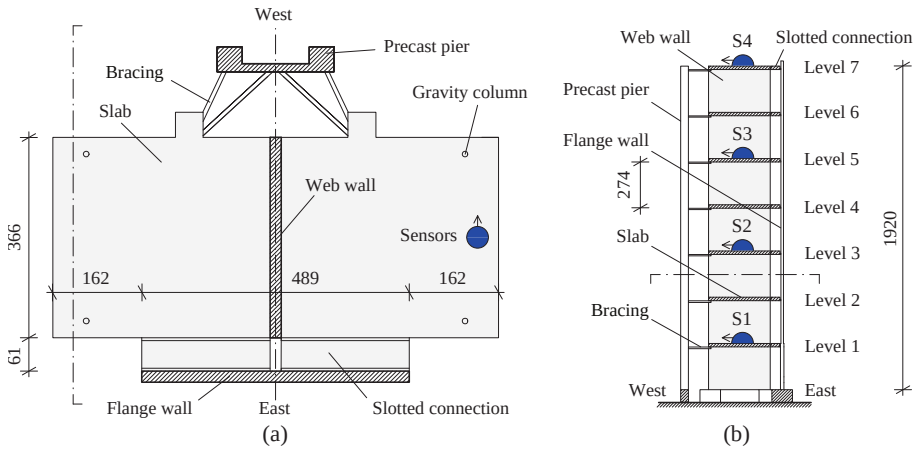

Figure 3.13: Scheme of the RC building: plan view (a) and vertical section (b)

Fernando earthquake from the Van Nuys station in 1971. Interval C was recorded after the second medium-intensity earthquake (EQ3), taken as the longitudinal component of the Northridge earthquake recorded from the Woodland Hills Oxnard Boulevard station in 1994. The last inspection interval (D) was recorded after a high-intensity 360° excitation (EQ4) recorded from the Sylmar Olive View Med during the Northridge earthquake of 1994.

The structure was instrumented with a dense network of sensors with a total of 45 channels: 29 longitudinal (three on each floor slab, one on the web wall at mid-height of each level, and one on the pedestal base), 14 transversal (2 on each floor slab), and 2 vertical (at the base, on the pedestal). The original data is sampled at 240 Hz. More details about the geometry and the instrumentation used can be found in [214–216]. Moreover, the data is freely available online at [217].

In [215], the results of modal identification obtained by means of different input-output and output-only methods are reported. Here, considering the white noise base excitation, in the undamaged condition, three lateral modes are identified with natural frequencies 1.72 Hz, 11.88 Hz, and 24.64 Hz, respectively. One torsional and one coupled lateral-torsional modes are also identified by some techniques and only during particular damage conditions. Moreover, the MAC values calculated between mode shapes identified through different techniques for these two modes are rather low, showing high level of uncertainties. As shown in [215], indeed, the first lateral mode has a strongly predominant contribution to the total response, making the identification of the torsional mode difficult as it may be covered by the former. In this work, 4 acceleration channels at the locations indicated in Figure 3.13 were used (*i.e.*, only longitudinal, at the levels 1, 3, 5, and 7), resampled at 100 Hz, with the intent of identifying the first lateral modes (in the east-west direction) using limited instrumentation.

The *Fejér-Korovkin 22* wavelet function with a level 8 was employed for decomposition, generating 256 components with the same frequency range, as the previous case study. In this section, the instantaneous natural frequencies and modal responses are estimated by using the output of DAMA and compared with the

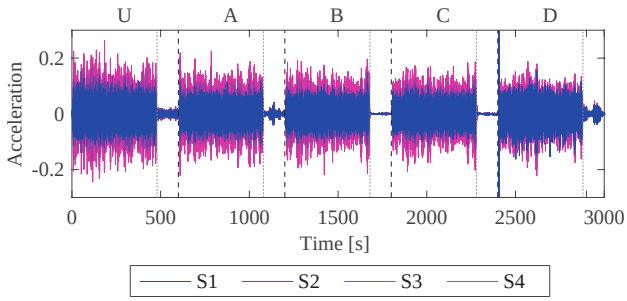

Figure 3.14: Multivariate vibration response of the RC building

results reported in [215] regarding the EFDD method, assumed as reference values.

In Figure 3.15a, the MAD obtained from the acceleration recordings collected at the four instrumented locations is reported. Here, a forgetting factor 0.9 is used to improve the readability. It is possible to notice that high-valued areas are widespread throughout the distribution, making it difficult to recognize different modal responses. Thereby, the noise-assisted variant presented in Section 3.2 considering 100 trials in the ensemble of noise-added signals (Figure 3.15b) was applied. In this analysis, a set of signal-adaptive Gaussian white noise sequences with standard deviation factor $\beta = 0.3$ was used, with reference to Equation (3.14). Figure 3.16 shows the residual variance as a function of the threshold η both for the original formulation (dashed lines) and for the noise-assisted variant (solid lines). It is observable that the first interval characterized by a high slope is more prominent in the result of the noise-assisted procedure, related to the fact that the lower value of MAD for noise-only areas has shifted around 0.25 (according to Equation (3.15)). It is also noticeable that in the averaged MAD (Figure 3.15b), the areas associated with the first three modal responses are more easily detectable than in the original distribution. Moreover, especially for conditions U and A, high values of the MAD are obtained also for the signal parts recorded under low-amplitude ambient vibration, allowing the extraction of modal responses even when the signal amplitude is very low since MAD is not based on the energy distribution in the time-frequency plane, in contrast with traditional TFRs. Concerning the ambient vibration parts of the signal recorded in conditions B, C, and D, narrower white areas are detected. Nevertheless, extracting high-valued areas in the MAD allows identifying modal responses

regardless of the signal amplitude, making the method suitable also for non-stationary recordings.

The red areas shown in Figure 3.15c represent the result of watershed segmentation applied to the masked MAD distribution, obtained by setting a threshold $\eta = 0.5$. After applying the MAC-based clustering with $\theta = 0.05$ on the partial reconstructed signals, the red areas are partitioned into different modes. The resulting decomposition, consisting of three separate modal contributions) is represented in Figure 3.15d.

After extracting the decoupled modal responses, the instantaneous frequencies are calculated using the modal contributions obtained at sensor S4 by means of the HT. In Figure 3.17, identified instantaneous values are superimposed on the reference estimates

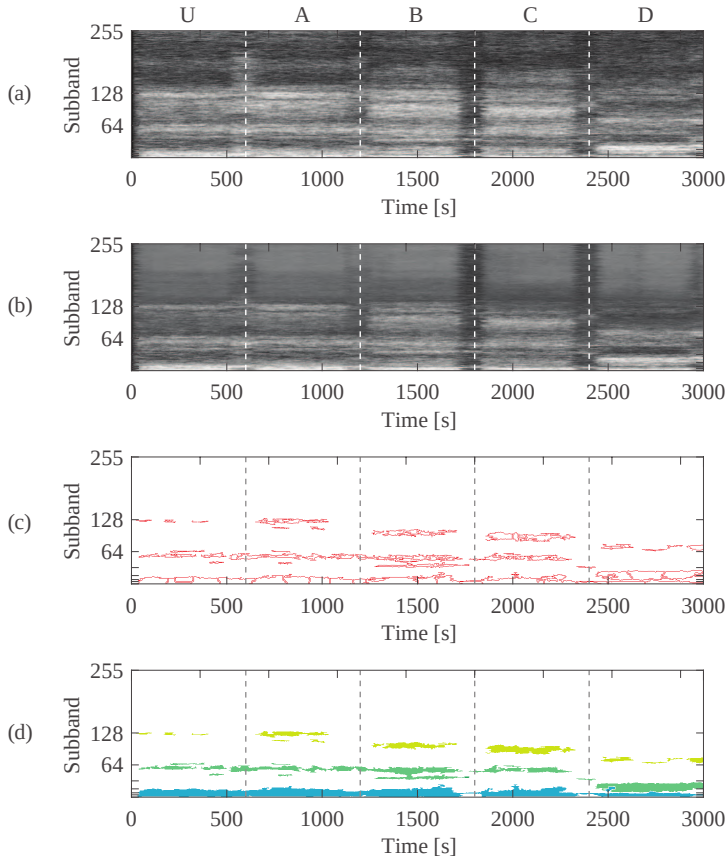

Figure 3.15: Smoothed MAD (a), noise-assisted MAD (b), watershed segmentation (c), and DAMA application (d)

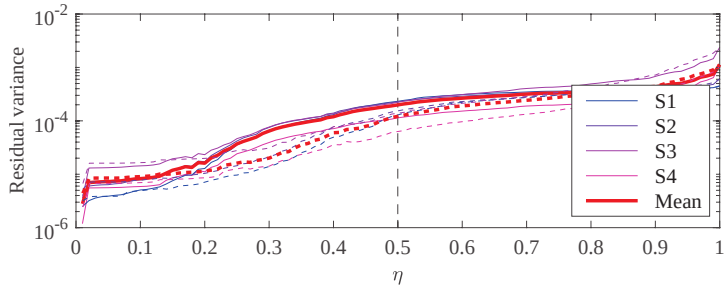

Figure 3.16: Parameter selection procedure: residual variance for different values of threshold; solid lines indicate the results of the noise-assisted method, while dashed lines indicate the use of forgetting factor only

obtained in [215] through EFDD, represented as constant frequencies over each condition. Due to system non-linearities, a significant shift in natural frequency is observable within the same condition when passing from a higher-amplitude white noise excitation to ambient vibration. While the instantaneous frequency of mode 1 is almost perfectly reconstructed, also tracking the shifts due to non-linearity, a slightly higher variability in identified values is notable for the higher modes. This fact may be due to the presence of a combined lateral-torsional mode in the frequency band between 7 Hz and 12 Hz [215], the shape of which is classified as "similar" to the shapes of the identified translational modes since only four acceleration channels are considered in this study to evaluate the MAC. This phenomenon can be observed for mode 2 in condition B, where two neighboring high-valued areas in the MAD are assigned to the same mode during the clustering process (Figure 3.15d), although they are well separated in the time-frequency distribution.

The uncertainties related to the second mode are also visible in the instantaneous estimate of the relevant mode shape (Figure 3.18), which is generally more dispersed with respect to those of modes 1 and 3. On the right side of Figure 3.18, the average mode shapes evaluated over each damage condition are reported, with the color changing from green to red as the damage increases. For modes 1 and 3, an increment in the displacement of the first level with damage is noticeable. As regards mode 2, the parameters estimated by sensor 1 are unstable, indicating that the instantaneous ratio between the modal responses obtained by sensor 4 and sensor 1 varies considerably over time. This phenomenon could be due both to noisy measurements and multicomponent responses. To confirm this fact, a PCA is conducted considering the modal responses extracted

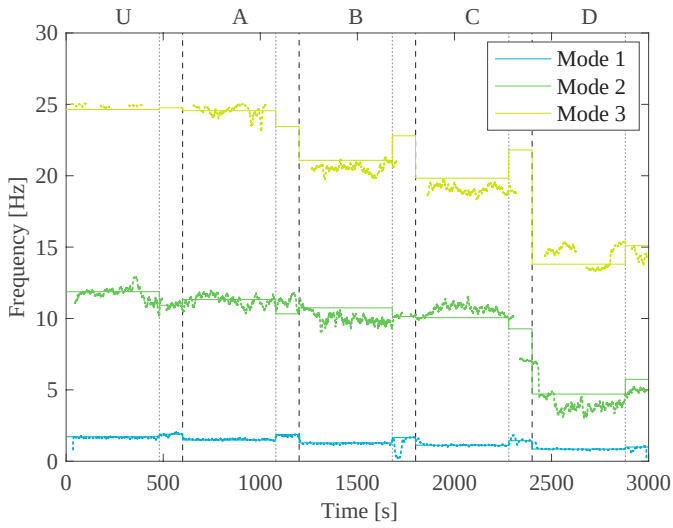

Figure 3.17: Theoretical (solid lines) and estimated (dots) instantaneous natural frequencies of the RC building

at all sensor locations in each damage scenario, the results of which are reported in Figure 3.19. In the lower-right part of each diagram, the variance explained by each PC is reported for each mode. High values in the first PC and low values for the other PCs denote mono-component and low-noise responses, meaning that MAD areas are properly clustered into separate modal responses. On the other hand, low values in the first PC represent noisy recordings or signals containing the information of two or more modal responses. Observing the parameters reported in Figure 3.19, the large variance obtained for modes 1 and 3 in the first PC denotes a good accuracy in the extraction of the first modal response. However, considering the values calculated for mode 2, especially for conditions U, A, and B, the extracted modal response seems to be multi-component. This property also appears in the diagram of component scores (represented as points in Figure 3.19), which are sparse in the plane of the first two principal components for mode 2, especially for condition B.

However, observing the principal directions, represented as lines starting from the origin in Figure 3.19, it is possible to notice that their projections on the PC 1 axis (interpretable as an estimate of mode shapes) are generally stable, *i.e.*, they change slightly as damage increases, except for the direction of sensor S1 for mode 2 which varies considerably in each diagram.

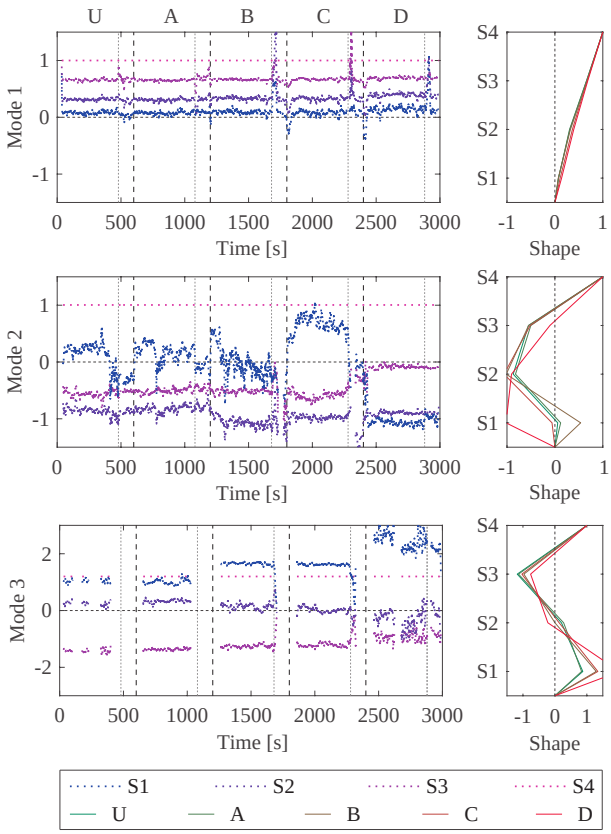

Figure 3.18: Instantaneous amplitudes (normalized over the amplitude of S4) of the identified mode shapes (left) and average values for each damage scenario (right)

Since a high variability in both instantaneous amplitude and principal direction is observed in conditions U, A, and B only for mode 2 at sensor location S1, the estimation error seems to be related to a low SNR in the frequency band of the second mode for the recording collected at the first level. In condition D, since considerable damage was experienced [215], the amplitude of the second mode at the location of sensor S1 increased, thus reducing the issues due to the low SNR. According to [215], the higher estimation error of the second lateral mode may also be due to the proximity of its natural frequency to the frequency of the oil column of the vibration table.

It is also observable that the instantaneous estimates of mode shapes are corrupted when passing from a damage scenario to another, as well as when the input excitation changes. This fact may be due to two phenomena. The first regards the delay in the masking

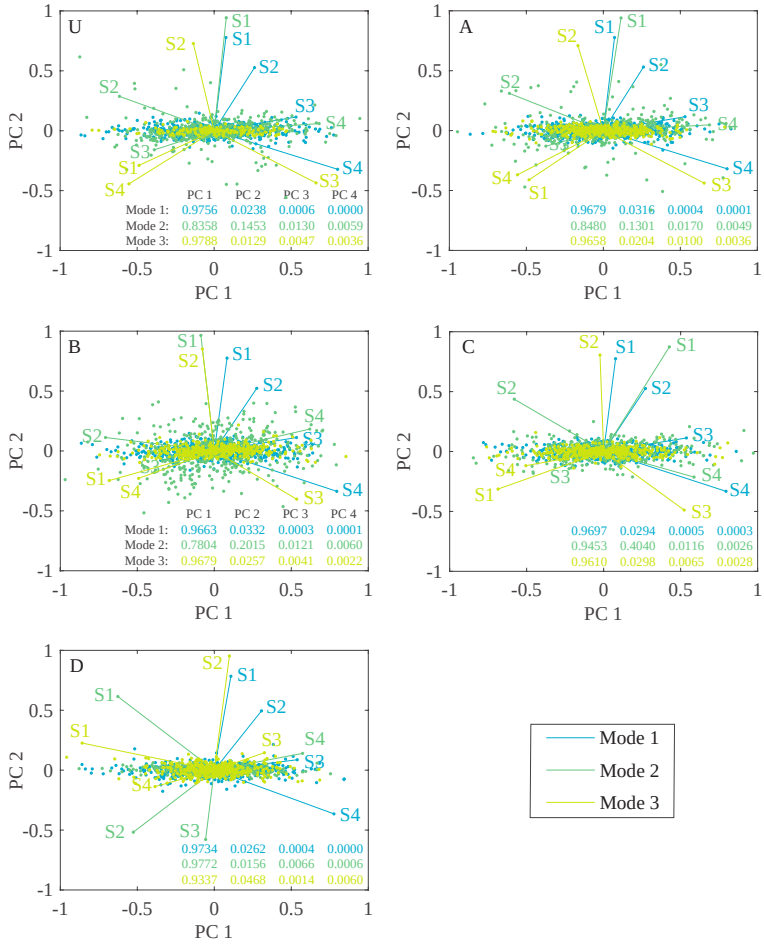

Figure 3.19: Principal directions and scores (represented as the first two PCs) of modal responses extracted from white noise recordings for each condition; the numbers on the lower-right part of each diagram represent the percentage of variance explained by each PC

matrix due to the forgetting factor adopted to improve the MAD readability. The reconstructed signal is indeed obtained through a bandpass filter which is adapted to the signal with a delay. The second reason is related to the assumption of slowly varying features, which is violated when a sudden change in the dynamics occurs, *i.e.*, when passing through recordings collected during different inspection intervals.

For comparison, the instantaneous natural frequencies were also extracted by using the HT on the IMFs obtained through the EMD, EEMD, and MEMD. In Figure 3.20, the estimated frequencies are represented superimposed to the reference values. In particular the EMD and EEMD were applied to the signal collected by sensor S4,

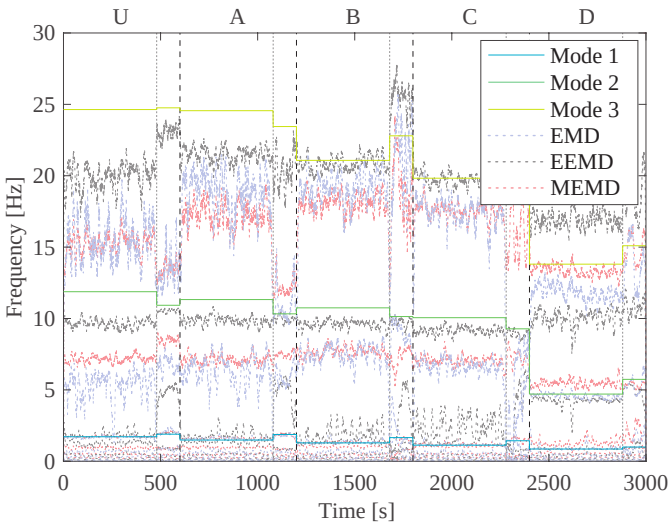

Figure 3.20: Instantaneous frequencies estimated through EMD and its variants

while the MEMD was applied by considered the four channels used in the previous analyses. It is possible to observe that, although the same median filter used to obtain the values reported in Figure 3.17 is employed, the identified values are considerably noisier in this case. Moreover, a high number of IMFs is generally extracted, not reflecting the real modal responses and showing mode mixing problems.

Damage identification of an RC bridge

The third case study is the S101 Bridge. The data used in this thesis were collected during an experimental campaign conducted by the Vienna Consulting Engineers (VCE) and the University of Tokyo in 2008 [218–220]. In this campaign, acceleration time histories under ambient vibration and different structural health conditions.

The case study, represented in Figure 3.21 and Figure 3.22, is a three-span post-tensioned concrete bridge built in the 1960s and demolished in 2008 due to the need for an additional lane underneath. The bridge slab was continuous, supported by two pairs of piers. The central and side spans were respectively 32 m and 12 m long. The cross section was 7.2 m wide, formed of beams with variable

Figure 3.21: View of the S101 Bridge [218]

height along the longitudinal direction, equal to 0.9 m in the middle of the central span, up to 1.7 m at the piers.

Before the demolition, a three-day experimental campaign was carried out, aimed at identifying the structural damage under progressive artificially induced damage scenarios, consisting of north-western pier settlements and loss of post-tension forces. In this application, only the conditions referred to the pier settlement are considered (summarized in Figure 3.23 and Table 3.1). After unloading the pier by means of a hydraulic jack, it was cut at the base (scenario A) and a slice 10 cm thick was extracted (Figure 3.24). Then, the jack was lowered in three progressive steps, each by 1 cm (scenarios B, C, and D). At the end of the third step the final measured settlement was 2.7 cm and the column was completely suspended. Afterward, some compensating plates were inserted at the bottom of the pier (scenario E).

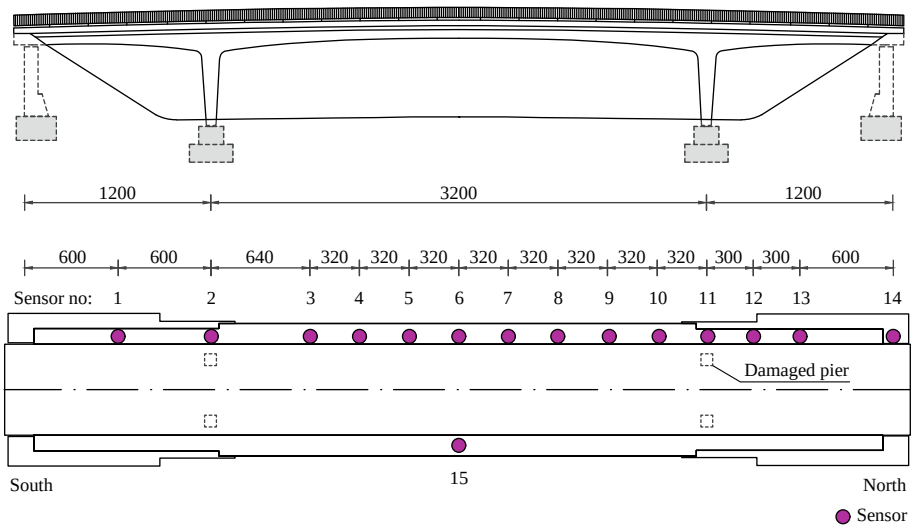

Figure 3.22: Configuration of the case study and sensor layout [218]; dimensions are indicated in centimeters

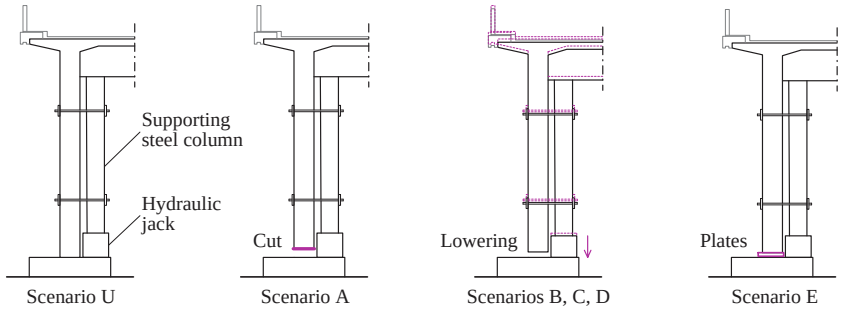

Figure 3.23: Schematic of progressively induced damage scenarios

The acceleration structural response was collected by using a dense BRIMOS [220] sensor grid consisting of 15 three-directional FBA-23 force balance accelerometers from Kinemetrics, with a sensitivity of 2.5 V/g under full-scale range of 1 g, and a resolution of 1×10^{-6} g. Raw signals were logged by means of a 16-bit ADC. The sensors were arranged on the structure as shown in Figure 3.22: 14 of them were positioned along the west side and 1 along the east side in order to also identify torsional modes. The original data were collected with a sampling frequency of 500 Hz. More details about the geometry and the instrumentation used can be found in [218, 221]. In Table 3.2 the results of identification procedures shown in [218] for the scenarios from U to E are reported. The percentage variation of natural frequencies with respect to the undamaged condition have also been computed and noted in Table 3.3. The

Damage scenario	Description
U	Undamaged structure
A	Cut of the north-western column
B	First step of lowering 1 cm
C	Second step of lowering 2 cm
D	Third step of lowering
E	Insertion of compensating plates

Table 3.1: Summary of progressively induced damage scenarios

Figure 3.24: Photographic documentation of the pier settlement process [218]

reference frequencies shown in Table 3.2 were calculated by the VCE using the BRIMOS software, which extracts the peaks of an averaged normalized power spectral density (ANPSD) obtained from windowed data [221].

In this application, five data sequences of 330 s collected in different damage conditions are analyzed, organized as a single sequence with a total duration of 1650 s. The first part of this signal refers to the condition U, collected before lowering the column, and is used to evaluate the parameters of the baseline configuration. The following conditions are A, B, C, and D.

Each signal was downsampled at 50 Hz and the *Fejér-Korovkin 22* wavelet function was used to obtain the preliminary TFR for each recording channel, with a decomposition level 8, thus generating 256 subbands. The MAD was then evaluated considering all the 15 recording channels. A noise-assisted procedure was applied considering an ensemble of 10 trials with noise components having a standard deviation of 30% with respect to that of the collected signal (see Section 3.2). A masking procedure is then performed, selecting the elements with MAD values higher than $\theta = 0.5$. In Figure 3.25, all the elements selected are represented in a time-frequency plane.

The ODSs associated with each point of the distribution were

Table 3.2: Natural frequencies identified during the experimental campaign conducted in 2008, reported in [218]

Mode	Damage scenario					
	U	A	B	C	D	E
1	4.05 Hz	3.95 Hz	3.96 Hz	3.92 Hz	3.62 Hz	3.98 Hz
2	6.30 Hz	6.08 Hz	6.01 Hz	5.88 Hz	5.39 Hz	5.91 Hz
3	9.69 Hz	9.44 Hz	9.44 Hz	9.28 Hz	8.22 Hz	9.34 Hz
4	13.29 Hz	12.15 Hz	11.65 Hz	10.79 Hz	10.06 Hz	10.92 Hz

Table 3.3: Percentage variation of natural frequencies with respect to the undamaged condition (with reference to data reported in Table 3.2)

Mode	Damage scenario				
	A	B	C	D	E
1	-2.47%	-2.22%	-3.21%	-10.62%	-1.73%
2	-3.49%	-4.60%	-6.67%	-14.44%	-6.19%
3	-2.58%	-2.58%	-4.23%	-15.17%	-3.61%
4	-8.58%	-12.34%	-18.81%	-24.30%	-17.83%

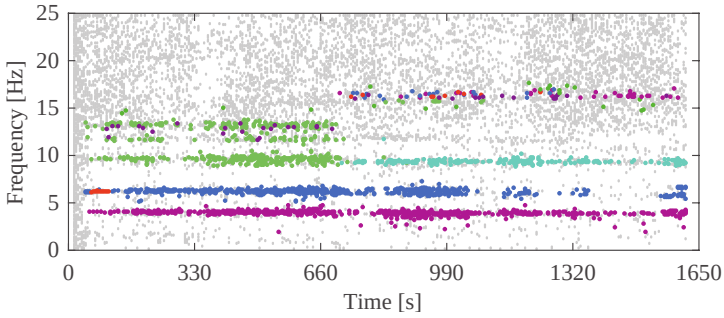

Figure 3.25: Clustering instantaneous ODSs

then normalized to have a unitary norm and the Debsity-Based Spatial Clustering of Applications with Noise (DBSCAN) algorithm [222] was applied for clustering, in order to group together all the the ODSs having Euclidean distance less than 0.1 between each other. Moreover, only clusters containing more than 10 points were considered for further analyses. Colors in Figure 3.25 represent different clusters, while grey points are classified as outliers since they do not comply with the aforementioned conditions.

A separate signal component for each cluster is therefore reconstructed through the application of the IWPT to the related subset of wavelet coefficients. The Hilbert transform is thus employed to evaluate the instantaneous frequency of each component extracted. In Figure 3.26, the identified values are reported and compared with the results of the HHT, evaluated for the signal collected by sensor 6, employing the EEMD algorithm for the extraction of the IMFs. Here, a considerable advantage in using the procedure proposed is noticeable since a clear mode mixing problem is observable in the results of the HHT. According to the results reported in [218], the MAD-based algorithm is able to correctly identify the frequencies of the first two modes (first flexural and first torsional, *i.e.*, violet and blue lines in Figure 3.26, respectively) for all the damage conditions. On the other hand, the instantaneous frequencies of IMFs are strongly variable (gray lines in Figure 3.26), and a single IMF is extracted in the frequency range between 4 Hz and 6 Hz, showing clear mode mixing issues.

The instantaneous amplitudes of the modal components reconstructed using the IWPT with the coefficients contained in the first two clusters are then evaluated Figure 3.27. A baseline configura-

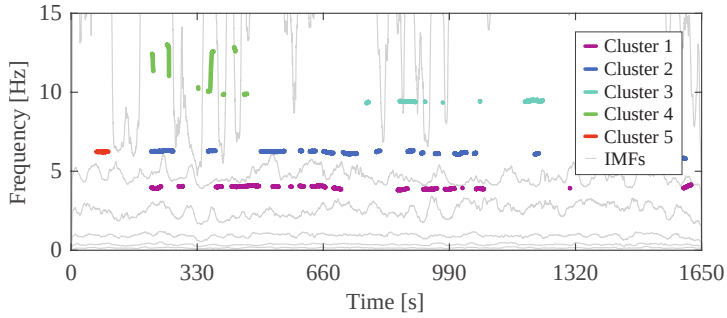

Figure 3.26: Instantaneous frequencies identified using the procedure proposed and the EEMD

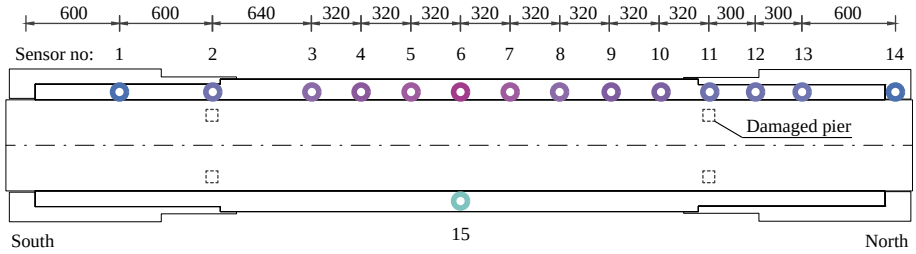

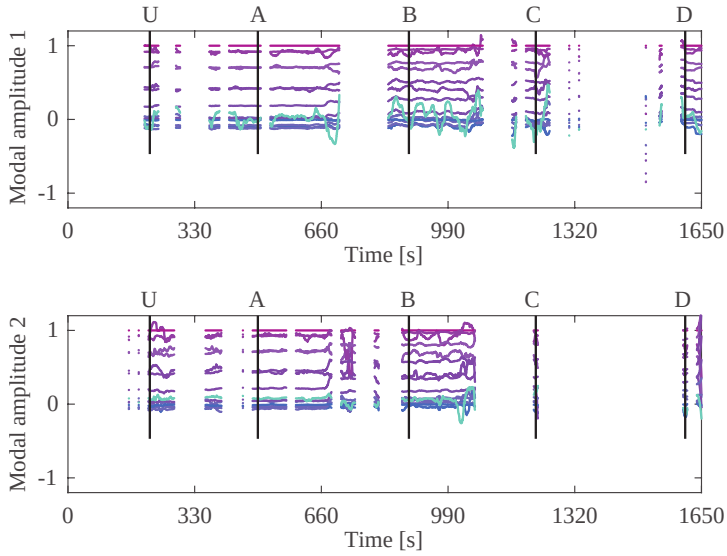

Figure 3.27: Instantaneous modal amplitudes of the first two clusters

tion (U) and four inspection instants (A, B, C, and D) are selected, one within each damage scenario, to simulate a periodic evaluation of the structural integrity. These instants are chosen when modal parameters are available for both the identified modes, to conduct a flexibility-based procedure employing the first two modal responses.

Flexibility-based damage identification

The instantaneous modal parameter identified through the DAMA can be employed for real-time damage identification. In particular, the variation in curvature or displacement of the Uniform Load Line (ULL), *i.e.*, the deflection shape under a unitary load vector) can be employed as a damage index. An instantaneous approximation of the structural flexibility matrix can be evaluated as

$$\mathbf{F}[t] = \sum_{j=1}^{p} \frac{1}{\omega_j^2} \boldsymbol{\phi}_j[t] \boldsymbol{\phi}_j^T[t] \tag{3.21}$$

where $\boldsymbol{\phi}_j[t]$ is the instantaneous mode shape evaluated using the set of components associated with the j-th cluster (or mode). It is highlighted that, in order to obtain a realistic estimate of the flexibility matrix, mass-normalized modal vectors should be used in Equation (3.21). However, assuming a uniform distribution of masses along with the axis of the structure, a proportional approximation of the flexibility matrix can be calculated [223]. Assuming that a unit load vector $\mathbf{p}$ is applied to the structure, the corresponding instantaneous displacement vector (*i.e.*, depending on the instantaneous flexibility) can be calculated as

$$\mathbf{u}[t] = \mathbf{F}[t]\mathbf{p} \tag{3.22}$$

The vector $\mathbf{u}[t]$, or its variation with respect to a baseline condition evaluated at the beginning of the monitoring process, can be monitored in time, generating an instantaneous damage index for each instrumented location. Considerable deviations from the baseline condition noticed for one or more instrumented locations may be indicative of ongoing damage.

Visualization of modal features

Although "automatization" is an attractive trend in recent SHM applications, human intervention is still essential both in the preliminary phase, when the monitoring process is designed and the operative algorithms are selected, and during decision

making.

Each point of the MAD is associated with an instantaneous vector $\boldsymbol{\phi}_k[t]$ which can be interpreted as an instantaneous ODS. This information can be exploited to obtain an intuitive color distribution in the time-frequency plane representative of the different modal responses forming the multivariate signal. A criterion to obtain such a representation may involve the selection of three recording channels, say the r-th, g-th, and b-th, and associating the amplitude of the wavelet coefficients $d_{i,k}[t]$, $i = r, g, b$, to color layers red, green, and blue to generate a color figure. Another approach, more suitable for densely instrumented structures, involves the sum of amplitudes at multiple locations in the determination of a single color layer.

For the baseline and each inspection instant, the instantaneous modal amplitudes were used to build an instantaneous mode shape vector which was then employed to estimate a proportional flexibility matrix. The ULL is therefore evaluated and the percentage variation in the displacement calculated for each instrumented location with respect to the baseline condition U is reported in Figure 3.28.

An outlier in the displacement of sensor 11 (close to the settled pier) is already noticeable from condition A, where the column was cut. However, other values with comparable percentage variation are registered around sensors 1, 2, and 14 during the first inspection. As the lowering of the column increases (*i.e.*, in conditions B, C, and D), the damage index becomes sharper around the settled pier, demonstrating to be particularly effective in localizing the anomaly.

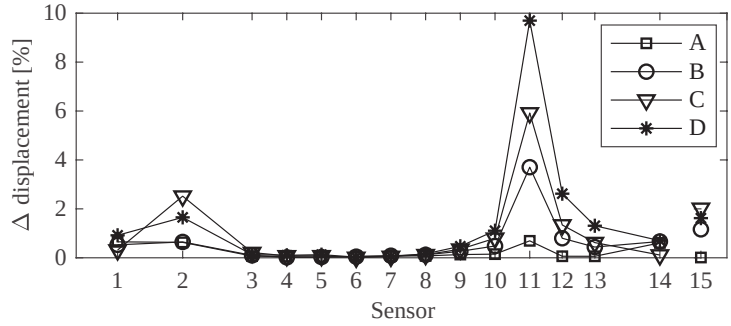

Figure 3.28: Damage localization in the inspection configurations

As a final analysis of this application, a comparison between the novel TFR proposed in this section and different spectrograms is shown in Figure 3.29. Let $\mathbf{D}_i \in \mathbb{R}^{2^n \times \overline{T}}$ be the matrix of wavelet coefficients obtained through the WPT at each instrumented location i. Due to the downsampling process of the WPT, $\overline{T} = T/2^n$, with T representing the total length of the original signal. The vector $\boldsymbol{\varphi}_k[t] \in \mathbb{R}^{r \times 1}$ formed of the elements of the TFR D_i corresponding to the time instant t and frequency subband k for all the recording locations $i = 1, \ldots, r$ can be interpreted as an instantaneous ODS of the analyzed structure.

The wavelet coefficients calculated through the WPT of each recording channel were masked through the approach presented in Section 3.3, thus generating 15 matrices $\overline{\mathbf{D}}_i$.

A color distribution is then generated, as shown in Figure 3.29a. Three color layers, corresponding to red, green, and blue, were defined as $\mathbf{R} = |\overline{\mathbf{D}}_{15}|$, $\mathbf{G} = \left|\sum_{i=8}^{14} \overline{\mathbf{D}}_i\right|$, and $\mathbf{B} = \left|\sum_{i=1}^{7} \overline{\mathbf{D}}_i\right|$, respectively, and then normalized to generate a standard RGB model.

On the other hand, the spectrograms reported in Figure 3.29b-d are generated using the data collected by sensors 3, 6, and 15, individually. It can be noted that each spectrogram provides different information based on the location where data is collected. Moreover, the energy distributions of Figure 3.29b-d do not enable the users to recognize different modal responses or notice if the dynamic behavior is changing. Conversely, the color coding of the multivariate dataset shown in Figure 3.29a allows discriminating between different modal responses since they are characterized by different colors. Moreover, an evolution of damage can be noticed around 660 s when the white area between 10 Hz and 15 Hz becomes green, highlighting the reduction of energy in this frequency range for the signal collected by sensor 15, which is confirmed in the related spectrogram.

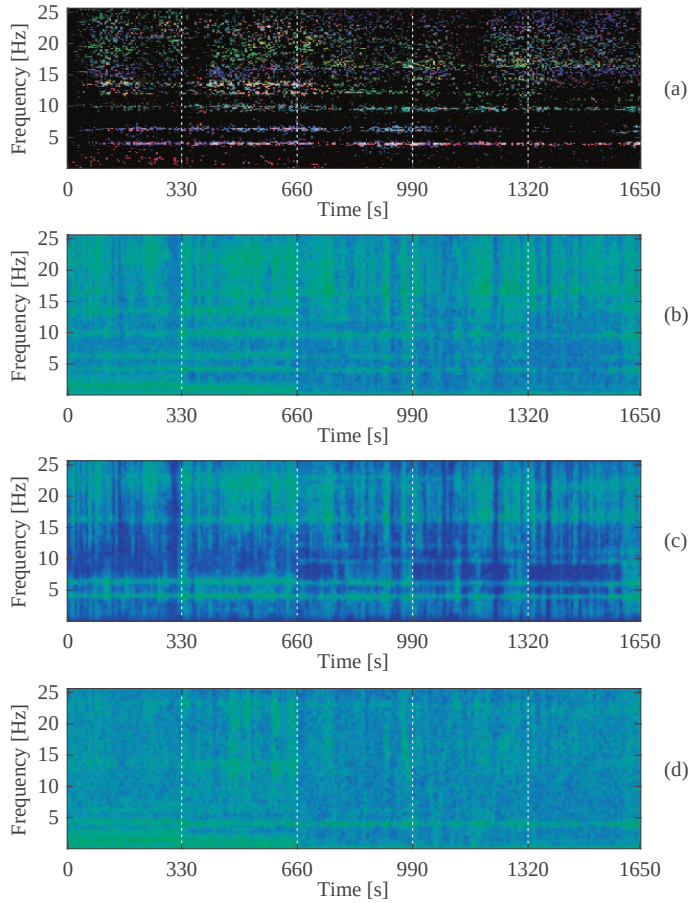

Figure 3.29: Visualization of natural frequencies in the time-frequency plain: masked wavelet coefficients (a), spectrogram of sensor 3 (b), spectrogram of sensor 6 (c), spectrogram of sensor 15 (d)

3.4 Edge computing in wireless sensor networks

An identification procedure is suitable for Wireless Smart Sensor Network (WSSN)-based systems if the algorithm is designed in order to allow each node to perform part of the processing operations independently, without knowing the information collected by the other nodes. Moreover, in order to perform the identification procedure in near real time, onboard operations must be simple and fast since the computational footprint of smart nodes is usually low.

In this context, a two-step identification method is proposed in this section, schematized in Figure 3.30. This algorithm is a variant

of the DAMA suitable for distributed sensing. The first step (*i.e.*, initialization step) of the algorithm consists of the construction of a Clustered Filter Bank (CFB), based on an initial dataset collected and processed in a centralized fashion. The second step involves distributed computing: each smart node, based on the information obtained in the first step, processes the collected vibration response individually, in real time. In particular, the microcontrollers embedded in each smart sensing node can collect, downsample, and transfer modal responses to the central monitoring station. Here, the data can be analyzed as responses of Single Degree Of Freedom (SDOF) structures through a TEO-based procedure and fused to obtain instantaneous modal parameters. Due to the filtering process, the noise sensitivity of the TEO is mitigated.

Step 1 is only applied at the beginning of the process. Then, Step 2 is performed recursively during the monitoring phase. However, since the modal parameters may vary consistently if damage or strong variations in environmental conditions occur, periodically updating the CFB could be necessary.

As aforementioned, in order to implement the n-level wavelet transform of a signal, the input can be convoluted with the equivalent filters obtained by cascading the lowpass and highpass filters associated with the selected wavelet, up to level n. The transform

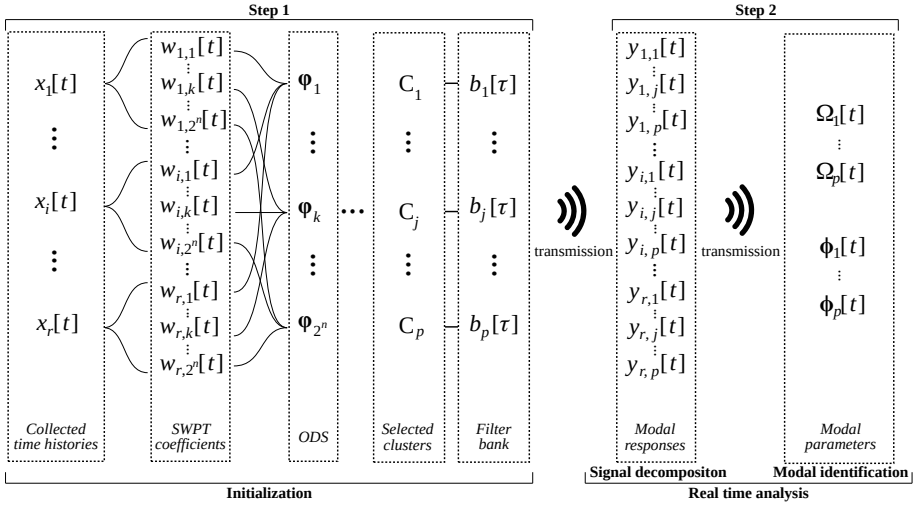

Figure 3.30: Workflow of the decentralized identification algorithm

is therefore conducted through the application of a filter bank of equivalent filters [20].

In this section, in order to decompose a signal $x[t]$ into a finite set of components $y_k[t]$ characterized by different frequency bands, the linear combination of which lead to the original signal, SWPT decomposition and reconstruction equivalent filters are applied in series, exploiting the perfect reconstruction property of wavelet filter banks [20]. Since the convolution operator $(*)$ is linear and time-invariant [224], a sequence of filtering operations can be performed in any order without changing the output result. It follows that the convolution of the original signal with a decomposition filter and then with a reconstruction filter gives the same output of a convolution between the original signal and the convolution of decomposition and reconstruction filters. Consider the signal and filters as discrete sequences in the time domain

$$y_k[t] = ((x * d_k) * r_k)[t] = (x * b_k)[t] \tag{3.23}$$

where $y_k[t]$ is the k-th component of the original signal $x[t]$, $d_k[\tau]$ and $r_k[\tau]$ are respectively the impulse responses of the k-th equivalent decomposition and reconstruction filters corresponding to the selected level of the transform, and $b_k[\tau]$ is the impulse response of the resulting filter obtained by the convolution between $d_k[\tau]$ and $r_k[\tau]$.

Since convolution is distributive over addition, a filtered version of the signal including m frequency bands of the SWPT (*e.g.*, from the k_1-th to k_m-th), can be computed as

$$y_{k_1,k_m}[t] = \frac{1}{m}\sum_{k=k_1}^{k_m}(x * b_k)[t] = \frac{1}{m}\left(x * b_{k_1,k_m}\right)[t] \tag{3.24}$$

where $b_(k_1, k_m)[\tau]$ is a filter obtained by summing the filters $b_k[\tau]$ associated with the considered m components. Assuming the system as linear, time-invariant and causal, the t-th sample of the filtered signal can be represented as

$$y_{k_1,k_m}[t] = \frac{1}{m}\sum_{h=0}^{N-1} x[t-\tau]b_{k_1,k_m}[\tau] \tag{3.25}$$

where $N-1$ is the filter order, $N = 2\overline{N} - 1$ is the length of $b_k[\tau]$, and $\overline{N}$ is the number of taps (*i.e.*, the length) of $d_k[\tau]$ and $r_k[\tau]$. Therefore, the filtering procedure can be carried out in real time by using only a subset of past samples of the input signal. However, this process introduces a delay in the output signal, which depends on the choice of parameters used to build the filter bank.

If the frequency bands $k_1, \ldots, k_m$ are properly selected, the component $y_{k_1,k_m}[t]$ could represent one of the structural modal contributions, which are linearly combined in the collected signal $x[t]$. Step 1 of the procedure proposed in this section is indeed an initialization step aimed at selecting the frequency range associated with the different modal components.

Step 1: Initialization

In a pre-processing stage, each sensor collects an acceleration time history (of user-defined duration) which is directly transmitted to the central monitoring station. Here, the signal collected at each node is decomposed using the SWPT, *i.e.*, through the convolution with a decomposition filter bank, generating 2^n wavelet components at the transform level n. Each component is related to a different frequency band, the energy of which is represented by the amplitude of the obtained wavelet coefficients.

Selecting a master sensor position (*e.g.*, the first sensor), it is possible to evaluate the operating deflection shapes by computing the mean over time of ratios between the k-th wavelet components of the master time history and other collected signals. In this way, 2^n ODSs can be computed as

$$\varphi_{i,k} = \frac{1}{s} \sum_{t=1}^{s} \frac{w_{i,k}[t]}{w_{1,k}[t]} \tag{3.26}$$

where $\varphi_{i,k}$ is the i-th element of the k-th ODS $\boldsymbol{\varphi}_k$, $w_{i,k}[t]$ is the t-th sample of the k-th wavelet component, computed on the signal collected by the i-th sensor, and s is the number of samples for each signal (*i.e.*, the length of the initialization signal window). For more robust results, the average can also be performed after excluding outliers. Using the concept of ODS similarity presented in Section

3.2, the MAC for each couple of neighboring shapes can be evaluated using Equation (3.11).

The process described above is similar to that of building a MAD. However, in this case, the time information of the TFR is lost since, instead of calculating the MAC between instantaneous ODSs, in this case, the MAC is evaluated on average ODSs calculated over a time interval of length s. Thereby, the output of this process is a vector (instead of a matrix, as it happens for the MAD), with values between 0 and 1 of size $2^n - 1$, which represents the similarity between consecutive average ODSs.

A clustering procedure is then performed by partitioning only the consecutive bandpass filters $b_k[\tau]$, the decomposition parts of which ($d_k[\tau]$) generate wavelet components with similar deflection shapes (*i.e.*, producing high MAC values).

The bandpass filters contained in each selected cluster can thus be summed as shown in (3.24), in order to obtain equivalent filters, following the rule:

$$b_{k_1}, b_{k_2} \in C_j \Leftrightarrow MAC_{k_1,k_2} \geq 1 - \theta \tag{3.27}$$

where MAC_{k_1,k_2} is the MAC calculated between the k_1-th and k_2-th average ODSs, C_j is a generic cluster, and θ is a user-defined threshold (with the same meaning as in Section 3.2). Furthermore, an energy-based selection procedure can be performed to discard the clusters the corresponding global energy E_j of which is lower than a chosen threshold Θ:

$$C_j \in \Gamma \Leftrightarrow E_j \geq \Theta \tag{3.28}$$

where Γ is the set of selected high-energy clusters. In this study, the global energy associated with the j-th cluster, which groups the wavelet components from the k_1-th to the k_m-th, was computed as:

$$E_j = \sum_{i=1}^{r} \sum_{k=k_1}^{k_m} \sqrt{\frac{1}{s} \sum_{t=1}^{s} w_{i,k}^2[t]} \tag{3.29}$$

The set of equivalent filter obtained this way forms a CFB . Therefore, the CFB consists of bandpass filters by which high-energy

signal components associated with different deflection shapes (*i.e.*, decoupled modal responses) can be extracted.

At the end of the initialization phase, the monitoring station transmits the CFB to each node of the WSSN . At the node level, the collected signal can be decomposed directly by calculating the convolutions with the different arrays of the filter bank. It should be noted that, after the construction of the CFB , small variations in frequency and even important variation in mode shapes can be registered since the decomposition is performed by using larger band-pass filters with respect to those associated with single wavelet components. This allows taking into account the changes in modal parameters associated with environmental variations or damage. On the other hand, because of relations (3.28) and (3.29), a signal component must exhibit a persistently high energy in the interval analyzed during Step 1 in order to imply the inclusion of the corresponding frequency band in the final filter bank. For this reason, high-energy peaks generated by transient features of nonstationary exciting input are generally neglected. The quality of extracted modal responses could also be further evaluated for example by observing their probabilistic features (*e.g.*, kurtosis [225]) in order to discard spurious modes generated by persistent harmonic components in the excitation.

The total complexity of Step 1, as reported in detail in Chapter A, is mainly due to the SWPT and is relatively high compared with that of the rest of the algorithm. However, although low-cost systems could take some seconds to perform the necessary initialization procedures, Step 1 only takes place when particular conditions occur and, once finished, gives way to Step 2 that consists of real-time analysis.

Step 2: Real-time analysis

Once the initialization phase is completed, each node has the same CFB which allows for the real-time decomposition of collected signals into decoupled modal responses, independently from other nodes. Therefore, in each node, the input signal is processed by convolution, as shown in Equation (3.25), with each array of the CFB generated in

Step 1. In particular, to calculate a new sample of the filtered signal $y[t]$, a window of new-coming data from $x[t-N+1]$ to $x[t]$ with the same length as the filter must be considered. After filtering, each component could also be downsampled (up to the Nyquist rate), in order to reduce the weight of data and easily transmit it to the monitoring station.

After obtaining the decoupled modal responses, thay can be analyzed as responses of SDOF structures to identify instantaneous natural frequencies and modal amplitudes. A nonlinear energy operator-based local method was used in this work, which allows online computing. In particular, the Discrete-time Energy Separation Algorithm (DESA)-1, which involves computing the TEO, was chosen. In the case of discrete signal analysis, the TEO is defined as [226]:

$$\Psi\left[y[t]\right] = y^2[t] - y[t-1]y[t+1] \tag{3.30}$$

where $y[t]$ is the t-th sample of a generic modal contribution. Several methods were implemented for the extraction of frequency and amplitude characteristics of non-stationary signals by using this operator. In particular, in DESA -1 [227], the instantaneous digital frequency Ω can be estimated as

$$\Omega[t] \approx \arccos\left(1 - \frac{\Psi[z[t]] + \Psi[z[t+1]]}{4\Psi[y[t]]}\right) \tag{3.31}$$

where Ω is the digital frequency, $\omega = \Omega F_s$ is the circular natural frequency, F_s is the sampling frequency, and $z[t] = y[t] - y[t-1]$. Since in this application the frequency is estimated online (*i.e.*, as new data is available), at the instant t, the values of $y[\bar{t}]$ with $\bar{t} > t$ must be unknown. For this reason, in (3.30) and (3.31), $y[t+2]$ must be intended as the last available value obtained from the convolution. In other words, an additional delay of 2 samples is introduced by using this algorithm for the estimation of instantaneous frequencies. The mathematical description of the total identification delay is reported in Chapter A.

It is possible to extract an instantaneous trend of the natural frequency from each modal response, through (3.31). It is possible to consider the modal responses extracted at only one instrumented location or, alternatively, to evaluate the multivariate instantaneous

frequency as an amplitude-based weighted average of the instantaneous frequencies obtained in each location [34], in order to avoid inaccurate estimates due to noisy recordings collected at the nodes of mode shapes. Using the TEO, it is possible, indeed, to capture also the instantaneous amplitude of the analyzed signal [227] as:

$$A[t] \approx \sqrt{\frac{\Psi[y[t]]}{1 - \left(1 - \frac{\Psi[z[t]] + \Psi[z[t+1]]}{4\Psi[y[t]]}\right)^2}} \tag{3.32}$$

However, the estimates of instantaneous frequency and amplitude are highly sensitive to noise, as the algorithm uses only a few input samples in the calculation. In order to mitigate the presence of spurious spikes in identified frequencies, a median filter can be applied on a window of the last $\mu + 1$ estimated values, obtaining the denoised frequency $\overline{\Omega}[t]$ as

$$\overline{\Omega}[t] = med[\Omega[t - \mu], \Omega[t - \mu + 1], \ldots, \Omega[t]] \tag{3.33}$$

Moreover, an estimation of the i-th element of the j-th instantaneous mode shape $\phi_j[t]$ can be simply computed as the ratio between the components $y_{i,j}[t]$ and $y_{r,j}[t]$ obtained by the convolution of signals registered at different positions (*i.e.*, $x_i[t]$ and $x_t[t]$, with r denoting a reference location) with the same filter $b_j[\tau]$ (see Equation (3.5)).

In this study, the identification of damping was not considered, for which, to date, robust identification methods are still lacking [228]. Furthermore, damping is not yet clearly correlated with damage and environmental conditions; therefore, further studies that go beyond the purposes of this thesis need to be conducted.

As demonstrated in Chapter A, Step 2 implies a computational burden in the order of $O(N)$ per input sample onboard each node. This makes it possible to obtain near-real-time estimates of instantaneous modal parameters even using low-cost systems. Most traditional identification techniques used in a decentralized fashion for the identification of instantaneous modal parameters require a higher computational burden and are often related to other disadvantages. In particular, processing a signal window of length N through

the STFT would imply a computational complexity in the order of $O(N \log N)$ per sample, using the Fast Fourier Transform (FFT) [20]. Moreover, it would also be necessary to extract the instantaneous trend of natural frequencies and mode shapes for each identified mode through a further ridge-extraction procedure, thus increasing the overall complexity. On the other hand, considering the HHT, such as in the algorithm used by [87], which does not require any ridge extraction, the computational burden can be considered as proportional to that of the FFT [229], but the results obtained are often affected by problems such as mode-mixing. Furthermore, in a decentralized topology, the IMFs computed by analyzing the signals collected in different instrumented locations may have different frequencies (and then be associated with different vibration modes), leading to a misleading identification of mode shapes.

Moreover, the computational cost of Step 2 for the monitoring station is particularly low compared to other recent centralized algorithms. For instance, considering the method based on Recursive Canonical Correlation Analysis presented in [70], the most demanding part related to the eigenspace update has a complexity in the order of $O(m^3)$ per input sample, with m denoting the number of eigenvectors of the block covariance matrix of structural responses, which depends on the number of data channels and is generally higher than the number of identified modes p which governs the computational complexity of the presented algorithm without considering any post-processing operations (see Chapter A). Similarly, the Equivalent Adaptive Separation Algorithm (EASI) algorithm used in [230] has a complexity in the order of $O(q^3)$ where q is the number of data channels [231]. Also, it should be noted that the decentralized implementation of the proposed algorithm enables a suitable downsampling of the data before transmission, which makes it appropriate for wireless systems. On the other hand, the algorithms presented in [70] and [230] require the data from all sensors available in the monitoring station in order to update the time-varying models.

It should also be noted that the method presented is designed for the online identification of modal parameters, but it could also be used for periodic inspections. In this case, after the initialization, the

sensing nodes could be periodically switched on for collecting signal in a given time interval, which is decomposed and downsampled onboard each node, and then transmitted to the monitoring station.

In the case of damage diagnosis for civil structures, it is also important to consider the long-term variability of identified parameters [232, 233]. The knowledge of their variation under different environmental conditions allows the construction of a model that may be used to limit the possibility of false alarms [234, 235]. This may be done, for example, by correlating the variation of estimated parameters with measured environmental conditions (such as temperature and humidity) and anthropic sources (such as the intensity of vehicular traffic) [236–238]. Besides, in order to restrain the fluctuation of identified parameters due to continuously changing operational phenomena (*e.g.*, moving cars on a bridge), suitable post-processing is necessary, *e.g.*, using a wide window for median filtering, as shown in Equation (3.33). In this case, the robustness of the algorithm to operational uncertainties increases, as the latency of resulting identified quantities, as shown in Chapter A.

Refreshing the CFB

A periodic refreshing procedure can be applied by updating the filter bank at user-defined intervals or at the occurrence of particular conditions (*e.g.*, upon reaching a user-defined variance value in the modal parameters estimation), as shown in Figure 3.31.

The updating procedure consists of a repetition of Step 1 at determined time intervals, at the occurrence of situations in which it may be convenient to update the filter bank (*e.g.*, when the signal amplitude is high, SNR increases and the effects of noise affect the procedure less), or when significant changes are noticed in the evaluated instantaneous frequencies. The updating procedure also reduces the risk of carrying out an incorrect identification based on a filter bank generated in the presence of narrow-band excitation.

If one of the conditions selected to start the updating procedure arises, the sensing nodes collect and transmit a limited signal window to the monitoring station, as it occurs during the initialization phase. Then, the procedures illustrated in this section are repeated and the

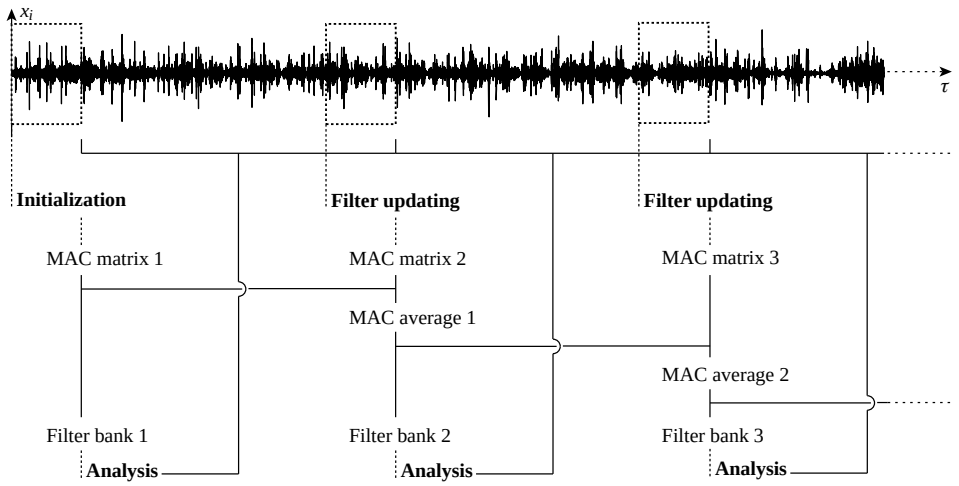

Figure 3.31: Workflow of the periodic CFB refreshing procedure

updated CBF is finally transmitted to each node, where real-time analyses start again using the new filters until the next update. The recursive clustering procedure to determine the updated filter bank can be performed by taking into account not only the parameters evaluated within the new signal window but also those computed at previous steps, by performing a weighted average, as shown in Figure 3.31. The updating criterion used in this application is the following:

$$\overline{MAC}^{l}_{k_1,k_2} = \frac{MAC^{0}_{k_1,k_2}}{2^l} + \sum_{\zeta=1}^{l} \frac{MAC^{\zeta}_{k_1,k_2}}{2^{l-\zeta+1}} \tag{3.34}$$

where $MAC^{0}_{k_1,k_2}$ is the value computed during the first initialization procedure and $MAC^{\zeta}_{k_1,k_2}$ are the values calculated during the subsequent updates, up to the l-th. At each iteration, the new part gains the same weight of the whole set of previous values, the older of which become negligible after a few updates.

If low-cost hardware with limited computational capacity is employed, it may be necessary to interrupt the real-time analysis during the filter updates, since clustering is an energy-consuming centralized operation (see Chapter A). To limit this issue and optimize resources, the CFB update procedure should be shortened as much as possible. For this purpose, a limited number of instrumented

locations can be selected as a reference and used to calculate the parameters on which the cluster procedure is based. Therefore, the MAC coefficients can be evaluated considering only the signals collected at the selected reference locations. If only two reference locations are considered, the average ratio between the filtered components shown in Equation (3.26) can be directly employed as a clustering variable. In this case, the condition (3.27) becomes

$$b_{k_1}, b_{k_2} \in \mathrm{C}_j \Leftrightarrow \frac{1}{s}\sum_{t=1}^{s}\left(\frac{w_{r_1,k_1}[t]}{w_{r_2,k_1}[t]} - \frac{w_{r_1,k_2}[t]}{w_{r_2,k_2}[t]}\right) \leq \theta \tag{3.35}$$

with r_1 and r_2 being the selected reference instrumented locations. Using a small number of signals for clustering leads to a consistent reduction in the computational burden of the updating procedure. This can be seen in detail in Chapter A, since the value of r reported in Table A.1 decreases accordingly. However, this simplified method may lead to the construction of a less accurate filter bank, depending on the choice of reference locations. In order to make the optimal selection, the locations have to be chosen at the points where maximum amplitudes of first modal shapes occur, avoiding the nodes, where the recorded accelerations are low and inaccurate.

Both for the original approach and for the simplified method, the computational complexity of the identification procedure, as well as the accuracy and delay of identified quantities, depend on the choice of setup parameters, as shown in Chapter A. In particular, the parameters concerning the wavelet transform (*i.e.*, the type of function, its order, and the transform level), the length of post-processing window, the MAC threshold used for filter bank construction, and its updating rate play a central role. The criterion for choosing these parameters may however vary according to the specific case study. For structures with quite distant vibration modes (in terms of natural frequency) and low-noise recordings, it is advisable to build a small filter bank in order to obtain modal parameters with little delay; on the other hand, in the case of noisy recordings and closely-spaced vibration modes, filter order and transform level must be increased, also increasing the delay. In this case, a more frequent filter update may also be necessary. Thus, high transformation levels and wavelet orders lead to more precise filtering, with the disadvantage of higher computational effort and

long delays due to demanding convolution procedures. Regarding the MAC threshold θ, the selection of a low value generally leads to filters with a wider band, which may result in the extraction of modal responses with low SNR or multi-component signals (in the case of consecutive modes with similar shapes). On the other hand, if the decomposition level is high and the signal analyzed is noisy or the window selected for the initialization phase is short, a low threshold could help in merging components of the same vibration mode, the shapes of which are slightly different due to estimation errors. A large value of the threshold however leads to narrow-band filters which must be frequently updated if estimated modal parameters fluctuate either for physical reasons or estimation uncertainties.

Damage identification of an RC bridge using wireless sensors

In this section, a practical application of the CFB -based decomposition is shown. The case study described in the third application of Section 3.3 is considered, assuming a distributed computational scheme. Specifically, the data was analyzed a posteriori, with the complete data set available. However, the analysis is conducted by considering only few samples at a time, simulating a real-time monitoring process.

Only the data recorded in the vertical direction was used, downsampled at 100 Hz. In order to set up the two-step procedure, a 100 s signal window for damage scenario U, recorded at each sensor position, was used in the initialization phase (Step 1). These signals were decomposed through a decomposition filter bank built by choosing the 14-th order *Fejér-Korovkin* wavelet (*fk14*) and decomposition level 6.

Afterward, the operating deflection shapes associated with each component and their MAC coefficients were computed as shown in Section 3.4. Then, a clustering procedure was performed in order to group the components characterized by high MAC value and similar frequency contents. To this aim, a threshold $\theta = 0.2$ was chosen for

MAC-based clustering, and only consecutive components compliant with condition (3.27) were assigned to the same cluster.

Consequently, an energy-based selection procedure was applied to the obtained clusters to select only the high-energy components. In Figure 3.32, the bandpass filters associated with the MAC-based clusters are represented in the frequency domain, together with their RMS energy values (represented as circles). In this phase, being interested in the identification of the first modes, only the frequency range between 0 Hz and 15 Hz was analyzed. In order to select the Θ parameter, in this application, the HPV energy of the signal in all the frequency ranges related to the different arrays of the CFB were calculated. Then, the final threshold Θ was considered as the mean of these RMS energy values. Therefore, only the clusters with energy higher than average (represented as a dashed line in Figure 3.32) were selected to form the final CFB , which is then transmitted to the sensor nodes.

Different selections for the parameter θ lead to different filters in the CFB . In Figure 3.33, the filter banks obtained by selecting different values of θ are reported as rectangles with a variable width, which represent the frequency range of each filter. As explained in Section 3.4, higher values lead to narrow-band filters, which may be unsuitable for noisy data. Moreover, although the criterion to select Θ is the same described above, the RMS energy threshold for

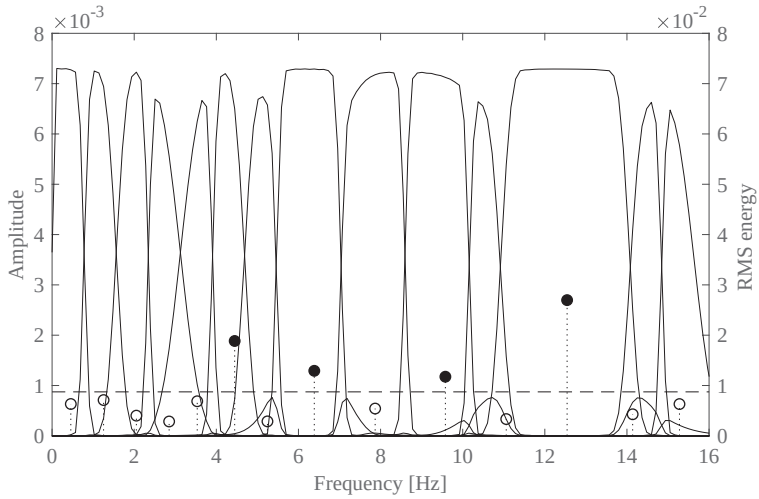

Figure 3.32: Representation of the filter bank in the frequency domain and the energy level (RMS) for each cluster (full circles indicate energy values over the average level, represented as a dashed line)

selecting high-energy components changes slightly for each case. The gray rectangles represent filters with high-energy components in the signal interval analyzed in Step 1. Specifically, the energy-based selection process results in a larger number of high-energy components for low values of θ. In Figure 3.33, the pink lines superimposed to the filter banks show how the equivalent filters of the CFB are divided as the MAC threshold θ increases.

Once completed the initialization phase, each node has the same CFB that allows for real-time decomposition. In Step 2, a signal obtained by merging 6 recordings related to different damage scenarios was analyzed in order to simulate modal identification under structural time-variant behavior. In particular, 15 acceleration time histories (*i.e.*, one for each instrumented location) of 1980 s were generated by merging the 330 s recordings related to scenarios U, A, B, C, D, and E, with reference to Table 3.1. Each signal was decomposed individually, simulating the operations performed onboard the sensor nodes (*i.e.*, convolution with the CFB).

While the decomposition is in progress, each sample obtained by convolution (or a subset of them if downsampling is performed) can be transmitted to the monitoring station, which carries out the real-time modal identification. In this application, all the modal responses were downsampled by a factor 3 (with a final sampling

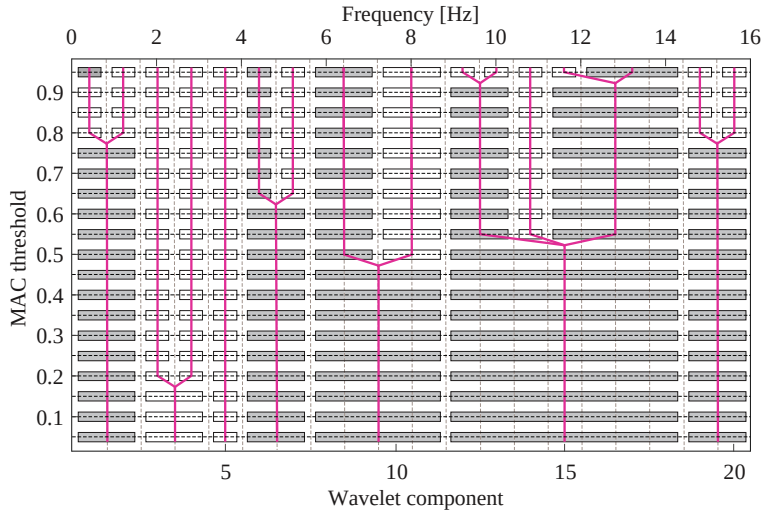

Figure 3.33: Filter banks obtained using different values of MAC threshold. Each filter is represented as a rectangle (empty for low-energy components and filled for high-energy components)

period of 0.03 s). Natural frequencies and mode shapes where then estimated through the TEO, as shown in Section 3.4. In order to obtain more accurate results, a median filter was applied using a window of 300 samples (*i.e.*, each sample of the resulting instantaneous parameters was computed as the median of the last 300 instantaneous values). Instantaneous frequencies, computed considering the signal collected by sensor 9, are reported in Figure 3.34, where the results obtained from the mere application of the two-step algorithm (blue lines) are also compared with the reference values of Table 3.2 (cyan dashed lines), with the natural frequencies obtained by performing a Frequency Domain Decomposition (FDD) over each damage scenario (orange dashed lines), and with the results obtained by periodically updating the CFB in the proposed identification process. This last case will be analyzed later in detail. In Figure 3.34, the frequency plots are also superimposed to the spectrogram obtained by means of the STFT, applied to the unfiltered signal collected in the same instrumented location.

In Figure 3.34, the vertical black dashed lines represent the entry into a different damage condition. In this figure, the identification latency due to convolution, DESA -1 algorithm, and median filtering is not represented. It can be computed as shown in Chapter A, resulting respectively in 8.76 s, 0.06 s, and 4.50 s (*i.e.*, 876 samples under the original sampling frequency, and 152 samples after down-

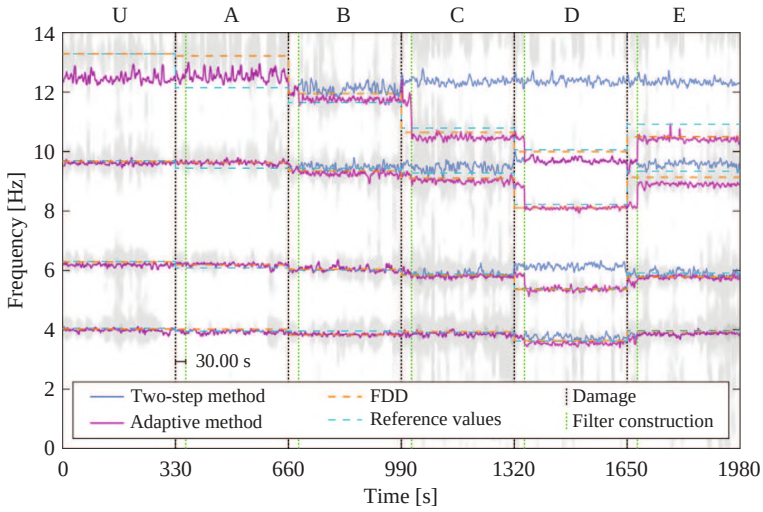

Figure 3.34: Comparison of identified natural frequencies over time. The lines of identified frequencies are superimposed on the spectrogram obtained by means of STFT (gray shade)

sampling by a factor 3), for a total of 13.32 s. This latency would involve a uniform translation of the diagrams in Figure 3.34 to the right.

In Figure 3.35, the identified mode shapes are represented over time: the plotted mesh interpolates the values estimated by sensors 1-14, while the black line plotted on the time-amplitude plane represents the component relevant to sensor 15, deployed on the opposite side of the deck.

Figure 3.36 shows the MAC coefficients computed by using the mode shapes identified through the two-step method and those reported in [218]. In particular, each MAC coefficient was computed considering the mode shape identified by means of the algorithm proposed, averaged over the entire duration of the considered damage scenario, and the corresponding reference mode shape (*i.e.*, related to the same mode and damage scenario) reported in [218].

The results show that the first mode was successfully identified for all the damage scenarios both in terms of frequencies and mode shapes, since the variation in frequencies is modest compared to the baseline U (see Table 3.3). Concerning the second mode, the two-step CFB decomposition is efficient for all the damage scenarios except for condition D, in which the percentage variation of frequency from the baseline is about 15%. The fourth mode is characterized by frequency variations higher than 10% already for condition B and, therefore, the identification results are poorly accurate for the following scenarios.

While for the monitoring station Step 2 is much less demanding than Step 1 in terms of computational complexity, considering also that the monitoring station generally is a wired system with a larger computing footprint, the computational cost of Step 2 is of fundamental importance for sensing nodes. As shown in Chapter A, the computational complexity of Step 2 for sensing nodes depends on the number of filters (*i.e.*, the number of modes identified) and their length. In this application, considering 4 modes extracted by filters of 1753 taps each (see Chapter A for more details), a total amount of 7012 multiply-accumulate operations is performed for decomposing each new sample of data by convolution. In particular, the Signed Long Multiply with Accumulate (SMLAL) instruction is considered,

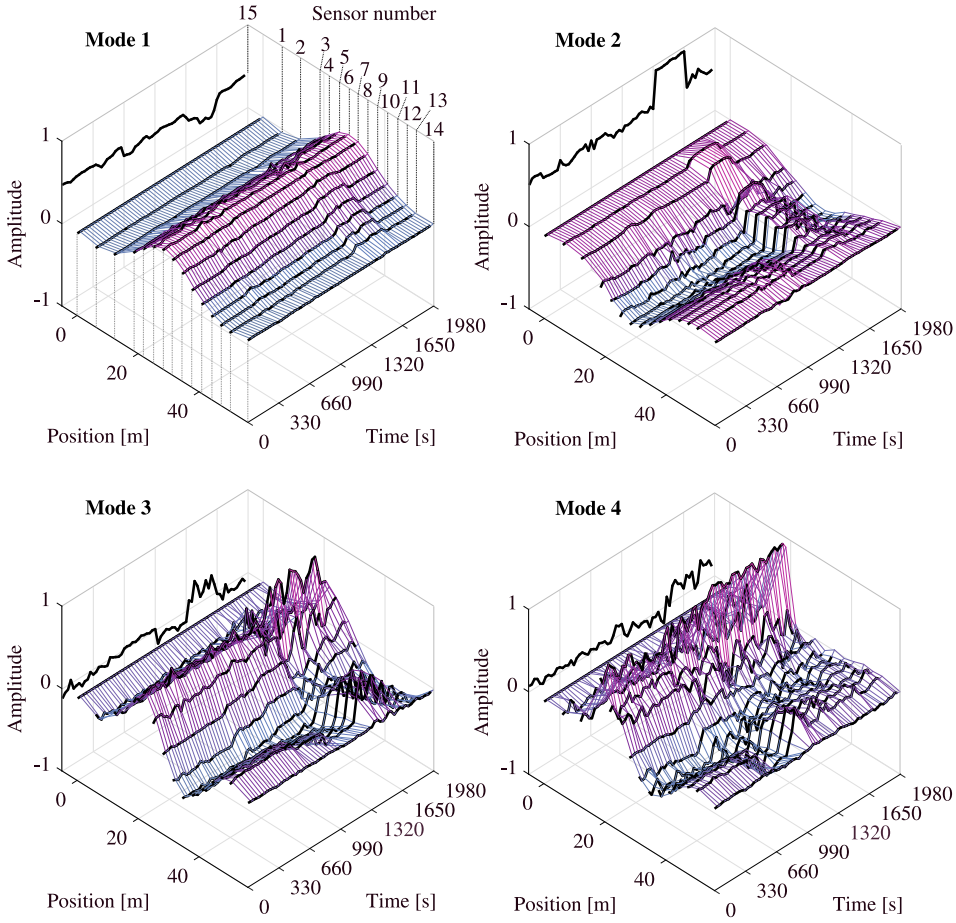

Figure 3.35: Mesh interpolation of the instantaneous mode shapes identified by the two-step method

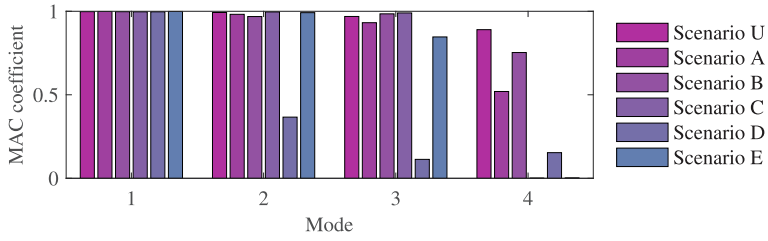

Figure 3.36: MAC coefficients computed by using the averaged mode shapes identified through the two-step method and those reported in [218]

which is more suitable for high-accuracy signal processing (*e.g.*, when operating with 16-bit or 24-bit ADC data) [239]. Considering, for example, the low-power X-scale PXA271processor (*i.e.*, the same implemented on the Imote2, an advanced platform largely used for SHM purposes [74, 79, 94], working at 13 MHz, and assuming an

average value of 4 cycles per instruction for the SMLAL [240, 241], each new sample of data requires an execution time of about 2.15 ms to be decomposed into four separate double-precision samples of modal responses. The reason why an average value is selected for the number of cycles is that it depends on the early termination of registers. However, the selected value is precautionary, as it is exceeded only in the event of an overflow [239–241]. It is also possible to optimize the convolution procedure using the integrated performance primitives [241], achieving even better performances.

Simulating the extraction of four modal responses from a signal of 2048 samples by means of the method proposed, about 57.442×10^6 clock cycles are overall necessary, regardless of the nature of the signal analyzed. The HHT is one of the most used methods for the identification of instantaneous frequencies and amplitudes in different fields of engineering. In particular, recent implementations in the civil field were proposed [75], together with online variants [229] which enable the real-time extraction of modal responses [86, 87]. Implementing onboard each node the empirical mode decomposition, which is the first step of the HHT, in which the signal is decomposed into IMFs, the computational cost would be strongly related to the signal features [242] and could be different for each node. Wang et al. [242] measured on average 22.528×10^6 clock cycles per extracted IMF on an ElectroCardioGraphy (ECG) signal of 2048 samples processed through a Nios II processor and using the stopping criterion proposed in [243]. However, a simulation of the most time-consuming condition, analyzed in the same work, lead to 1.380×10^6 clock cycles per sifting iteration, which is more than 10 times higher than the initial test with the ECG signal. Considering the computational complexity estimated by [229] in the worst case, instead, the total number of cycles involved in the decomposition of a 2048-sample sliding window with extra 256 samples overlap (in both sides, for a total of 2560 samples) for the extraction of 11 IMFs (assuming EMD as a dyadic filter bank) is 55.757×10^6, which is comparable with the effort of the presented algorithm. In this evaluation, 10 sifting iterations were assumed per IMF; moreover, 3 clock cycles were considered for simple multiplications, 1 for additions, 1 for comparisons, and 50 for divisions, which can generally take between 20 and 100 cycles [240]. However, IMFs do not have pre-

determined frequency values and it is difficult to discern between physical and noise-generated components onboard the microcontroller, requiring the transmission of all identified IMFs with no possibility for downsampling. This issue makes online implementations on WSSN s unfeasible. Comparing the method proposed with another wavelet-based approach for online identification of modal parameters presented in [244], the computational complexity of the signal decomposition part is exactly the same since it involves a filtering process through an adaptive wavelet filter bank. However, the wavelet function selected in [244] is complex, increasing the necessary number of cycles per operation, and the online recursive least squares algorithm for the identification of modal parameters is not suitable for onboard processing and filter updating since it requires matrix multiplications at each collected data sample. Moreover, centralized identification of modal parameters with instantaneous feedback updating of the filter bank would involve high wireless transmission rates, making the algorithm unsuitable for implementation on WSSN s.

In order to mitigate the problems associated with a static definition of the CFB , the refreshing procedure presented in this section was applied. Specifically, the identification process was performed by considering the first CFB as the one already used in the previous analyses, followed by 5 updating steps (one every 330 s, at the beginning of the signal segments related to different damage conditions). For each step, a signal decomposition was carried out by considering a time window of 30 s, and the matrix of MAC coefficients was computed by using the operating deflection shapes of each signal component. With the aim of speeding up the procedure, the decomposition can be carried out by considering a reduced frequency band: in this work, only the interval between 0 Hz and 15 Hz was considered. The MAC matrices related to each updating step are reported in Figure 3.37 (first row). In order to avoid the inaccurate estimation of modal parameters due to the inefficient choice of the signal windows necessary to build the filter banks, the average procedure described in Equation (3.34) was applied the MAC matrices. For each step, the new filter bank is then evaluated by using the related averaged MAC matrix, reported in the second row of Figure 3.37 for each update.

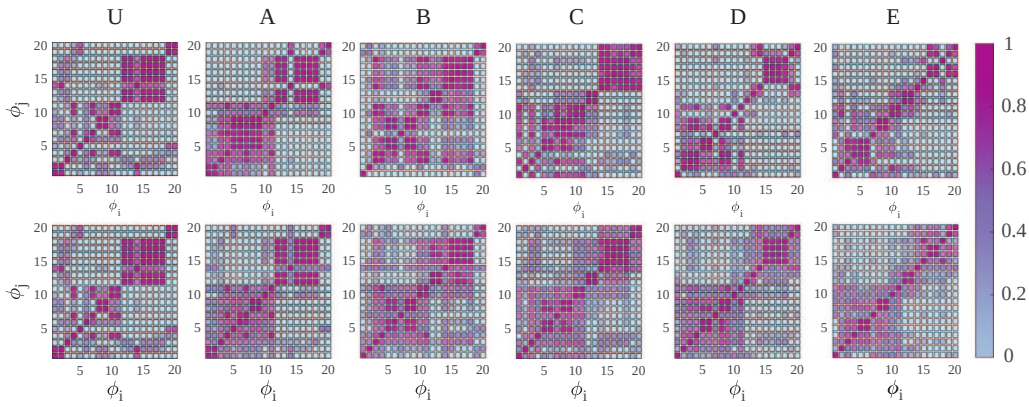

Figure 3.37: MAC matrices computed for each step (first row) and related average matrices used for updating the CFB (second row)

It is observable that high values in the MAC matrices related to the condition A are quite widespread (not only close to the diagonal), but the matrices used to build the filter banks are less sensitive to this fact due to the performed average procedure. In Figure 3.34, Figure 3.38, and Figure 3.39 the instantaneous modal parameters identified using the refreshed CFB are shown, together with the related MAC coefficients, computed by using the mode shapes reported in [220] as references.

It is worth noting that, in Figure 3.34, considering the adaptive procedure, the delay in estimated modal parameters seems to increase when important variations in frequency occur and the filter bank is updated. This is due to the fact that signal windows of 30 s at the beginning of each damage scenario (*i.e.*, the interval between the black and green vertical dashed lines) are processed through the filter bank of the previous scenario while a new window of data is recorded to perform the updating procedure. The parameters identified in these intervals are generally characterized by higher error with respect to the values identified after the updating. However, the identification latency is the same as the two-step implementation. Considering also filter updates, which nevertheless take place only at the occurrence of specific conditions, the maximum latency in the estimation of modal parameters through the updated filters is 43.27 s in this application. Considering the frequency values reported in Figure 3.34, it can be noted that, except for the fourth mode

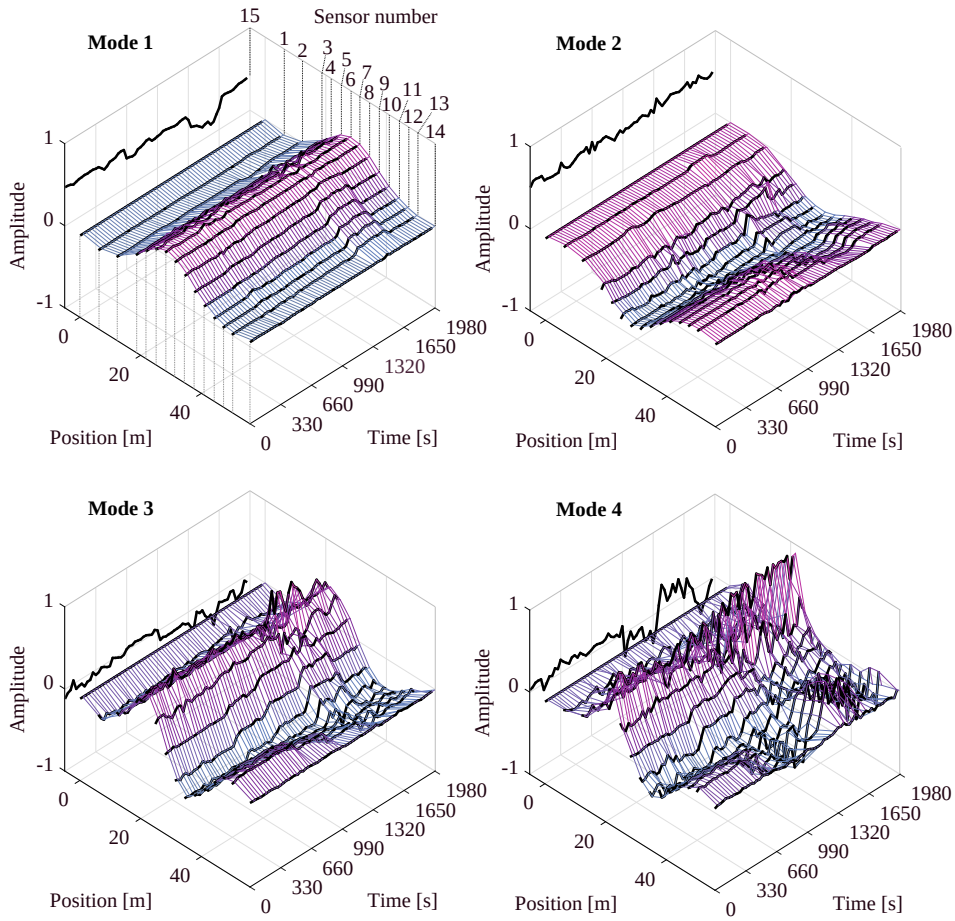

Figure 3.38: Mesh interpolation of the instantaneous mode shapes identified by the adaptive method

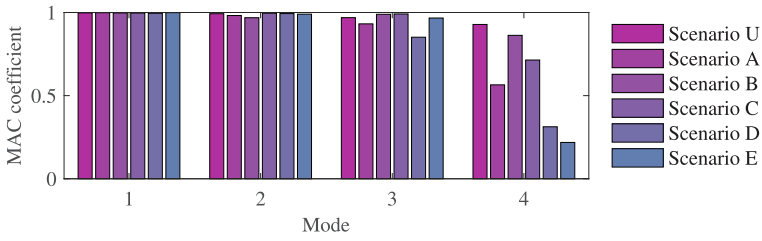

Figure 3.39: MAC coefficients computed by using the averaged mode shapes identified through the adaptive method and those reported in [218]

in conditions U and A, the parameters estimated by the updated CFB -based procedure approximate the reference ones even under substantial variations, with a certain latency due to filter updating. It is also possible to observe that the identified instantaneous natural frequencies correspond to the ridges of the spectrogram obtained

by means of the STFT, also reported in Figure 3.34.

Both instantaneous frequency estimates obtained through the proposed method processed through a median filter with the same window of 300 samples in order to make the plots more readable since DESA -1 produces results very sensitive to noise. However, in Figure 3.34, it can be observed that the adaptive method generally produces smoother trends. In fact, by applying the adaptive procedure, although structural characteristics vary over time, each filter is always centered on the maximum frequency peak of the identified mode and, through the refreshing process, the noise is minimized by eliminating the frequency components associated with different ODSs. Conversely, if natural frequencies vary and the filters are static, the noise components gradually gain in importance, making identification results noisier. Considerable improvement can be noticed observing the MAC coefficients of Figure 3.36 and Figure 3.39, especially for damage scenario D. In particular, the first three modes are characterized by MAC values higher than 0.93 for all the damage scenarios, except D, which has a value of 0.85 for the third mode. The fourth mode has gained an average accuracy improvement of 0.21, mainly due to the MAC values related to scenarios C and E.

As aforementioned, a simplified clustering method that does not involve the calculation of the whole set of operating deflection shapes can also be performed, especially when the length of filters and the decomposition level are high, involving a high computational effort. In a further analysis, considering the *fk22* function (see Figure 3.1 for the frequency domain representation of the filter bank) and a decomposition level 7, the ratios between the wavelet components were directly considered as clustering variables. In particular, two different cases were analyzed: the first involved sensor locations 4 and 6 as references, while the second is referred to locations 4 and 15. In Figure 3.40, the results of the clustering procedure for the two mentioned cases is reported. Small circles represent the signal ratios calculated between the components associated with each bandpass filter recorded at the considered reference locations. Specifically, filled circles refer to case 1, while empty circles refer to case 2. Moreover, gray circles represent low-energy components,

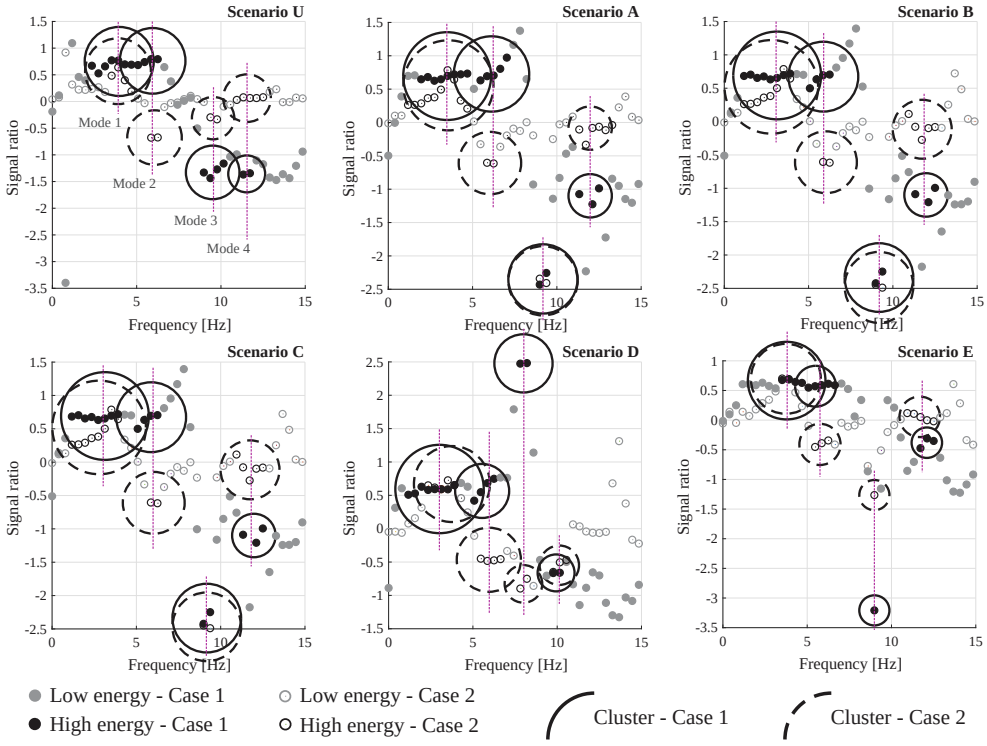

Figure 3.40: Simplified clustering procedure

while the black ones represent high-energy components. The high-energy components were partitioned in clusters, represented by larger circles (solid borders for case 1 and dashed for case 2), with a radius proportional to the energy of each cluster.

As concerns the first case (reference sensors 4 and 6), it can be noted that the first two modes are difficult to identify as different clusters since the ratios between the filtered components are very similar, especially for the undamaged condition. On the other hand, as regards the second case (reference sensors 4 and 15), the first modes can be clearly separated since the signal ratios have opposite sign. Indeed, sensor 15 is arranged on the opposite side of the deck with respect to sensor 4 and allows identifying torsional modes. However, for the third and fourth modes, the signal ratios are poorly accurate in this second case since sensor 15 is close to the nodes of the higher mode shapes. It should be noted that the clustering procedure can be also carried out by simultaneously observing both

the considered cases. However, using the full MAC-based method, the risk of incurring errors that could affect the evaluation of modal parameters is minimized.

As an example of using the modal parameters identified in this application, a flexibility-based damage identification procedure is applied, using the displacement variation of the ULL [245] as a DSF (similarly to Section 3.2. Here, the natural frequencies of the first three modes, identified through the refreshed CBF-based algorithm, were considered. Besides, only the instrumented locations from 1 to 14 (representing the behavior of the west side of the bridge deck) were taken into account.

Knowing p natural frequencies and modal vectors, it is possible to estimate the flexibility matrix of the structure, as shown in Equation (3.21). Since the mass matrix of the structure is unknown, the modal matrix cannot be mass-normalized. However, if masses are equally distributed along the structure, the mass matrix could be assumed as diagonal, such that $\mathbf{M} = \mu\mathbf{I}$, where μ is a constant value, equal to the mass associated with each Degree Of Freedom (DOF) of the structure, and $\mathbf{I}$ is the identity matrix. In this application, the mass matrix was assumed as the identity matrix, since masses are not significantly variable along the longitudinal axis of the bridge. Therefore, a proportional flexibility matrix is employed to calculate the ULL .

In Figure 3.41a, the instantaneous ULL is represented over time, while Figure 3.41b shows the average lines obtained for each damage scenario. Since the flexibility matrix is not mass-normalized, the displacements are not representative of real physical quantities.

In order to perform the damage identification, the absolute variation in terms of displacements (here denoted as Δ) with respect to the values of the undamaged condition was considered as a damage-sensitive feature. Here, the presence of damage is detected if outliers are identified in the set of computed variations, while damage localization is accomplished by seeking the outlier location. Figure 3.42a represents the real-time damage identification process: the instantaneous Δ values are represented, computed by using the ULL estimated during the first initialization procedure (as a baseline) and the instantaneous ULL s reported in Figure 3.41a.

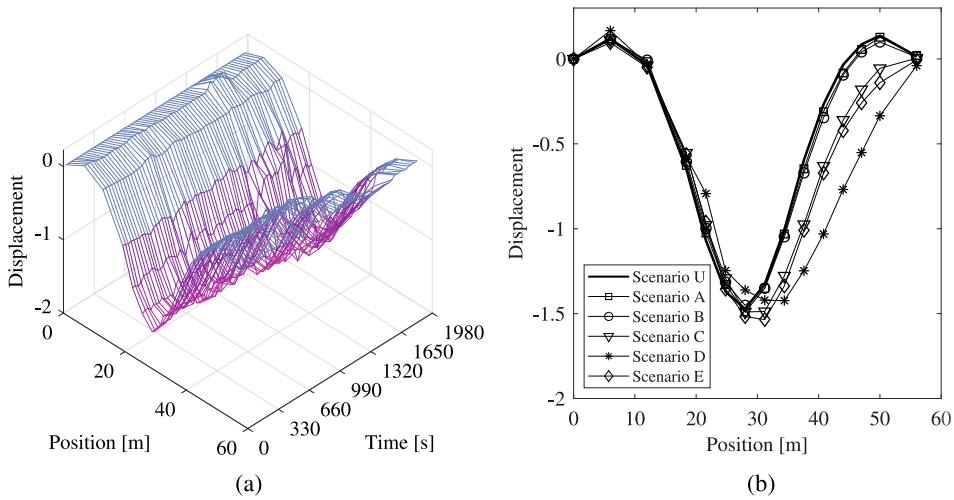

Figure 3.41: Mesh interpolation of the instantaneous uniform load lines (a) and averaged lines over time for each damage scenario (b)

Also, in Figure 3.42b, the percentage variations computed by using the ULL s of Figure 3.41b are plotted versus sensor locations (the origin of the position axis is assumed on the south border). For both the instantaneous and averaged analyses, clear outliers were evaluated in the damage index. Specifically, the outliers are defined as the terms higher than two standard deviations from the mean of the damage index. In the first case, the outliers were computed for each time instant, with the instantaneous mean calculated over the sensor locations. In the second case, the analysis was performed on the static values represented in Figure 3.42b, for each damage scenario.

For the instantaneous analysis, even by using few modes (*i.e.*, the first three modes in this application), the damage identification was successfully achieved for each damage scenario from A to E, since a persistent outlier in damage features occurs close to sensor 11 (*i.e.*, at the damaged pier location). On the other hand, the static evaluation leads to an uncertain scenario for conditions A and B, where the maximum value of the damage index is close to sensor 1. The analysis of instantaneous variation allows considering the persistence of the identified damage as a further tool to determine if the damage is real or generated by short-term effects.

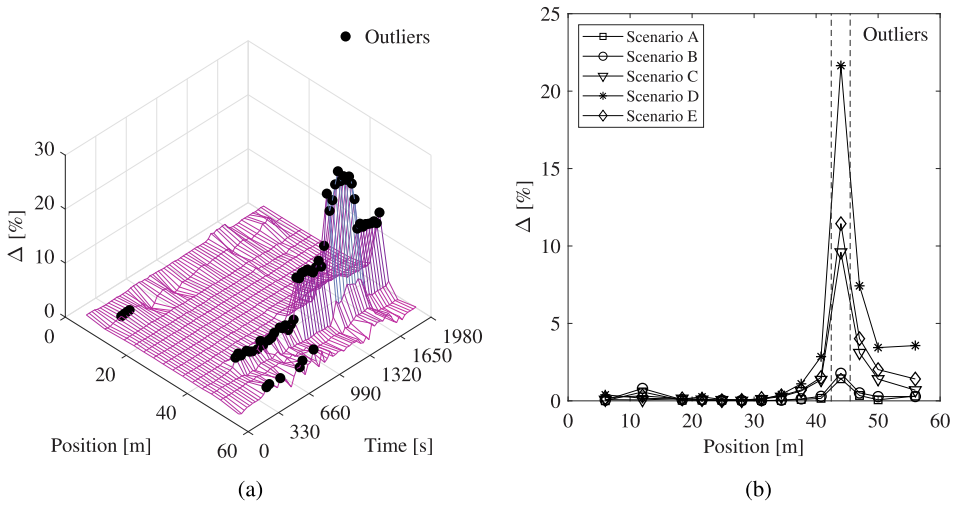

Figure 3.42: Instantaneous damage identification (a) and averaged results (b)

3.5 Seismic structural health monitoring

This section aims at applying the MAD to structures with nonlinear behavior. Also, a variant of the DAMA suitable for nonlinear systems and short recordings is presented.

A particular dynamic feature of nonlinear systems consists of the frequency-energy dependency of their oscillations that involves variations in the Frequency Response Function (FRF) depending on the level of excitation [54]. Thus, frequencies and amplitudes of NNM are typically time-varying and energy-dependent [62]. Considering a structure with nonlinear displacement-dependent stiffness, excited by a generic forcing function, assume the discrete-time acceleration response collected by an accelerometer deployed at the i-th material point as the combination of p dominant resonant components $\ddot{q}_j[t]$:

$$\ddot{x}_i[t] = \sum_{j=1}^{p} \phi_{i,j}[t]\ddot{q}_j[t] + v_i[t] \tag{3.36}$$

where $\phi_{i,j}[t]$ is the i-th element of a time-varying and energy-dependent j-th mode shape, $q_j[t]$ is a monocomponent function of time with a narrow frequency band (generally, depending on the

damping) centered around the time-varying and energy-dependent damped frequency $\omega_{d,j}[t]$, $\ddot{q}_j[t]$ is its double time derivative, and $v_i[t]$ is the recording noise, modeled here as a Gaussian white noise component. In general, p can be considered as the number of dominant resonant components in the structural response that exceed the noise threshold given by the $v_i[t]$ term. Each term of the summation in Equation (3.36) is called here Nonlinear Modal Response (NMR) and represents the time-domain description of a single NNM during the application of a given excitation.

In general, assuming $\phi_{i,j}[t]$ as a non-zero-mean function, its Fourier transform $\Phi_{i,j}[\omega]$ evaluated in $\omega = 0$ is $\Phi_{i,j}[0] \neq 0$. Moreover, other peaks in the spectrum of $\Phi_{i,j}[\omega]$ appear centered at frequencies $\omega_{\bar{k}}$ which depend on the nature of non-linearity and on the instantaneous frequencies of the system (which, in turn, depend on the energy of excitation). Also, assume that $\Phi_{i,j}[0] \gg \Phi_{i,j}[\omega_{\bar{k}}]$, *i.e.*, the fluctuations in time of the elements of instantaneous mode shapes around their mean values have modest amplitude compared to their mean values. This assumption should be verified by observing the final results of the identification procedure. However, in general, the nonlinear excursion slightly affects the mode shapes. Moreover, the frequency spectrum of the noise component $V_i[\omega]$ is constant and can be considered negligible compared to the amplitude of the NMR s if high-performance accelerometers are employed (*i.e.*, having high resolution and sensitivity, and low noise floor, such as the specific instrumentation typically used for SHM applications [58]).

For a given mode $\hat{\jmath}$, according to the convolution theorem, the product between $\phi_{i,\hat{\jmath}}$ and $\ddot{q}_{\hat{\jmath}}$ in time domain is equivalent to a convolution between their Fourier spectra in the frequency domain (indicated as $\Phi_{i,\hat{\jmath}}[\omega]$ and $Q_{\hat{\jmath}}[\omega]$, respectively). Through the assumptions made above, considering a time-windowed slice of the structural response such that the frequency spectrum has clear peaks at the instantaneous natural frequency values, the following relation is admissible if modes are well-distanced:

$$\left(\Phi_{i,\hat{\jmath}} * Q_{\hat{\jmath}}\right)\left[\omega_{\hat{\jmath}}\right] \approx \sum_{j=1}^{p}\left(\Phi_{i,j} * Q_j\right)\left[\omega_{\hat{\jmath}}\right] \tag{3.37}$$

with $*$ denoting the convolution operator and $\omega_{\hat{\jmath}}$ the frequency value where $\Phi_{i,\hat{\jmath}} * Q_{\hat{\jmath}})[\omega_{\hat{\jmath}}]$ is maximum. Thus, considering a narrow bandpass filter centered in $\omega_{\hat{\jmath}}$ with impulse response described by $b_{\hat{\jmath}}[t]$,

$$\frac{\left(b_{\hat{\jmath}} * \ddot{x}_i\right)[t]}{\left(b_{\hat{\jmath}} * \ddot{x}_r\right)[t]} \approx \frac{\phi_{i,\hat{\jmath}}[t]}{\phi_{r,\hat{\jmath}}[t]} \tag{3.38}$$

where r indicates a reference location. Assuming the Rosenberg definition of NNM [62], the ratio on the right-hand side of Equation (3.38) represents a point in the two-dimensional projection of the configuration space onto the directions of i and r. Indeed, different points in the configuration space can be evaluated considering specific time instants of the narrow frequency subband of the multi-component signal that instantaneously isolates a single NMR .

Considering a generic frequency value ω_k, Equation (3.37) is no more valid for frequencies far from $\omega_{\hat{\jmath}}$. Moreover, $V_i[\omega_k]$ may be non-negligible compared to $\sum_{j=1}^{p}\left(\Phi_{i,j} * Q_j\right)[\omega_k]$. In particular, considering a narrow bandpass filter with central frequency $\omega_k \neq \omega_{\hat{\jmath}}$, the noise component is likely to prevail, leading to $(b_k * \ddot{x}_i)[t] \approx (b_k * v_i)[t]$. On the other hand, in $\omega_k = \omega_{\hat{\jmath}}$, the frequency component generated by the variability of $\phi_{i,j}[t]$ may lead to spurious peaks in the frequency spectrum of $\ddot{x}_i[t]$. However, considering the assumptions made, such peaks have modest amplitudes, proportional to the fluctuations of the elements of mode shapes.

In general, the i-th element of the ODS associated with the k-th subband can be computed as:

$$\varphi_{i,k}[t] = \gamma_k^{(t)} \frac{(b_k * \ddot{x}_i)[t]}{(b_k * \ddot{x}_r)[t]} \tag{3.39}$$

However, calculating $\varphi_{i,k}[t]$ for different values of $k = 1, \ldots, 2^n$ for the evaluation of the MAD, the following three different situations can occur:

1. Using b_k with central frequency $\omega_k = \omega_j$ (*i.e.*, coinciding with an instantaneous natural frequency of the system), $\varphi_{i,k}[t]$ represents an element of the j-th instantaneous mode shape and Equation (3.39) becomes equivalent to Equation (3.38);

2. Using b_k with central frequency $\omega_k = \omega_{\hat{k}}$ (*i.e.*, coinciding with a signal component generated by the fluctuations of mode shapes), $\varphi_{i,k}[t]$ depends on the nature of nonlinearity;
3. Using b_k with central frequency ω_k different from the previous conditions, $\varphi_{i,k}[t]$ varies over time without reflecting the structural behavior (*i.e.*, is the ratio between filtered noise components).

The MAD can thus be computed even in the case of nonlinear structural responses using the ODS obtained as shown in Equation (3.39). In this case, however, the spurious similarity of neighboring ODSs generated by time-varying modal amplitudes must be taken into account. In particular, if the inequality $\Phi_{i,j}[0] \gg \Phi_{i,j}[\omega_{\bar{k}}]$ is not verified, the readability of the MAD may be affected, making the identification of NNMs challenging.

Different from other TFRs that represent the energy of the signal in a time-scale or time-frequency plane, the MAD only relies on the "similarity" between ODSs. In other words, the magnitude of the wavelet components and, therefore, the level of excitation in a given frequency range, has not a fundamental role in MAD formation, which only depends on the ratios between wavelet components generated at different locations. Thus, the only requirement for the application of the proposed method is that the level of excitation in the entire frequency range of acquisition generates a structural response which exceeds the noise floor of the instrumentation. This requirement is generally satisfied in all SHM applications and is much less demanding than the typical assumption involving white noise excitation.

Similar to the theoretical part of Section 3.4, in this section, a filter bank formed of the bandpass filters $b_k = d_k * r_k$ is considered, with d_k and r_k denoting the k-th equivalent decomposition and reconstruction filters associated with an n-th level SWPT.

Based on the idea that signal subbands forming similar instantaneous ODSs are likely to belong to the same modal component, a new algorithm for the decomposition of nonlinear structural response into decoupled NMR s is proposed in this section. In this context, the MAD is used as the starting point of the algorithm, necessary to select the wavelet components corresponding to physical modes

over those describing noise. The use of a forgetting factor is not indicated to improve the readability of the MAD when dealing with short and strongly non-stationary recordings. Although the noise-assisted approach can still be pursued, the final distribution may be noisy and not suitable for the application of image processing techniques, such as the watershed transform for the extraction of decoupled NMR s (see Section 3.2). Moreover, due to the strong non-stationarity of seismic events, clear ridges in the MAD may not be visible and disconnected areas may belong to the same NMR . For these reasons, a clustering procedure is applied to partition the instantaneous ODSs into sets referring to separate modes. Upon reconstructing the signal of each identified cluster, the instantaneous parameters of decoupled structural responses can be exploited for damage identification. The procedure proposed in this work for the extraction of decoupled modal responses is illustrated in Figure 3.43 and explained in detail below.

First, the instantaneous ODSs obtained in Equation (3.39) from the filtered components of the multivariate signal are used to evaluate a MAD, as shown in Equation (3.11). A decomposition matrix $\mathbf{M}$, having the same size as the MAD is then generated using the following rule:

$$\mu_k[t] = \begin{cases} 1 & \text{if } m_k[t] \geq \eta \\ 0 & \text{if } m_k[t] < \eta \end{cases} \tag{3.40}$$

where $\mu_k[t]$ is a generic element of $\mathbf{M}$ (k denotes the row index and t is the column index) and η is a user-defined threshold. The optimal value of η can be determined by analyzing the residuals

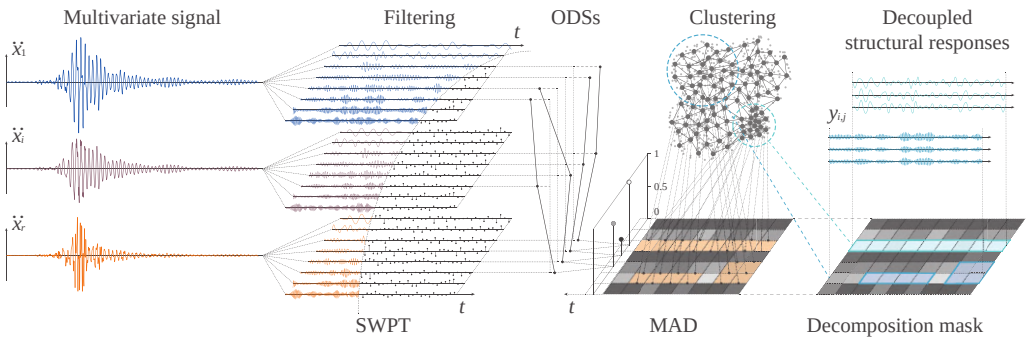

Figure 3.43: Workflow of the variant proposed for the identification of nonlinear system

of the decomposition algorithm. However, $\eta = 0.5$ can be generally adopted and a lower value may be considered depending on the number of instrumented locations if the noise-assisted procedure is carried out, as shown in Section 3.2.

The **M** matrix represents a "mask" of 1 and 0 values that selects high-valued areas in the MAD. Morphological operations, such as erosion, can be applied to **M** if a high transformation level is selected for signal decomposition since filter overlaps may origin spurious ODS similarities. In a morphological operation, each element $\mu_k[t]$ is interpreted as a pixel in the time-frequency distribution and is adjusted based on the value of neighboring pixels [246]. Erosion, in particular, replaces each value with the local minimum of its neighborhood and can be used to remove spurious elements. Considering the matrix $\widetilde{\mathbf{M}}$, obtained using morphological operations on **M**, the set S of ODSs representing physical modes is generated by selecting, among the elements $\varphi_{i,k}[t]$ identified using Equation (3.39), only the ODSs which are similar to each other in the neighboring subbands, *i.e.*, generating high MAD values and, hence, 1 values in the $\widetilde{\mathbf{M}}$. This selection procedure can therefore be written as:

$$\boldsymbol{\varphi}_k[t], \boldsymbol{\varphi}_{k+1}[t] \in S \Leftrightarrow \tilde{\mu}_k[t] = 1 \tag{3.41}$$

where $\varphi_k[t] = [\varphi_{1,k}[t], \ldots, \varphi_{r,k}[t]]^T$ and $\tilde{\mu}_k[t]$ is a generic element of $\widetilde{\mathbf{M}}$.

The k-means algorithm [247] is thus applied to partition the set of selected instantaneous ODSs into different clusters referring to separate modes. However, the number of clusters is a parameter required to initialize the k-means algorithm and, especially when dealing with high-dimensional data, its determination is not straightforward. For this reason, in this study, a self-organizing map (SOM) [248] is employed to help the user in the selection of the optimal number of clusters.

The SOM is a type of unsupervised neural network that generates a low-dimensional (generally two-dimensional) representation of the input space (the dimension of which is equal to the number r of channels that form the multivariate signal) approximating the data distribution through a user-defined number of neurons [248]. These

neurons, upon training the neural network, can be represented on a regular grid with hexagonal or rectangular mesh to visualize the obtained low-dimensional approximation of the input data. This process is possible since the trained map preserves the topological properties of the input space. Thus, the visualization of the U-matrix, *i.e.*, the map of Euclidean distances between the weight vectors of a SOM (that are the coordinates of each neuron in the input space) may be useful for the selection of the number of clusters. Upon training the SOM, the input data (that in this application consist of the r-dimensional ODSs), can indeed be represented on a plane, where the number of clusters can be visually (or automatically, using suitable algorithms) inferred.

It is worthy to note that the step involving SOMs is not strictly necessary for the aim of this procedure, however, it may facilitate the selection of the number of clusters. Moreover, due to the variability over time of ODSs during the nonlinear excursion, non-convex clusters may be generated in the original ODS space. However, the approximation generated by the SOM generally mitigates this phenomenon. Therefore, applying the k-means algorithm to the weights of the neurons of the trained SOM may improve the performance of the decomposition technique. In this case, however, a further step is required to generate the final sets of ODSs associated with different modes. The clusters of weight vectors should indeed be converted into sets of original ODSs by selecting the elements of the original space classified by each neuron in the obtained clusters.

In this work, the k-means algorithm is applied to the weight vectors obtained upon training the SOM using the input ODSs. After using the k-means method, in order to retrieve the clusters in the input space, the ODSs are associated with the cluster C_j of the neuron which classifies them. Once the clustering process is completed, a reconstruction mask $\mathbf{R}_j$ is built for each cluster C_j, selecting the elements of the filtered signals previously used to generate the clustered ODSs. The elements $\rho_{j,k}[t]$ of $\mathbf{R}_j$ can thus be defined as:

$$\rho_{j,k}[t] = \begin{cases} 1 & \text{if } \boldsymbol{\varphi}_k[t] \in C_j \\ 0 & \text{otherwise} \end{cases} \tag{3.42}$$

Due to the perfect reconstruction property of the selected filter bank, the decoupled j-th NMR $y_{i,j}[t]$ associated with the location i can be directly retrieved by summing the filtered components associated with the same cluster for each time sample:

$$y_{i,j}[t] = \sum_{k=1}^{2^n} \rho_{j,k}[t] \left(b_k * \ddot{x}_i\right)[t] \tag{3.43}$$

As already mentioned in the previous sections, it is worthy to note that the process described above can be seen as the construction of a signal-adaptive filter bank with band-variable filters capable of extracting decoupled modal responses through cutoff frequencies selected based on the clustering process. This process can be therefore intended as an adaptive generalization of the CFB -based identification algorithm.

Upon reconstruction, each monocomponent NMR can be processed through the HT to evaluate its instantaneous frequency, which is interpreted here as one of the time-varying natural frequencies of the nonlinear structure. Moreover, the j-th time-varying mode shape $\phi_j[t]$ can be evaluated considering the vector $y_j[t]$ of NMR s normalized over a reference value $y_{r,j}[t]$:

$$\boldsymbol{\phi}_j[t] = \frac{\mathbf{y}_j[t]}{y_{r,j}[t]} \tag{3.44}$$

Damage identification of a nonlinear system

In this section, the MAD is evaluated for two nonlinear case studies. The NMR s are extracted through the presented procedure and instantaneous modal parameters are identified, enabling the application of a flexibility-based method for damage identification. It is shown that the dynamic behavior of the structure during the maximum excursion in the nonlinear field can be related to the structural damage, revealing effects that cannot be identified using low-amplitude ambient vibration. In particular, the localized increase in curvature in flexural-type structures or anomalous interstory displacements in shear-type frames can be detected using the instantaneous flexibility matrix built from the modal parameters

identified during the seismic event. If these effects vanish or are attenuated in the short term, they may indicate the presence of breathing cracks.

The first case study considered in this section is a two-dimensional, 4-DOF , shear-type frame with masses equal to m=8 × 10^4 kg, damping coefficients equal to c=5 × 10^5 Ns/m, and stiffness consisting of a linear part equal to k_l=2 × 10^8 N/m plus a nonlinear part which is a function of the displacement, modeled to simulate a softening behavior, typical of RC frame structures. In particular, the equation of motion of the i-th level of the system can be written as:

$$m\ddot{x}_i + c\sum_{j=1}^{r} p_{i,j}\dot{x}_j + \sum_{j=1}^{r} p_{i,j}\left(k_l x_j + k_3 x_j^3 + k_5 x_j^5\right) = -m\ddot{s} \quad (3.45)$$

where x_j is the relative displacement of the j-th DOF with respect to the ground, the nonlinear stiffness coefficients are assumed as k_3=−3 × 10^{11} N/m^3 and k_5=1.8 × 10^{14} N/m^5, $\ddot{s}$ is the acceleration of the seismic motion applied at the base of the structure, and $p_{i,j}$ are the elements of a tridiagonal matrix with $p_{i,i} = 2$ on the main diagonal, except for $p_{r,r} = 1$ (*i.e.*, at the top level of the frame), and $p_{i,j} = -1$ in the other non-zero elements. The nonlinear stiffness coefficients were selected to simulate strong softening nonlinear effects in the displacement range of the structural response, keeping the overall instantaneous stiffness always positive. In linear conditions, *i.e.*, only considering the linear stiffness k_l, the natural frequencies of the numerical benchmark are 2.76 Hz, 7.96 Hz, 12.19 Hz, and 14.96 Hz.

At each level, a simulated uniaxial sensing device was considered, recording the absolute acceleration of the system in the direction of the seismic motion. A scheme of the case study with the deployment of simulated sensors (indicated as S#) is reported in Figure 3.44. In this test, the seismic motion recorded by the station located in Mirandola (Italy) during the Emilia earthquake of May 20th, 2012 was used. The acceleration time histories collected by each simulated sensor with a sampling frequency of 50 Hz, together with the input excitation, are reported in Figure 3.45a. Here, PGA indicates the peak ground acceleration, while PRA indicates the peak response acceleration at the top level. The total duration of the recording

is 40.96 s. In order to simulate the instrumentation noise, a white Gaussian noise component with a standard deviation of 0.02 m/s^2 (*i.e.*, the 1.11% of the standard deviation of the response collected at the top of the building, or the 0.13% of the peak response collected at the same point) was included in the analyzed response. The Fourier spectrum of the input excitation is reported in Figure 3.45b, where the natural frequencies f_j of the benchmark are also indicated. In this figure, it is possible to notice that the first mode is the most stimulated by the Emilia earthquake, while the others are less excited.

Between time instants 10.70 s and 11.60 s, a uniform decrease (following a linear function) of k_l in time was induced at the base level to

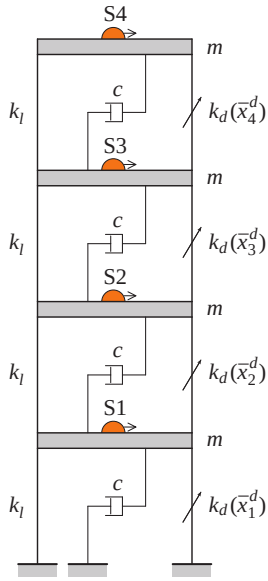

Figure 3.44: Scheme of the nonlinear numerical model

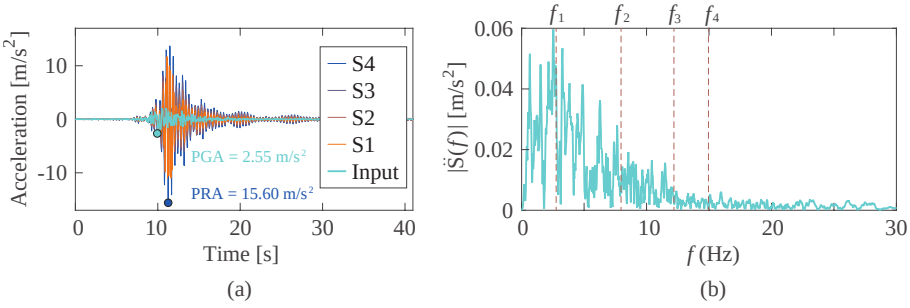

Figure 3.45: Structural responses of the numerical model (a) and frequency spectrum of the seismic ground acceleration (b)

simulate progressive damage, passing from the "undamaged" State 1 to a "damaged" State 2 with a final linear stiffness of 1.8×10^8 N/m. A representation of the force-displacement and stiffness-displacement diagrams obtained during the dynamic tests are reported in Figure 3.46 for each level. Moreover, the instantaneous stiffness of each level in time is represented in Figure 3.47. From this last graph, it is possible to notice that the excursion in the non-linear field leads to much lower instantaneous stiffness values than the residual stiffness of the damaged condition, for all the levels.

Using the multivariate signal consisting of the four acceleration channels collected by sensors S1, S2, S3, and S4, a MAD was computed following the noise-assisted approach. In particular, an ensemble of 100 different white Gaussian noise sets with a standard deviation of 0.05 m/s^2 were added to the collected structural responses to obtain the average distribution reported in Figure 3.48.

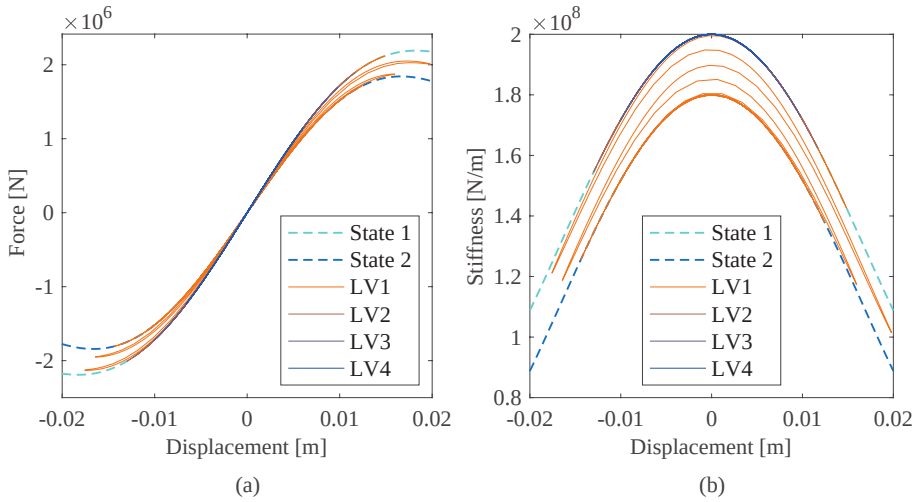

Figure 3.46: Force-displacement (a) and stiffness-displacement (b) diagrams of each level (LV)

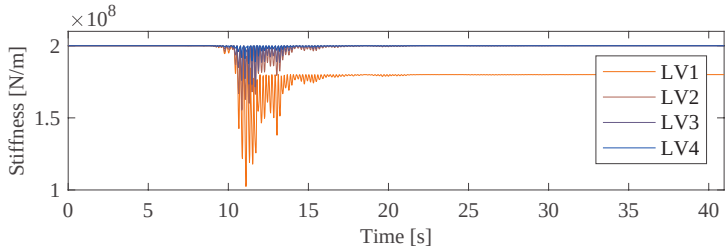

Figure 3.47: Instantaneous stiffness of each level

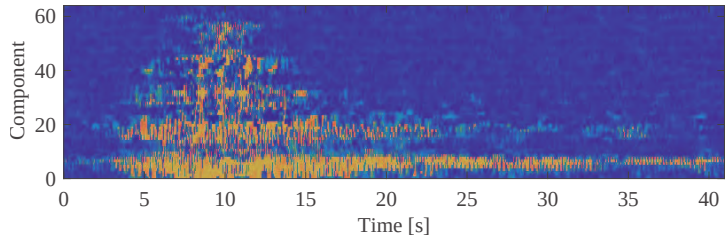

Figure 3.48: Modal assurance distribution of the numerical nonlinear model

Here, MAD values are represented in a time-component plane where the component axis represents the k index used in Equation (3.39) indicating the frequency bands. In this figure, orange areas indicate $m_k[t]$ values close to 1, while blue areas indicate values close to 0. A mask matrix was then built, as described in Equation (3.40), to select the ODSs that generated MAD values over a threshold $\eta = 0.5$.

In order to apply the k-means algorithm, the number of clusters was determined by analyzing the U-matrix of a SOM trained with the selected set of ODSs that generated MAD values over the selected threshold. The map is sized considering that the SOM is a quantizing method and, to have a satisfactory resolution to visualize the data distribution, at least 50 items (on average) should be classified by each node, otherwise the resolution of the outcome will be limited by the sparsity of data. Moreover, the array of neurons should have horizontal and vertical dimensions complying with the largest principal components of the input data [248]. Therefore, in this study, the number of neurons is selected as a number close to $N/100$, with N denoting the number of observations (*i.e.*, the 26091 selected ODSs), forming a square array. Indeed, since the input vectors are normalized ODSs, *i.e.*, vectors lying on the surface of an r-dimensional hypersphere, the variance explained by their first two principal components is likely to be the same. In particular, a 15×15 map with a hexagonal grid consisting of 225 neurons was employed.

The training process was performed over 200 epochs, in which all the selected ODSs are used to update the weights of neurons in batch mode (*i.e.*, at the end of each epoch). In Figure 3.49, two representations of the trained SOM are reported. Figure 3.49a shows a two-dimensional projection of the neurons (orange dots) and the connections of the SOM (blue lines) onto the first two weights,

i.e., the DOF s of the structure corresponding to levels 1 and 2. Here, the light blue points are the vectors of the input space. On the other hand, Figure 3.49b shows the U-matrix of the SOM, *i.e.*, a low-dimensional representation of the selected ODSs. In this figure, the neurons are depicted as orange hexagons, while the color of their connections depends on their Euclidean distance. In particular, light blue connections denote close neurons, while dark blue connections denote larger distances. Moreover, the size of the hexagons of Figure 3.49b is proportional to the number of ODSs classified by each cluster. From a visual analysis of the U-matrix, it is easier to identify a reasonable number of clusters, *i.e.*, dense areas in the low-dimensional distribution. These areas are light blue regions populated by large orange hexagons, delimited by dark blue boundaries. In this study, 4 clusters can be clearly identified, the first in the left-lower region, the second from the central part to the right-lower corner, the third in the right-upper region, and the fourth in the left-upper part. Although in this work a manual selection of the number of clusters is performed, image processing techniques can be applied to the U-matrix to automatically identify the most likely number of clusters [249].

The k-means algorithm was then applied to the weight vectors of the neurons, partitioning the set of selected ODSs into 4 clusters. An illustration of the clustered ODSs is reported in Figure 3.50a, where the instantaneous wavelet components associated with the selected

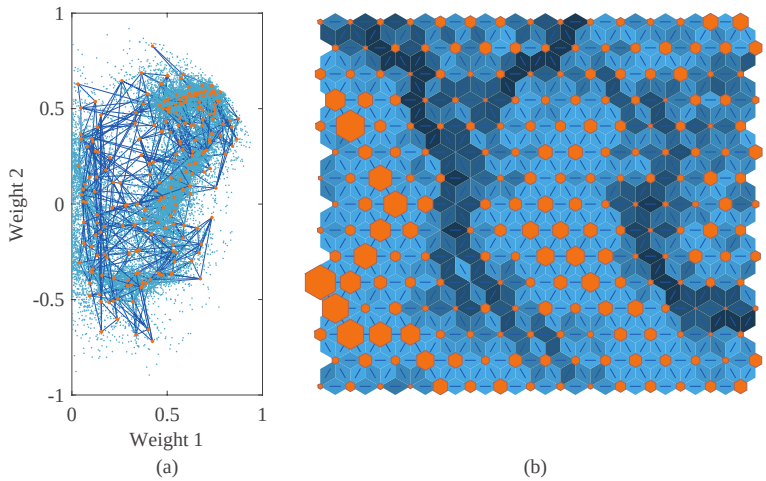

Figure 3.49: Self-organizing map (a) and corresponding U-matrix (b)

ODSs are represented as points in the time-component plane, with a color depending on the belonging cluster. In Figure 3.50b, the ODSs associated with each point of Figure 3.50a are illustrated in the space domain, along with the height of the structure. Moreover, the average trend of each cluster is indicated as an orange dashed line. It is possible to observe how the shapes belonging to the same cluster are similar between each other and the average curves may be interpreted as an estimate of the mode shapes of the structure. However, in this phase, it is not possible to distinguish between ODSs before and after the seismic event, *i.e.*, possibly referring to an "undamaged" and a "damaged" condition since, in this case, the differences are minimal compared to the variability of the ODSs in a given cluster. More sophisticated clustering methods not requiring the knowledge of the number of clusters may also be applied, such as the DBSCAN [222] (as in Section 3.3), which is however very sensitive to the distance thresholds, that is another parameter required in the mentioned procedure. On the other hand, the SOM-based criterion is not very sensitive to the number of neurons forming the map, which is the only parameter needed for the realization of the U-matrix.

The NMR of each identified node was then reconstructed by summing the wavelet components used to obtain the ODSs referring to a given cluster (*i.e.*, to a single modal component). The instanta-

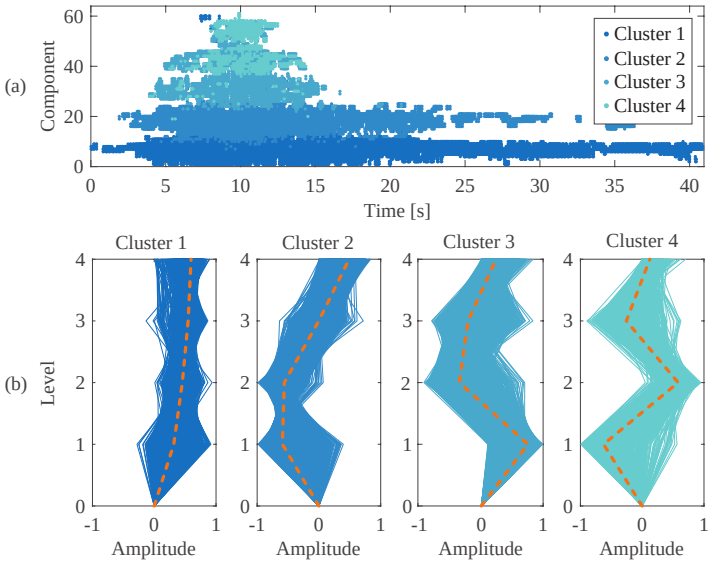

Figure 3.50: Results of the clustering process

neous resonant frequencies were thus identified using the HT. In this study, the HHT is also considered to have a comparison with one of the most used techniques for the instantaneous identification of nonlinear systems in the time domain [71]. In particular, the fast and adaptive variant presented by Thirumalaisamy and Ansell [37] of the MEMD algorithm proposed by Rehman and Mandic [35] was employed to extract the IMFs from the input multivariate dataset, and the HT was used to obtain the reference parameters for comparison, *i.e.*, instantaneous frequencies and amplitudes. The MEMD was applied to the set of 4 structural responses collected during the seismic excitation at the different levels of the numerical benchmark, aiming to identify a maximum of 10 IMFs. The IMFs were extracted considering a sifting tolerance of 0.01 (*i.e.*, the sifting procedure is stopped when the mean-squared error between the IMFs obtained in current and in the previous iteration is lower than 0.01). It was also noted that by further decreasing the tolerance, the results did not vary and thus the outcomes of this application do not depend on the selected parameters. In the algorithm by Thirumalaisamy and Ansell [37], two order-statistic filters are applied to calculate the envelopes for sifting, avoiding spline interpolation, which may become burdensome in multivariate applications. Another parameter of the algorithm is thus the window size for order-statistic filters, which is determined, for each iteration, as the median of distances between consecutive local extrema of the signal (minima or maxima) in this application.

In Figure 3.51, both the instantaneous frequencies obtained through the procedure presented in this application and those obtained using the HHT are reported, superimposed on the theoretical values of the instantaneous frequencies obtained using the numerical model shown above. In particular, the instantaneous frequencies of the numerical benchmark during the seismic event are reported in blue (from light to dark blue referring to modes from 1 to 4, respectively) over time. Solid lines indicate the theoretical values, calculated by resolving the eigenproblem of the system at each time instant, considering varying stiffness. On the other hand, dashed lines with the same color of theoretical curves represent the instantaneous identified values. Due to the application of a noise-assisted procedure which involves the introduction of stationary noise com-

ponents, the NMR s extracted through clustering, and thus the dashed lines illustrated in Figure 3.51, have a length limited to the regions where the signal has high amplitudes. However, these results are enough for S^{2}HM if the DSF is evaluated in the instant of the maximum nonlinear excursion. Orange lines in Figure 3.51, indicate the instantaneous frequencies of the IMFs identified by applying the MEMD to the multivariate structural response. To improve the readability of the diagrams, a median filter over 101 samples was used on all the identified parameters, *i.e.*, at each time instant, the instantaneous frequency estimate is assumed as the median value computed on a window of 101 samples centered in the considered instant. In the figure, a good agreement of the parameters identified through the proposed procedure with the theoretical curves is observable (blue lines) for the first three modes. In particular, in the instant of maximum excursion in the nonlinear field, indicated as condition B using a vertical dashed line, an accurate estimate of natural frequency is achieved for all modes. On the other hand, the instantaneous frequencies obtained through the HHT (orange lines) follow the theoretical curves only for the first two modes, showing to have no physical meaning at lower frequencies.

Figure Figure 3.52a shows the instantaneous amplitude of the first two modes, computed through the HT of the reconstructed NMR s. The shapes formed of these amplitudes are referred to as "mode shapes" since they are ODSs evaluated at the resonant frequencies and are, therefore, an estimate of the instantaneous mode shapes of the structure. Moreover, in Figure 3.52b three instantaneous conditions, namely A, B, and C, corresponding to the instants prior, during (*i.e.*, at the instant of peak response acceleration) and after the

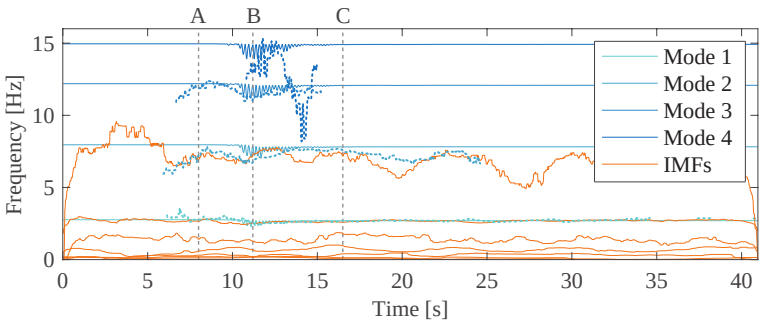

Figure 3.51: Instantaneous natural frequencies (theoretical in solid lines and identified in dashed lines) and results of the Hilbert-Huang transform

seismic strong motion, are analyzed in detail. It should be noted that, as supposed in the theoretical description of the presented approach, in this case, the fluctuations of mode shapes due to nonlinearities are generally modest compared to their mean values. Therefore, the spurious components due to nonlinearities do not affect the accuracy of the method. Indeed, the identified instantaneous mode shapes well approximate the theoretical values, especially in condition B.

The instantaneous estimates of natural frequencies and mode shapes identified in conditions A, B, and C were used to generate the ULL corresponding to each condition (see Equation (3.22)). In Figure 3.53, the ULL and the Inter-Story Drift (ISD) estimates obtained from this analysis are reported. As expected, the ISD in condition B is generally higher, especially for the base level. On the other hand, keeping in mind the curves of Figure 6, conditions A and C should have similar ISD s for all the levels except for the first, where a residual stiffness loss of 10% was simulated.

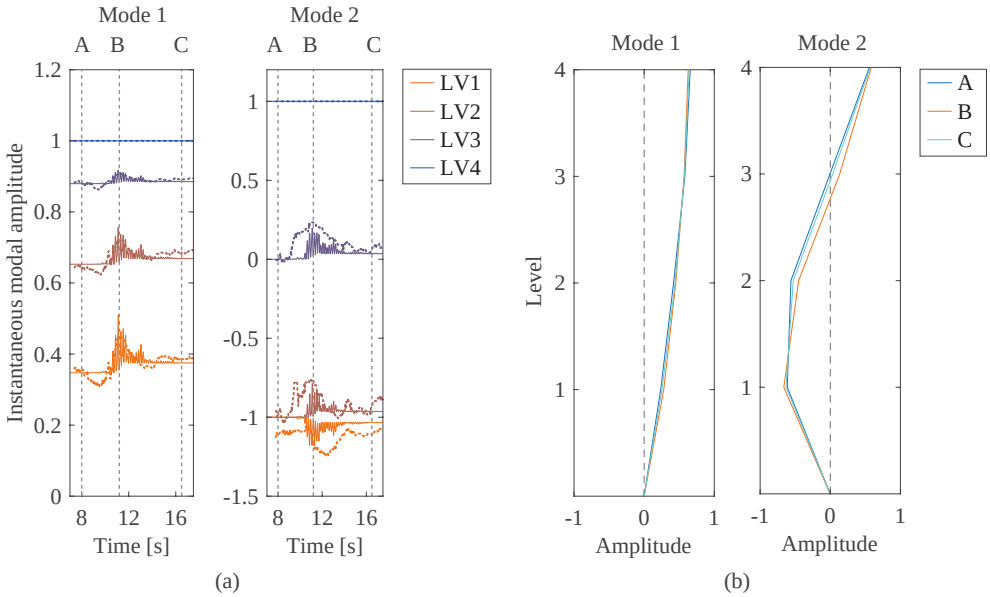

Figure 3.52: Instantaneous amplitudes of the first two modes (a) and instantaneous mode shapes at the inspection samples (b)

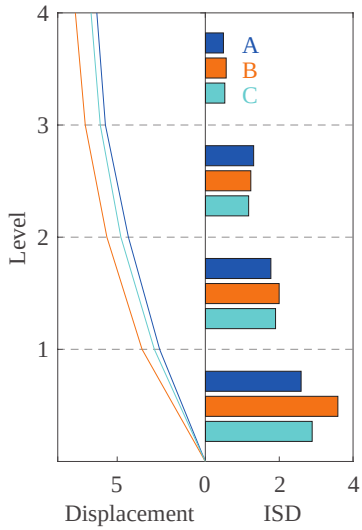

Figure 3.53: Uniform load lines and inter-story drifts at the inspection samples

Damage identification of an RC building

The second case study considered in this section is a five-story RC building tested on a shaking table at the University of California, San Diego, through the George E. Brown Jr. Network for Earthquake Engineering Simulation program (NEES-UCSD) between May 2011 and May 2012. The plan dimensions were 6.60 m×11.00 m and the total height was 21.34 m, with a floor-to-floor distance of 4.27 m. The shaking was impressed in the longitudinal (east-west) direction, in which the building had two RC frames as a lateral-load resisting system. The beams had a cross-section of 0.30 m×0.71 m, with varying connection details, and the floor system consisted of a 0.20 m thick concrete slab on all levels. More details about the specimen can be found in technical reports [250–253] and a schematic representation of the geometry is reported in Figure 3.54.

Dense sensor equipment was originally deployed on the structure. In this study, only five acceleration channels were considered (S1-S5), positioned in the northern-eastern quadrant of the plant, at the floor level, in the direction of the seismic motion, as illustrated in Figure 3.54. Moreover, displacement measurements collected through linear (N1-N3) and string (B1-B2) potentiometers are used as reference for damage identification in this study. Detailed information on the sensor setup can be found in technical reports [250–253]. In particular,

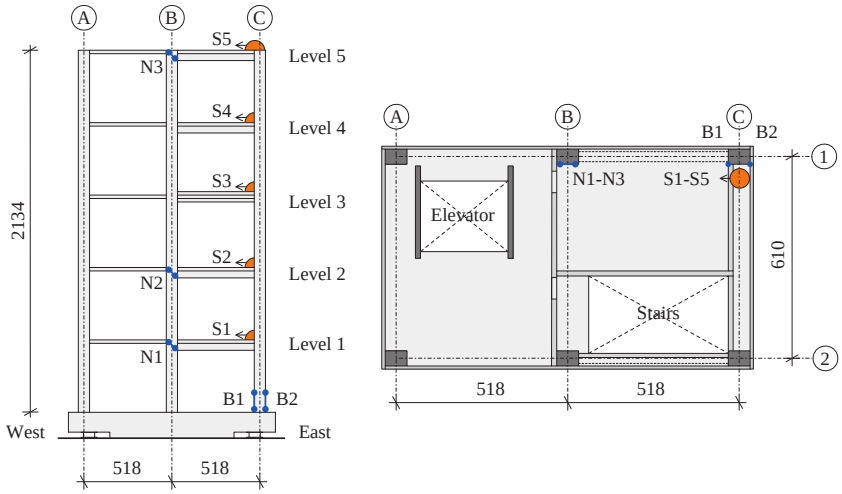

Figure 3.54: Lateral and plant scheme of the specimen, adapted from literature [250]; dimensions in centimeters

the linear potentiometers measure the diagonal elongation of three beam-column nodes, while the string devices are used to estimate of the rotation at the base of the eastern column, calculated as

$$\vartheta = \frac{\Delta_{B1} - \Delta_{B2}}{d} \tag{3.46}$$

where Δ_{B1} and Δ_{B2} are the displacements collected by the two sensors, while d is the distance between them.

In the original testing campaign, the structure was first subjected to seven seismic motions with functioning base isolator devices and then tested with six seismic motions with increasing intensity with the basement of the building fixed to the shaking table. The acceleration time histories used in this study (Figure 3.55) were collected during the fourth test performed using the 2007 Pisco earthquake (Ica station, Peru) as input excitation with fixed-base configuration. The original sampling frequency was of 200 Hz, downsampled at 50 Hz in this study. The total duration of the recording is 327.68 s.

As described in the reports of the experimental campaign [250], the building was designed to reach its performance targets during the fifth seismic motion with the fixed-base configuration. Indeed, minimal damage was observed following the first two motions, with the structure remaining serviceable. Limited structural cracking

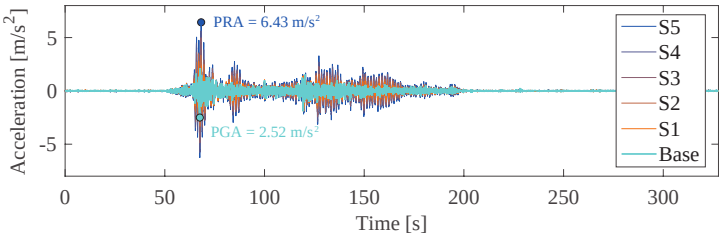

Figure 3.55: Structural responses of the RC case study

was also observed following the application of the fourth motion, especially at the bases of the first-floor columns and in the slab of the first level.

The multivariate signal collected from sensors S1-S5 was used to generate the MAD through a noise-assisted procedure similar to that applied in the first case study (Figure 3.56a), using a threshold value of $\eta = 0.5$. The MAD was thus employed to extract the ODSs which are then clustered through SOM and k-means. As in the previous analysis, four clusters were selected, obtaining the distribution illustrated in Figure 3.56b.

The instantaneous natural frequencies identified through the procedure proposed in this section and those obtained by means of the HHT are shown in Figure 3.57a, superimposed on the spectrogram evaluated through the STFT of the structural responses collected by sensor S5. The implementation features of the HHT and the approach for selecting the window size of order-statistic

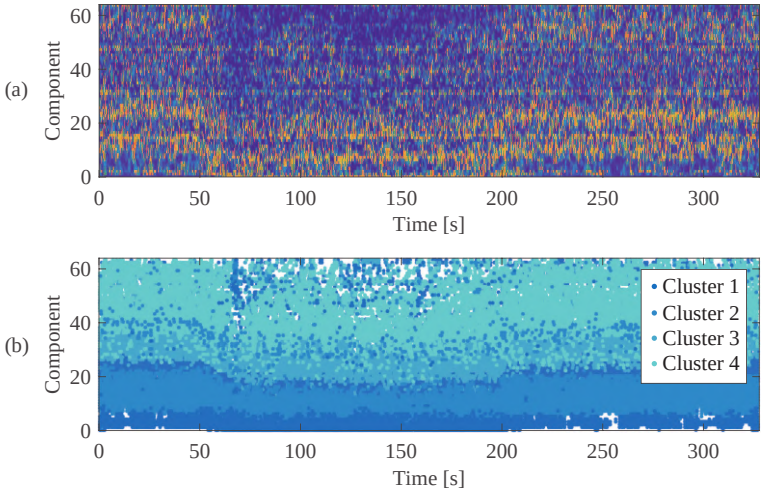

Figure 3.56: Modal assurance distribution (a) and extracted clusters (b) of the experimental case study

features are the same used for Case study 1. A median filter of 501 samples was used to improve the readability of the figure. It is possible to notice that the instantaneous frequencies obtained by the method proposed better approximate the ridges of the spectrogram, especially for the first three modes. Although the performances of HHT are higher than in the previous analysis, non-physical IMFs are extracted at low frequencies.

Observing the reference measurements obtained from potentiometers (Figure 3.56b), it is possible to notice that local minima in the identified frequencies are close to the point where maximum diagonal elongation is recorded at the nodes. In this instant, nonlinear effects can be observed since a residual displacement is present in sensor N1.

The inspection instants A, B, and C indicated in Figure 3.57 were considered to evaluate the first four mode shapes and the corresponding ULL s before, during, and after the seismic strong motion. In particular, condition B was selected at the instant of peak response acceleration, which is in the proximity of a local minimum of the instantaneous natural frequencies. Observing the

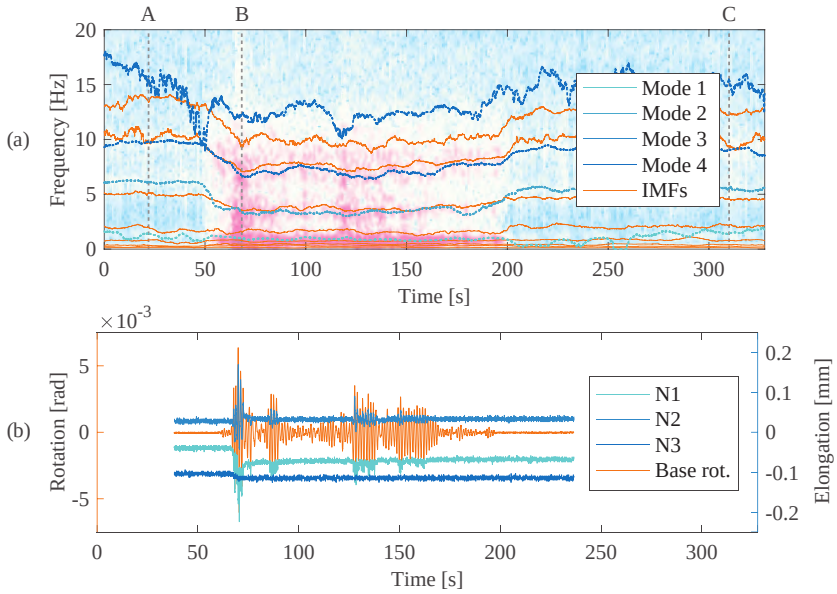

Figure 3.57: Instantaneous identified natural frequencies (a) and recordings of the potentiometers (b)

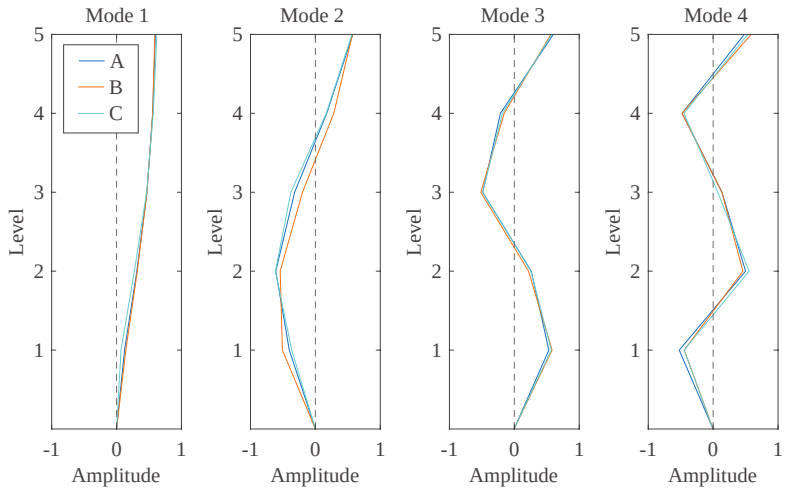

Figure 3.58: First four instantaneous mode shapes at the inspection samples

modal amplitudes of these three conditions in Figure 3.58 it is possible to notice a slight variation, which confirms the applicability of the method since the oscillation due to nonlinearities is generally modest compared to the average value. Nevertheless, the accurate estimation of such small variations enables the application of a flexibility-based method for damage detection and localization.

In Figure 3.59, the ULL s of the building corresponding to the inspection time instants A, B, and C are shown. Since information about the structural masses is missing, mode shapes were normalized to an identity matrix, assuming a uniform distribution along with the height of the building. Moreover, since the structural behavior may be far from the shear-type approximation, the curvature of ULL is used as a DSF in this case. A general increment in curvature is registered for each level in condition B, while after the seismic motion, only the first level has a residual difference in curvature, in agreement with the damage observed during the visual inspections [251]. Although the deformation of beam-column nodes is not the only effect that may affect the curvature of the ULL , this result is also confirmed by the recording of sensor N1 (Figure 3.57b), where clear residual elongation can be noticed.

Moreover, the rotation at the base of the structure in condition B is visibly higher than pre– and after–earthquake conditions, high-

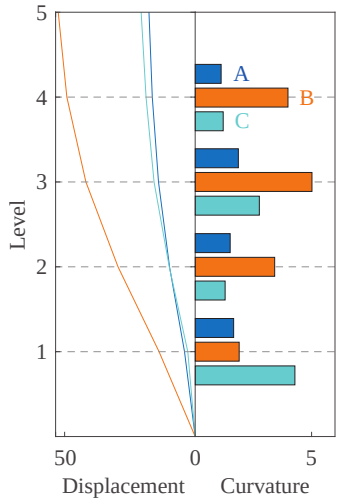

Figure 3.59: Uniform load lines and their curvature values at the inspection samples

lighting the presence of breathing cracks at the base of the first level columns, also confirmed by the visual inspections. Considerable rotation at the base of the building is also recorded by the reference potentiometers B1-B2, as shown in Figure 3.57b.

3.6 Data transmission in dense sensor networks

A large number of civil structures and infrastructures built in the last century are now close to, or even beyond, the end of their rated life cycle. Several types of SHM systems have been deployed to assess their integrity, initially consisting of wired solutions and more recently based on wireless sensing systems. For both these types of networks, dealing with large infrastructures is generally challenging since long cables should be deployed or high transmission ranges should be covered. In the case of WSN s, multihop transmissions have been largely employed to limit the coverage issue. Section 3.4 presented a decentralized algorithm for modal identification suitable for star or tree-topology sensor networks. Sometimes, especially for large bridges or viaducts, the star topology is unsuitable. On the other hand, due to the geometry of typical infrastructures or tall buildings, the line topology (*i.e.*, a chain of devices formed of

two-way links between one node and the next one) may be more appropriate. However, sensing nodes involved in transmitting their own collected data in addition to passing data acquired by other devices typically saturate the transmission band and rapidly drain batteries.

In this section, a decentralized procedure is proposed for line-topology networks which involve the updating of the truncated SVD of the collected signal (*i.e.*, the input matrix) onboard each node, before transmitting the data to the next one. Each updating involves low computational effort, being suitable for microcontrollers with a small computational footprint. Moreover, the weight of transmission packages is considerably reduced, and a user-selected upper limit can be fixed regardless of the network size. This allows the complete reconstruction of all the collected channels by a coordinator device at the end of the line-topology network without involving the transmission of all the collected samples. Besides, if the MAD is only required for visualization purposes, without the need of extracting the decoupled modal responses of the system, a more economic transmission is necessary.

The instantaneous ODSs vectors used in Equation (3.11) can be expressed as

$$\boldsymbol{\varphi}_k = \boldsymbol{\psi}_k^T \mathbf{X} \tag{3.47}$$

where $\boldsymbol{\psi}_k$ is the impulse response of the equivalent wavelet filter associated with the k-th frequency band and $\mathbf{X}$ is the input matrix, *i.e.*, a matrix formed of column vectors containing the structural responses collected by different acquisition channels. In this section, the time dependence of $\mathbf{X}$ and $\boldsymbol{\psi}_k$ will not be specified for simplicity. Moreover, in this algorithm the WPT is used as a filtering operator which decomposes each channel into different wavelet components, each associated with a different frequency band. In the classical WPT algorithm, the wavelet components are downsampled by a factor 2^n after being calculated using the equivalent wavelet filter bank. The output is indeed critically sampled. For simplicity of notations, in this section, the time instant at which the parameters of the algorithm are calculated (after downsampling) is indicated as ξ. Therefore, $\boldsymbol{\psi}_k$ is the ODS evaluated at the ξ-th time instant, using the input matrix $\mathbf{X} = [\mathbf{x}_1[t - \overline{N} + 1, t], \ldots, \mathbf{x}_r[t - \overline{N} + 1, t]]^T \in \mathbb{R}^{\overline{N} \times r}$,

where $\mathbf{x}_i[t_1, t_2]$ is a vector containing the samples of the collected sequence $\mathbf{x}_i[t]$ in the time interval between t_1 and t_2, r is the number of instrumented locations, $\overline{N} = \lambda(2^n - 1) - n + 1$ is the length of the equivalent wavelet filter at the transform level n, and λ is the length of the wavelet lowpass and highpass filters associated with the selected wavelet function [254]. Substituting Equation (3.47) into (3.11), the instantaneous MAD values can be expressed as

$$m_k = \frac{\left|\boldsymbol{\psi}_k^T \mathbf{X}\mathbf{X}^T \boldsymbol{\psi}_{k+1}\right|^2}{\boldsymbol{\psi}_k^T \mathbf{X}\mathbf{X}^T \boldsymbol{\psi}_k \boldsymbol{\psi}_{k+1}^T \mathbf{X}\mathbf{X}^T \boldsymbol{\psi}_{k+1}} \tag{3.48}$$

Moreover, considering the SVD of the input matrix $\mathbf{X} = \mathbf{U}\boldsymbol{\Sigma}\mathbf{V}^T$, an approximation of $\mathbf{X}$ can be expressed as a function of its most relevant singular vectors (and values) considering a truncated SVD

$$\mathbf{X} \approx \widehat{\mathbf{U}}\widehat{\boldsymbol{\Sigma}}\widehat{\mathbf{V}}^T \tag{3.49}$$

where the columns of matrices $\widehat{\mathbf{U}}$ and $\widehat{\mathbf{V}}$ contain the first s left and right singular vectors of $\mathbf{X}$, respectively, while $\widehat{\boldsymbol{\Sigma}}$ is a diagonal matrix containing the first s SV. In order to have a good approximation of $\mathbf{X}$ in Equation (3.49), the s parameter can be selected according to the criterion proposed by Gavish and Donoho [255], which allows determining the optimal rank of $\widehat{\mathbf{U}}$ and $\widehat{\mathbf{V}}$ to reconstruct signals containing either a known or unknown noise level. In the mentioned approach, the threshold to select the most relevant SVs is calculated as a function of the aspect ratio $r/\overline{N}$ of the input matrix and the median of its SVs.

In the numerator of Equation (3.48), the correlation matrix of the input can thus be expressed as $\mathbf{X}\mathbf{X}^T \approx \widehat{\mathbf{U}}\widehat{\boldsymbol{\Sigma}}\widehat{\mathbf{U}}^T$. Also, assuming $\boldsymbol{\gamma}_k^T = \boldsymbol{\psi}_k^T \widehat{\mathbf{U}}$, an estimate of the instantaneous MAD values is given by

$$m_k \approx \frac{\left|\boldsymbol{\gamma}_k^T \boldsymbol{\Sigma}^2 \boldsymbol{\gamma}_{k+1}\right|^2}{\boldsymbol{\gamma}_k^T \boldsymbol{\Sigma}^2 \boldsymbol{\gamma}_k \boldsymbol{\gamma}_{k+1}^T \boldsymbol{\Sigma}^2 \boldsymbol{\gamma}_{k+1}} \tag{3.50}$$

In some applications, it may be convenient to build the input matrix by progressively increasing the number of columns of $\mathbf{X}$, *i.e.*, appending single columns to the input matrix, leaving the remaining part unchanged. In this case, the SVD of $\mathbf{X}$ can be first

calculated using only a subset of its columns (*i.e.*, only a subset of recording channels) and then updated through rank-1 perturbations, as shown by Brand [256], to include the information contained in the remaining columns.

Let $\mathbf{U\Sigma V}^T$ be the SVD of $\mathbf{X}_c$, which is the matrix formed of the first c columns of $\mathbf{X}$. The decomposition of $\mathbf{X}_{c+1}$ can be written in the form $\mathbf{U\Sigma}\left[\mathbf{V}^T\mathbf{0}\right] + \mathbf{ab}^T$, where $\mathbf{a} \in \mathbb{R}^{\overline{N}}$ contains the elements of $x_{c+1}[t-\overline{N}+1, t]$, $\mathbf{b} = [0, 0, \ldots, 1]^T \in \mathbb{R}^{c+1}$, and $\mathbf{0}$ is a zero-valued column vector. The updated matrices of the decomposition $\widetilde{\mathbf{U}}\widetilde{\mathbf{\Sigma}}\widetilde{\mathbf{V}}^T = \mathbf{U\Sigma}\left[\mathbf{V}^T\mathbf{0}\right] + \mathbf{ab}^T$ can be calculated through the following steps [256]:

1. Calculate the vector

$$\boldsymbol{\alpha} = \mathbf{a} - \mathbf{U}\mathbf{U}^T\mathbf{a} \tag{3.51}$$

   and its norm $||\boldsymbol{\alpha}||$;
2. Compute the SVD of the matrix

$$\mathbf{K} = \begin{bmatrix} \mathbf{\Sigma} & \mathbf{U}^T\mathbf{a} \\ \mathbf{0} & \|\boldsymbol{\alpha}\| \end{bmatrix} \tag{3.52}$$

   obtaining $\mathbf{K} = \mathbf{YHZ}^T$;
3. Update the SVD matrices as

$$\widetilde{\mathbf{U}} \leftarrow \begin{bmatrix} \mathbf{U} & \overline{\boldsymbol{\alpha}} \end{bmatrix} \widehat{\mathbf{Y}} \tag{3.53}$$

$$\widetilde{\mathbf{V}} \leftarrow \begin{bmatrix} \mathbf{V}_e & \mathbf{b} \end{bmatrix} \widehat{\mathbf{Z}} \tag{3.54}$$

$$\widetilde{\mathbf{\Sigma}} \leftarrow \mathbf{H} \tag{3.55}$$

   where $\overline{\boldsymbol{\alpha}} = \boldsymbol{\alpha}/\|\boldsymbol{\alpha}\|$, $\mathbf{V}_e = [\mathbf{V}^T\mathbf{0}]^T$, and $\widehat{\mathbf{Y}}$, $\widehat{\mathbf{Z}}$ are the truncated versions of $\mathbf{Y}$, $\mathbf{Z}$, *i.e.*, containing their first c columns.

Steps 1-3 should be repeated to include all the columns of the input matrix.

A scheme of the data management approach proposed in this section is reported in Figure 3.60. All the nodes of the network,

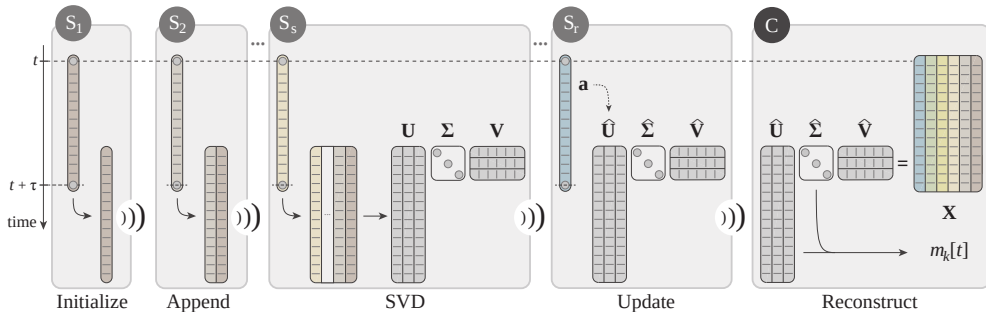

Figure 3.60: Outline of the proposed procedure for data acquisition using line-topoloty sensor networks

synchronized to the same time reference, form an array of the sampled signal, *e.g.*, the acceleration response of a physical point of the structure, of length $\overline{N}$. The first node of the network initializes the data management procedure by transmitting the collected array to the second node. Up to the s-th node, each device appends the collected array to the received matrix and proceed with the transmission. In this phase, the weight of transmitted packets grows linearly with the number of nodes. Onboard the s-th node, upon appending the collected array, an SVD of the matrix of collected signals $\mathbf{X}_s$ is performed to obtain the matrices $\mathbf{U}$, $\mathbf{V}$, and $\mathbf{\Sigma}$, such that $\mathbf{X}_s = \mathbf{U}\mathbf{\Sigma}\mathbf{V}^T$. This process is performed in the "economy" mode, which removes zero rows in the $\mathbf{\Sigma}$ matrix. The decomposition matrices are then transmitted to the next node. This step involves the transmission of $s(\overline{N} + s + 1)$ elements since $\mathbf{\Sigma}$ is a diagonal matrix.

From the s-th to the r-th node, which is the last sensing node of the network, the array of the collected signal is used as an updating a vector, as shown in Equations (3.51)–(3.55). In particular, $\widetilde{\mathbf{U}}$, $\widetilde{\mathbf{V}}$, and $\widetilde{\mathbf{\Sigma}}$ are obtained by updating the received decomposition matrices and truncated to a rank equal to s, generating matrices $\widehat{\mathbf{U}}$, $\widehat{\mathbf{V}}$, and $\widehat{\mathbf{\Sigma}}$, respectively. The obtained matrices are thus transmitted to the next node. In this phase, the number of elements transmitted from a node i to the next one is $s(\overline{N} + i + 1)$. It is worthy to note that, in the case of a traditional append-and-transmit procedure in a line-topology network, the weight of transmitted packets would be $\overline{N}i$, with $i = 1, \ldots, r$. For large networks, s is generally much lower than r and the convenience of using the procedure proposed is evident. Indeed, the power consumption of wireless sensing systems

typically entails the most demanding part of node operations, especially for long-distance transmission [257]. The maximum weight of transmitted packets can be fixed by selecting a suitable s parameter. This selection can be made by following the criterion proposed by Gavish and Donoho [255], applied to a complete input matrix collected before implementing the decentralized procedure. Moreover, the computational complexity to perform the update onboard each node is in the order of $O(\overline{N}s + s^3)$ [256].

At the end of the network, a coordinator device is generally installed to gather the transmitted datasets and make it available to the user. It usually has a microcontroller or microprocessor with a larger computational footprint with respect to the other sensing nodes since filtering or other signal processing operations may be performed at this point to reduce the data weight before cloud uploading or local storing. Here, an estimate of the complete set of collected signals can be reconstructed as shown in Equation (3.49). This set forms a multivariate signal which can be employed to obtain the decoupled modal responses through the method proposed in Section 3.3.

It should be noted that, according to Equation (3.50), if only the MAD should be calculated in the monitoring process, the $\mathbf{V}$ matrix is not necessary and can thus not be updated and transmitted, reducing both the computational effort and the packet weights; indeed, in this case, the transmitted element would be $s(\overline{N} + 1)$ for nodes $i > s$.

At the end of the data collection process, an approximation of the acquired signal in the interval $[t-\overline{N}+1, t]$ can be reconstructed using Equation (3.49). A set of instantaneous deflection shapes referred to the ξ-th instant can then be calculated through Equation (3.47) and the MAD at the same instant can be obtained using Equation (3.11) or (3.50). At this point, the proposed identification procedure involves the selection of ODSs that generate high MAD values using a threshold θ, as shown in Figure 3.61 (see also Section 3.2 for more details on the threshold). In order to identify the instantaneous mode shapes of the system, the set of selected ODSs are partitioned into p clusters using the k-means algorithm. The average curve obtained for each cluster is then assumed as an identified mode shape.

It is worthy to note that the traditional k-means algorithm is

unable to discard outliers from noisy distributions. The thresholding operation performed using the MAD is thus necessary to obtain robust identification outcomes. Moreover, the application of the k-means algorithm needs the number of clusters as a setup parameter. However, in modal identification problems, this parameter (here denoting the number of identified modes) is not known a priori. Several methods have been proposed in the literature to identify the optimal number of clusters. In this study, the silhouette-based approach is used [258], where silhouette values (*i.e.*, a measure of how similar an object is to its own cluster compared to other clusters, ranging from -1 to 1) are calculated for different setups, *i.e.*, different values of p. The setup where a maximum silhouette value is reached is selected as the optimal setup. This procedure requires to apply the k-means algorithm multiple times. However, upon the selection of the optimal p parameter, this value can be employed for the long-term identification procedure, as it will be shown in the application section.

In real-time applications, variants of the k-means algorithm or other clustering algorithms able to handle streaming data should be employed. In this work, an online variant of the k-means algorithm is used, consisting of the following steps:

1. Apply the traditional k-means algorithm to the set of $\boldsymbol{\varphi}_k[\xi]$ with $k = 1, \ldots, 2^n$ and evaluate the p centroids having coordi-

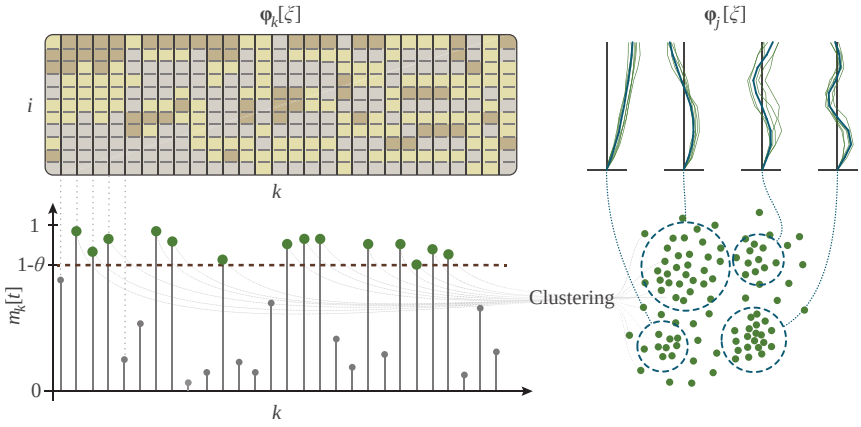

Figure 3.61: MAD-based procedure for modal identification

nates described by vectors $\boldsymbol{\mu}_j[\xi]$.

2. At time instant $\xi + 1$, calculate the distance between each vector $\boldsymbol{\varphi}_k[\xi + 1]$ and each centroid coordinate vector $\boldsymbol{\mu}_j[\xi]$, and assign each vector $\boldsymbol{\varphi}_k[\xi + 1]$ to the cluster with the closer centroid.
3. Update the centroid coordinates as

$$\boldsymbol{\mu}_j[\xi + 1] = \alpha\boldsymbol{\mu}_j[\xi] + (1 - \alpha)\overline{\boldsymbol{\varphi}}_j[\xi + 1] \tag{3.56}$$

where $\overline{\boldsymbol{\varphi}}_j[\xi+1] = \frac{1}{l}\sum_{k=1}^{n_j}\boldsymbol{\varphi}_k[\xi+1]$ is the mean of the $\boldsymbol{\varphi}_k[\xi+1]$ vectors assigned to the j-th cluster, while α is a user-defined "forgetting factor".

Following the application of the k-means algorithm, the wavelet components that generate the vectors $\boldsymbol{\varphi}_k$ associated with each cluster may be used to reconstruct decoupled modal responses through the IWPT. Since these responses are mono-component, *i.e.*, they have a single dominant frequency, the Hilbert transform can be employed to identify the instantaneous natural frequencies of the system.

Due to noise, which can generate random similarities between consecutive ODSs (*i.e.*, $\boldsymbol{\varphi}_k$ and $\boldsymbol{\varphi}_{k+1}$, spurious elements can be included in the clustering procedure, affecting the accuracy of the identified instantaneous modal parameters. The robustness of the method may be improved by calculating averaged modal parameters using different ξ instants or applying filtering techniques to the identification outcomes. The method proposed here can be applied to identify modal parameters either in a continuous fashion or in periodic inspection intervals.

Damage identification of a densely instrumented RC building

The benchmark studied in this section is the same as Section 3.3, where a centralized identification algorithm was employed for modal identification using 4 sensing nodes. Conversely, in this section, the data is processed simulating the use of a line-topology smart WSN consisting of 15 sensors (see Figure 3.62), where the signal collected at different instrumented locations is used to update the identification

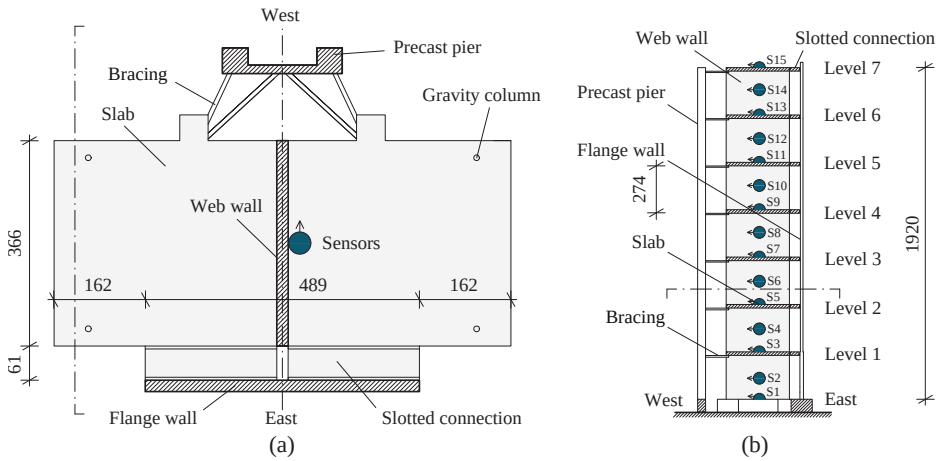

Figure 3.62: Scheme of the case study and sensor layout: (a) plan view and (b) lateral view; adapted from [216]

results through rank-1 perturbations onboard the sensing nodes, employing the framework of the algorithm presented in the previous sections.

This section aims to show that the denser distribution of sensor leads to more accurate identification results. Besides, no relevant information is lost by applying the presented strategy for data compression, while the volume of the transmitted data can be considerably reduced compared to a traditional implementation. The suitability of the procedure for early damage localization is shown by studying the structural conditions related to different low-damage scenarios.

The inspection time series collected during white noise excitation relevant to conditions U, A, and B are used in this application (see Section 3.2 for more details). In this application, each time history has a duration of 458 s and a sampling frequency of 60 Hz. A unique signal, with a total duration of 1374 s, generated by appending the mentioned time series one at the end of the previous one, is employed in this study to simulate ongoing damage. Low-pass filter and downsampling of factor 4 were applied to the original signal, sampled at 240 Hz, before using the data.

During the two seismic tests considered in this work, "slightly" and "moderate" nonlinear responses were registered. During the first test, limited yielding occurred at the base of the web wall,

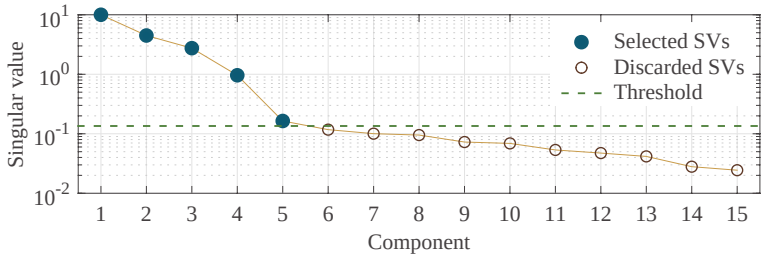

Figure 3.63: Selection of the most significant singular values

generating cracks up to the fourth floor and a maximum roof drift ratio (defined as the ratio between the maximum lateral displacement at the uppermost level and the distance of this level to the base of the wall) equal to 0.28%. During the second seismic test, the maximum roof drift ratio was equal to 0.75%. More details about the original testing setup and structural behavior can be found in [214, 215].

Before applying the modal identification algorithm, a study is conducted on the relevance of singular components (*i.e.*, values and vectors) of the collected structural responses. In Figure 3.63, the 15 SVs obtained through the SVD of the original input matrix are reported on a logarithmic scale. A threshold for the selection of the most relevant components is calculated employing the method proposed by Gavish and Donoho [255] for signals with an unknown noise level. In this case, the first 5 SVs are above the selected threshold and can be used to obtain a good approximation of the input matrix.

Simulating the use of a line-topology network, in a traditional data acquisition process, the weight of the transmitted packets would increase linearly with the number of sensors. This trend is represented in Figure 3.64 and compared with the packet weight referred to the proposed decentralized approach. In this figure, the packet weight is expressed as the number of floating-point data values (with the single or double precision format, depending on the specific applications) that are transmitted from a node to the next one in the path to reach the end of the network. As explained before, the maximum packet weight can be adjusted by the user by selecting a suitable number of SVs in the approximation of the input matrix. In this study, the 5 SVs lying over the selected threshold are employed, resulting in a considerable decrement of

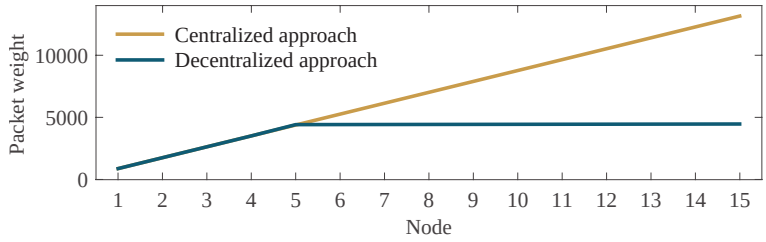

Figure 3.64: Packet weight in a line-topology network

total transmission weight. In particular, the weight of the last packet transmitted to the coordinator would be 13155 for the transmission of the original input matrix, while only 4465 for the transmission of the approximated one. Power consumption concerning transmission is approximately proportional to the packet weight; therefore, the proposed method entails a considerable power saving, especially for the last nodes. Specifically, in the considered case study, the last node undergoes a reduction of 66% in power consumption related to data transmission. This allows optimizing maintenance interventions for battery replacement since the power consumption tends to be more uniform throughout the network.

Upon selecting the number of most relevant SVs, the most suitable number of clusters for applying the proposed identification procedures is sought using the silhouette-based method. In this analysis, both the original input matrix and the approximation obtained using the first 5 singular components were used for comparison. The silhouette-based approach is applied to the ODSs obtained using the input matrices relevant to a set of different "testing" time samples. The most recurrent result over the testing samples is then assumed as the optimal p parameter. In particular, 123 testing input matrices $\mathbf{X} = \left[\mathbf{x}_1[t-\overline{N}+1,t],\ldots,\mathbf{x}_r[t-\overline{N}+1,t]\right]^T$ were selected considering different time samples t equally distributed in the complete structural response (formed of U, A, and B recordings, with 41 testing samples in each of them). In Figure 3.65a-b, the results of this analysis are reported, referred to the case of a complete input matrix and approximated version, respectively. Each thin brown line reported in this figure is relevant to the set of ODSs computed from a given input matrix. In particular, each point of these lines indicates the average silhouette width obtained by applying the k-means algorithm with a different value of p, which is reported on the abscissa of the diagram.

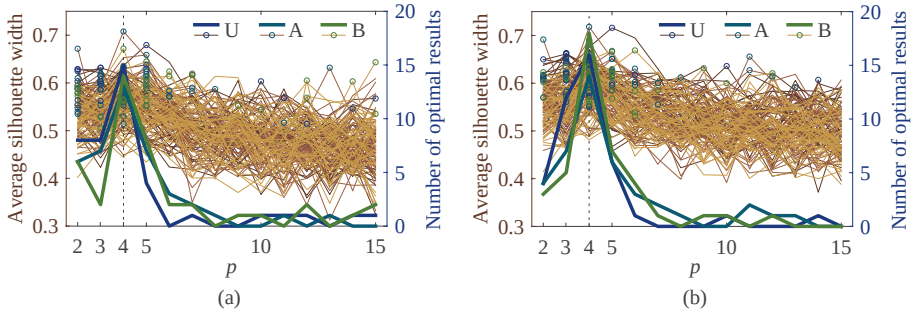

Figure 3.65: Selection of the most suitable number of clusters using (a) original input matrices and (b) approximations of the input matrices

These lines have three different colors (from dark brown to light brown) corresponding to the test input matrices selected in different structural conditions (*i.e.*, U, A, and B, respectively). For each line, the global maximum is highlighted through a circle that indicates the optimal number of clusters resulting from the analysis of the specific input matrix. The cumulative number of optimal results obtained for each p value is then calculated to improve the robustness of the selection approach. Three thick lines, referring to the cumulative number of optimal results for each p value obtained in the three structural conditions (*i.e.*, calculated using 41 test instants each) are also reported in Figure 3.65. It is possible to notice that the maxima of these lines, *i.e.*, the most suitable p value for clustering, are at $p = 4$ for each structural condition and both considering the original and the approximated input matrices. This result indicates that the selection of the p parameter can generally be done in the initial phase of the procedure and then employed during the long-term identification process. Moreover, the optimal number of clusters is the same using the two versions of the input matrix, denoting that no useful information is lost during the approximation process

The multivariate signal consisting of the 15 collected time histories in the three structural conditions was employed to obtain the MAD reported in Figure 3.66a. Here, high values (close to 1) are depicted in yellow, while low values (close to 0) are represented in blue. Low-valued horizontal bands can be clearly noticed in the time-component plane around the 5th and the 35th components. In this plot, the component indicated on the vertical axis represents the k index used in Equation (3.11). The MAD is used to select the wavelet

components which generate similar ODSs (using a threshold level $\theta = 0.1$), hence discarding the components related to noise. The ODSs generated by the selected components are then partitioned using the k-means algorithms into 4 clusters, which is the optimal p parameter obtained in the previous analysis. A forgetting factor $\alpha = 0.99$ was selected to perform the online clustering procedure. A representation of the clustered components in the time-component plane is reported in Figure 3.66b. Here, each vector $\boldsymbol{\varphi}_k[\xi]$ is depicted in the time-component plane (indicated through the ξ and k indices, respectively) as a point having a color that depends on the assigned cluster.

The decoupled modal responses associated with each cluster are thus calculated using the IWPT and the instantaneous frequencies are identified by applying the HT on the obtained monocomponent responses. Figure 3.66c shows the identified instantaneous frequencies for all the identified modes. A median filter is applied to the obtained results to improve the readability of the plot, replacing each instantaneous frequency entry with the median of 1000 neighboring entries (*i.e.*, using a kernel of 16.67 s). In this figure, a slight decrement of the natural frequencies can be noticed when passing from condition A to B, especially for modes 1 and 4.

In Figure 3.66c the results obtained through the original DAMA are also reported in gray, as well as the reference values identified using the FDD [259]. It is possible to notice that all the results are in good agreement, especially for the first mode. However, the use of 15 sensing nodes has allowed the successful identification of 4 modes in the range between 0 Hz and 30 Hz, compared to the 3 modes identified using the DAMA with 4 sensors.

The reconstructed decoupled modal responses are then employed to evaluate the instantaneous mode shapes of the structure by calculating the ratio of Equation (3.6). Before applying this procedure, the responses obtained at the base level (using sensor S1) are subtracted from the responses of the upper levels in order to convert the absolute horizontal acceleration measurements to relative accelerations. This step is suggested in the literature [215] to improve the results of modal identification when dealing with white noise base excitation tests. Figure 3.67 shows the instantaneous amplitudes of

the shapes identified through the procedure proposed in this work. Slight variations can be observed when passing from condition U to A in modes 1 and 4, while moderate differences for all modes are noticeable when passing from A to B. In particular, the shape of mode 3 in the third structural condition is considerably different from the previous conditions. This is also observable in the average shapes in right-hand side of Figure 3.67, where the reference shapes of the undamaged condition identified using the DAMA (employing 4 sensors) and the FDD (employing 15 sensors) are also reported. It should be noted that the second shape is not reported for the DAMA since it was not identified using the limited sensor configuration. In both the instantaneous and average representations of Figure 3.67, the shapes are normalized to have a unitary norm.

The identified instantaneous natural frequencies and mode shapes can be employed in SHM applications for damage identification, relying on different methods based on modal parameters. The displacement and curvature have been largely used as flexibility-

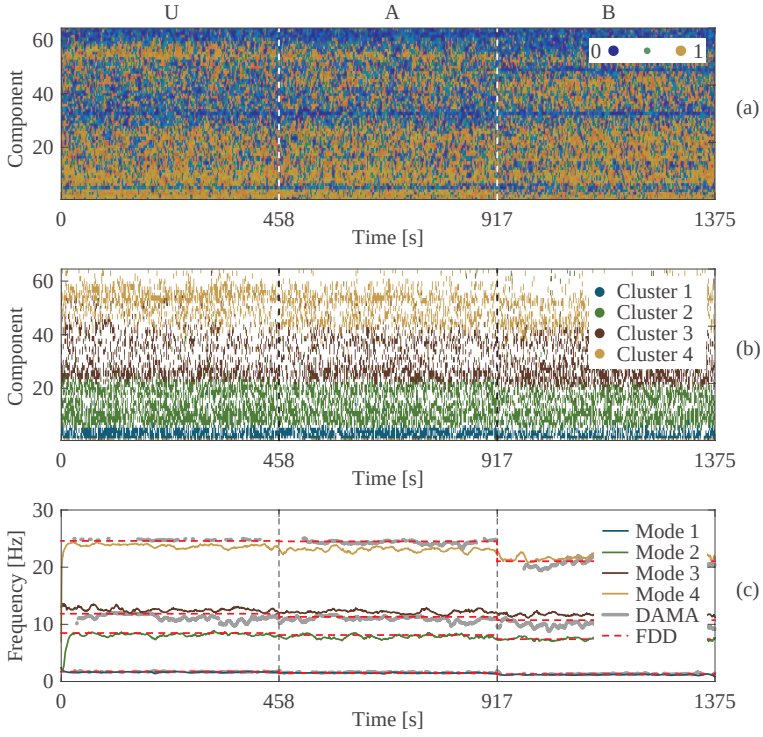

Figure 3.66: Modal assurance distribution (a), clustered components (b), and identified instantaneous frequencies (c)

based indices [260, 261], while the interpolation method has shown superior performance when the errors in the computation of the curvature may affect the results [262]. In this study, a flexibility-based approach is addressed for this purpose to provide an example of using identified parameters in SHM applications. The adopted approach consists of evaluating the Uniform Load Surface (ULS) of the structure (which degenerates into a line – ULL – for structures with one-dimensional development).

In this study, the curvature of the ULL , evaluated through the central difference method, is employed as a DSF. Specifically, the damage index is calculated as

$$D_j[t] = \frac{\chi_{I,j}[t] - \bar{\chi}_{B,j}}{\text{std}\left(\chi_{B,j}\right)} \tag{3.57}$$

where $\chi_{I,j}[t]$ is the curvature at the j-th node in the inspection instant, $\bar{\chi}_{B,j}$ is the mean of the curvature values at the same node in a baseline interval, and $\text{std}\left(\chi_{B,j}\right)$ is the standard deviation in the considered baseline interval. Assuming a normal distribution for the DSF, a threshold for damage localization can be selected as $\delta = 3$ in order to minimize the occurrence of false positives to less than 0.1% [263]. Therefore, if $D_j[t] > \delta$, the j-th location is likely to be damaged at the t-th instant. Assuming also that real damage is persistent in time, $D_j[t]$ values over the threshold for a limited time interval where the general trend is below the threshold can be considered as false positives. On the other hand, spurious $D_j[t]$ values below the threshold where the general trend exceeds it, can be considered as false negatives.

Figure 3.68 shows the instantaneous ULL and the curvature-based damage index calculated as shown above. In particular, in Figure 3.68a, both the instantaneous estimates and the averaged curves representing the ULL are reported. A clear variation is noticeable when passing through different structural conditions. In Figure 3.68b, the values below the threshold are depicted in gray. For the condition U, some false positives are registered at the lower levels in short time intervals. On the other hand, for conditions A and B, a generally positive trend is registered at the base of the structure. Moreover, the damage index grows in condition B

and other damaged locations are identified at the mid-height of each story throughout the structure. This information corresponds to the description of the structural state, observed through the visual inspections conducted during the experimental campaign [214, 215].

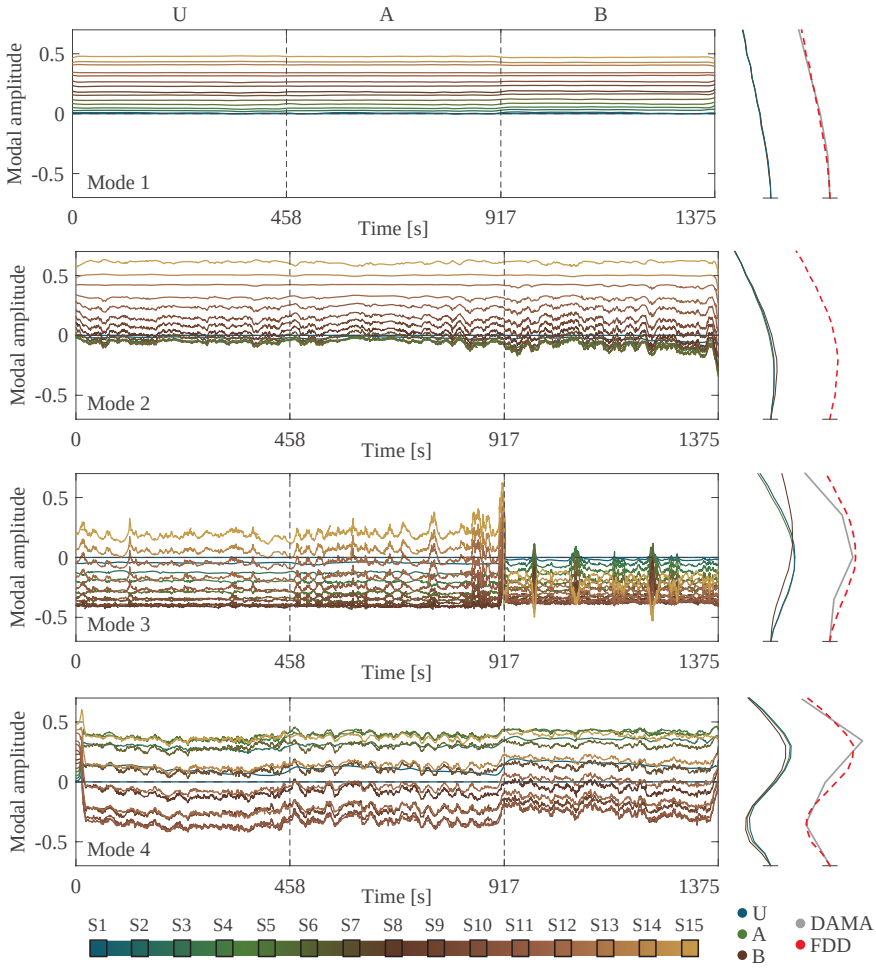

Figure 3.67: Instantaneous amplitudes of the identified modes (left) and averaged identified shapes for each condition (right)

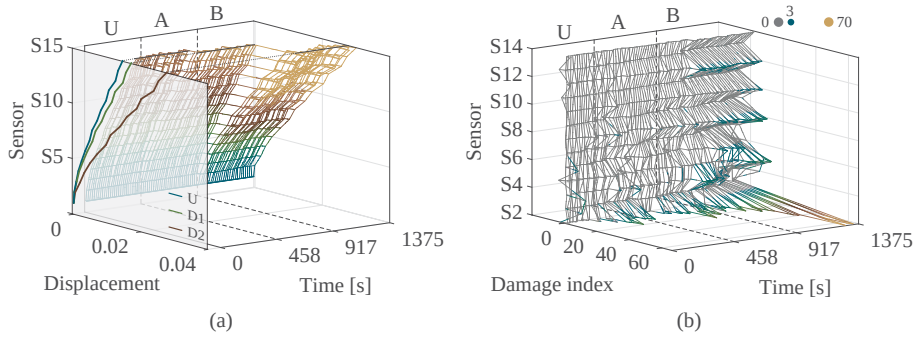

Figure 3.68: Instantaneous uniform load line (a) and damage index (b)

Exploiting traffic | 4

Traffic is undoubtedly the most important and prominent excitation source for civil bridges and viaducts. As shown in Chapter 1, several researchers attempted to mitigate the complex phenomena that this kind of excitation could induce in the short term or to exploit the quasi-static part of the structural response to identify dense DSFs. Besides excitation, vehicles are also (and primarily) a means of transport. Nowadays, it is unthinkable that a vehicle, either an ordinary car or a micromobility vehicle, such as a bicycle or kick scooter, does not carry any sensing device. Indeed, smartphones are advanced sensing devices in all respects, which can record acceleration, position, and other dynamic and static measurements and upload them to the Internet.

This chapter studies how traffic can be exploited for SHM on two fronts. First, heavy vehicles are considered as a form of excitation for bridges. In this case, vehicle dynamics and vehicle-bridge interaction (VBI) would strongly affect recordings on board the vehicles. Therefore, a direct form of SHM is studied in this chapter for this kind of vehicle, involving sparse sensor networks deployed on the bridge. Second, light micromobility vehicles, which are stiff and light compared to bridges and footbridges, are exploited in an ISHM strategy to identify modal parameters from drive-by recordings collected by smartphones.

Therefore, this chapter has two main objectives:

1. Propose a unified and automatic identification strategy for estimating both dense quasi-static structural features and modal parameters using sparse sensor networks (consisting of down to just one sensing device). The procedure is based only on acceleration recordings collected on the bridge, without the need for additional devices to track the vehicle location. Section 4.1 shows how acceleration recordings can be used to obtain curvature, one of the most used DSFs in SHM, removing the complex procedures (and thus approximations) which are generally necessary for traditional methods to calculate it from identified mode shapes. Then, Section 4.2 presents the unified identification algorithm. In this context, a strategy proposed for automatic selection and processing of signal windows related to the vehicle passage makes the method particularly suitable for crowdsourced cloud computing applications. This original approach brings considerable advantages, as it enables accurate localization of structural anomalies using limited (and thus low-cost) instrumentation, suitable for widespread monitoring, and removes the need for data synchronization. Moreover, differently from most literature methods [1, 2], the damage entity can be quantified without any knowledge on the structural masses and avoiding the use of finite element models.
2. Identify the modal parameters of footbridges using multiple types of data collected by smartphones installed on passing micromobility vehicles. The procedure proposed in this study fuses the datasets obtained by accelerometer, gyroscope, magnetometer, and GPS using a Kalman filter. Multiple datasets collected in crowdsourced applications mitigate the effects of noise and allow identifying a dense DSF for SHM purposes.

The study related to the first objective is supported by the results obtained using the acceleration data collected on three viaducts of the Italian A24 motorway, analyzed in several works by Aloisio et al. [118, 149, 264, 265]. Moreover, the results obtained for a numerical case study in different damage scenarios are reported to show the potentialities of the proposed method for damage detection, localization, and quantification. The study related to the second objective is supported by the results collected during an experimental

campaign conducted on a footbridge in Bologna (Italy).

4.1 From acceleration to curvature

Isostatic schemes, such as simply supported beams, are typically considered for the design of RC bridges and viaducts due to their capacity to accommodate the expansion (or contraction) effects of environmental loads, such as temperature, that would instead generate unwanted stress states in hyperstatic structures. In this study, the simply supported beam will be considered as representative of a span of common RC viaducts.

Literature in the field of SHM reports several cases where the effectiveness of dynamic identification methods is affected by structural nonlinearities [266]. Moreover, in civil structures, damage is often related to an increment in the degree of nonlinearity [56]. However, material and geometrical nonlinearities, as well as those related to the boundary conditions, are generally activated by significant displacements. Since the method proposed in this section is conceived for ordinary traffic loads, it is assumed that the structure is subjected to small displacements and thus behaves linearly.

In general, the equation of motion of a linear simply supported beam with uniform cross-section subjected to a generic load function acting orthogonally to the axis of the structure $p(z,t)$ can be represented as

$$\mu \frac{\partial^2 u(z,t)}{\partial t^2} + d \frac{\partial u(z,t)}{\partial t} + EI \frac{\partial^4 u(z,t)}{\partial z^4} = p(z,t) \tag{4.1}$$

where μ is the mass per unit length, d is a damping coefficient, and EI is the flexural stiffness, given by the elastic modulus of the material E and the inertia of the section I. In Equation (4.1), $u(z,t)$ is a function in space (z) and time (t) that indicates the structural displacement response in the direction of the load, while the $\partial^d f / \partial x^d$ operator indicates the d-th derivative of the function f with respect to x. Using the superposition principle, the structural response can be

written as a linear combination of modal responses:

$$u(z,t) = \sum_{m=1}^{\infty} \phi_m(z) q_m(t) \tag{4.2}$$

where $\phi_m(z)$ is the m-th mode shape of the structure and $q_m(t)$ is a function of time that presents a peak in the frequency domain around the damped m-th circular frequency $\omega_{d,m}$ which, in the case of low damping, can be assumed as the m-th natural (circular) frequency of the structure

$$\omega_m = \frac{m^2\pi^2}{l^2}\sqrt{\frac{EI}{\mu}} \tag{4.3}$$

where l is the length of the beam. In free vibration conditions, *i.e.*, $p(z,t) = 0$, if damping is small, the structural response can be approximated as

$$u(z,t) = \sum_{m=1}^{\infty} c_m \sin\left(\frac{m\pi z}{l}\right) e^{-\xi\omega_m t} \sin\left(\omega_m t\right) \tag{4.4}$$

with c_m representing a constant depending on the initial conditions and ξ denoting the modal damping ratio, here assumed as equal for all the vibration modes.

Typically, in SHM applications, accelerometers are employed to collect the structural responses. The collected acceleration, in the case of free vibration, can be described using the following equation:

$$\frac{\partial^2 u(z,t)}{\partial t^2} = \sum_{m=1}^{\infty} c_m \sin\left(\frac{m\pi z}{l}\right) \ddot{q}_m(t) \tag{4.5}$$

where

$$\ddot{q}_m(t) = \omega_m^2 e^{-\xi\omega_m t}\left[\left(\xi^2 - 1\right)\sin\left(\omega_m t\right) - 2\xi\cos\left(\omega_m t\right)\right] \tag{4.6}$$

The Fourier transform of the acceleration can thus be calculated as

$$A_a(z,f) = \mathcal{F}\left[\frac{\partial^2 u(z,t)}{\partial t^2}\right] = \sum_{m=1}^{\infty} c_m \sin\left(\frac{m\pi z}{l}\right) Q_m(f) \tag{4.7}$$

with $Q_m(f)$ representing a normalized transfer function of the SDOF system associated with the m-th mode:

$$Q_m(f) = \frac{\omega_m^3 \left(1 + \xi^2\right) + 4j\pi\xi\omega_m^2 f}{\omega_m^2 + \left(\xi\omega_m + 2j\pi f\right)^2} \tag{4.8}$$

Considering now a single moving load with magnitude P, a constant speed v and negligible mass, the load function can be written as $p(z,t) = P\delta(z - vt)$ and, if damping is small, the displacement response of the structure becomes [267]:

$$u(z,t) = \frac{Pl^3}{48EI} \sum_{m=1}^{\infty} \frac{1}{m^2\left(m^2 - \alpha^2\right)} \sin\left(\frac{m\pi z}{l}\right) \left[\lambda_m(t) - \frac{\alpha}{m} e^{-\xi\omega_m t} \sin\left(\omega_m t\right)\right] \tag{4.9}$$

with

$$\alpha = \frac{vl}{\pi}\sqrt{\frac{\mu}{EI}} \tag{4.10}$$

$$\lambda_m(t) = \sin\left(\frac{m\pi vt}{l}\right) \Pi\left(\frac{vt}{l} - \frac{1}{2}\right) \tag{4.11}$$

where $\Pi(t)$ is a rectangular function used to limit the support of $\lambda_m(t)$ to the interval $t \in [0, l/v]$, *i.e.*, when the load is on the beam, and δ denotes the Dirac delta function. The acceleration response, obtained by double derivative thus reads:

$$\frac{\partial^2 u(z,t)}{\partial t^2} = -\frac{Pl^3}{48EI} \sum_{m=1}^{\infty} \frac{1}{m^2\left(m^2 - \alpha^2\right)} \sin\left(\frac{m\pi z}{l}\right) \left\{\left(\frac{m\pi v}{l}\right)^2 \lambda_m(t) + \frac{\alpha}{m}\ddot{q}_m(t)\right\} \tag{4.12}$$

and its Fourier transform is

$$\begin{aligned} A_v(z,f) &= \mathcal{F}\left[\frac{\partial^2 u(z,t)}{\partial t^2}\right] = \\ &= -\frac{Pl^3}{48EI} \sum_{m=1}^{\infty} \frac{1}{m^2\left(m^2 - \alpha^2\right)} \sin\left(\frac{m\pi z}{l}\right) \left[L_m(f) - \frac{\alpha}{m} Q_m(f)\right] \end{aligned} \tag{4.13}$$

where $L_m(f)$ is a function depending on the quasi-static effects of

the moving load and has the following expression:

$$L_m(f) = \frac{\pi v m^3}{2l\left(\frac{l^2 f^2}{v^2} - \frac{m^2}{4}\right)} e^{j\pi\left(\frac{m-1}{2} - \frac{lf}{v}\right)} \sin\left(\frac{\pi l f}{v} - \frac{m\pi}{2}\right) \tag{4.14}$$

Comparing Equations (4.7) and (4.13), it is possible to notice that, except for the constants, the second equation has an additional term represented by Equation (4.14). The expression of $L_m(f)$ can be obtained by applying the modulation theorem to a *sinc* function, as shown in Chapter B. The resulting function presents a sharp peak at a frequency value that grows with m, assuming however lower magnitude. Also, $L_m(f)$ decreases with f^2. It can be therefore be assumed that the term $L_m(f)$ has a non-negligible contribution in the structural response only in the low-frequency range. On the other hand, the function $Q_m(f)$ carries information about the m-th vibration mode of the structure, and thus it generally governs the medium-high-frequency content of the response spectrum.

Vehicular traffic, though as an ensemble of moving loads, induce manifold effects in the structural vibration response, namely (1) quasi-static effects due to the deflection of the structure under the weight of the passing vehicles, (2) dynamic effects due to instantaneous equilibrium between inertial, elastic, and dissipative forces, and (3) short-term effects, here addressed as "noise", mainly given by the interaction between the vehicle wheels and the uneven road surface. The first phenomenon, described in Equation (4.14), is closely related to the instantaneous vehicle location and mainly affects the lowest (typically sub-hertz) frequency range in the spectrum of the structural response. The second family of effects can be modeled as the superposition of a set of structural vibration modes, described in Equation (4.8), the first of which generally populate the frequency range between few hertz and few dozen hertz for the most common RC viaducts. Finally, noise affects the entire spectrum, with the majority of its energy concentrated at the higher frequencies.

Due to the particular structure of the response spectrum, different structural features can be analyzed by individually processing different frequency bands. In this study, the attention is posed on the low-frequency range, with the aim of extracting quasi-static damage-sensitive features which depend on the location of the vehi-

cle (*i.e.*, the influence line), as well as modal parameters (*i.e.*, natural frequencies and sparse estimates of the mode shapes) of the first dominating dynamic contributions.

As shown in Section 3.2, the MAD can be used to build adaptive filter banks able to extract decoupled modal contributions from the structural response collected at different instrumented locations. In the mentioned study, critically sampled signal components were extracted using wavelet filter banks, with the aim of reducing the weight of identified parameters. Besides, if the structure can be modeled as a linear time-invariant system, static filter banks can be employed, improving the efficiency of the identification procedure. In this section, the aforementioned concepts are employed in the structural identification of civil infrastructures under the following assumptions:

1. A vehicle is modeled as a single constant load, regardless of the spacing between the wheel axles;
2. Only one vehicle at a time passes through the bridge with a constant velocity;
3. The vehicle-bridge coupling effects are neglected.

The first two assumptions allow considering the loading function as $p(x,t) = P\delta(x - vt)$. If multiple axles are present, the suppression of certain frequency values in the response spectrum should be taken into account. However, in the following sections, it is shown that the first assumption can generally be legitimately considered. Moreover, due to the modest length of single spans in RC infrastructures, the second hypothesis can be generally assumed in the case of fluid traffic. Finally, concerning the third point, RC infrastructures are typically massive with respect to ordinary cars.

In the following parts, two identification approaches, based on the low-frequency and (medium-)high-frequency effects, respectively, are proposed to obtain different structural features which may be of particular interest for the assessment of the structural integrity.

Low-frequency effects

Applying a sub-hertz lowpass filter to the structural acceleration response collected at location distant ζl (with $\zeta < 1$) from the first support during the passage of a vehicle with constant velocity v, in the interval $t \in [0, l/v]$, from Equation (4.12), it is possible to define

$$\begin{aligned} h^{(\zeta)}[t] &= \left(\left. \frac{\partial^2 u(z,t)}{\partial t^2} \right|_{z=\zeta l} * \bar{b}_0 \right)[t] \approx \\ &\approx -\frac{Pl^3}{48EI} \sum_{m=1}^{\gamma} \frac{\pi^2 v^2 \sin(m\pi\zeta)}{l^2 (m^2 - \alpha^2)} \sin\left(\frac{m\pi v t}{l}\right) \end{aligned} \tag{4.15}$$

where $*$ is the convolution operator, $\bar{b}_0[t]$ is the impulse response of the lowpass filter, and γ indicates a small number of contributions with the majority of their frequency content in the sub-hertz interval. Assuming the distance traveled by the vehicle as $z = vt$, it is possible to obtain a function of space which represents the double derivative of the displacement influence line of the structure with respect to space as:

$$\begin{aligned} h^{(\zeta)}[z] &= \sum_{m=1}^{\gamma} h_m^{(\zeta)}[z] \approx \\ &\approx \sum_{m=1}^{\gamma} -\frac{Pl^3}{48EI} \frac{\pi^2 v^2 \sin(m\pi\zeta)}{l^2 (m^2 - \alpha^2)} \sin\left(\frac{m\pi z}{l}\right) \end{aligned} \tag{4.16}$$

The function $h^{(\zeta)}[z]$ is thus the influence line of the curvature of the beam in the normalized location ζ and is therefore also proportional to the influence line of the bending moment. Due to the Maxwell-Betti reciprocal work theorem, Equation (4.16) can also be interpreted as the curvature of the deflection shape of the beam subjected to a force P statically applied at the instrumented location.

It should be noted that $h^{(\zeta)}[z]$ can be identified using a single sensing device deployed on the structure, offering however a dense description of the structural behavior, depending on the sampling frequency of the collected data. Moreover, curvature is a well-established DSF that is typically obtained through double

derivation upon identifying mode shapes through a set of limited sensors. The traditional approach generally involves the introduction of computational errors (*e.g.*, due to the central difference method), which may affect the robustness of the outcomes in the presence of noisy identified parameters. Besides, the curvature is typically estimated only at the instrumented locations. Conversely, the proposed method exploits the collected acceleration to infer information about curvature in potentially continuous locations, without performing any approximations in the derivation process.

It is worth noting that the second hypothesis reported in Section 4.1 related to the constant vehicle speed is here fundamental to consider the double derivative in time (*i.e.*, bridge acceleration) as a double derivative in space (*i.e.*, bridge curvature). Indeed, passing from one quantity to another, a multiplication factor depending on the change of variable is involved. This factor can be calculated based on the vehicle speed. However, a varying speed would lead to a non-constant factor that affects the estimated curvature. Further studies on removing this dependence based on information on the instantaneous vehicle velocity (or an estimate based on data collected from cameras or optical sensors) must be conducted.

Considering loads consisting of two axles, an equivalent function in space can be obtained by calculating $h^{(\zeta)}[z] * \epsilon_w[z]$, where $\epsilon_w[z] = \delta[z] + \delta[z + w]$, w is the distance between the wheel axles and $\delta[z]$ is a discrete Dirac delta function, thus obtaining

$$h^{(\zeta)}[z] * \varepsilon_w[z] = h^{(\zeta)}[z] + h^{(\zeta)}[z + w] \tag{4.17}$$

Physically, this function represents the influence line of the curvature of the beam when the first load is at location z and the second is at location $z + w$. In the frequency domain, the spectrum of Equation (4.17) can be obtained as a simple point-by-point product, *i.e.*, $H^{(\zeta)}[f]E_w[f]$, where $H^{(\zeta)}[f]$ and $E_w[f]$ are the spectra of $h^{(\zeta)}[z]$ and $\epsilon_w[z]$, respectively, reported in Figure 4.1. Considering the frequency values $f_s^{(1)}$ and $\bar{f}_s$, defined as

$$f_s^{(1)} = \left(s + \frac{1}{2}\right) \frac{v}{l} \tag{4.18}$$

$$\bar{f}_s = \left(s - \frac{1}{2}\right)\frac{v}{w} \tag{4.19}$$

representing the s-th zeros of $H_1^{(\zeta)}[f]$ (*i.e.*, the frequency spectrum of $h_1[z]$) and $E_w[f]$, respectively, it is possible to assume that $H^{(\zeta)}[f] \approx H^{(\zeta)}[f]E_w[f]$ if $f_1^{(1)} \ll \bar{f}_s$, *i.e.*, if $w \ll l$. In particular, assuming the limit

$$\frac{f_s^{(1)}}{\bar{f}_s} = 3\frac{w}{l} \leq \frac{1}{3} \tag{4.20}$$

will guarantee that the double load affects $H^{(\zeta)}$ of up to 13%. As a geometrical limit, it can thus be posed that $l \geq 10w$. This condition can be generally assumed in the case of large civil infrastructures. However, the effect of multiple loads generally produces a smoother influence line. In the specific case of two axles, this can be observed analytically since the effect of $E_w[f]$ is of reducing the higher perceptible contributions (with an m index close to γ) of $h^{(\zeta)}[z]$. Since higher-frequency contributions are attenuated, the resulting function in space is smoother.

In addition to the aforementioned geometrical constraints, the sampling frequency of the accelerometers should be selected based on the required resolution of the influence line. In particular, considering the vehicle velocity v and the required spatial resolution r, the minimum sampling frequency can be obtained as $f_s = v/r$ [268].

This study only considers individual vehicles traveling the bridge deck. This is an admissible assumption for minor bridges in regular traffic conditions. Indeed, considering the safety distance while driving, which is typically determined using the "two-second rule of thumb", vehicles driving at 50 km/h should have an in-between distance of about 30 m. However, multiple vehicles could be on the same bridge span in busy traffic conditions. Moreover, there may be vehicles in opposite directions. Knowing the loading pattern is essential to estimating the influence lines in these cases. In such situations, deconvolution strategy could be used to decouple the effects of multiple loads (under the assumption of linear-elastic structural behavior) [121]. The decoupled time histories can thus be employed for influence line identification. This aspect needs further investigation.

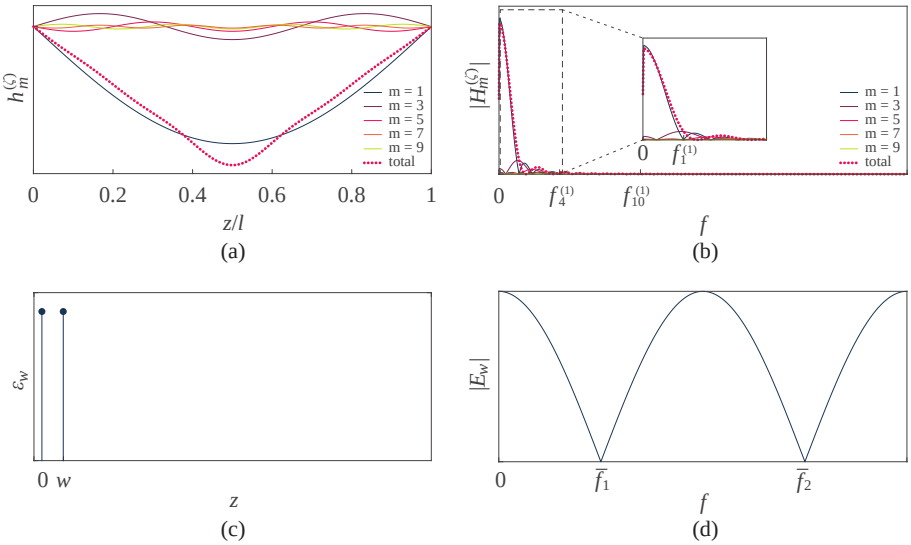

Figure 4.1: Quasi-static components of the structural response in space (a) and frequency domain (b); two-axle excitation in space (c) and frequency domain (d)

High-frequency effects

The high-frequency range of the response spectrum of the structure under a single moving load is analogous to the response spectrum obtained in free vibration condition, reported in Equation (4.7). Here, each term of the summation is related to a different resonant frequency of the structure and presents a peak in the frequency domain around the frequency ω_m. Assuming that the signal collected by the i-th accelerometer deployed on the structure is formed of a part representing the structural response and an instrumentation noise term $\eta_i[t]$, as shown in Figure 4.2, Equation (4.5) can be rewritten as

$$x_i[t] = \sum_{m=1}^{\infty} \phi_{i,m} \ddot{q}_m[t] + \eta_i[t] \tag{4.21}$$

where $x_i[t]$ is the acceleration collected by the i-th sensor and $\phi_{i,m}$ is the i-th element of the m-th mode shape. Assuming the noise term as white Gaussian, *i.e.*, having an ideally flat spectrum, each modal contribution in the summation of Equation (4.21) has a limited range in frequency where the structural response is higher than the instrumentation noise. Therefore, modal responses can be extracted using suitable bandpass filters with impulse responses $\bar{b}_m$ centered

at the natural frequencies of the systems ω_m and having a width equal to the frequency band that exceeds the noise threshold.

Section 3.3 showed how these filters can be simultaneously generated and applied to the collected data to extract modal contributions adaptively through the MAD. In this chapter, a filter bank suitable for the extraction of modal contributions in civil infrastructures under moving loads is generated based on this technique. It is also shown how modal parameters, *i.e.*, natural frequencies and mode shapes, can be identified from decoupled modal responses.

Consideration on multiple moving loads

Although the application of the MAD-based decomposition algorithm in the case of a single moving load is similar to the case of impulsive load or broadband noise excitation, the presence of multiple loads theoretically affects the outcome of the procedure. In particular, considering a vehicle having two wheel axles, the frequencies close to $\bar{f}_r$ are suppressed in the structural response due to the particular spectrum of the load function shown in Figure 4.1d. Nevertheless, in real applications, vibration transmitted by the adjacent spans – due to the passage

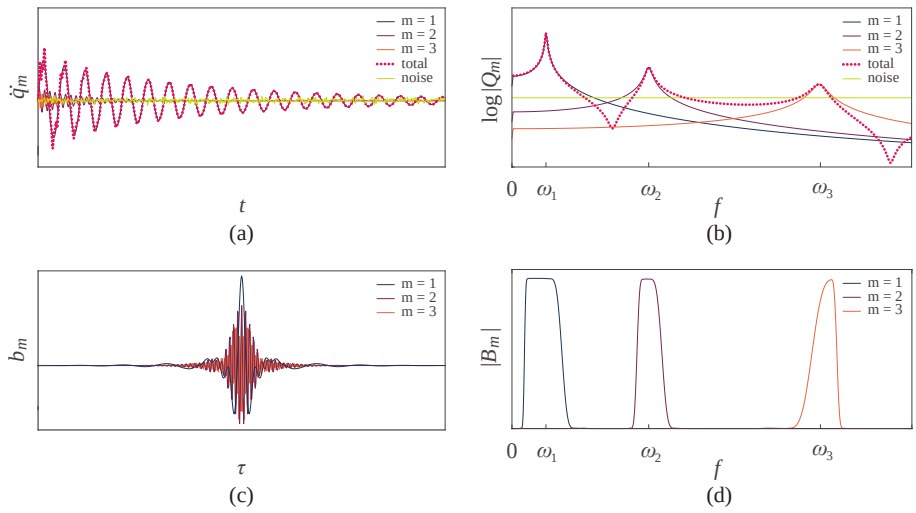

Figure 4.2: Modal components of the structural response in time (a) and frequency domain (b); bandpass filters in time (c) and frequency domain (d)

of other vehicles – and other loads, such as wind, will form a more complex loading function, which can be represented in the form:

$$p(z,t) = v(z,t) + P[\delta(x - vt) + \delta(x - w - vt)] \tag{4.22}$$

where $v(z,t)$ is an additional distributed noise function due to ambient and operational vibration. Considering the structure as a linear system, the structural response will include the effects of both moving loads and environmental phenomena. While the first are likely to prevail, the other effects produce contributions of the structural response that populate the spectral ranges close to $\bar{f}_r$. The similarity of the ODSs that generate high-valued regions in the MAD is intended in a vectorial sense (cosine similarity), *i.e.*, ODSs which have similar ratios between their elements will generate MAD values close to 1, regardless of the amplitude of each specific element of $\boldsymbol{\varphi}_k[t]$. Therefore, the MAD does not depend directly on the amplitude of the signal components. For this reason, if the term $v(z,t)$ generates a structural response that exceeds the noise floor level of the accelerometers in all the frequency spectrum, the MAD will be robust to suppressed frequency bands due to multiple loads.

4.2 A unified identification framework

In Section 4.1, a method for estimating dense quasi-static features of a structure modeled as a simply supported beam using potentially a single sensor is shown. In particular, a lowpass filter is employed to extract the curvature influence line of the structure from acceleration data. However, curvature influence lines obtained in this way are sensitive to noise and dynamic effects. On the other hand, modal parameters are only defined at the instrumented locations but are generally more robust to noise. Thereby, a combination of the information obtained through the two aforementioned features may provide insights about the presence, approximate location, and entity of structural damage. In the following, a novel strategy for SHM of civil infrastructures is presented based on these concepts. Specifically, a filter bank that includes the filters able to extract

both quasi-static and dynamic features is first presented. Then, an approach for damage identification is proposed based on the identified features.

Considering a set of column vectors $\mathbf{b}_j^{(t)}$ containing the coefficients of the impulse responses $\bar{b}_j^{(t)}[\tau]$ with $\tau = 1, \ldots, N$, where N is the filter length, a filter bank matrix at the t-th time instant can be represented as follows:

$$\mathbf{B}_t = \left[\mathbf{b}_0, \mathbf{b}_1^{(t)}, \ldots, \mathbf{b}_p^{(t)}\right] \tag{4.23}$$

Here, the term $\mathbf{b}_0$ contains the coefficients of the lowpass filter $\bar{b}_j^{(t)}[\tau]$ used in Section 4.1 to extract the quasi-static structural features. In this study, it is assumed that $\mathbf{b}_0$ does not depend on the time instant, *i.e.*, the lowpass filter does not evolve over time, and therefore the apex (t) is dropped. On the other hand, the terms $\mathbf{b}_j^{(t)}$ with $j = 1, \ldots, p$ indicate the adaptive time-dependent bandpass filters.

Considering a matrix $\mathbf{X}_t$ with the form

$$\mathbf{X}_t = [\mathbf{x}_{t,1}, \mathbf{x}_{t,2}, \ldots, \mathbf{x}_{t,r}] \tag{4.24}$$

where $\mathbf{x}_{t,i}$ are column vectors containing the samples of the acceleration signal $x_i[t]$ in the interval $[t - N/2, t + N/2]$, a set of decomposed signals can be computed as:

$$\mathbf{Y}_t = \mathbf{X}_t^{\mathrm{T}}\mathbf{B}_t = \begin{bmatrix} y_{1,0}[t] & y_{1,1}[t] & \cdots & y_{1,p}[t] \\ y_{2,0}[t] & y_{2,1}[t] & \cdots & y_{2,p}[t] \\ \vdots & \vdots & \ddots & \vdots \\ y_{r,0}[t] & y_{r,1}[t] & \cdots & y_{r,p}[t] \end{bmatrix} \tag{4.25}$$

It should be noted that the elements $y_{i,0}[t]$, upon changing the variable in $z = vt$, represent the estimates of curvature at the i-th location, when the load is applied in z. Conversely, due to the Maxwell-Betti reciprocal work theorem, $y_{i,0}[t]$ can also be interpreted as the structural curvature in z generated by a static load applied at the i-th instrumented location. On the other hand, the terms $y_{i,m}[t]$ with $m = 1, \ldots, p$ are the t-th samples of the m-th modal responses collected at the i-th location.

When moving loads enter and leave the monitored bridge span, a peak in acceleration is typically registered due to the dynamic effect of the load passing on the bridge joint. These peaks can be used in an automated procedure to trigger the calculation of quasi-static and dynamic structural features. The parameters identified in these time intervals can thus be averaged by considering different passing vehicles to improve the robustness of the estimate. In particular, the curvature influence line in position ζl (which is the i-th instrumented location) can be computed as

$$h^{(\zeta)}[z]\Big|_{z=vt} = y_{i,0}[t] \tag{4.26}$$

with $t = 0$ the instant when the load enters the bridge span and $t = l/v$ the instant when the load leaves the bridge span. An average influence line $\bar{h}^{(\zeta)}[z]$ can be computed upon normalization (*e.g.*, to the maximum value in the considered interval) to remove the dependence on the vehicle weight. Considering baseline and inspection estimates of the average influence lines identified in two different time instants, the (spatial) point-by-point difference between them can be employed as a dense feature for damage identification. It should be noted that the spatial resolution of this feature depends only on the sampling frequency of $y_{i,0}[t]$. A schematic workflow of the procedure proposed is illustrated in Figure 4.3: (1) upon collecting the signals and building the filter banks through the MAD, which can be updated at given time intervals, (2) analysis windows are selected as the intervals between the entering and leaving of a vehicle in the bridge span. The acceleration signals are then (3) filtered and (4) normalized to obtain sparse estimates of the modal parameters at the instrumented locations and dense curvature influence lines. Modal parameters, intended as frequencies and amplitudes of $y_{r,p}[t]$, can be easily extracted either in the time (*e.g.*, using the Hilbert transform [269] or non-linear energy operators [226]) or frequency domain (*e.g.*, peak picking). Both dense and sparse identified parameters can then be employed for damage identification.

In the common practice, structural damage is assessed by comparing two states of the monitored system, namely, a baseline (here addressed as "undamaged") condition and an inspection (possibly

damaged) condition. In this study, the structural curvature is used as a DSF. In particular, we assume that an increment in curvature is representative of damage, modeled as a local stiffness loss. This way, the difference in the curvature estimate, obtained either from influence lines or modal parameters, calculated between the inspection and the baseline condition is assumed here as a damage index. Therefore, prominent peaks in the function of the damage index indicate damaged areas.

The magnitude of the difference of curvature (here called "difference function" for simplicity), under certain assumptions, can also be representative of the damage entity. In the following, these assumptions and the method proposed to quantify structural damage using the identified influence lines are described in detail.

As aforementioned, for a simply supported beam, according to the Maxwell-Betti theorem, the influence line calculated in a given location using a moving load has the same profile of the beam deflection shape when it is subjected to a load applied at the instrumented location. In isostatic structures, the bending moment distribution $M[z]$ due to an unknown concentrated load applied at a certain location $z = \zeta l$ does not depend on the structural stiffness

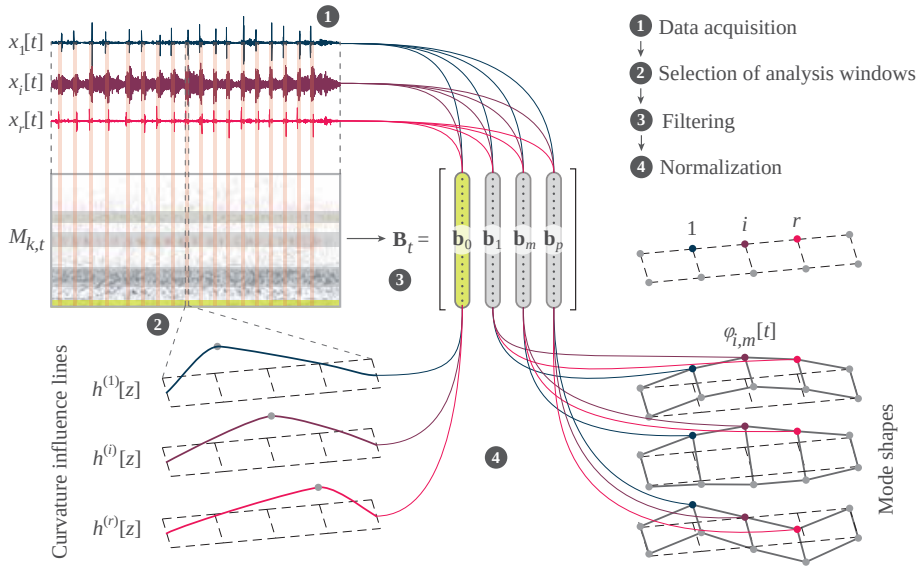

Figure 4.3: Workflow of the procedure proposed for feature extraction

$EI[z]$ and has a triangular shape with a maximum $M_\zeta = M[\zeta l]$. In this case, the difference between the normalized curvatures $\bar{h}_u^{(\zeta)}[z]$ and $\bar{h}_d^{(\zeta)}[z]$ identified in a baseline and inspection time intervals, respectively, can be written as

$$\Delta\chi(z) = \bar{h}_d^{(\zeta)}[z] - \bar{h}_u^{(\zeta)}[z] = \frac{M[z]}{C_d EI_d[z]} - \frac{M[z]}{C_u EI_u[z]} \tag{4.27}$$

where the normalization factors C_u and C_d are

$$C_u = \max\left(\frac{M[z]}{EI_u[z]}\right); \qquad C_d = \max\left(\frac{M[z]}{EI_d[z]}\right) \tag{4.28}$$

Let $EI_u[z] = EI_u$ be constant with z in the undamaged condition and consider the damage as a localized stiffness reduction at the location $\bar{z}$ with the following constraint on the damage entity:

$$EI_d[\bar{z}] \geq \frac{M[\bar{z}]}{M_\zeta} EI_u \tag{4.29}$$

This condition is assumed to have the normalization factors both equal to

$$C_u = C_d = \frac{M_\zeta}{EI_u} \tag{4.30}$$

In this case, Equation (4.27) in the damaged location becomes

$$\Delta\chi[\bar{z}] = \frac{M[\bar{z}]}{M_\zeta}\left(\frac{EI_u}{EI_d[\bar{z}]} - 1\right) \tag{4.31}$$

The local stiffness of the damaged beam can thus be identified as:

$$EI_d[\bar{z}] = \beta[\bar{z}] EI_u \tag{4.32}$$

with

$$\beta[\bar{z}] = \left(\frac{M_\zeta}{M[\bar{z}]}\Delta\chi[\bar{z}] + 1\right)^{-1} \tag{4.33}$$

It should be noted that the ratio $M_\zeta / M[\bar{z}]$ can be easily determined upon localizing the damage (*i.e.*, localizing a peak in the difference function) and does not depend on the load magnitude but only on its position (*i.e.*, the instrumented location). Moreover, due to the assumption of Equation (4.29), a reliable value of β can be

effectively determined only far from the instrumented location. On the other hand, close to the instrumented location, a local maximum in the curvature function still describes the damage location, but its amplitude is not representative of the damage entity.

It should also be observed that, for a given cutoff frequency f_l of the lowpass filter used to identify the influence line, the accuracy of β depends on the speed of the vehicle v and the spatial extension of the damage. Specifically, the frequency of the filtered signal should be high enough to describe the localized irregularity of the curvature properly, *i.e.*, the period of the filtered signal should be at most half the time it takes for the vehicle to overcome the damaged part. In other words, the minimum spatial extension of the damage to properly identify its entity is

$$D_{min} = \frac{v}{2f_l} \tag{4.34}$$

Identification of influence lines of an RC viaduct using sparse sensors

In this section, the data collected by the University of L'Aquila during an experimental campaign conducted between February and June 2019 on the viaducts of the A24 motorway will be used to test the proposed methods. The Italian A24 motorway connects Rome to the Adriatic Sea and has a considerable number of viaducts, given the complex orography of the territory. Many viaducts consist of single-span post-tensioned prestressed beams in a simply-supported isostatic configuration (Figure 4.4). The trapezoidal cross-section, shown in Figure 4.5, is 2.30 m high and has two 3.85 m-wide cantilevered wings. The bridge spans are supported by pairs of piers with a hollow cross-section placed at a center distance of about 40 m.

Ten biaxial FBAs were used to record the deck response to traffic excitation, deployed as shown in Figure 4.5. The accelerometers were organized in two measurement chains, each guided by the main recording unit connected to a Wi-Fi access point and synchronized by GPS. The data was originally sampled at a frequency of 200 Hz, and an anti-aliasing filter with a cutoff frequency of 40 Hz was

(a) (b)

Figure 4.4: Detail of the supports (a) and side view of an A24 viaduct (b) [118]

used. In this thesis, three viaducts are studied, namely, Cerchiara, Temperino, and Biselli. Acceleration time histories of 1500 s collected in the vertical direction and downsampled at 50 Hz are employed for structural identification. In these time intervals, a car with a mass of 1750 kg and wheel axles distant 2.50 m, as shown in Figure 4.5c, excited the bridge by moving back and forth (in this section addressed as Direction 1 and Direction 2) multiple times, at a speed of between 30 km/h and 60 km/h.

The accelerometers S1, S5, S6, and S10 are located near the expansion joints. The recordings of these devices are used to select the signal intervals recorded during the passage of the car, as

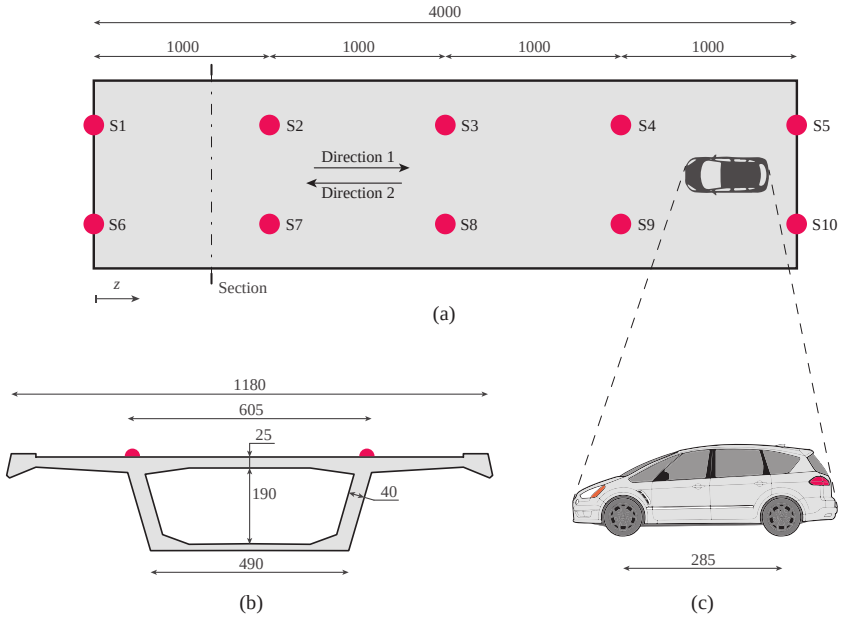

Figure 4.5: Plan (a) and section (b) views of the bridge spans, adapted from [118], and car scheme (c); dimensions in cm

shown in Figure 4.6, where the acceleration signals collected on the Cerchiara viaduct are shown. In particular, considering the speed and the geometry of the car, two close acceleration peaks (*i.e.*, distant in time between 0.2 s–0.4 s, generated by the wheels passing on the expansion joints) are used as a triggering sequence to identify the passing car. Specifically, a triggering sequence in sensor S1 followed by a triggering sequence in S5 within 6 s indicates a car driving in Direction 1. Conversely, a triggering sequence in sensor S5 followed by a triggering sequence in S1 within the same time interval indicates a car driving in Direction 2. In this study, individual moving cars were considered. The identified intervals will be used in the evaluation of quasi-static and dynamic structural features.

In order to build a filter bank capable of extracting the modal responses of the structure, the MAD was applied to the multivariate signal consisting of all the 10 recording channels. The SWPT was used to obtain the preliminary signal decomposition, employing the *fk22* wavelet function. A DBSCAN procedure was then applied to the relevant ODSs, identifying four different vibration modes (for all the three viaducts), represented in Figure 4.7 on a time-frequency plane. In the application of the DBSCAN algorithm, a neighborhood search radius of 0.1 was used, employing the Euclidean distance as a distance metric. In Figure 4.6, the MAD obtained for the Cerchiara viaduct is represented in the time-frequency plane. White regions in Figure 4.7 indicate MAD values close to 0, while the elements that exceed the $1 - \theta$ threshold (here selected as 0.5) are partitioned into four clusters indicated by different colors. A zoom view is reported in the upper-right part of the figure to better show the components

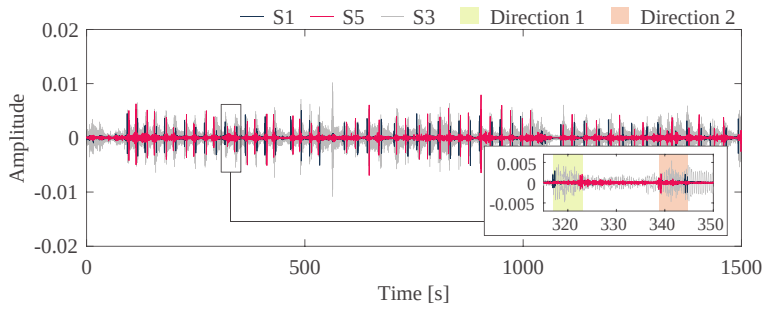

Figure 4.6: Collected acceleration and identification of passing vehicles (Cerchiara viaduct)

related to the higher modes, which are generally more difficult to identify.

The equivalent bandpass filters which can be used to extract the identified modes are calculated as shown in Section 3.4, considering a wireless sensing system. It should be noted that, in this study, the time dependence of the cutoff frequencies is neglected since the structural behavior in the short term does not present varying modal features. In the lower-left part of Figure 4.7, the four frequency bands analyzed to extract the modal contributions are highlighted.

For each time interval identified during the car passage, here addressed as "sample interval" or simply "sample", the modal parameters are estimated by applying the Hilbert transform to the decoupled modal contributions. The mean of the instantaneous frequencies calculated through the Hilbert transform is reported in Figure 4.8 for each sample. It is possible to observe that slight variations may manifest in identified frequencies. The robustness of the identification can be improved by considering average estimates computed over a large set of samples. The average values of modal frequencies are reported in Figure 4.9, together with the average amplitudes of the mode shapes. It should be noted that, due to the comparable geometry of the viaducts, the modal parameters of the different case studies are similar. Moreover, the mode shapes are in good agreement with the estimates obtained through the FDD [259],

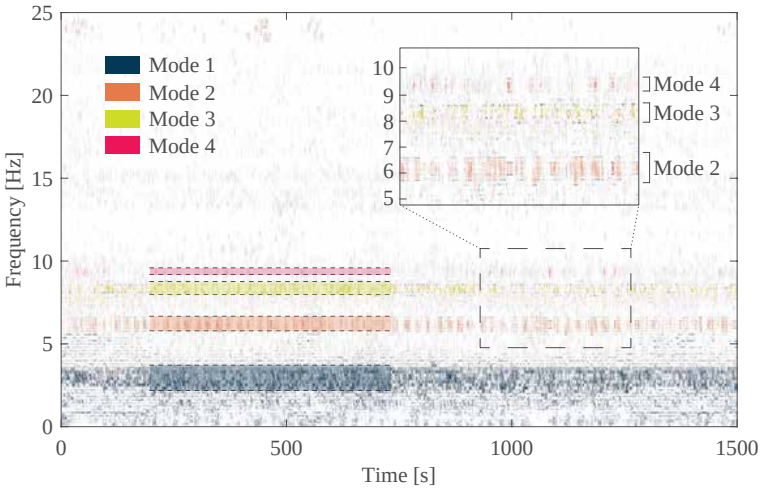

Figure 4.7: Modal assurance distribution and identification of vibration modes (Cerchiara viaduct)

applied in this study to the entire set of signals with a duration of 1500 s.

In this case study, the elements of the lowpass filter $\mathbf{b}_0$ used for the extraction of the quasi-static features was selected considering a clustered filter consisting of the first two wavelet filters, *i.e.*,

$$b_0[\tau] = (d_1 * r_1)[\tau] + (d_2 * r_2)[\tau] \tag{4.35}$$

where $d_k[\tau]$ and $r_k[\tau]$ are the impulse responses of the equivalent decomposition and reconstruction filters, respectively, associated with the k-th outcome of the SWPT.

In Figure 4.10, the lowpass filtered signal $y_{i,0}[t]$ obtained for the Cerchiara viaduct is reported for sensors S2, S3, and S4. The highlighted intervals are the identified samples related to passing cars. In the zoom view, it is possible to observe that the maxima of the filtered signals are consistent with the locations where they are collected. Specifically, the signal related to S2 has a maximum in the left part of the sample interval when the car moves in Direction 1, while the signal collected in S4 has a maximum in the right part of the identified interval. Conversely, the order of the peaks is exchanged in the interval related to Direction 2. Moreover, the signal of sensor S3 has a maximum between the other two in both configurations.

Different estimates of the curvature influence lines are extracted from the sample intervals and the estimates related to Direction 2 are switched before changing the time variable t into the spatial variable $z = vt$. Then, the extracted curves were interpolated to have the same number of points (in this case, 100 points), representing a regular set of equally-spaced locations. In Figure 4.11, all the estimates of the influence line are shown in gray for each case study and sensor

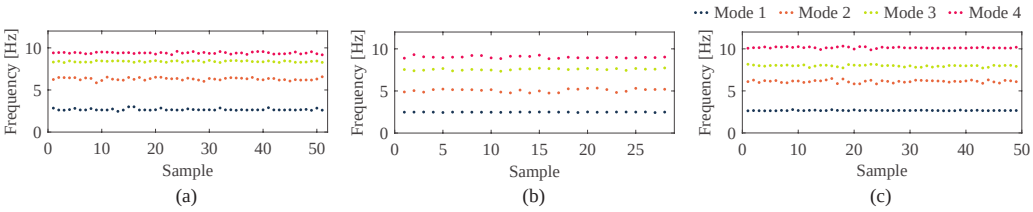

Figure 4.8: Identified natural frequencies for each acceleration sample: Cerchiara (a), Temperino (b), and Biselli (c)

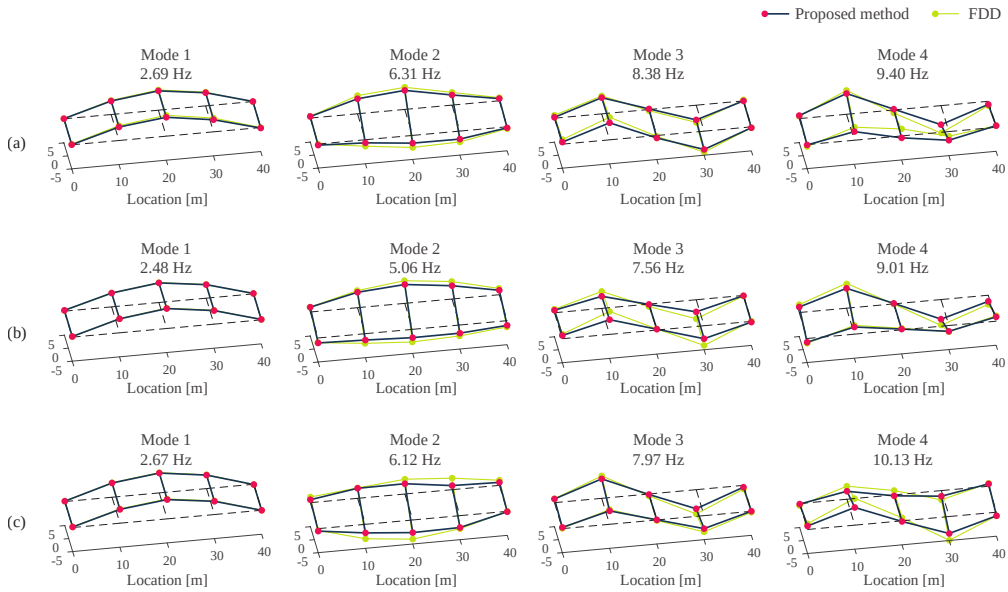

Figure 4.9: Identified average mode shapes: Cerchiara (a), Temperino (b), and Biselli (c)

location. In particular, each gray line represents the mean between the influence lines calculated in a given sample interval by the two sensors at the opposite sides of the deck (indicated in the lower-right corner of each plot). The average of the identified influence lines is also reported in magenta and compared with the curvature of the structural deflection calculated using the flexibility matrix (only at the three instrumented locations) as shown in Equation (3.22), represented in blue. The flexibility-based curvature was evaluated using the set of identified modal parameters, as indicated in Equation (3.21), and the results shown in Figure 4.11 are obtained as the mean of the lines evaluated at the two sides of the deck.

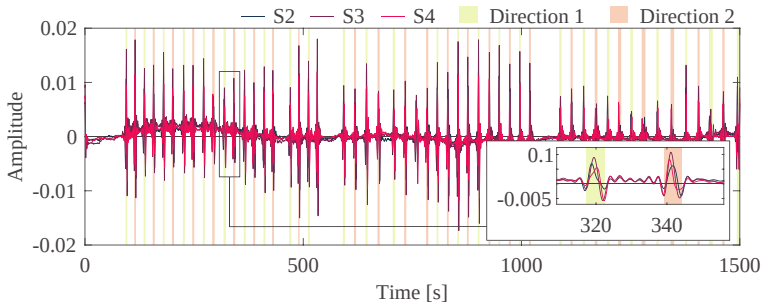

Figure 4.10: Low-frequency filtered acceleration component and identification of influence lines (Cerchiara viaduct)

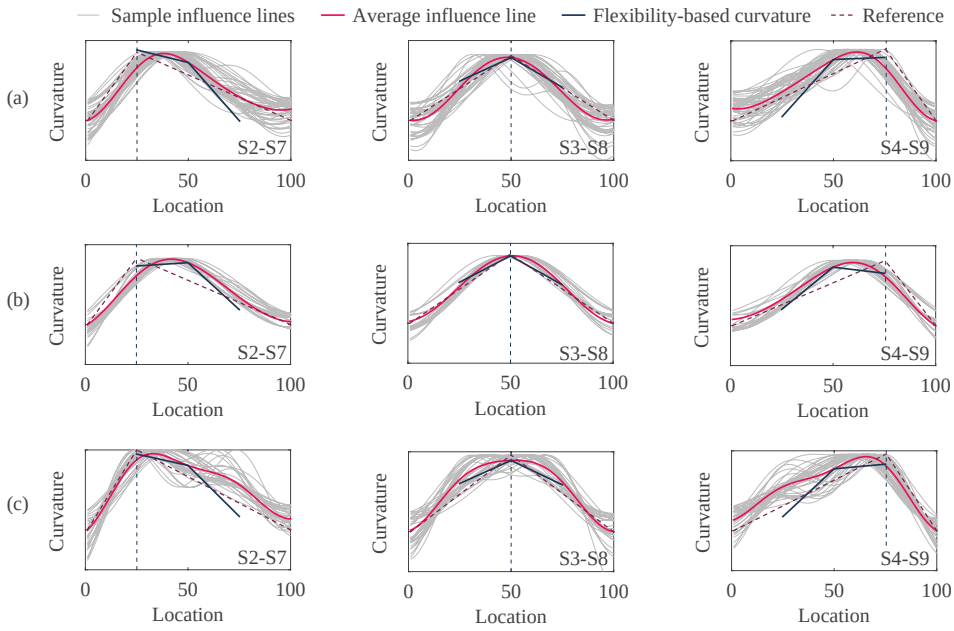

Figure 4.11: Identified curvature influence lines: Cerchiara (a), Temperino (b), and Biselli (c)

In general, the curvature (or bending moment) influence line of a simply-supported beam should have two linear segments, with a maximum in the point where the influence line is evaluated (in this case, the instrumented location, highlighted by a vertical dashed line in Figure 4.11). However, due to the lowpass filter applied to the acceleration time history in the proposed method, the higher frequency components that contribute to sharpening the influence line are dropped. Therefore, the influence line results smoother than the theoretical result. It should also be noted that only three points of curvature can be calculated using the flexibility-based method using the sensor layout of this application due to the limitations of the central difference method. The results obtained through the flexibility-based procedure are slightly different from the theoretical result, but they are in good agreement with the dense feature obtained through the proposed method. Despite the differences between the estimated values and the theoretical shape of the influence line, the results shown can be effectively used to localize structural anomalies in an SHM procedure. This aspect is shown in the numerical case study presented in the next section.

Damage identification of a numerical model using sparse sensors

The second case study analyzed in this chapter is a numerical model of a simply-supported beam with structural characteristics similar to the viaducts analyzed in the previous section. Specifically, the length of the beam is 40 m and the cross-section is modeled as shown in Figure 4.5b, with an overall flexural stiffness $EI = 105.96 \times 10^6$ kNm^2. Modal damping of 5% was assumed for all the vibration modes. Three uniaxial accelerometers were simulated, collecting the acceleration in the vertical direction at the locations indicated in Figure 4.12. A single row of sensors was used in this case study since the beam was modeled as a unidimensional structure.

In order to simulate the application of the damage identification procedure proposed in this chapter, four damage locations were considered, resulting in the seven damage conditions summarized in Table 4.1. Specifically, individual or multiple localized damages (modeling the impacts generated by vehicles underneath the bridge or cracked regions) were simulated in the segments L1, L2, and L3. On the other hand, location D simulated a diffuse stiffness reduction (*e.g.*, due to spalling), and was used to generate three damage conditions of different entity. In this case study, the moving load was modeled as a single force P, passing over the structure (from left to right, as shown in Figure 4.12) with a constant speed.

In a first analysis, the influence lines were determined by processing the clean acceleration signal, sampled at 100 Hz, collected in a single interval representing the passage of a moving load on the beam. Specifically, Figure 4.13 shows the curvature influence lines (normalized to the maximum value) obtained through a lowpass filter consisting of the first two components of a WPT of level 7

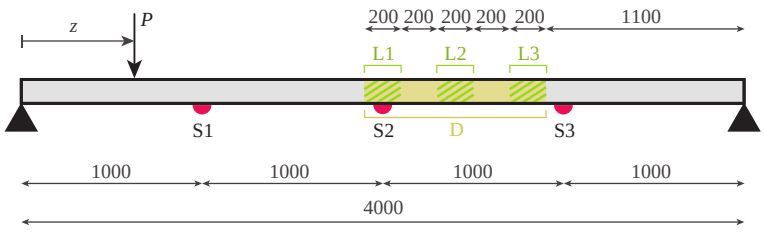

Figure 4.12: Scheme of the numerical benchmark; dimensions in cm

Table 4.1: Description of the damage conditions

Damage condition	Stiffness reduction
DC1	30% in L1
DC2	30% in L2
DC3	30% in L3
DC4	5% in D
DC5	10% in D
DC6	15% in D
DC7	10% in L1 and 30% in L3

(with a resulting cutoff frequency of 0.78 Hz) generated using the *fk8* function. The results obtained for each sensing location (indicated in the lower-right corner of each plot) and damage condition are plotted in solid lines, while the differences between the normalized influence lines calculated in the undamaged and each damaged scenario are reported as dotted lines. In this study, different vehicle speeds were considered. In particular, Figure 4.13a and Figure 4.13b were obtained simulating the passage of a vehicle with a speed of 15 m/s. In this case, the location was discretized in 264 points. On the other hand, Figure 4.13c shows the results obtained using a speed of 3 m/s, and the location was discretized in 1332 points. It should be noted that each result was obtained considering only one sensor.

In the cases of localized damage, clear local maxima of the difference functions (highlighted by a circle) are close to the real damaged areas, independently of the vehicle speed. However, sharper peaks can be identified using the slow vehicle. In this situation, it is also possible to identify the presence of multiple damages (condition DC7). Similarly, high values in the difference function were always identified in the proximity of the diffuse damage, and, in the case of a slow vehicle, the damage index was less affected by dynamic effects, resulting in a more accurate damage localization.

Upon identifying the location of the damaged areas, the stiffness loss can be quantified using Equation (4.33). The results of damage quantification using the values identified by sensor S1 (explicitly written in Figure 4.13) are reported in Figure 4.14 in the form $(1-\beta)\times 100\%$. It should be noted that, according to (4.34), for a vehicle moving at 15 m/s, the smaller damage that can be correctly quantified has an extension D_{min} of 9.6 m (considering the lowpass frequency of

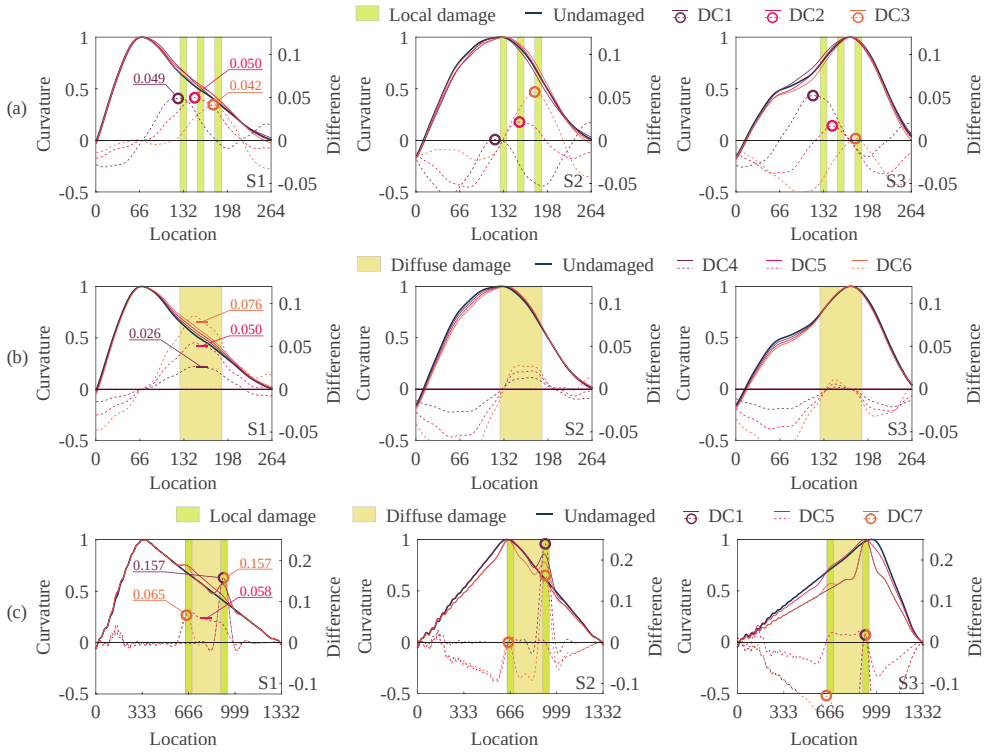

Figure 4.13: Influence lines identified in the numerical benchmark and difference functions for different damage entity and vehicle speed: (a) Local damage, 15 m/s; (b) Diffuse damage, 15 m/s; (c) Mixed damage, 3 m/s

0.78 Hz corresponding to the first two wavelet components). Indeed, the identified values reported in Figure 4.14a underestimated the damage entity since the damaged interval (2 m) was much lower than D_{min}. On the other hand, for the same vehicle speed, the entity values related to the diffuse damage reported in Figure 4.14b are more accurate, especially for low damage levels. Finally, considering the vehicle speed as 3 m/s (for which D_{min} is 1.9 m), the damage entity can be correctly identified also for the localized damage conditions.

While specific inspection vehicles traveling at 3 m/s can be used in a controlled environment (*i.e.*, constant speed and exact path) with high-sensitivity accelerometers, faster vehicles are more representative of ordinary traffic conditions, where noise sources are generally non-negligible. Therefore, in further analysis, the recorded time histories were polluted by introducing a considerable Gaussian

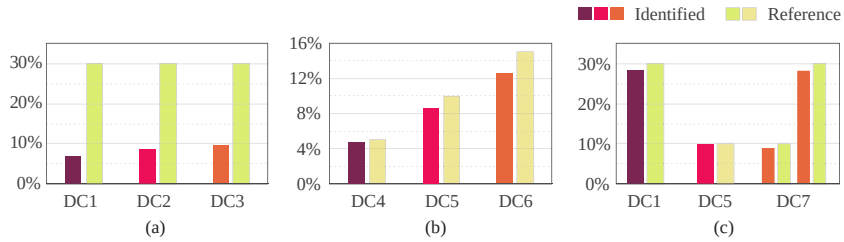

Figure 4.14: Identified damage entity for different vehicle speed: (a) Local damage, 15 m/s; (b) Diffuse damage, 15 m/s; (c) Mixed damage, 3 m/s

white noise component with a standard deviation equal to the 50% of the standard deviation of the collected acceleration. The significant noise level represents different phenomena, including instrumentation noise, slightly non-constant vehicle velocity, and non-straight path. In this case, 100 sample intervals for the undamaged and each damage condition from DC1 to DC6 were considered to calculate an average influence line from the normalized sample estimates, which was then used to compute the damage index (*i.e.*, the difference function). The results of this analysis are reported in Figure 4.15. Specifically, this figure shows the influence line obtained for each sample (thin lines), together with their average curves (thick lines), as well as the difference functions (dotted lines) for each sensor location (S1, S2, and S3) and damage conditions (from DC1 to DC6). In this case, the difference functions are corrupted by noise, and localizing damage becomes challenging. However, by combining the difference functions, *i.e.*, by summing them for each spatial location, the damage localization can be improved, as shown in Figure 4.16.

In a particularly noisy environment, peaks in the difference function can also be generated by dynamic effects. Although modal parameters cannot identify the exact location of damage, they can be employed to identify the damaged regions where the difference function peaks are likely related to actual damage. Figure 4.17 shows the difference function obtained from the average curvature (computed on 100 noisy samples) obtained using the modal flexibility approach. Three structural deflections were calculated considering a load vector $\mathbf{u}$ with the nonzero load element at location S1, S2, and S3, respectively (see the lower-right part of each plot). High values in the difference function were obtained between sensors S2

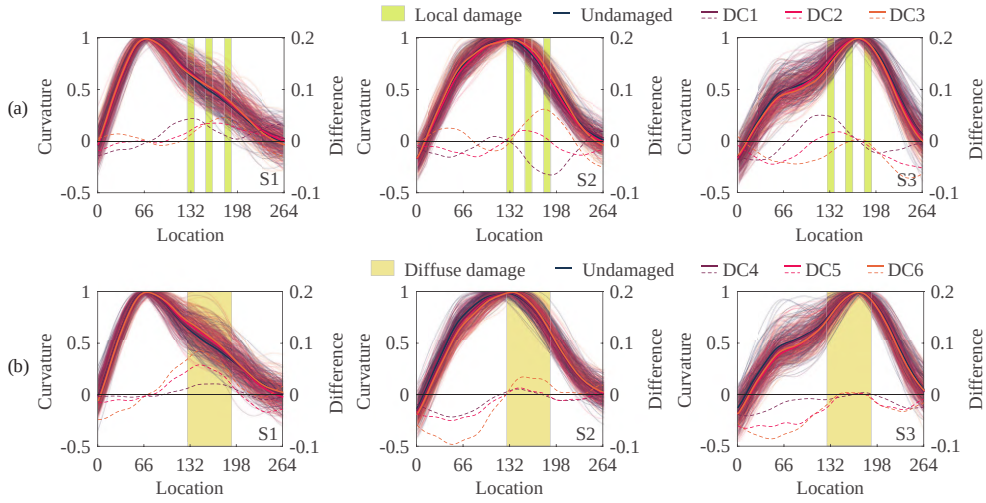

Figure 4.15: Influence lines identified in the simulated noisy environment (solid lines) and corresponding difference functions (dotted lined): (a) Local damage; (b) Diffuse damage

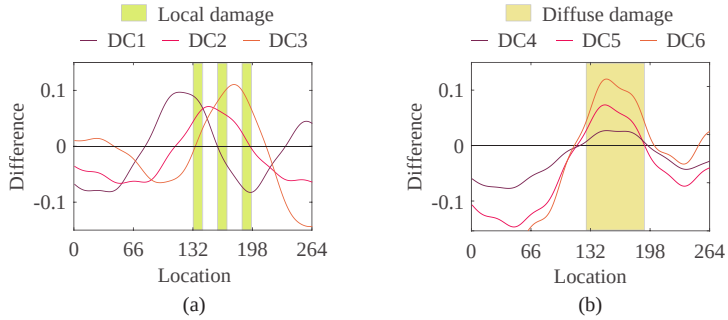

Figure 4.16: Cumulative difference function obtained in the simulated noisy environment: (a) Local damage; (b) Diffuse damage

and S3. Thereby, the local peaks in the difference functions obtained from the influence lines between locations 0 and 66 (Figure 4.16a) are probably generated by dynamic effects and are not related to an actual stiffness loss. The results obtained for damage quantification in the noisy environment using sensor S1 are reported in Figure 4.18. As expected, the local damage conditions were not correctly quantified. Moreover, the diffuse damage conditions show results less accurate than those reported in Figure 4.14. However, Figure 4.18a still shows similar identified values for all the local damage conditions, and Figure 4.18b correctly reports an increasing trend due to the growing damage entity.

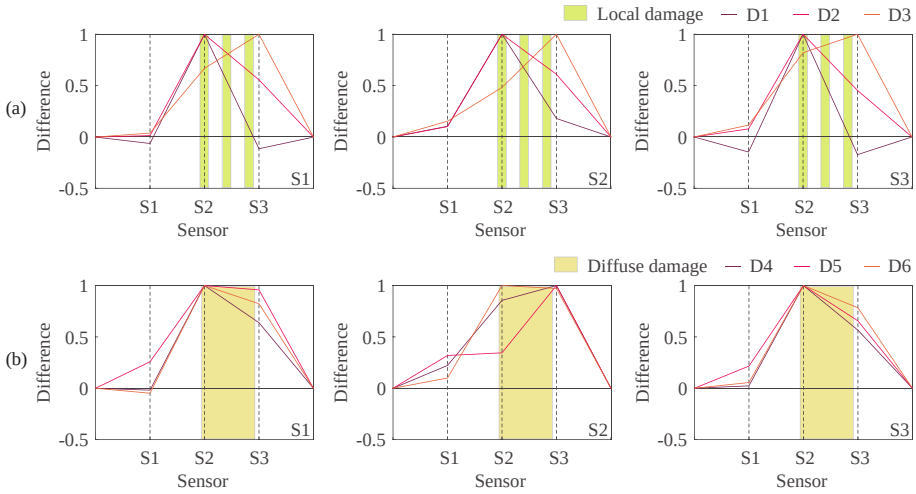

Figure 4.17: Normalized difference function obtained from modal parameters: (a) Local damage; (b) Diffuse damage

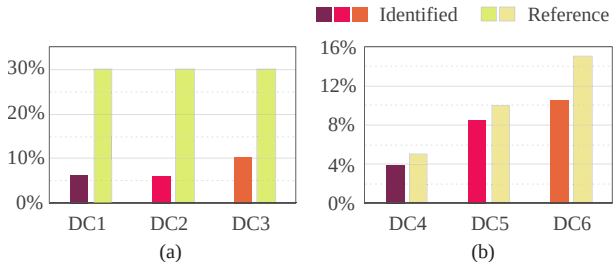

Figure 4.18: Identified damage entity in the noisy environment: (a) Local damage; (b) Diffuse damage

4.3 Crowd participation

In general, using a smart monitoring system involves a migration from the traditional planned maintenance, which may involve unnecessary expenses, to condition-based maintenance, performed when certain indicators show signs of decreasing performance or impending failure. While the common practice in SHM is to periodically measure the structural response (*e.g.*, displacements or accelerations) using dedicated sensors, new crowdsourcing strategies based on smartphone data can be highly convenient, especially for applications at a territorial scale. Smartphones are now essential elements even while driving or walking around cities, as they offer turn-by-turn navigation information, travel times, and route details. Besides, in the context of an SHM strategy, built-in GPS and IMU sensors can provide helpful information on the precise position of the vehicle, its velocity, and vibration data.

An ever-increasing number of social networks and "community-driven" GPS navigation services have shown that a human-centered system can actively contribute to the crowdsourcing of valuable data to improve or provide accurate information on the environment around us [270]. The significant diffusion of smartphones enabled citizens to become the carriers of distributed sensing devices, being themselves the smart sensors of cities and transportation infrastructure.

The sector of shared micromobility (*i.e.*, bike sharing and scooter sharing services) is incredibly expanding in several areas of the world [271]. Combined with the enormous potentialities of smartphones as sensing devices, this phenomenon opens up new avenues for ISHM, especially considering that, in this case, sensing devices are free for the infrastructure owner. This economic saving can be devolved to motivate the users to use shared vehicles and thus provide monitoring data through rewards and discounts. A "gamification" of the monitoring process has already shown particularly effective in this context [272]. Moreover, from a social viewpoint, this strategy would create a human-centered monitoring paradigm to promote the civil sense and raise the awareness and protection of the built inheritance, fostering a sustainable approach for managing the urban

environment based on maintenance.

Regarding the technical aspect, smartphones already have dedicated applications that enable users to unlock and use shared vehicles. Integrating these applications with recording, processing, and transmission tools is straightforward since most health and navigation apps already collect data in full respect of privacy. In the framework of the envisioned application, the mobile app should autonomously interact with a cloud-based backend solution in charge of carrying out the analyses required and provide feedback to involved stakeholders.

The monitoring strategy proposed in this section aims at achieving both the optimization of maintenance operations, resulting in minor management costs and safer roads and infrastructures: the installation of sensors on civil infrastructures that becomes particularly expensive when their number is large in a densely built area, is avoided, also cutting the costs related to their maintenance and management. Moreover, information on the state of health of urban bridges can help to identify anomalies and adopt an "on-demand" maintenance policy, thus resulting in generally safer infrastructures and more effective maintenance procedures. This strategy also promotes the shared micromobility as an alternative and sustainable transport system within cities. In principle, smartphones installed on shared vehicles could be used for various monitoring applications in the built environment, including assessing the health of road bridges, footbridges, and the state of road pavements [169]. This study focuses on identifying dynamic parameters of urban infrastructures (bridges and footbridges) that can be employed to automatically detect structural anomalies that may undermine the functionality of these key elements of the city traffic network. Although the practical development of a mobile application with a cloud-based backend solution is beyond the scope of this work, this section shows the theoretical framework and the experimental results that demonstrate the applicability of the proposed monitoring strategy.

In this section, a procedure to estimate dense (*i.e.*, with high spatial resolution) dynamic structural features from the set of data collected using smartphones is proposed. The procedure processes the data collected by several smartphones, each fixed on a vehicle

moving on the bridge, continuously acquiring data during the passage on the bridge.

Most smartphones in commerce have built-in GPS and IMU sensors, such as MEMS accelerometers, gyroscopes, and magnetometers. Several mobile applications use the data measured by such sensors to provide the users with route indications and other interactive functions. Since strict synchronization of different data types is unnecessary for most traditional applications, the data is typically collected asynchronously. Moreover, GPS measurements are generally less frequent than IMU recordings to optimize the power management of mobile devices.

Considering the time interval delimited by the instants t_0 and t_T when the vehicle enters and leaves the bridge, respectively, assume that a mobile application installed on a smartphone generates a vector $\mathbf{z}_k$ as soon as a measurement is collected (say, at the k-th instant). The vector $\mathbf{z}_k$ can contain information about the acceleration and the angular velocity collected along three orthogonal axes, three magnetic field measurements, and three position logs, including latitude, longitude, and altitude. Since data is generally measured asynchronously, the vector $\mathbf{z}_k$ has a varying size in time. Specifically, $\mathbf{z}_k \in \mathbb{R}^M$, where M is the variable number of measurements.

To analyze smartphone measurements collected on the bridge, the time interval $[t_0, t_T]$, during which the vehicle is physically on the bridge, should be first identified. Most civil infrastructures have statically determined schemes guaranteed by expansion joints that accommodate sliding movements of the restraints. A smartphone deployed on a moving vehicle that crosses a bridge will likely experience vertical acceleration peaks at the vehicle passage through expansion joints. These peak accelerations in the neighborhood of the ends of the bridge (which are easily accessible through built-in GPS sensors) make it possible to identify time instants t_0 and t_T accurately. This procedure exploits a simple yet effective approach to extract precisely the time histories of GPS and IMU recordings corresponding to the bridge crossing. However, if the bridge has no expansion joints, the GPS data can be used to select an approximate interval of the measurement time histories included between two geographical points identified as the bridge ends.

The data measured by each smartphone during its travel on the bridge in the interval $[t_0, t_T]$ (that vary for each vehicle), is stored in a cloud database and processed according to the procedure illustrated on the right-hand side of Figure 4.19. Since smartphones are generally connected to the Internet, this procedure is particularly suitable for crowdsourced cloud computing applications. Specifically, it includes the following operations:

1. Identification of the sensor location: the GPS and all the IMU measurements, except the vertical accelerations, are used to estimate the vehicle (and sensor) location with a high spatial resolution;
2. Identification of the bridge dynamic features: the vertical accelerations are used to retrieve the features (in terms of resonant frequencies and modal amplitudes) of the dynamic response of the bridge;
3. Estimation of the average modal amplitude components: the dynamic features, identified at positions that depend on the specific path of the vehicle, are realigned at the locations identified at point (1); this way, the modal amplitudes identified by different vehicles can be averaged.

Specifically, IMU and GPS data are fused through an extended Kalman filter to obtain the vehicle position along the axis of the bridge. Simultaneously, a bandpass filter is used on the vertical

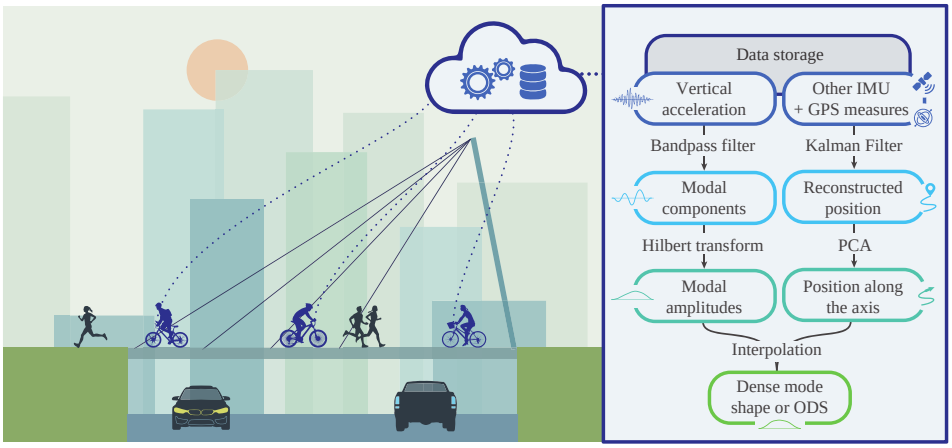

Figure 4.19: Scheme of the proposed crowdsourcing strategy

acceleration data to obtain the instantaneous dominant frequency and the amplitude (here addressed to as "modal amplitude") of the structural response in a user-determined frequency range of interest (RoI). The RoI is determined before the crowdsourcing application commences, based, *e.g.*, on previous monitoring data or an available finite element model of the monitored structure, and its boundaries are selected to include the resonant frequency of a vibration mode of interest. The proposed procedure calculates the amplitudes of the modal or ODSs with high spatial resolution and can provide a more accurate estimate of the dominant resonant frequency within the RoI.

It should be noted that, since the measured datasets (here called "samples") are relevant to different vehicles, both the length of the time histories and the positions where the data are measured change with the speed of the vehicle and its specific path. A realignment procedure of dynamic features is proposed herein to interpolate this data to a user-defined spatial grid along the bridge axis. Thanks to the distributed data collection through crowdsensing, several data samples are available and provide a large set of identified modal amplitudes. The averaging of these estimates can improve their robustness by mitigating the unavoidable noise component contained in each of them. The steps of the proposed method are described in detail in the following subsections.

Identification of the sensor location

The Extended Kalman Filter is a widely used iterative tool for combining uncertain measurements to obtain accurate information about nonlinear dynamic systems [273]. In particular, the nonlinear equations that describe the evolution of the state of the system (state transition model) and its relationship with the measurements (observation or measurement model) are linearized locally by computing their Jacobians. If the measurements collected to update the state of the EFK are acquired asynchronously and with a varying sampling frequency, as it usually happens in smartphones, a continuous-discrete version of the EFK (CD-EKF) can be employed. In this case, the evolution of the state is described as a continuous function (in particular, a stochastic differential equation) and is updated as soon

as a new measurement is collected [274]. In this section, the symbol $\mathbf{x}(t)$ denotes a vector dependent on continuous time, while $\mathbf{x}_k$ is the discrete value of $\mathbf{x}$ at time t_k, *i.e.*, the instant when measurements are taken. It is highlighted that round brackets are herein employed to indicate a continuous function, in contrast with square brackets used in previous chapters, used to indicate discrete sequences. In this section, square brackets are replaced by the subscript notation mentioned above to simplify notations.

The system and measurement models of the CD-EFK assumed in this study are described, respectively, by the following equations:

$$\begin{aligned} \dot{\mathbf{x}}(t) &= g(\mathbf{x}(t)) + \mathbf{w}(t) \\ \mathbf{z}_k &= h\left(\mathbf{x}_k\right) + \mathbf{v}_k \end{aligned} \tag{4.36}$$

where $\mathbf{z}_k$ is the vector containing the discrete measurements; $\mathbf{x}(t)$ and its discrete version $\mathbf{x}_k = \mathbf{x}(t_k)$ are vectors containing the state variables; $\mathbf{w}(t) \sim \mathcal{N}(\mathbf{0}, \mathbf{Q}(t))$ and $\mathbf{v}_k \sim \mathcal{N}\left(\mathbf{0}, \mathbf{R}_k\right)$ are the process and observation noise, respectively, both assumed as zero-mean multivariate Gaussian noise processes with covariance matrices $\mathbf{Q}(t)$ and $\mathbf{R}_k$. The differentiable nonlinear functions $g(\mathbf{x})$ and $h(\mathbf{x})$ are the state transition and the observation function, respectively.

In this study, a 28-element state vector is employed to track the orientation (expressed as the four elements of an orientation quaternion), the velocity, the position, the Magnetic, Angular Rate, Gravity sensor biases, and the geomagnetic vector. Moreover, the initial state $\mathbf{x}(t_0)$ and the noise vectors $\mathbf{w}(t)$ and $\mathbf{v}_k$ at each time t are assumed as mutually independent. Chapter C of this thesis shows the structure of the state vector, the state transition function, and the observation functions.

In the EFK procedure, two steps, namely the prediction and update steps, alternate, with the prediction continuously advancing the state until the next measurement becomes available. From a practical point of view, although the state transition model assumed in the CD-EFK is continuous, prediction steps are carried out at discrete (yet arbitrary distanced) time instants. In this study, a constant frequency f_s equal to the sampling frequency of the vertical acceleration is selected for this purpose. This is meant to estimate the

state parameters at the time instants when the vertical acceleration is measured.

In the update step, the a priori prediction of the current state is combined with the measurement collected at time t_k to refine its estimate. It should be noted that, while $g(\mathbf{x})$ has a fixed size, depending on the structure of $\mathbf{x}$, the observation function $h(\mathbf{x})$ has a size that depends on the variable structure of $\mathbf{z}_k$. In Appendix A, the different structures for the function $mathbf h(x)$ are reported for each possible measurement. Also, more details on the EFK implementation for the application described in this section are provided in Chapter C.

Upon calculating the estimated state vector in the interval $[t_0, t_T]$ with a sampling frequency f_s, here indicated as $\hat{\mathbf{x}}$, the estimated position information $\hat{\mathbf{y}}$ contained in $\hat{\mathbf{x}}$ is organized in a reconstructed position matrix $\mathbf{Y} = [\hat{\mathbf{y}}_0, \dots, \hat{\mathbf{x}}_T]^T \in \mathbb{R}^{N\times 3}$ where N indicates the number of instants in the interval between t_0 and t_T. In particular, the vector $\hat{\mathbf{y}}$ consists of the position of the smartphone obtained by converting into local coordinates the position in geodetic coordinates (*i.e.*, latitude, longitude, and altitude) contained in the state vector. Specifically, the geodetic coordinates are the elements from 14-th to 16-th of the state vector reported in Chapter C. The origin of the local coordinates system (defined in north-east-down format) is assumed at the midspan of the bridge.

For the purposes of the presented algorithm, it is convenient to express the location information along the bridge axis. If the structure analyzed has a straight axis, the position data can be efficiently projected onto it by extracting the first principal component from the dataset $\mathbf{Y}$. Specifically, let the SVD of $\mathbf{Y}$ be

$$\mathbf{U}\mathbf{\Sigma}\mathbf{V}^T = \mathbf{Y} \tag{4.37}$$

where $\mathbf{U} \in \mathbb{R}^{N\times N}$ and $\mathbf{V} \in \mathbb{R}^{3\times 3}$ are the matrices containing the left singular vectors and right singular vectors of $\mathbf{Y}$, while $\mathbf{\Sigma} \in \mathbb{R}^{N\times 3}$ is the diagonal matrix of singular values. It should be noted that, since $\mathbf{Y}$ is formed of three column vectors representing the position in the local coordinate system, the projection of the three-dimensional position data onto the principal direction, that is, the direction in

which the position data explains the higher variance (*i.e.*, the axis of the bridge), can be calculated as

$$\mathbf{y} = \mathbf{U\Sigma s} \tag{4.38}$$

where the vector $\mathbf{s} = [1, 0, 0]^T$ simply extracts the first principal component (*i.e.*, the first column vector) from the matrix $\mathbf{U\Sigma}$. This way, the vector $\mathbf{y} = [y_0, \ldots, y_T]^T$ contains the dense estimates of the position of the sensor for the entire time interval when the vehicle crosses the bridge.

Identification of bridge dynamic features

This section describes the identification of the dynamic structural parameters (*i.e.*, natural frequencies and modal amplitudes) from the vertical acceleration recorded by a single smartphone.

Let the structural response collected on the moving vehicle in terms of vertical acceleration $\ddot{u}$ be

$$\ddot{u}(y,t) = \sum_{i=1}^{\infty} \phi_i(y)\ddot{q}_i(t) \tag{4.39}$$

where $\phi_i(y)$ is a component of the i-th mode shape function at location y and $\ddot{q}_i(t)$ is the double derivative of the i-th modal contribution to the structural displacement.

Let $b_p(\tau)$ be the impulse response of a bandpass filter having low and high cutoff frequencies equal to $f_l = f_p - \epsilon$ and $f_h = f_p + \epsilon$, respectively, where f_p is the central frequency of the selected interval (*i.e.*, the frequency RoI) and ϵ is a small number. Consider a slow vehicle (compared to the oscillating velocity of the structure) and well-distanced vibration modes. If f_p coincides with the p-th resonant frequency of the structure, applying the filter $b_p(\tau)$ to the acceleration response, the modal contributions with $i \neq p$ are canceled, as shown in the previous chapter, and a narrow-band signal, with frequency content close to the p-th mode is obtained:

$$\left(\ddot{u} * b_p\right)(y,t) = \sum_{i=1}^{\infty} \phi_i(y) \left(\ddot{q}_i * b_p\right)(t) \cong \phi_p(y)\ddot{q}_p(t) \tag{4.40}$$

The amplitude $a_p(y,t)$ of the structural response can be calculated as the absolute value of the analytic signal obtained from Equation (4.40) using the Hilbert transform [275]. Assuming the excitation of the bridge as a stationary and uncorrelated white noise process, different vehicles crossing the bridge at different times are all subject to different vibration amplitudes at a given location y_k (and corresponding time t_k). While the term $\phi_p(y_k)$ is the same in all the cases, the input excitation and, consequently, $\ddot{q}_p(t_k)$ varies randomly. Therefore, averaging the amplitude of the filtered signals extracted from different samples (measured by different vehicles passing on the bridge), it is possible to obtain the p-th mode shape $\phi_p(y)$, except for a normalization factor. It is observed that the location of the vehicle is a function of its velocity and time. Then, to correctly average the modal amplitudes, the measurements of different vehicles must be defined at the points of a unique spatial grid. It is also noted that the Hilbert transform provides the absolute value of the instantaneous amplitude. Thereby, the absolute values of the mode shapes are identified in this procedure.

If the central frequency f_p of the filter is not coincident with a resonant frequency of the structure or closely spaced modal contributions are included in the RoI $[f_l, f_h]$, $\phi_p(y)$ represents the average of the ODSs included in $[f_l, f_h]$. Nevertheless, in the proximity of one or more resonant frequency peaks, the ODS can also be used as a damage-sensitive feature for SHM purposes [262, 276].

The proposed method provides a more accurate estimate of the dominant frequency within the RoI through a simple peak-picking procedure on the frequency spectrum of the vertical acceleration data, carried out, *e.g.*, considering the maximum spectral amplitude within the RoI. An instantaneous estimate of the resonant frequency within the RoI can also be identified from the filtered acceleration data using the Hilbert transform [275]. The time-dependent frequency obtained in this way can be averaged over time to obtain a single value of the dominant resonant frequency. If the structure is formed by independent spans, this procedure can be applied separately to each of them, extracting the frequency values from signals recorded on spatial subdomains corresponding to the different structural elements. The cutoff frequencies of the bandpass filter $b_p(\tau)$ - *i.e.*, the

boundaries of the RoI - should enclose a range of frequencies large enough to accommodate the variation of the resonant frequency due, for example, to varying environmental conditions. Indeed, the proposed method is able to operate with frequency shift within the frequency RoI. Nevertheless, higher frequency variations would be identified by the disappearance of the peak.

Multiple RoIs can be employed to identify different modes. However, the structure should be sufficiently excited in all the frequency RoIs to allow a reliable identification using the relatively low-performance sensors embedded into smartphones.

Identification of the average modal amplitude components

In general, different vehicle speeds and changes of speed of a given vehicle lead to a variable spatial resolution of the identified modal amplitudes between different samples and to a non-uniform spatial resolution for the same sample. This hampers their direct averaging. In order to compute the amplitudes $a_p(y,t)$ at the same points of a fixed spatial grid that is unique for all the vehicles, a linear interpolation of the shapes is carried out at equally spaced locations along the longitudinal axis of the bridge.

Let $\mathbf{a}_p = [a_p(y_0,t_0),\ldots,a_p(y_T,t_T)]$ be a set of acceleration amplitudes measured by a moving vehicle at the instants t_k in the interval $[t_0,t_T]$ with a constant sampling frequency f_s, where y_0 and y_T are the start and end locations of the measurement. Moreover, consider the vector $\mathbf{y} = [y_0,\ldots,y_T]^T$ of sensor location identified in the same interval. Each couple of elements $(y_k, a_p(y_k,t_k))$ relates a physical location on the bridge y_k with the amplitude value a_p measured at that location at a time t_k. These couples are used to interpolate the data collected during the recording interval $[t_0,t_T]$, at equally spaced physical locations $\bar{y}_k$ chosen within the spatial interval $[y_0,y_T]$.

This procedure allows estimating the amplitudes $a_p^s(\bar{y}_k)$ for each sample $s = 1,\ldots,S$, that is, for each measurement collected by a smartphone, at the same points $\bar{y}_k$ and to obtain the average values

of the shapes at locations $\bar{y}_k$:

$$\left|\phi_p\left(\bar{y}_k\right)\right| C \cong \frac{1}{S}\sum_{s=1}^{S} a_p^s\left(\bar{y}_k\right) \tag{4.41}$$

where C is a scale factor constant over y. It should be noted that the accuracy of the estimate increases with S; thereby, the crowdsourcing nature of the proposed approach acquires fundamental importance. Local variations of such average amplitudes can be used to identify anomalies in the modal profile (*e.g.*, damage due to local stiffness reduction) through one of the several methods proposed in the literature based on mode shapes or ODSs [3, 276, 277].

Modal identification of a footbridge using crowdsensing

The methodology presented to obtain the main dynamic features of a bridge using crowdsourced data is applied in this section to a real case study to demonstrate its feasibility. Specifically, a smartphone fixed on a common city bicycle crossing a lively footbridge is used to collect multiple data types in different data acquisition scenarios that can occur in practice. A single bicycle model was employed during the tests to simulate the use of a standard shared vehicle, which is the same for all the users. The dynamic response of this type of structure under operational loads is generally high enough to overcome the high noise floor of standard smartphone sensors. Crowdsourcing data is obtained by repeating the analysis several times. The results of the analysis (modal amplitudes and the first natural frequency) are compared to those obtained by other researchers during a vibration test using a traditional technique

The investigated case study is a footbridge for both pedestrians and cyclists, which crosses the A13 motorway between Bologna-Padova (Italy) in the proximity of the entrance to the Bologna ring road (see Figure 4.20). Detailed information on this structure can be found in [278].

The overall free span of the footbridge is about 90 m (Figure 4.21a). The primary structural system is a three-hinged tied arch

Figure 4.20: A13 footbridge: aerial view

formed by two A-shaped steel frames contrasting at the center of the footbridge (Figure 4.21b). The arch rise is 20 m at midspan, and the minimum distance between the deck and the motorway level is 6 m. The width of the deck varies between 10 m at the two ends and 2.5 m at the midspan. The A-shaped frames present a tubular cross-section with variable dimensions obtained by welding different S355 steel plate elements. The bridge deck balances the horizontal thrust generated by the arch. A fan-shaped cable-stayed system converging to the center of the arch supports the deck (Figure 4.21c). A system of stabilizing ropes contributes to enhancing the structural behavior for gravitational loads and wind-related effects along the deck. The deck is supported at its ends by two reinforced concrete abutments. As for the external anchoring system, the four supports of the A-shaped steel frames prevent vertical displacements and rotations along the longitudinal axis of the deck. Moreover, two transversal restrains located on the abutments along the longitudinal axis of the footbridge prevent the transversal displacements. Four visco-elastic damper actuators (Domain-Jarret type), which only allow slow displacements, control the structural displacements in the longitudinal direction due to thermal action, and prevent large displacements due, for instance, to earthquakes or wind. Drilled piles make the foundation system. The road surface of the footbridge is made of a plastic material (Figure 3b) and therefore is relatively smooth

In the past, vibration tests were carried out on the footbridge to estimate the main mode shapes and frequencies. The results are

Figure 4.21: A13 footbridge: (a) Lateral view (Northside), (b) A-shaped frame and detail of the deck pavement, (c) Cable-stayed system

presented in [279] and reported in Figure 4.22. Two closely spaced bending modes were identified: the first presents a symmetrical mode shape, whereas the second shows an anti-symmetric mode shape.

Experimental tests were performed using a common city bicycle (Figure 4.23a), a smartphone, and support (Figure 4.23b) to fix the device to the vehicle (Figure 4.23c). During the tests, the pressure in the inner tube of the bicycle wheels was about 203 kPa (2 atm). The temperature measured at the test location was between 15 °C

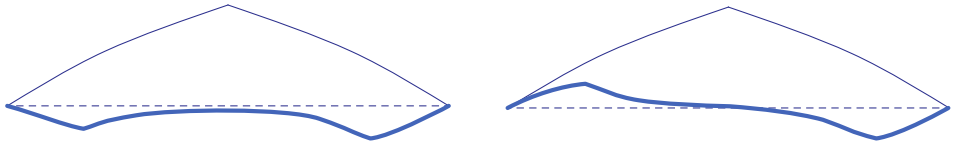

Mode 1: f = 2.523 Hz **Mode 2:** f = 2.562 Hz

Figure 4.22: A13 footbridge: Results of the dynamic tests (adapted from [279])

Figure 4.23: Instrumented bicycle: (a) Side view, (b) Smartphone support, (c) Detail of the smartphone position

and 21 °C. However, further tests conducted with −2 °C have shown that the environmental effects did not perceptibly affect resonant frequencies of the bridge. The following measurements were acquired and used in this study: triaxial acceleration, triaxial angular velocity, triaxial magnetic field, position in terms of latitude, longitude, altitude, together with the horizontal GPS accuracy, employed to determine the variance of the GPS measurements. A time stamp in the reference time of the mobile device is collected along with each measured quantity and employed in the KF to perform data fusion. A "calibration" sample, measured by the smartphone mounted on the bicycle standing, not in movement, was used to compute the error variances of the other measurement. The relevant values are reported in Table 4.2. The sampling frequency is 100 Hz for IMU data and 1 Hz for GPS data. The smartphone used during the tests is an iPhone SE (second generation, 2020) connected to the Internet. It includes a 16-bit 6-axis Bosch Sensortec IMU module with a typical accelerometer sensitivity of 16 384 LSB/g at a recording range of ±2 g [280]. The results reported in the section were obtained using measurements recorded by a single phone. In a preliminary phase of the investigation test, different smartphones were used to assess the correct functioning of the GPS and IMU modules.

The measurements were acquired using the MATLAB Mobile app, which allows recording data from the different sensors of the smartphone and transmitting them directly to the MathWorks Cloud. This way, the data is directly transmitted to a personal computer, where the algorithm operates.

Four types of tests were carried out. Each test aims at simulating a distinct cyclist's behavior and, in turn, a data acquisition scenario that could occur in practical applications. The tests differ in terms of smartphone location, bicycle use, and recording length. Precisely:

- Test type 1: 36 data samples (18 in each direction) were collected riding back and forth the bicycle across the footbridge with the smartphone fixed to the top tube, as shown in Figure 4.23c. The duration of each sample ranges between 45 s and 70 s (depending on the user's velocity). This test type simulates the typical situation in which a cyclist crosses the footbridge.
- Test type 2: 4 data samples (2 in each direction) were collected walking the bicycle back and forth across the footbridge with the smartphone fixed to the top tube, as shown in Figure 4.23c. The approximate duration of each sample is 100 s. This test type simulates the behavior of a cyclist who crosses the bridge walking instead of riding (for instance, due to the difficulty of overcoming the deck slope by riding the bicycle).
- Test type 3: 1 data sample collected while the bicycle was standing on the footbridge with the smartphone fixed to the top tube, as shown in Figure 4.23c. The recording time is 300 s. This test type simulates the behavior of a cyclist who stops on the footbridge (for instance, to start a conversation with somebody) while recording data.
- Test type 4: 1 reference data sample with the smartphone placed directly on the bridge (at 1/4 of the bridge span from the eastern support). The recording time is 300 s.

Measurement	Variance
Acceleration	$0.01\,\mathrm{m}^2/\mathrm{s}^4$
Angular velocity	$0.001\,\mathrm{rad}^2/\mathrm{s}^2$
Magnetic field	$50\,\mu\mathrm{T}^2$
Position (average)	$25\,\mathrm{m}^2$

Table 4.2: Reading error variance

Table 4.3: Reading error variance

Test type	Smartphone location	Movement	Recording lenght	Number of samples
1	Bicycle	Riding	45-70 s	36
2	Bicycle	Walking	90-110 s	4
3	Bicycle	Standing	300 s	1
4	Footbridge	No movement	300 s	1

The main characteristics of the different tests are reported in Table 4.3. During all the tests, the bridge was quite lively: all tests were carried out in operational conditions, with at least one pedestrian or a runner crossing the bridge. Vibration generated by moving people and vehicular traffic in the motorway underneath the footbridge contributed to exciting the structure during the tests.

It is highlighted that this proof-of-concept study is conducted under the following assumptions:

- All the recording samples are collected throughout the bridge without interrupting, stopping, and/or going back. Although the KF allows realigning the data to the physical location where it was collected, more complex actions, such as stopping and returning, may increase the noise level in the recorded dataset. However, in a long-term crowdsourced application, the effects of these types of anomalies would be mitigated. Also, some rules (in terms of time to cross the bridge and/or speed variability) could be included to discard particular recordings.
- The bridge is lively and constantly excited by pedestrians, traffic underneath, and/or wind. As in the previous case, some rules could select only the samples where the recorded vibration in the RoI exceeds a given threshold.
- One single vehicle and one single user are involved in the experimental campaign. Although different bicycles and body properties can potentially vary the identified parameters, in the case of shared vehicles, they are likely to have almost uniform properties.
- No vehicle-bridge interaction or roughness effects are considered.

Moreover, it is assumed that the shift in resonant frequencies due to environmental variation and early damage are always included

within the selected RoI. For urban bridges, a polymeric or wooden pavement is much less sensitive to temperature variations compared to asphalt, which is one of the the most well-known sources of variation in modal parameters for regular bridges [281]. Nevertheless, in general, environmental variations affect natural frequencies less than 10% for these types of structures [68]. Thereby, a sufficiently wide RoI (*i.e.*, the natural frequency estimated in a previous identification process ±10-20%) should be sufficient to avoid issues related to the frequency shifts that the structure could undergo during the monitoring process.

The time series of the vertical accelerations recorded during all the tests are used to retrieve the main modal parameters of the structure. The identification of the modal amplitudes is carried out using multiple sensor data (*i.e.*, acceleration, angular velocity, magnetic field, and position) recorded according to the test type 1 and processed using the procedure described in Section 4.1.

Figure 4.24a displays the power spectra of the 42 vertical acceleration time series collected during all the tests described in Table 4.3. Test type 4 is not affected by human action (riding or walking), bicycle dynamics (vehicle-bridge interaction), or road roughness and is used as a reference recording. As shown in the figure, riding and walking test types have a higher level of noise with respect to the other tests due to the moving vehicle and the user action. However, an accurate estimate of the resonant frequency can be calculated for all the test types by extracting the maxima of the frequency spectra of vertical acceleration in an RoI between 2.2 Hz and 2.8 Hz (selected as 2.5 ± 0.3 Hz, based on the reference frequencies identified in a previous study [279] and reported in Figure 4.22). The frequencies identified in this study are reported in Figure 4.24b as orange circles. All the frequencies identified using measurements of both the moving and the static sensors are in agreement with the reference values. This shows that the human biomechanics and the pavement roughness do not significantly affect the identification results in this application. In fact, the pavement of pedestrian bridges is typically smooth, and the speed of bicycles is generally low, thus reducing the effects of the road surface profile on the recorded response [130, 152]. As already mentioned, the dynamic parameters identified by the

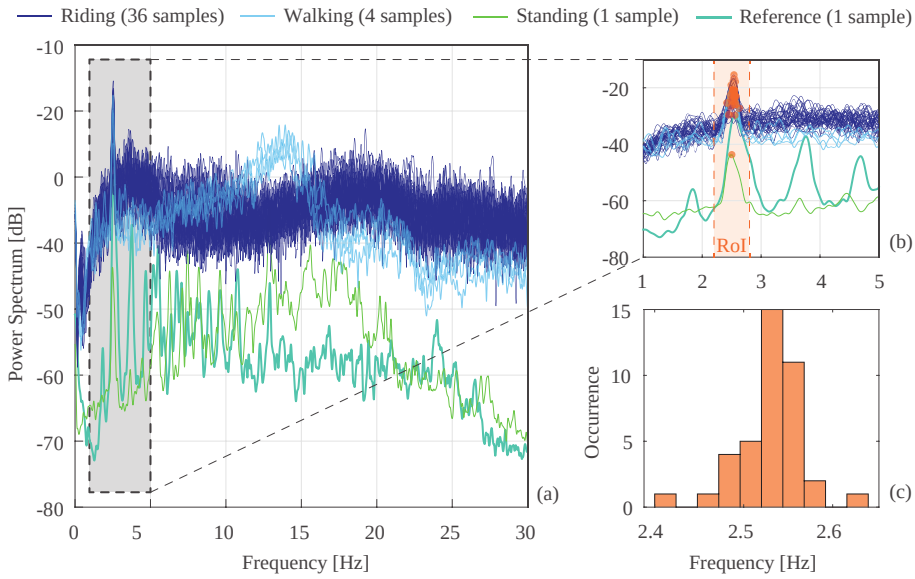

Figure 4.24: Power spectra relevant to different test types (a), identified frequency values (orange circles) in a zoom view (b), and statistical distribution of the identified results (c)

procedure proposed in this section are average values over a given frequency range. Thereby closely spaced modes, in general, cannot be distinguished. Figure 4.24c shows the statistical distribution of the resonant frequencies identified using test types 1 and 2. The mean of this distribution is 2.533 Hz, and its standard deviation is 0.035 Hz.

The vertical acceleration data of test type 1 is also employed to identify modal amplitudes. As mentioned in the previous section, closely spaced modes cannot be distinguished by the proposed procedure and the shape identified in each frequency range is a combination of the ODSs in that range. Further to this the proposed procedure allows identifying the absolute values of the operational shapes amplitudes but not their signs; thereby, a symmetric and anti-symmetric mode, such as those in Figure 4.22, cannot be distinguished. However, it must be noted that the final goal of the procedure proposed herein is to use the information extracted from the measurements to identify the onset of possible damage. Local damage affects all the operational and mode shapes at the damage location, except those with a node at that location. This means that the shape identified using the procedure proposed herein, which is

a combination of ODSs, is affected by damage and can be used for its identification. In the case of the considered bridge, the similarity of the two mode shapes (Figure 4.22) makes the procedure more robust since their absolute values are very close, almost coincident. Thereby, the effect of possible damage will be reflected in both of them.

In this study, the amplitude information corresponding to the first two modes of the bridge is extracted by filtering the acceleration time history through a narrow bandpass filter with lower and upper cutoff frequencies equal to 2.2 Hz and 2.8 Hz, respectively. The amplitude is then extracted through the Hilbert transform and converted from time to space domain. To this aim, the CD-EFK illustrated in Section 4.3 is employed to estimate, with a high spatial resolution, the path of the moving bicycle. The path is sampled at 100 Hz, as the vertical acceleration measurements. In the initialization step, the initial quaternion orientation, position, and magnetic field values of the state vector are set to the values obtained from a reference direction, while other quantities are set to 0. The reference direction was calculated a priori, simply connecting the two ends of the bridge. This way, assuming that the bicycle is aligned with the bridge axis when it enters and leaves the structure, the EFK converges rapidly due to fewer uncertainties on the initial parameters. Moreover, since the magnetic field recording was very noisy, the initial values of additive noise were set relatively high. However, in practical applications, the data collection would start a while before entering the bridge. Therefore, there would be enough time for the initial parameters and corresponding noise values to be well-calibrated. Table 4.4 shows the additive noise values used in this application for each state element. The initial state covariance was assumed as a diagonal matrix with nonzero elements equal to 10^{-3}.

The initial and final instants of the measurements used in this procedure were selected by observing the vertical acceleration time history. Figure 4.25 shows that prominent peaks occur when passing over the expansion joints at the ends of the bridge. However, the entry peak also affects the collected data since a transient vibration component due to the bicycle dynamics is generated. This component generally vanishes within about 3 s in this case study.

Table 4.4: Reading error variance

State element	Noise variance
Quaternion	1×10^{-1}
Acceleration	$5 \times 10^{-3}\ \mathrm{m^2/s^4}$
Angular velocity	$3 \times 10^{-6}\ \mathrm{rad^2/s^2}$
Magnetic field	$1 \times 10^{-1}\ \mu\mathrm{T}^2$
Position	$1 \times 10^{-6}\ \mathrm{m^2}$
Accelerometer bias	$3 \times 10^{-1}\ \mathrm{m^2/s^4}$
Gyroscope bias	$3 \times 10^{-3}\ \mathrm{rad^2/s^2}$
Magnetometer bias	$20\ \mu\mathrm{T}^2$

Figure 4.26 shows the densely reconstructed positions (namely, "sample paths") obtained through the EFK. In this figure, the reference line represents the longitudinal axis of the bridge, and the time-varying instantaneous vehicle speed is represented using the colormap reported on the right-hand side. It is possible to observe a spatial scattering due to inaccuracies of the reconstruction, especially in the central part, where the footbridge becomes narrower. Moreover, due to the less frequent sampling of GPS location, some paths have small jumps in their shape. It should be noted that these jumps are mainly in the direction orthogonal to the reference line. Therefore, they slightly affect the principal paths along the longitudinal bridge axis obtained through PCA.

The main steps of the procedure proposed in this study for reconstructing the ODS associated with the selected frequency RoI are shown in Figure 4.27. First, the vertical acceleration data (Figure 4.27a) is filtered (Figure 4.27b), and its amplitude is calculated as the absolute value of the related analytic signal (Figure 4.27c). Then, interpolating the modal amplitudes of each sample along with the related principal paths projected on the bridge axis leads to a time-to-space conversion (Figure 4.27d), as explained in Section 4.3. All the irregularities of the reconstructed profile are due to recording

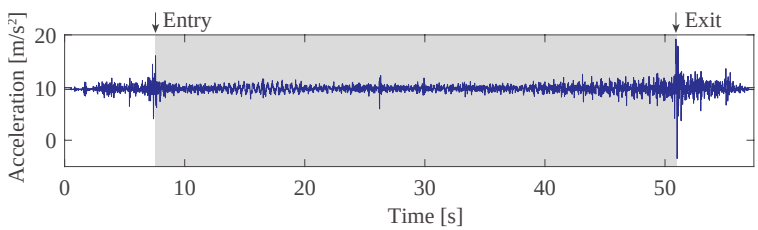

Figure 4.25: Selection of the interval of interest based on vertical acceleration peaks

noise, as well as to the disturbance generated by the operational conditions (*i.e.*, runners' excitation), cyclist movements, and road surface variability. However, as demonstrated by Champoux et al. [282], the resonant frequencies of an average bicycle are mostly over 20 Hz and thus very different from those of typical bridges. Therefore, the vehicle characteristics are effectively removed from the recorded response by means of the filtering procedure [146].

Walking typically generates a narrow-band excitation that varies with walking/running speed [167]. If pedestrian force excites the structure in the frequency RoI, the structure is likely to resonate, thus producing a high vibration response that is beneficial to structural identification. In crowdsourcing applications, pedestrians are likely to walk at variable speeds, and walking excitation is generally mixed with other sources, such as traffic and wind. The availability of large sets of modal parameters, identified from crowdsourced responses, enables averaging out the effect of the variability in the source of vibration and obtaining an accurate estimate of the modal parameters.

The sample shape reported in Figure 4.27c-d shows the dynamic effect on the collected acceleration measurement due to the first expansion joint. It is possible to observe that in the left part of the figure, between 0 sand 2.5 s (Figure 4.27c), a steeply decreasing acceleration amplitude is recorded due to the free vibration response of the bicycle system following the impulsive excitation generated while overcoming the joint.

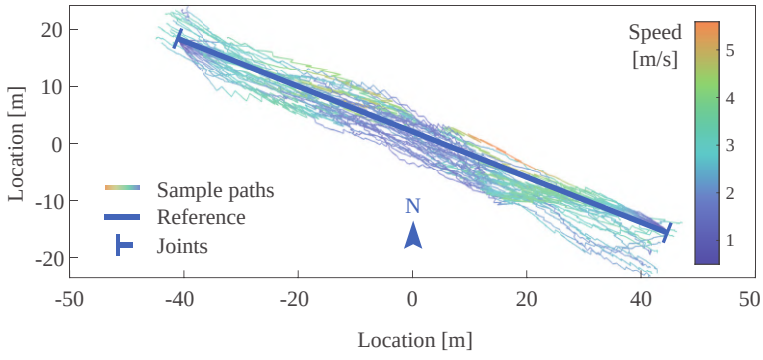

Figure 4.26: Reference and estimated crossing path

All the sample shape amplitudes are finally superimposed, as shown in Figure 4.28, and the average can be calculated at a user-selected spatial grid through interpolation. In this study, 100 equally spaced amplitude values projected on the bridge longitudinal axis were computed, as reported in Figure 4.28 in dark blue. This result represents the average ODS computed in the frequency RoI obtained from the 36 samples of test 1. Therefore, it represents the absolute values of the modal shape amplitudes of the first two closely spaced modes. The identified profile is in good accordance with the reference first mode shape, especially for the central part, as represented in Figure 4.28. It is indeed possible to notice a slight asymmetry in the shape that presents higher amplitudes on the left-hand side. The terminal portions of the identified profile (*i.e.*, below –45 m and over +45 m) are not reported in the figure since they are affected by the free vibration of the bicycle generated by the passage on the expansion joints. As noted by Siringoringo and Fujino, vehicle bounce and pitch motions could hide the bridge response [150]; thereby, it is generally recommended to discard the signal collected close to expansion joints. It should be noted that since bicycles are generally slower than regular vehicles, these intervals are relatively short and do not significantly reduce the inspection range. On the other hand, the considerable reduction of the inspection range due to vehicle dynamics is a well-known issue for cars and trucks [156]. Also, due to slight inaccuracies in the acquisition process, some sample shapes are slightly shorter than others. The average shape was computed only at the points all the 36 sample shapes are available.

Due to the relatively low performances of smartphone sensors and on the variable nature of operation conditions and vehicle effects on the collected measures, individual samples do not provide reliable results if used for structural identification. Moreover, due to technical issues, data collection could be discontinuous, especially for older smartphone models. However, in a crowdsensing application, the high number of identified features reduces the uncertainty of the identified values. In this study, a preliminary feasibility analysis was conducted considering only 36 samples; however, through hundreds of datasets collected by different users in a crowdsourcing strategy, the identified features are likely to improve further. Moreover, a simple procedure can be designed to facilitate

the automatic acquisition of the samples based on the identification of the vertical acceleration peaks at the ends of the bridge. This

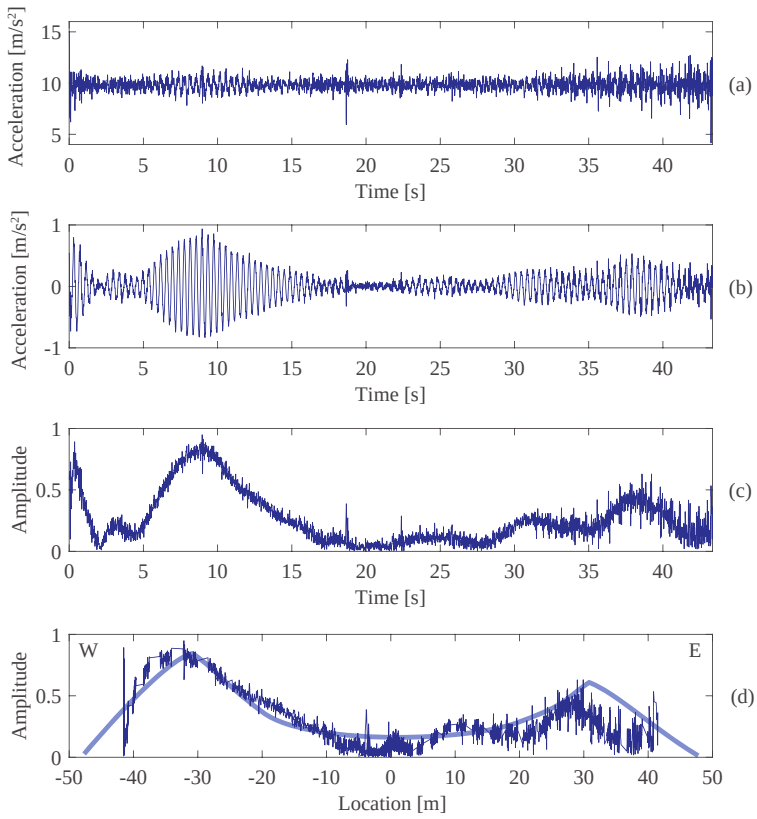

Figure 4.27: Steps of the procedure for a data sample: (a) vertical acceleration, (b) filtered signal, (c) filtered amplitude, (d) reconstructed sample shape

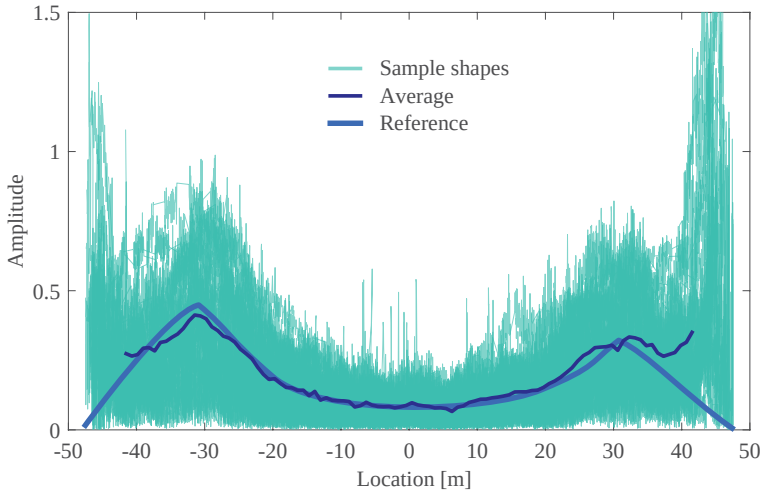

Figure 4.28: Reference and identified modal amplitude

way, the data could be processed in a cloud-based, fully automatic framework. The periodic inspection of the average profile shown in Figure 10 may enable the detection of localized changes, possibly related to structural damage, that can motivate the owners of the infrastructure to arrange further inspections. The reader can refer to exhaustive literature [3, 262, 277, 283] for the employment of the identified damage-sensitive features for damage identification.

Improving efficiency 5

Smart devices for structural health monitoring provide edge computing capabilities to reduce wireless transmission and, thus, power consumption. Although effective algorithms have been proposed in the last few decades, traditional microcontrollers require heavy data flow between the memory and the central processing unit that involves a considerable fraction of the total energy consumption. Phase Change Memory (PCM) has recently emerged as an attractive solution in the field of resistive non-volatile memory for analog in-memory computing, which is a valid approach to avoid data being conveyed among distinct elaboration units. However, it has never been envisaged in SHM applications. As this technology is still in an embryonic state, several challenges related to nonlinearities and non-idealities of the memory elements and the energy expenditure related to the memory reprogramming process may undermine its usage. In this chapter, the application of a novel identification approach for civil infrastructures is investigated using phase change memories. The main computational core of the presented algorithm, consisting of 1-dimensional convolutions, is particularly suitable for implementations involving analog in-memory computing, thus showing the great potential of this technology for structural health monitoring applications. The test unit is an embedded phase change memory provided by STMicroelectronics and designed in 90-nm smart power Bipolar-CMOS-DMOS technology with a Ge-rich Ge-Sb-Te alloy for automotive applications. Experimental results obtained for a viaduct of an Italian motorway support the efficacy of the method. Moreover, the influence of non-idealities on the outcomes of damage identification based on both dynamic and quasi-static

structural parameters is examined.

5.1 Behind filtering

Consider the impulse responses $b_m[\tau]$, with $\tau = 1, \ldots, N$, of one low-pass ($m = 0$) and p bandpass ($m = 1, \ldots, p$) filters such that the central frequencies of the bandpass filters coincide with the first p resonant frequencies of a vibrating structure and their frequency bandwidth is small compared to the distance between consecutive modal frequencies. Let the coefficients of these filters be organized in column vectors $\mathbf{b}_m \in \mathbb{R}^N$. A filter bank matrix can be defined as follows:

$$\mathbf{B} = \left[\mathbf{b}_0, \mathbf{b}_1, \ldots, \mathbf{b}_p\right] \tag{5.1}$$

Here, the term $\mathbf{b}_0$ encloses the coefficients of the low-pass filter that can be employed to extract quasi-static structural features. On the other hand, the terms $\mathbf{b}_m$ indicate the bandpass filters used to extract different modal contributions from the acceleration time response. Specifically, considering a matrix $\mathbf{X}_t$ such that

$$\mathbf{X} = [\mathbf{x}_{t,1}, \mathbf{x}_{t,2}, \ldots, \mathbf{x}_{t,r}] \tag{5.2}$$

where $\mathbf{x}_{t,i}$ are column vectors collecting the samples of the acceleration signal $x_i[t]$ recorded at the instrumented locations $i = 1, \ldots, r$ in the time interval $[t, t + N]$, a set of decomposed signals can be calculated as

$$\mathbf{Y}_t = \mathbf{X}_t^{\mathrm{T}}\mathbf{B} = \begin{bmatrix} y_{1,0}[t] & y_{1,1}[t] & \cdots & y_{1,p}[t] \\ y_{2,0}[t] & y_{2,1}[t] & \cdots & y_{2,p}[t] \\ \vdots & \vdots & \ddots & \vdots \\ y_{r,0}[t] & y_{r,1}[t] & \cdots & y_{r,p}[t] \end{bmatrix} \tag{5.3}$$

The elements $y_{i,0}[t]$, upon changing the time variable into space (*i.e.*, $z = vt$), represent the samples of the curvature influence line of the beam at the i-th location. Due to the Maxwell-Betti reciprocal work theorem, $y_{i,0}[z]$ is also the structural curvature of the beam generated by a static load applied at the i-th instrumented location. Moreover, the terms $y_{i,m}[t]$ with $m = 1, \ldots, p$ are the t-th

samples of the m-th decoupled modal contributions collected at the i-th location. Therefore, the m-th column vector of $\mathbf{Y}_t$, except when $m = 0$, is an instantaneous (the m-th) mode shape of the instrumented structure.

Based on these concepts, the following identification algorithm is proposed:

1. Collect the structural acceleration response at r instrumented locations when a vehicle is passing on the bridge.
2. Filter each response into $p + 1$ signal components using Equation (5.3).
3. For each sensor location, consider $y_{i,0}[t]$ for $t = 1, \ldots, T$, where T is the time interval referred to the passage of a single vehicle on the bridge, and normalize this sequence with respect to its maximum value, obtaining

$$h^{(i)}[z]\big|_{z=vt} = \frac{y_{i,0}[t]}{\max_{t\in[1,T]}(y_{i,0}[t])} \tag{5.4}$$

   Equation (5.4) represents the (normalized) dense influence line of the curvature of the bridge at the i-th instrumented location.
4. Consider $y_{i,m}[t]$ ($m = 1, \ldots, p$) for $t = 1, \ldots, T$ and calculate the mean of the absolute value of the m-th modal amplitude at the i-th location as

$$\phi_{i,m} = \frac{1}{T}\sum_{t=1}^{T}\left|y_{i,m}[t]\right| \tag{5.5}$$

   The vector $\boldsymbol{\phi}_m$ collecting all the $\phi_{i,m}$ for $i = 1, \ldots, r$ is an estimate of the m-th mode shape of the structure, in absolute value.

This procedure is schematized in Figure 5.1. It should be noted that the acquisition interval can be triggered to select only the structural response referred to the vehicle passage automatically, *e.g.*, using the signal collected at the bridge expansion joints (see also Chapter 4). The identified parameters can be stored in each sensing node and averaged to the new incomes to improve the robustness to recording noise. Then, the averaged parameters can be transferred

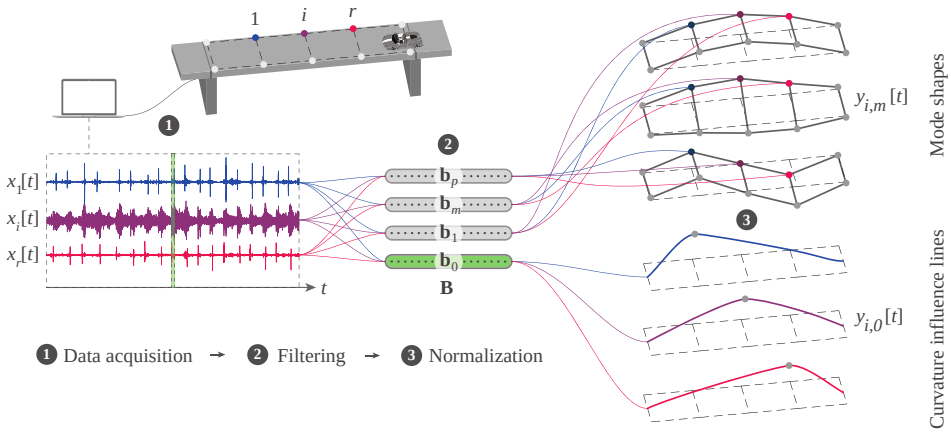

Figure 5.1: Scheme of the unified algorithm

to a central unit or directly uploaded in a cloud-based platform at user-defined intervals. Since phase information is neglected (*i.e.*, the sign of the elements of the identified shapes), strict synchronization is not necessary between the sensing nodes. Moreover, each node can operate individually.

The filters $b_m[\tau]$ should be highly selective in frequency to avoid the mixing of different contributions that would affect the accuracy of the identified structural parameters. In this paper, wavelet filters are employed. The procedure to generate suitable filters for the monitored structure is described herein.

The WPT can be implemented using low-pass and high-pass wavelet filters applied recursively n times to the input signal, where n is the selected maximum level of the wavelet transform. This implementation is known as Mallat algorithm or Fast Wavelet Transform (FWT) [211]. Specifically, considering a complete decomposition tree, the output coefficients of the wavelet packet transform $d^{(l)}_{i,2k}[t]$ and $d^{(l)}_{i,2k+1}[t]$ obtained by decomposing the coefficients $d^{(l-1)}_{k}$ at the previous level $l-1$ can be calculated as

$$d^{(l)}_{i,2k}[t] = d^{(l-1)}_{k}[t] * \bar{g}_0[2\tau] \tag{5.6}$$

$$d^{(l)}_{i,2k+1}[t] = d^{(l-1)}_{k}[t] * \bar{g}_1[2\tau] \tag{5.7}$$

where $*$ denotes the convolution operator, $k = 0, \ldots, 2^{l-1}$ indicates the subband index of the obtained coefficients, and $g_0[\tau] = \bar{g}_0[-\tau]$ and $g_1[\tau] = \bar{g}_1[-\tau]$ are the impulse responses of the low-pass and high-pass filters associated with a selected wavelet function, respectively. The root of the tree $d_0^{(0)}[t]$ can be assumed coincident with the discrete signal $x_i[t]$ collected at location i if the sampling frequency of the collected signal is sufficiently high – this is known as the wavelet crime [212]. Due to the linearity property of the convolution operator, the decomposition of the signal shown in Equations (5.6) and (5.7) can also be implemented as a one-step (or batch) filtering procedure using 2^n equivalent filters that produce the coefficients at the final transformation level n. These filters can be obtained by cascading (*i.e.*, performing recursive convolution upon upsampling the filter at each iteration) $g_0[\tau]$ and $g_1[\tau]$ n times in a particular order [20]. For simplicity, let $G_0(z)$ and $G_1(z)$ be $g_0[\tau]$ and $g_1[\tau]$ in the z-transform domain, respectively. Due to the convolution theorem, the frequency representation of an equivalent bandpass filter $b_m[\tau]$ corresponding to the subband $k = m$ at the transform level n can be obtained as

$$B_m(z) = \prod_{l=0}^{n-1} G_{l*}\left(z^{2^l}\right) \tag{5.8}$$

where $G_{l*}(z)$ can be either $G_0(z)$ or $G_1(z)$ depending on the level l and on the desired equivalent filter. For instance, $G_{l*}(z) = G_0(z) \forall l$ to generate the low-pass filter $b_0[\tau]$. In Equation (5.8), z^k represents an upsampling in the time domain by a factor k, *i.e.*, the upsampled filter $g_{l*}[\tau]$ at level l can be obtained as

$$g_{l*}[\tau] = \begin{cases} g_*\left[\frac{\tau}{2^l}\right] & \text{if } \tau = \xi 2^l, \xi \in \mathbb{Z} \\ 0 & \text{otherwise} \end{cases} \tag{5.9}$$

where $g_*[\tau]$ is either $g_0[\tau]$ or $g_1[\tau]$ depending on the level l and on the desired equivalent filter, and ξ is an integer value. Consequently, the number of null coefficients of $g_{l*}[\tau]$ increases with l, while the number of non-zero coefficients is constant.

Each filter obtained through this procedure at level n has a bandpass range width of $F_s/2^{n+1}$, where F_s is the sampling frequency of the collected signal.

In Section Section 3.2, the equivalent decomposition filters were obtained by cascading *Fejér-Korovkin 22* wavelet filters. These filters have a relatively high number of taps (*i.e.*, 22), which generate equivalent filters that may be particularly challenging for implementations in smart sensing nodes. For instance, considering the wavelet transform level 6, each equivalent filter has 1326 taps.

In this paper, the reverse biorthogonal wavelet function with three vanishing moments is used for signal decomposition. Specifically, the low-pass and high-pass analysis filters have 4 taps, are symmetrical (anti-symmetrical for the high-pass filter), and are formed of only two coefficients, the higher of which is three times the lower, as shown in Figure 5.2. Although most equivalent filters obtained through this wavelet function are scarcely selective, the low-pass filter, as well as some bandpass filters, are acceptable for identification purposes, as it will be shown later. In particular, ordering the equivalent filters obtained by cascading the wavelet filters in all the possible orders with an increasing central frequency, the $(2^{n-l}+1)$-th filters are sufficiently selective, especially for low l values (with $l = 1, \ldots, n$). These filters have a center frequency equal to

$$F_l = \frac{F_s}{2^{l-1}} \tag{5.10}$$

Sampling the structural response (*i.e.*, selecting F_s) such that the structural resonant modes have a natural frequency close to the F_l values allows the extraction of the corresponding modal contributions.

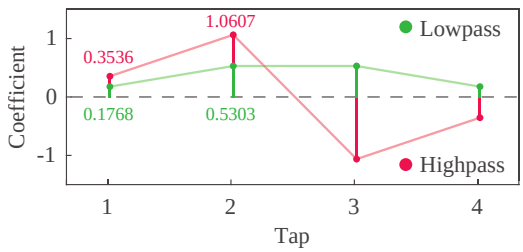

Figure 5.2: Reverse biortogonal 3.1 wavelet decomposition filters

5.2 Memories and convolutions

Conventional computing systems employ separate processing and memory units, involving a considerable motion of data, which is expensive in terms of time and energy. This has become a central issue due to the recent growth of highly data-centric applications. In-memory computing overcomes traditional computer architectures, enabling the possibility to perform some tasks in the memory itself and, consequently, avoiding the need to move data between separated processing units [284]. Exploiting the physical attributes of dedicated memory arrays, computational tasks are performed within its confines and peripheral circuitry without deciphering the content of the individual memory elements.

PCMs rely on the reversible transition of a chalcogenide material between its crystalline (or SET) and amorphous (or RESET) state. The amorphous phase tends to have low electrical conductance, which reaches values that are several orders of magnitude higher in the crystalline phase. The transition between SET and RESET state is achieved with the application of a corresponding current pulse, which properly modifies the memory cells lattice structure; the SET pulse is a trapezoidal current pulse, which initially melts and then gradually crystalizes the cell phase, producing a cell in a high-conductance state. The SET pulse can be modulated in amplitude, width of the flat portion, and decaying slope. On the opposite, the RESET pulse consists in a higher current flow and it is applied in order to melt the central portion of the cell; the molten material quenches into the amorphous phase, producing a cell in the low-conductance state. The RESET pulse can be modulated in amplitude and width. The order of magnitude of both current pulses amplitude is hundreds of microampere, while their duration could range between tens and hundreds of nanoseconds. Thus, PCMs are already an effective alternative to conventional binary non-volatile memories (NVMs), as in the actual development state, their cells can effectively store digital "0" or "1" values [285, 286]. These two states correspond to a deep-RESET and a deep-SET state, respectively, and they are achieved through the application of high-amplitude RESET or SET pulse sequences. Furthermore, due to their considerable conductance contrast, the change in read current is quite large,

opening up the opportunity for multilevel cell (MLC) operations [287] due to the intrinsic capability of a memory cell to encode more than one bit of digital data per cell. In other words, PCM cells are able to store a range of intermediate states between the deep-RESET and the deep-SET states. This can be addressed exploting appropriate pulse sequences, called programming sequence, where the combination of different RESET and SET pulses allows the cells to reach a predefined intermediate conductance.

In this context, PCM devices lay among the most appetible enabling technologies for analog in-memory computing. Their multilevel storage capability becomes crucial, as it allows the execution of analog multiplications simply exploiting Ohm's and Kirchhoff's laws [288, 289]. Given a cell with conductance b, a single multiplication is achieved by applying a voltage x to the cell, and thus the readout current I satisfies $I = bx$. If N voltage values are applied to different parallel cells, the sum of their currents y is

$$y = \sum_{\eta=1}^{N} I_\eta = \sum_{\eta=1}^{N} b_\eta x_\eta \tag{5.11}$$

From this result, it is possible to conceive the whole memory as a conductance matrix $\mathbf{B}$ with dimensions $M \times N$. Then, applying a voltage vector $\mathbf{x}$ to each row, it is possible to obtain a Matrix-Vector Multiplication (MVM) as

$$\begin{bmatrix} y_1 \\ \vdots \\ y_M \end{bmatrix} = \begin{bmatrix} b_{11} & \cdots & b_{1N} \\ \vdots & \ddots & \vdots \\ b_{M1} & \cdots & b_{MN} \end{bmatrix} \begin{bmatrix} x_1 \\ \vdots \\ x_N \end{bmatrix} \tag{5.12}$$

In this study, the elements of $\mathbf{B}$, which are in the range bwtween 10 mS and 100 mS together with the null value, are proportional to the coefficients of the reverse biorthogonal low-pass and high-pass wavelet filters, whereas the voltage vector x contains the sampled input signal, and the current readout $\mathbf{y}$ represent a sample of the filtered components. Thus, Equation (5.12) can be seen as the operation to obtain the i-th row of $\mathbf{Y}_t$ in Equation (5.3), *i.e.*, if $\mathbf{B}$ is the filter bank matrix, the current readout is the decomposed signal obtained using the PCM-based node deployed at a given instrumented location.

A simplified schematic of the PCM is reported in Figure 5.3, where the notations used for the conductance values, input voltage, and current readout are expressed in the signal processing format employed in the previous sections. In this representation, the memory array consists of memory cells connected between each other through BitLine (BL), *i.e.*, the vertical connections, and WordLine (WL), *i.e.*, the horizontal connections. Each interval $\mathbf{x}_{t,i}$ of the input signal is given as an input to a BL in the form of a voltage $x[t+\eta]$. Therefore, each memory cell connected to a given BL receive the same input voltage. On the other hand, the memory cells connected to a given WL contain the different coefficients of a filter impulse response $b_\zeta[\eta]$. The sum of output currents of the memory cells connected to a given WL (*i.e.*, $y_\zeta[t]$) constitutes the result of the convolution between the input signal and the filter stored in the ζ-th WL. Filters that share the same input data can be implemented in the same BLs and different WLs. It should be noted that the power consumption of a MVM operation is directly proportional to the values of both $\mathbf{x}$ and $\mathbf{B}$, as the total current required to calculate the single elements of $\mathbf{y}$ is given by Equation (5.11).

From a practical viewpoint, several challenges characterize the behavior of PCM cells. First of all, low-frequency (flicker) noise affects the values of $\mathbf{B}$, as random electron traps are located in the cell lattice. Moreover, cell conductance tends to decrease due to the amorphization and relaxation phenomena of the crystal lattice. Also, different cells respond differently to the same programming pulses, and the response of the same cell to subsequent programming cycles shows a large variability. These phenomena lead to dispersion and

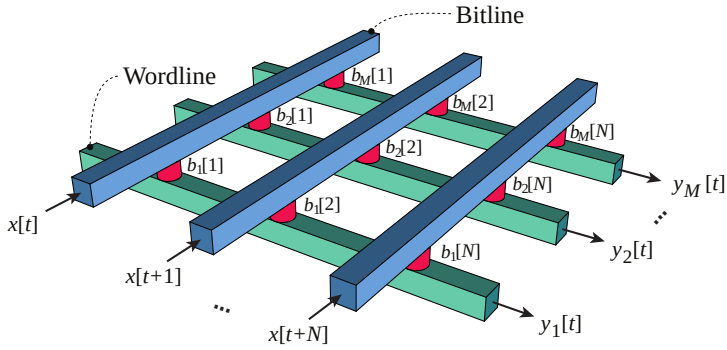

Figure 5.3: Schematics of the PCM array

inaccuracy of the conductance levels (*i.e.*, to the elements of the **B** matrix) and thus of the MVM operation. Several solutions to mitigate such undesired phenomena have been proposed, mainly focused on material technology [290], post-processing compensations [112, 291], or dedicated programming algorithms [287, 292–294].

In this work, the programming algorithm proposed in [292] was exploited to store the filter coefficients in an embedded PCM (ePCM) test chip designed and manufactured by STMicroelectronics [295]. The test chip is manufactured in 90-nm smart power Bipolar-CMOS-DMOS technology featuring a specifically optimized Ge-rich Ge-Sb-Te (GST) alloy and was originally intended for digital storage in automotive applications. An evaluation board was also employed and customized in this study, as shown in Figure 5.4. This board allows the configuration of current pulses applied to cells, exploiting the voltage and current regulators integrated on the test chip. The operations performed on the memory array were implemented through a dedicated guided user interface (GUI) available on a personal computer. To access the PCM array a high-precision Source Meter Unit (SMU) was employed, together with a low-drop power supply.

Upon defining a conductance target interval by specifying its mean value and relative tolerance, each cell is first stimulated with a start SET and a start RESET pulse [292, 296], as they grant better temporal drift retention [292, 297]. Then, for each cell, a partial SET sequence begins with a minimum SET amplitude A_{MIN}, with the aim of gradually increase its conductance. After a predefined time T_{WAIT}, the cell conductance is measured. If it falls within the target interval, the sequence is terminated, otherwise, if the conductance is lower than the required limit, the cell is stimulated with a new SET pulse increasing its amplitude by a user-defined interval ΔA. If, instead, the conductance is above the upper limit, the whole process is restarted from the initial SET and $RESET$ pulses.

In this study, 48 memory cells of a PCM test chip provided by STMicroelectronics were programmed in a laboratory environment to store 24 low and 24 high *rbio3.1* decomposition filter coefficients. The following parameters were used in the described programming algorithm: $A_{MIN} = 150\,\mu A$, $T_{WAIT} = 1\,ms$, and $\Delta A = 10\,\mu A$. The

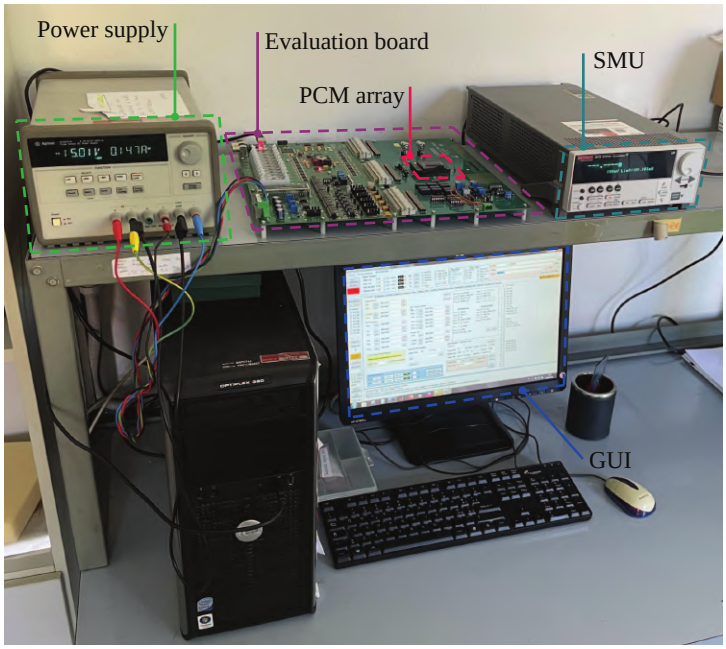

Figure 5.4: Laboratory setup for PCM testing

coefficients of each filter were converted in conductance values $b_\zeta[\eta]$, which were then stored into specific memory cells. In particular, low filter coefficients were converted into 18 µS, while high filter coefficients were converted into 54 µS, considering that a scale factor of 2 relates the coefficients of the high-pass and low-pass filter (see Figure 5.2). The initial conductance value of every filter coefficient was memorized with a maximum tolerable error of ±5%, and the mean number of intermediate steps required to program memory cells was 9.

An effective method for evaluating the above-mentioned long-term effects on PCM cells is to bake the memory array in a thermal chamber for some dozens of hours in order to accelerate the amorphization phenomena of the crystal lattice [298]. Recent studies have represented the behavior of PCM cells in time as a power model with the form [288].

The conductance of the PCM cells was observed using a current SMU in the laboratory following the time schedule reported in Figure 5.5. The filter coefficients are collected with a sampling period of 6000 s in low sampling frequency (LF) observation intervals, while

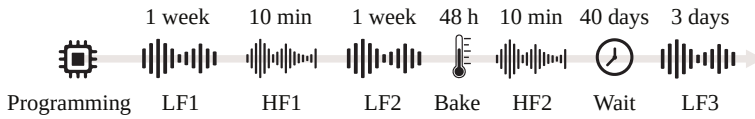

Figure 5.5: Observation schedule of programmed filters

every 0.02 s in high sampling frequency (HF) intervals. Between LF2 and HF2, the memory array was baked for 48 hours at 150 °C to evaluate the effects of time-related non-idealities at an ideal infinite time after programming.

Figure 5.6 shows the conductance in time of all the monitored cells. Thin lines represent the behavior of individual cells, while the reference power law [288], fitted to the first two drift intervals, is represented as a thick line for high and low coefficients. According to the power law, the coefficients recorded during the interval LF3 (*i.e.*, after bake and additional 40 days at room temperature) correspond to an equivalent observation time in the order of tens of years since programming. It is therefore assumed that short-term drift effects have completely vanished.

The coefficients observed in the two HF intervals are used to build the 6 low-pass (one for each transformation level) and 4 high-pass (only used in the first four transformation levels) wavelet filters employed in this study to filter the structural vibration response. Each filter is time-dependent due to a noise-related variability, as the stored coefficients are affected by the aforementioned non-idealities.

As explained, the signal can be decomposed into different wavelet components either using a set of equivalent filters corresponding to a given transformation level (*i.e.*, batch approach) or performing a

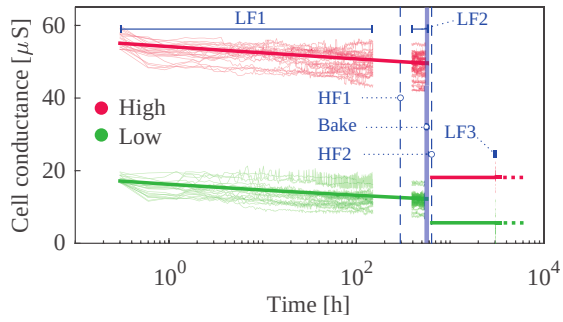

Figure 5.6: Drift of the programmed PCM cells

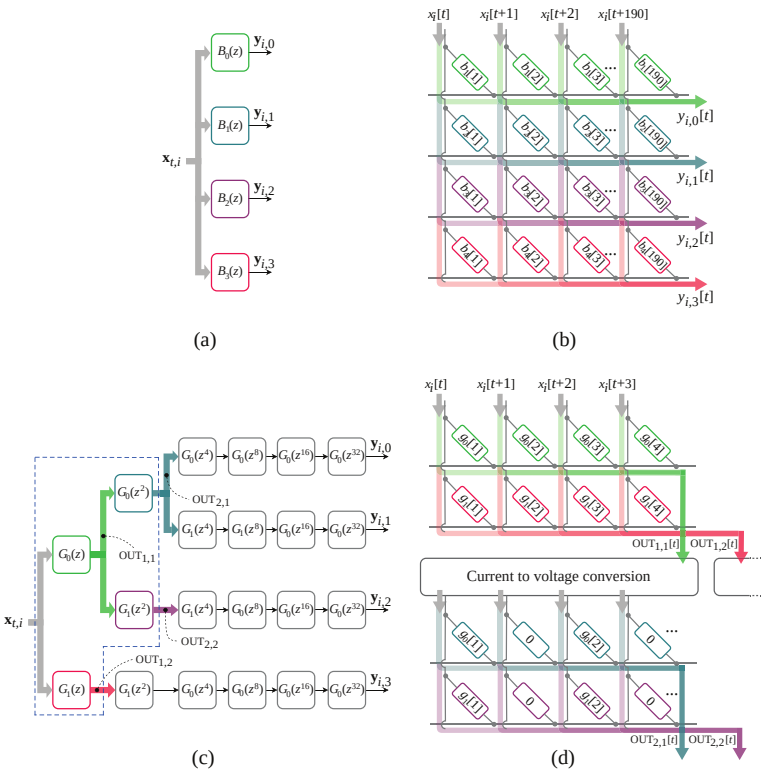

Figure 5.7: Filtering through the batch (a) and recursive (c) modes, and their respective implementation in a PCM-based architecture (b,d); in (d) the architecture of the dashed portion of (c) is represented

recursive procedure. The batch approach is represented schematically in Figure 5.7a-b, and compared to the recursive procedure in Figure 5.7c-d (the last figure shows only the first two levels of the transform). In this paper, the recursive implementation of the signal decomposition task on the PCM-based architecture is proposed and compared with a batch implementation in terms of power consumption and accuracy of the results. Both algorithms are implemented using real observation of the filter coefficients in PCMs, collected as described in the PCM programming section, in the laboratory. The structures of the filtering algorithms were simulated in this study using the MATLAB environment. The input signal, consisting of pre-collected structural vibration data, is sampled and filtered using low-pass and high-pass wavelet filters in a fast wavelet transform implementation – see Equations (5.6) and (5.7) – to retrieve the signal components associated to a wavelet decomposition level equal to n (in this case, $n = 6$). If a batch procedure is adopted, the input samples are decomposed by m (in this case, $m = 4$) equivalent filters

whose impulse response is the inverse z-transform of $B_m(z)$ in Equation (5.8). In this case, the filter bank consists of $N_F = 4$ filters, each with $N_T = 190$ taps. The implementation of this strategy is shown in Figure 5.7b, where 4 WLs and 190 BLs are required. On the other hand, the recursive implementation is represented in Figure 5.7c. The filter bank consists of 6 layers, each of them having a different number of filters N_F, ranging from 2 to 4, with an increasing number of taps N_T, ranging from 4 to 97, with an increasing number of null values (Figure 5.7d). As illustrated in Figure 5.7d, the coefficients of each filter are implemented in a single WL and different BLs, as every tap must be multiplied with a different value of the input signal. If two or more filters share the same input values (*i.e.*, filters 1 and 2 in this case), they are programmed in different WLs, sharing however the same BLs. Thereby, their outputs are available at the same time and can be cast to the next filters. Between the two filter layers, a current-to-voltage conversion is processed.

In Table 5.1, the features of batch and recursive approaches are summarized, together with the number of non-zero coefficients per filter N_{ON}.

The recursive procedure has two principal advantages with respect to the memorization of equivalent filters: (1) it drastically reduces the power consumption of the sensing device, and (2) it reduces the noise effects of non-ideal PCM elements.

The performances in terms of power consumption of batch and recursive implementations were compared considering the energy required to entirely process a single input sample in both cases, neglecting the cost of current-to-voltage conversion steps. Assuming that the energy is given by $E = \int_0^T x_S I dt$, where x_S is the supplied

Table 5.1: Parameters of the batch and iterative filter banks

Filter bank	Layer	N_T	N_F	N_{ON}
Batch	I	190	4	190
Iterative	I	4	2	4
	II	7	3	4
	III	13	4	4
	IV	25	4	4
	V	49	4	4
	VI	97	4	4

voltage, I is a current and T is the operating time interval, the energy per input sample E' is

$$E' = \int_0^T x_S I dt = x_S K \bar{\imath} \tau \tag{5.13}$$

where K is the total number of taps to fully process the sample, $\bar{\imath}$ is the mean cell current, and τ is the time required by the PCM array to compute a single product. As x_S and τ are equal in both implementations, the product $K\bar{\imath}$ is the actual energy benchmark. In the batch implementation, $K = \sum N_F N_T = 760$ and $\bar{\imath} = 10.6\,\mu\text{A}$, whereas in the recursive procedure, $K = 1245$ and $\bar{\imath} = 0.61\,\text{mA}$, thus, the power required by the iterative strategy is only 9.43% of the power required by batch filtering, neglecting, in a first approximation, the contribution of current to voltage conversion circuits. In fact, even if the iterative implementation involves more taps than the batch procedure, the total required current is much lower as, according to Equations (5.8) and (5.9), and Table 5.1, a large number of coefficients are null, thus involving no current consumption.

In order to compare the performance of batch and recursive implementation, 15 samples of the 4 equivalent filters used in this study were stored in PCM elements and observed after a 48 h baking. Figure 5.8 compares the observed interval (between tap 50 and 65) of the equivalent filter directly memorized in PCM elements (*i.e.*, using a batch approach, see Figure 5.7a) with the equivalent filter obtained by convolving the low-pass and high-pass coefficients observed in the interval HF2 according to Figure 5.7c. Specifically, both for the recursive and batch implementation, the filter observed at 100 different time samples collected every 0.02 s is reported (light green and magenta spreads), together with their average (solid green and magenta lines). It is possible to observe that the coefficients of the filter obtained through recursive implementation are closer to the reference values (*i.e.*, the ideal filter that does not account for the PCM non-idealities), although the spread – which represent the short-term noise – is generally higher. The selective performance of the four filters is observable in the frequency domain: Figure 5.9 shows the equivalent filters obtained through a recursive implementation before and after baking. As in the previous representation, the filter coefficients observed at 100 different time samples are reported

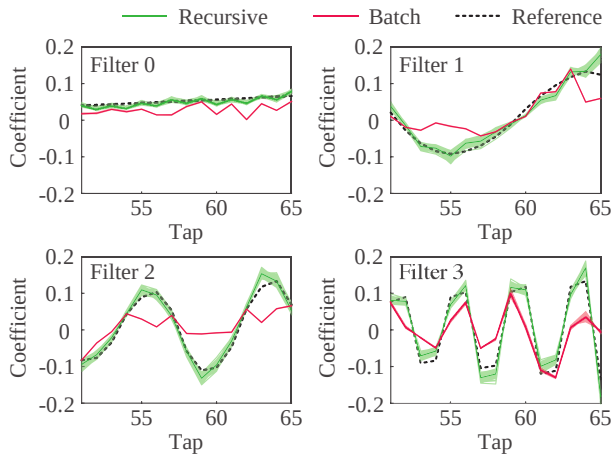

Figure 5.8: Noise effects on the equivalent filter for a level 6 transform

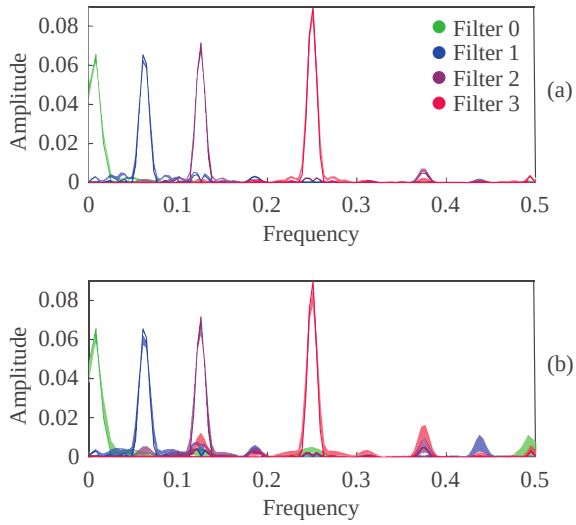

Figure 5.9: Selected filters in the frequency domain: pre-bake (a) and post-bake (b) environment

as spread and average lines. Although the spread increases after baking, the selective performance of the filters is comparable.

Identification of structural parameters using a PCM prototype

This section presents the identification results obtained using the proposed algorithm on the experimental data collected on a viaduct of the Italian A24 motorway. Specifically, dynamic and quasi-static identification results are obtained using filters programmed and

observed in the test PCM unit. These results are obtained using the memory cells in freshly programmed and long-term conditions, represented by pre-and post-bake environments (*i.e.*, the observation intervals HF1 and HF2, respectively).

The viaduct, called Temperino [118, 149, 264, 265], consists of a series of single-span post-tensioned prestressed beams in a simply-supported isostatic configuration. The case study is described in the application part of Section 4.2. In this paper, individual moving cars were considered.

Since this study is aimed at investigating the usability of PCMs in structural identification applications, the modal parameters identified using the proposed algorithm and implementation technology will be compared to reference parameters identified using a widely used algorithm for structural identification, namely, the FDD [259]. Precisely, a traditional centralized application of the FDD is employed using 10 acceleration time histories of 1500 s collected at all the locations shown in Figure 4.5a-b, subsampled at 50 Hz. This method allows the identification of four vibration modes with natural frequencies $\bar{F}_m$ equal to 2.48 Hz, 5.06 Hz, 7.56 Hz, and 9.01 Hz.

In order to identify the mode shapes of the first, second, and fourth modes using the proposed method, the signal is resampled at a frequency of 41.5 Hz. This way, since $\bar{F}_1 \approx F_3$ and $4F_1 \approx 2\bar{F}_2 \approx \bar{F}_4$, the filters corresponding to a decomposition level 6, with central frequencies $F_3 = 2.59$ Hz, $F_2 = 5.19$ Hz, and $F_1 = 10.38$ Hz, can be effectively employed to extract the modal contributions associated with the modes 1, 2, and 4, respectively. It should be noted that, in this study, it is assumed that the resonant frequencies of the structure (of a rough estimate of them) are already known, *e.g.*, from previous monitoring campaigns, in order to design the filters for identification. This is a reasonable assumption since preliminary tests are usually performed before designing a monitoring system. A low-pass filter obtained for a decomposition level 5 is also employed to extract the quasi-static response component with a frequency lower than $F_s/2^6 = 0.64$ Hz.

Figure 5.10 shows time windows of the filtered signals obtained using the filters observed in the intervals HF1 and HF2 (*i.e.*, in the pre- and post-baking environment), compared to the reference filtered

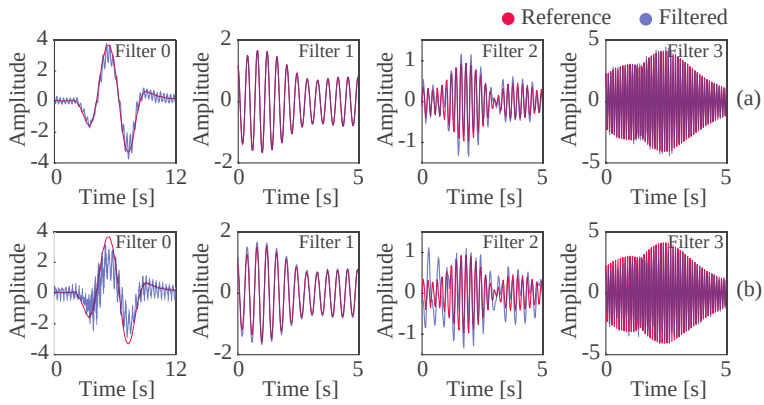

Figure 5.10: Filtered signals in pre-bake (a) and post-bake (b) environment; filter 0 indicates the low-pass filter, while filters 1, 2, and 3, are band-pass filters with central frequencies F1, F2, and F3, respectively

signals obtained using ideal filters that do not include the noise generated by PCM cells. Moreover, Figure 5.11 shows the error of the filtered signal for each filter. Specifically, nRMSE represents the normalized RMS error. The normalization is obtained by dividing both the reference and the filtered signals by their standard deviation. It is possible to observe that the low-pass filter is generally affected by a higher noise level and, as expected, the noise increases in the post-bake environment. Moreover, the nRMSE of filter 1 is generally the lowest, denoting a good quality of the extracted first modal contribution.

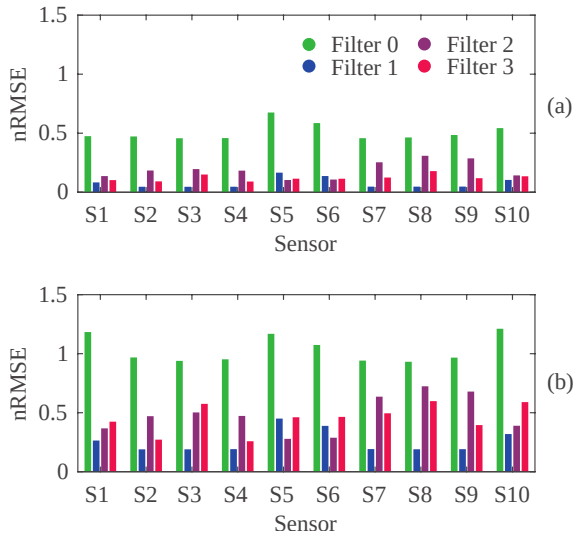

Figure 5.11: Normalized root mean square error of the filtered signals in pre-bake (a) and post-bake (b) environment

Although the error in the filtered signal is non-negligible, the mode shapes reconstructed using the extracted modal contributions (Figure 5.12) are very close to the reference ones – obtained using the traditional FDD – both for the pre- and post-bake environments. In Figure 5.12, the sign of mode shapes is determined using the sign identified through the preliminary FDD-based identification. The high accuracy is confirmed using the MAC [58, 192]. Figure 5.13 shows that values close to 1 are obtained comparing the reference and identified shapes, especially for the first two modes. Since the identification method proposed in this paper provides absolute values of the modal amplitudes, their sign is determined based on the reference identified values.

It should also be noted that, although the central frequencies of the filters do not correspond exactly to the resonant frequencies of the structure, the identification results are in good agreement with the reference parameters. The method is therefore also robust to slight variations of the resonant frequencies, *e.g.*, due to varying temperature conditions.

Figure 5.14 shows the influence lines identified in pre- and post-bake environments. In particular, the average results are obtained considering 24 individual estimates computed during as many vehicle crossings. Although the estimates are visibly affected by noise compared to the reference estimates, the maxima of the influence lines are in the right location (*i.e.*, with reference to Figure 4.5a, at the instrumented location, indicated in the top-left corner of each plot). Also, the results obtained in the pre- and post- bake environments are very similar to each other, denoting a good performance of the algorithm for long-term applications. The literature has already shown that, although the noise level can be high in quasi-static parameters, they are generally very sensitive to structural damage. Moreover, considering a larger set of individual estimates, the noise level would decrease.

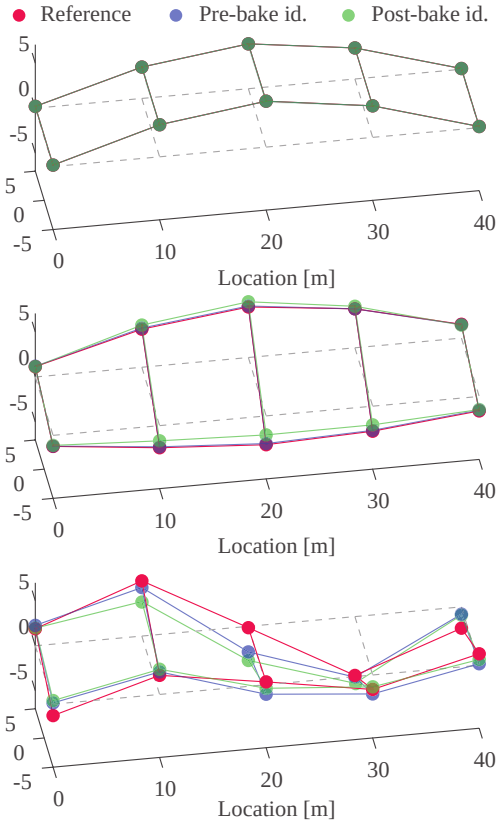

Figure 5.12: Reference and identified mode shapes; from top to bottom, output of filters 1, 2, and 3

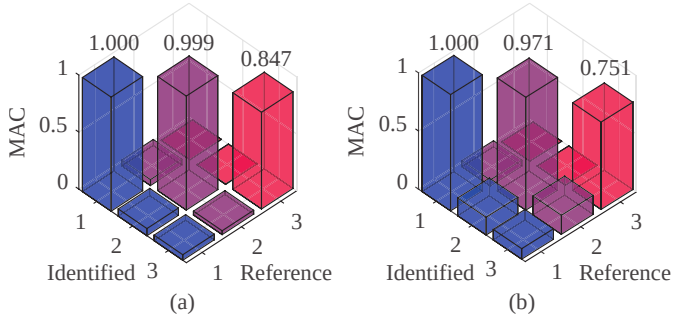

Figure 5.13: Modal assurance criterion matrices calculated between identified and reference mode shapes in pre-bake (a) and post-bake (b) environment

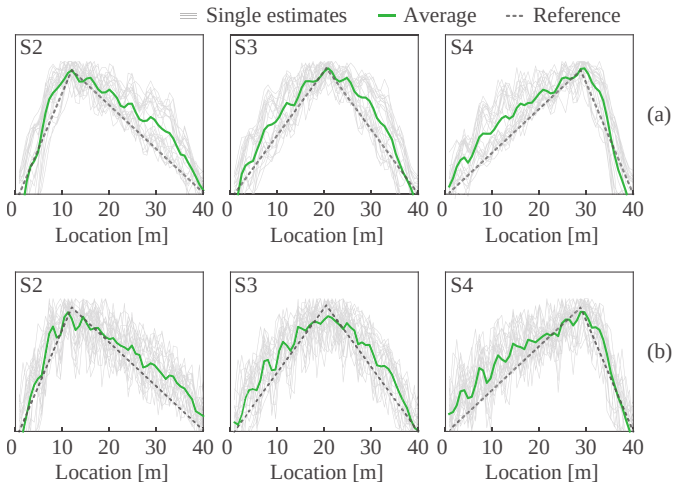

Figure 5.14: Influence lines identified in pre-bake (a) and post-bake (b) environment for different sensor locations

Integrating information 6

Information on the presence and location of cracks in concrete and steel structures can be extremely valuable to support operators in decision-making related to structural management and scheduling informed maintenance, especially when the SNR of structural vibration response is too low. Moreover, understanding the strain state of critical portions in the monitored structural element is critical supporting information to form a complete picture of the structural behavior.

This chapter investigates machine learning tools to solve the Human-Powered Vehicle inverse problem to reconstruct the conductivity distribution of a piezoresistive sensing film consisting of a smart conductive paint applied to structural components. Conductivity reductions identified during long-term monitoring can provide helpful information about the presence of cracks, the strain state of the structural substrate, and the presence of humidity that may accelerate material degradation. Two Machine Learning tools are studied in this chapter to reconstruct a dense conductivity distribution within the painted area by using only voltage measurements collected at sparse boundary locations. Since one of the most challenging aspects of using supervised learning tools for real applications is generating a representative training dataset, this paper presents a new approach to test the suitability of synthetic datasets built using a finite element model of the sensing surface. Results are reported for four sensing specimens fabricated with two different techniques (using carbon nanotubes and graphene

nanosheets, respectively).

6.1 Electrical impedance tomography

EIT is a soft-field imaging method that uses applied electrical excitations and measurements obtained along the boundaries of a conductive body to estimate its distribution of electrical properties. In short, EIT consists of the forward and inverse problems. The former involves calculating the voltage distribution on the boundary of the interrogated body when the boundary electrical excitation and the spatial conductivity properties of the body itself are known a priori. On the other hand, the inverse problem consists of estimating the conductivity distribution using boundary current excitations and voltage measurements. The EIT inverse problem can be solved when an alternating current excitation is applied and both voltage magnitudes and phases are recorded. In the case of a direct current (DC) excitation, the EIT problem specializes to become Electrical Resistance Tomography (ERT).

ERT forward problem

Let Ω be a conductive body with conductivity distribution σ and boundary Γ. Considering a given number of electrodes deployed along Γ, if DC is injected using at least two of them (a source and a sink), the electric flow in Ω can be described using Kirchoff's law, which correlates σ with the electric potential distribution ϕ in the absence of any current source or sink inside of Ω:

$$\nabla \cdot \sigma \nabla \phi = 0 \tag{6.1}$$

Let $\mathbf{n}$ be an outward unit vector normal to Γ, and $j = \sigma \nabla \phi \cdot \mathbf{n}$ be the current density in Ω. Given σ, the knowledge of ϕ on the boundary $\phi\big|_\Gamma$(known as Dirichlet boundary condition) is sufficient to uniquely determine ϕ. Similarly, knowing j (known as Neumann boundary condition) allows determining ϕ up to an additive constant. An operator that relates Dirichlet and Neumann data can be defined as $\Lambda_\sigma : \phi\big|_\Gamma \rightarrow j$, which is known as the Dirichlet to Neumann (DtN)

map. This operator – or its inverse Λ_σ^{-1}, the Neumann to Dirichlet (NtD) map – represents the response of the system that is electrically interrogated at its boundary.

In this study, electrical current and voltage were applied and measured, respectively, at discrete electrodes, using a finite element (FE) model. In a FE formulation, the region in which the problem is solved is segmented into a finite number of elements. A collection of these elements is herein called "mesh", and this work employed linear triangular elements. In the FE solution, a weak formulation of the differential Equation (6.1) was solved at the mesh nodes using the Complete Electrode Model (CEM) [180]. Let a current I_q be applied to the conductive body using Q electrodes having areas E_q, with $q = 1, \ldots, Q$. If the region of the boundary covered by the electrodes is called Γ_1 and the remaining part of the boundary is denoted as Γ_2, the boundary conditions necessary to solve the ERT forward problem can be posed using the CEM as follows:

$$\begin{aligned} \int_{E_q} j &= I_q \quad \text{on} \quad \Gamma_1 \\ j &= 0 \quad \text{on} \quad \Gamma_2 \end{aligned} \tag{6.2}$$

A further condition can be imposed to model the contact impedance z_q between the q-th electrode and the body:

$$\phi + z_q j = V_q \tag{6.3}$$

where V_q is the voltage measured at the q-th electrode, with respect to some arbitrary reference. The solution was thus interpolated over each element using shape functions along the edges of the elements. For more details about the FE implementation, the reader can refer to [175, 180].

The solution was thus interpolated over each element using shape functions along the edges of the elements. For more details about the FE implementation, the reader can refer to [175, 180].

ERT inverse problem

The inverse problem, as formulated by Calderón [299], consists of recovering σ from Λ_σ by injecting currents in a subset of electrodes

and measuring the voltage using all the others. Arranging these quantities in vectors ($\mathbf{i}_q \in \mathbb{R}^Q$ and $\mathbf{v}_q \in \mathbb{R}^Q$, respectively), a discrete equivalent DtN map can be represented in matrix form as:

$$\mathbf{i}_q = \mathbf{Y}\mathbf{v}_q \tag{6.4}$$

where $\mathbf{Y}$ represents the transfer admittance matrix (which has real elements in the case of direct current). Different measurement protocols can be applied using predefined interrogation patterns (*i.e.*, given sets of $\mathbf{i}_q$ vectors) that allow building a basis for the space of $\mathbf{Y}$. The set of $\mathbf{i}_q$ and $\mathbf{v}_q$ vectors obtained through interrogation can be employed to reconstruct $\mathbf{Y}$ by inverting Equation (6.4). Therefore, the inverse problem in the discrete case becomes recovering a vector $\boldsymbol{\sigma} \in \mathbb{R}^M$ containing the conductivity values of all the M elements of the FE mesh from $\mathbf{Y}$. Alternatively, the inverse problem can be defined in terms of the transfer impedance $\mathbf{Z} = \mathbf{Y}^{-1}$, which is the discrete counterpart of an inverse operator $\Lambda_\sigma^{-1} : j \rightarrow \phi|_\Gamma$. Also, the inverse problem can be defined for difference imaging, where the variation of conductivity between two different time instances or states (generally, a baseline and an inspection instant) is recovered from a variation in the NtD map. In all these cases, the inverse problem is ill-posed and ill-conditioned [180], which also becomes extremely unstable in the presence of noise.

Several methods have been proposed to solve the inverse problem using a priori information, which mainly consist of regularization criteria [180] that constrain the solution to rule out the variations that cause instability. These methods generally require the calculation and inversion of a sensitivity matrix that represents the derivative of the voltage measurements with respect to a conductivity parameter. However, complex inversion operations may hinder portable applications where the computational footprint of processing devices is generally limited.

6.2 Regularization approaches

Given a current interrogation pattern, consider the matrix of measured boundary voltages $\mathbf{V} = \mathbf{ZI}$, where $\mathbf{V} = [\mathbf{v}_1, \ldots, \mathbf{v}_Q]$ and

$\mathbf{I} = [\mathbf{i}_1, \ldots, \mathbf{i}_Q]$, with the column vectors $\mathbf{v}_q$ and $\mathbf{i}_q$ defined above. For simplicity of notation, let $\mathbf{v}$ be a vector containing all the elements of $\mathbf{V}$ arranged in a single column.

Considering difference imaging, the voltage measurement used as an input to the inverse EIT problem can be defined as $\delta\mathbf{v} = \mathbf{v}^{(c)} - \mathbf{v}^{(0)}$, where $\mathbf{v}^{(0)}$ and $\mathbf{v}^{(c)}$ are the voltage vectors measured in two different states. A similar difference can be defined in the forward problem, as:

$$\delta\mathbf{v}_\mathbf{f} = \boldsymbol{f}(\boldsymbol{\sigma} + \delta\boldsymbol{\sigma}) - \boldsymbol{f}(\boldsymbol{\sigma}) \tag{6.5}$$

where $\boldsymbol{f}(\bigcirc)$ is the output of the forward problem evaluated at the conductivity in its argument, and $\delta\boldsymbol{\sigma}$ is the conductivity change between the two considered states. Truncating the Taylor series expansion of $\boldsymbol{f}(\boldsymbol{\sigma} + \delta\boldsymbol{\sigma})$ to the first term and defining the sensitivity matrix as the Jacobian $\mathbf{J} = \partial\boldsymbol{f}(\boldsymbol{\sigma})/\partial\boldsymbol{\sigma}$, an estimate $\delta\hat{\boldsymbol{\sigma}}$ of the difference in the conductivity distribution can be calculated by minimizing the difference between $\delta\mathbf{v}$ and $\delta\mathbf{v}_f \approx \mathbf{J}\delta\boldsymbol{\sigma}$, as follows:

$$\delta\hat{\boldsymbol{\sigma}} = \arg\min_{\delta\boldsymbol{\sigma}} \left(\|\mathbf{J}\delta\boldsymbol{\sigma} - \delta\mathbf{v}\|^2 + \alpha\|\mathbf{R}(\delta\boldsymbol{\sigma})\|^2 \right) \tag{6.6}$$

Here, the symbol $||\bigcirc||$ denotes the vector norm of its argument, $\mathbf{R}(\delta\boldsymbol{\sigma})$ is a regularization matrix, and the scalar parameter α controls its relative contribution. Common regularization approaches are summarized in the referenced work [300]. In this study, the Total Variation (TV) approach is employed, according to which

$$\mathbf{R}(\delta\boldsymbol{\sigma}) = \int_\Omega \nabla\delta\boldsymbol{\sigma}\mathrm{d}\Omega \tag{6.7}$$

and can be practically implemented in an iterative procedure [180].

6.3 Machine-learning-aided tomography

In this section, two alternative ML techniques, namely, an artificial Deep Neural Network (DNN) and a Radial Basis Function Network (RBFN), were employed to solve the inverse problem. Since supervised learning algorithms were used, specific considerations were

necessary for the construction of a training dataset. Herein, the architecture of the ML tools is described, as well as their training process.

Preparation of the training set

DNNs and RBFNs have gained considerable interest in the last decades and are currently some of the most popular supervised ML tools used for regression due to their effectiveness in solving nonlinear problems. A training dataset representing examples of input-output pairs must be used to train the ML tools in the preliminary training phase. Then, in the application phase, the trained network can generate an output based only on input data, following the structure learned from the training set.

Let $\mathbf{v}^{(c)}$ and $\boldsymbol{\sigma}^{(c)}$ be the voltage measurements collected in the selected interrogation pattern and the conductivity distribution of a given (c-th) condition of the inspected body, respectively. A normalized difference of voltage measurement and conductivity distribution in configuration c can be defined as:

$$\begin{aligned} \delta\overline{\mathbf{v}}^{(c)} &= \frac{\mathbf{v}^{(c)} - \mathbf{v}^{(0)}}{\hat{v}} = \frac{\left[v_1^{(c)}, \ldots, v_K^{(c)}\right]^T - \left[v_1^{(0)}, \ldots, v_K^{(0)}\right]^T}{\hat{v}} \\ \delta\boldsymbol{\sigma}^{(c)} &= \boldsymbol{\sigma}^{(c)} - \boldsymbol{\sigma}^{(0)} = \left[\sigma_1^{(c)}, \ldots, \sigma_K^{(c)}\right]^T - \left[\sigma_1^{(0)}, \ldots, \sigma_K^{(0)}\right]^T \end{aligned} \tag{6.8}$$

where $\mathbf{v}^{(0)}$ and $\boldsymbol{\sigma}^{(0)}$ represent the boundary voltage at the electrode locations and the conductivity values of the mesh elements, respectively, corresponding to the baseline configuration, while $\hat{v}$ is the absolute value maximum of the elements in $\mathbf{v}^{(0)}$. A training set can be defined as $\mathcal{T} = \{\delta\overline{\mathbf{V}}, \delta\boldsymbol{\Sigma}\}$ with $\delta\overline{\mathbf{V}} = \left[\delta\overline{\mathbf{v}}^{(1)}, \ldots, \delta\overline{\mathbf{v}}^{(C)}\right]$ and $\delta\boldsymbol{\Sigma} = \left[\delta\boldsymbol{\sigma}^{(1)}, \ldots, \delta\boldsymbol{\sigma}^{(C)}\right]$ being the input and output matrix of the ML tool, respectively. The set $\mathcal{T}$ contains C instances and can be built by solving only the forward problem. By assuming a given conductivity distribution $\boldsymbol{\sigma}^{(0)}$, the voltage at the boundary $\mathbf{v}^{(0)}$ can be calculated using Equation (6.1). The entire training set can be generated by simulating a number (C) of different configurations of the body (*e.g.*, random conductivity distributions) and then solving the forward problem for each of them.

In this work, two training datasets were assembled, the first by simulating random polygonal areas with reduced conductivity, and the second by simulating cracks (*i.e.*, narrow areas with zero conductivity. The first dataset was generated through the following algorithm:

1. Select a random number of polygons between 0 and P
2. Select a random location on the sensing surface for the center of each p-th polygon
3. Select a random radius size of a circumference circumscribed to each polygon between 0 and R_p
4. Select a random number of edges for each polygon between 0 and K_p
5. Select K_p random points on each circumference and draw the polygons using the selected points as vertices
6. Reduce the conductivity of each polygonal region of a random value between 0% and 100% and collect the final conductivity values in a vector $\boldsymbol{\sigma}^{(0)}$
7. Solve the forward problem using Q different current injections according to a given interrogation pattern and collect the results in a vector $\mathbf{v}^{(0)}$
8. Calculate $\delta\overline{\mathbf{v}}^{(c)}$ and $\delta\boldsymbol{\sigma}^{(c)}$ using Equation (6.8) and build the entire training set

On the other hand, the algorithm to generate cracks was defined as follows:

1. Select a random number of cracks between 0 and P
2. Select a random location on the sensing surface as the starting point of each p-th crack
3. Select a random total crack length between 0 and R_p
4. Select a random number of portions to subdivide the total crack length between 0 and K_p
5. Select K_p random values for the length and inclination of each portion
6. Draw a broken line that represents the resulting crack on the FE mesh
7. Set the conductivity of all the FE elements that contain the crack line as 0 S/m and collect the final conductivity values in a vector $\boldsymbol{\sigma}^{(0)}$

8. Solve the forward problem using Q different current injections according to a given interrogation pattern and collect the results in a vector $\mathbf{v}^{(0)}$
9. Calculate $\delta\overline{\mathbf{v}}^{(c)}$ and $\delta\boldsymbol{\sigma}^{(c)}$ using Equation (6.8) and build the entire training set

The simulated data included in the training set can be different from real-world data, which generally includes noise due to measurement errors and imperfections in the sensing surface or the electrodes. Two strategies to improve the quality of the reconstructed conductivity were adopted in this study. The first concerns the normalization shown in Equation (6.8), which is aimed at making the experimental and simulated data comparable in terms of their voltage magnitude. This way, the normalized voltage is still representative of the relative conductivity variation (*i.e.*, minor voltage differences should represent modest conductivity variations). On the other hand, jitter was included in the training set to aid generalization and noise tolerance [301]. Here, jitter indicates the addition of noise in the input of the training set (hence, on $\mathbf{v}^{(c)}$). Indeed, it was demonstrated that training with noise is equivalent to a form of regularization in which an extra term is added to the error function [302], following the same idea behind Equation (6.6). Therefore, this method can lead to considerable improvements in network generalization while also reducing the risk of overfitting the generally limited training set [303]. Thus, noise was added to the input voltage measurements. The training set that includes jitter was obtained as $\widetilde{\mathcal{T}} = \{\mathcal{T}_1, \ldots, \mathcal{T}_S\}$, where

$$\mathcal{T}_s = \left\{\delta\widetilde{\mathbf{V}}_s, \delta\boldsymbol{\Sigma}\right\} \tag{6.9}$$

with $\delta\widetilde{\mathbf{V}}_s = \left[\delta\overline{\mathbf{v}}^{(s,1)} + \boldsymbol{\varepsilon}_{s,1}, \ldots, \delta\overline{\mathbf{v}}^{(s,C)} + \boldsymbol{\varepsilon}_{s,C}\right]$ and $\boldsymbol{\varepsilon}_{s,c}$ is a different Gaussian-distributed random vector for each value of $s = 1, \ldots, S$ and $c = 1, \ldots, C$ such that

$$\boldsymbol{\varepsilon}_{s,c} \sim \mathcal{N}\left(0, \gamma\,\mathrm{std}\left(\frac{\mathbf{v}^{(0)}}{\hat{v}}\right)\right) \tag{6.10}$$

where γ is a user-determined parameter, and $std(\bigcirc)$ denotes the standard deviation of the elements in its argument. In Equations (6.9) and (6.10), S is the number of times the original training set $\mathcal{T}$

is repeated with noise in $\widetilde{\mathcal{T}}$. Therefore, the number of instances of $\widetilde{\mathcal{T}}$ is SC.

Quality assessment of the training set

Consider real voltage measurements $\delta\overline{\mathbf{V}}^{*} = \left[\delta\overline{\mathbf{v}}^{(1)}, \ldots, \delta\overline{\mathbf{v}}^{(C_r)}\right]$ organized the same way as $\delta\overline{\mathbf{V}}$, formed of C_r columns, with $C_r \ll C$. This matrix can be easily built by interrogating a real body in different conditions. It should be noted that only voltage measurements are needed to build $\delta\overline{\mathbf{V}}^{*}$; therefore, the damage pattern must not be necessarily known. This test can either be conducted in the preliminary monitoring campaign that is generally carried out before deploying the sensing device on real structures or directly on the data collected while monitoring a real structure, for which the eventual damage state is unknown.

In this application, the voltage space – also addressed to as "input space" hereafter – is K-dimensional, *i.e.*, each dimension is represented by a voltage measurement. The objective of this section is to define a simple procedure to understand if $\delta\overline{\mathbf{V}}^{*}$ has the same structure as $\delta\overline{\mathbf{V}}$, *i.e.*, if the sample vectors of $\delta\overline{\mathbf{V}}^{*}$ and $\delta\overline{\mathbf{V}}$ populate the same regions of the K-dimensional space. Here "structure" is intended on both population density and location in space. If the structure of the two sets is similar, it is possible to assume that the synthetic dataset is representative of real situations. On the other hand, if the two sets $\delta\overline{\mathbf{V}}^{*}$ and $\delta\overline{\mathbf{V}}$ form two clusters, *i.e.*, the samples of the two sets are well-separated in the voltage measurement space, it is impossible to correctly reconstruct the conductivity distribution associated with real measurements using a neural network trained using synthetic data.

Due to the high-dimensionality of the problem, it is complicated to study the voltage space structure simply by observing the data. The Self-Organizing Map (SOM) [248] provides a low-dimensional representation of the original input space so that the user can observe a detailed distribution of the input samples. In this section, a correlation coefficient that expresses the similarity between the real and synthetic datasets $\delta\overline{\mathbf{V}}^{*}$ and $\delta\overline{\mathbf{V}}$ is presented to assess the quality of synthetic data generated through FE simulations.

SOMs are unsupervised learning tools that operate through two steps, consisting of (1) training the network and (2) mapping input data in a low-dimensional space. In the first step, a set of training instances is used to generate a network of neurons that approximates the input space. In this phase, competitive learning is employed, a variant of Hebbian learning, particularly suitable for finding the intrinsic structure of unlabeled datasets [304].

Let $\delta\overline{\mathbf{V}}^{+}$ be the union of the real and synthetic datasets, such that $\delta\overline{\mathbf{V}}^{+} = [\delta\overline{\mathbf{V}}, \delta\overline{\mathbf{V}}^{*}]$. In this application, a SOM is trained using the $C + C_r$ instances contained in $\delta\overline{\mathbf{V}}^{+}$ as input samples. No labels or conductivity distributions need to be associated with the voltage dataset since the SOM is an unsupervised learning tool. Without loss of generality, consider a competitive layer formed of a square grid (or map) of neurons with a size of $P \times P$. Each neuron associated with a weight vector $\mathbf{w}_p = [w_{p1}, \ldots, w_{pK}]^T \in \mathbb{R}^K$, with $p = 1, \ldots, P^2$, in which $\mathbf{w}_p$ represents the coordinates of the nth neuron in the K-dimensional input space.

During the training phase of the SOM, for each column vector $\delta\overline{\mathbf{v}}^{(c)}$ in the input space $\delta\overline{\mathbf{V}}^{+}$, the grid node $\mathbf{w}_p$ whose weights best describe the position of $\delta\overline{\mathbf{v}}^{(c)}$ in the K-dimensional space is sought (*i.e.*, the node closest to $\delta\overline{\mathbf{v}}^{(c)}$). The selected node $\hat{\mathbf{w}}^{(c)}$ is identified as the "best matching unit" (BMU) [305]. To measure the distance between vectors, the Euclidean distance is typically employed, which is computed between the input and each weight vector as [305–307]

$$d_{pc} = \left\| \delta\overline{\mathbf{v}}^{(c)} - \mathbf{w}_p \right\| = \sqrt{\sum_{k=1}^{K} \left(\delta\bar{v}_k^{(c)} - w_{pk} \right)^2} \tag{6.11}$$

where $\delta\bar{v}_k^{(c)}$ represents the k-th element of $\delta\overline{\mathbf{v}}^{(c)}$. In the traditional algorithm, also called "online" or "sequential" [305], following the determination of each BMU, the weights of the winning and adjacent neurons are updated according to the equation

$$\mathbf{w}_p^{(c)} = \mathbf{w}_p^{(c-1)} + h_p(c) \left[\delta\overline{\mathbf{v}}^{(c)} - \mathbf{w}_p^{(c-1)} \right] \tag{6.12}$$

where $\mathbf{w}_p^{(c)}$ denotes the weight of the n-th neuron following the BMU determination for the c-th input sample. In Equation (6.12), $h_p(c)$ is the neighborhood function, which acts as a smoothing kernel

defined over the neuron locations and is generally maximum at the BMU location. It is usually written in terms of a Gaussian function [308, 309] as follows:

$$h_p(c) = \alpha(c) \exp\left(\frac{-\left\| \hat{\mathbf{w}}^{(c)} - \mathbf{w}_p^{(c)} \right\|^2}{2\rho(c)} \right) \tag{6.13}$$

where $\mathbf{w}_p^{(c)}$ and $\hat{\mathbf{w}}^{(c)}$ represent the coordinates of the p-th node and of the BMU, respectively, while $\alpha(c)$ and $\rho(c)$ denote the learning factor and a user-selected neighbor radius [309], respectively. Generally, both $\alpha(c)$ and $\rho(c)$ tend to decrease as the iteration index c increases.

In this work, the batch learning algorithm [305] is used to train the SOM. The update of the weights is thus postponed to the end of each training period. This variant can only be applied if the entire set of input data is available during the training phase.

The output space obtained using SOMs (*i.e.*, the locations of the map nodes) can be represented in a low-dimensional fashion (usually two-dimensional). One of the most used approaches consists of representing the neurons on a regular grid with hexagonal or rectangular mesh [308], in which each has a color proportional to the Euclidean distance between two map nodes. This method can, indeed, be used to visualize multidimensional spaces more easily.

Once the training process is concluded, consider a new voltage sample. It is possible to define a classification process consisting of associating to the considered sample the closest – in the Euclidean sense – neuron of the SOM. In other words, the BMU of the considered sample is the outcome of the classification process. It is also possible to build a "topological matrix" or "sample hit matrix" $\mathbf{Y} \in \mathbb{Z}^{P \times P}$ that indicates how many samples in a testing set are assigned (*i.e.*, classified into) each neuron of the network.

Let $\mathbf{y}^* \in \mathbb{Z}^{P^2}$ and $\mathbf{y} \in \mathbb{Z}^{P^2}$ be the elements of the topological matrices obtained by classifying the subsets $\delta\overline{\mathbf{V}}^*$ and $\delta\overline{\mathbf{V}}$, respectively, arranged in column vectors. A sample correlation coefficient between

the sample hits in $\mathbf{y}^*$ and $\mathbf{y}$ can be calculated as

$$\lambda = \frac{\sum_{p=1}^{P^2} \left(y_p^* - \bar{y}^*\right)\left(y_p - \bar{y}\right)}{\sqrt{\sum_{p=1}^{P^2} \left(y_p^* - \bar{y}^*\right)^2 \sum_{p=1}^{P^2} \left(y_p - \bar{y}\right)^2}} \tag{6.14}$$

where y_p^* and y_p indicate the elements of $\mathbf{y}^*$ and $\mathbf{y}$, respectively, and $\bar{y}^*$ and $\bar{y}$ denote their mean values.

Considering a space described by all the elements from the synthetic and real datasets, the coefficient λ describes how the two datasets are reciprocally distributed in that space. Specifically, if λ is close to 1, the samples of the real dataset populate the same regions as the samples of the synthetic dataset and are similarly distributed in them. On the other hand, if λ is close to 0, the two datasets form two different clusters, and a DNN trained using the synthetic dataset would not learn much about the regions of the input space populated by real data, being ineffective in the prediction of the conductivity distribution.

Deep neural network

In this study, the Sheffield measurement protocol [183] was employed, which is also known as the adjacent interrogation pattern and generates $Q - 3$ voltage measurements for each current interrogation. Specifically, the data acquisition process consists of injecting direct current to adjacent pairs of electrodes. For each pair, the resulting boundary voltages across all the other pairs of adjacent electrodes (except those that include the electrodes used for current injection) were recorded simultaneously. This process was repeated until DC was injected into all unique adjacent pairs of boundary electrodes. Thereby, the entire voltage dataset contains $Q(Q-3)$ voltage measurements, which are employed to build the $\mathbf{V}$ matrix.

The first ML tool employed in this work consists of a DNN with three hidden layers, each containing N neurons, in addition to the input and output layers (having $Q(Q-3)$ and M neurons, respectively). After the input layer, batch normalization was performed, followed by the fully connected hidden layers that implement an

exponential linear unit activation function. At the end of the network, one last fully connected layer operated as the output layer for regression, without any activation function.

The forward propagation of the network in the central hidden layers can be written as

$$\mathbf{x}_l = \mathrm{elu}\left(\mathbf{W}_l \mathbf{x}_{l-1} + \mathbf{b}_l\right) \tag{6.15}$$

where $\mathbf{x}_l \in \mathbb{R}^N$ and $\mathbf{b}_l \in \mathbb{R}^N$ are the output and the bias vectors of the l-th layer, respectively, while $elu(\bigcirc)$ represents the exponential linear unit activation function. $\mathbf{W}_l \in \mathbb{R}^{N\times N}$ is the matrix of the weights of the l-th layer (*i.e.*, containing the weights associated with the connections between the neurons of the $(l-1)$-th and the l-th layer). It should be noted that, since the input and output layers have different numbers of neurons, the size of $\mathbf{x}_l$, $\mathbf{b}_l$, and $\mathbf{W}_l$ vary accordingly between l=1 and l=4. Let $\mathbf{D}$ be the entire set of DNN parameters, defined as $\mathbf{D} = \{\mathbf{W}_1, \ldots, \mathbf{W}_l, \mathbf{b}_1, \ldots, \mathbf{b}_l\}$. The training procedure is conducted to determine the elements of $\mathbf{D}$ using the samples of the training dataset $\mathcal{T}_s$ as follows:

$$\mathbf{D} = \arg\min_{\mathbf{D}} \left(\|\delta\boldsymbol{\Sigma} - \boldsymbol{x}(\mathbf{D}, \delta\widetilde{\mathbf{V}})\|^2 \right) \tag{6.16}$$

where $\boldsymbol{x}(\bigcirc)$ is the output of the neural network.

Radial basis function network

RBFN is a feedforward neural network with a single hidden layer, which uses a Radial Basis Function (RBF) as a nonlinear activation function for each neuron. In this work, an RBFN with the number of neurons smaller than the space of the output ($N < M$) was used to approximate the output conductivity distribution. In particular, a Gaussian function ϕ_n was employed as the RBF for each n-th neuron, which is defined as follows:

$$\phi_n = \exp\left(-\frac{\|\delta\tilde{\mathbf{v}} - \mathbf{c}_n\|^2}{2b^2}\right) \tag{6.17}$$

where $\delta\tilde{\mathbf{v}}$ is a generic difference voltage measurement, and the centers $\mathbf{c}_n$ of the RBFs were selected as the centroids of the clusters

obtained using the k-means clustering algorithm on the set of training inputs. Moreover, given a vector $\mathbf{d}$ containing the Euclidean distances $\|\delta\tilde{\mathbf{v}} - \mathbf{c}_n\|$ between all the possible combinations of indices c, the spread parameter b is selected as:

$$b = \hat{d} + std(\mathbf{d}) \tag{6.18}$$

where $\hat{d}$ is the mean of the elements in $\mathbf{d}$ and is the same for all the RBFs. The results obtained by testing different RBFNs with different spread factors using a simulated validation dataset show that the parameter defined as in Equation (6.18) generally provides the best approximation of the reference conductivity distribution in this study. Given the RBFs, the output $\boldsymbol{x}$ of the RBFN was calculated using:

$$\boldsymbol{x} = \sum_{n=1}^{N} \mathbf{w}_n \phi_n \tag{6.19}$$

where $\mathbf{w}_n$ contains the weights associated with the connections between the neurons in the output layer and the n-th neuron in the hidden layer. The weight vectors $\mathbf{w}_n$ were determined upon defining the parameters of the RBFs (*i.e.*, $\mathbf{c}_n$ and b) by carrying out a training procedure of the network using the training dataset $\tilde{\mathcal{T}}$. Specifically, the following least-squares problem was solved:

$$\mathbf{W} = \delta\boldsymbol{\Sigma}\boldsymbol{\Phi}^{\dagger} \tag{6.20}$$

where $\mathbf{W} = [\mathbf{w}_1, \ldots, \mathbf{w}_N] \in \mathbb{R}^{M \times N}$ is the complete weight matrix, and $\boldsymbol{\Phi} \in \mathbb{R}^{N \times SC}$ is the matrix of ϕ_n for each instance $\delta\tilde{\mathbf{v}}^{(s,c)}$, while $\bigcirc^{\dagger}$ means the Moore-Penrose pseudoinverse of its argument.

Crack identification

This section presents the results obtained using the proposed machine learning framework to solve the inverse ERT problem in four specimens fabricated with two different techniques, the first based on Multi-Walled Carbon NanoTube and the second based on Graphene NanoSheet (GNS). The sensing layers were fabricated by depositing piezoresistive (*i.e.*, MWCNT or GNS-based) thin films on substrates consisting of PolyEthylene Terephthalate (PET) sheets.

The procedure to fabricate the MWCNT thin film consists of mixing 0.339 g of MWCNT with an outer diameter of 8 nm (NanoIntegris) and 0.806 g of N-Methyl-2-Pyrrolidinone (NMP) (Sigma-Aldrich) with 33.855 g of 2 wt.% Poly-(Sodium 4-Styrenesulfonate) (PSS) solution, obtained by dissolving the PSS (Sigma-Aldrich) into deionized water. The mixture was then immersed in an ice bath and subjected to high-energy tip ultrasonication (5 s on and 5 s off; 6.35 mm tip; 30 min at 30% amplitude) for 1 h to disperse the MWCNT. Lastly, an appropriate amount of latex solution (Kynar Aquatec) and DI water were added to the MWCNT dispersion to generate sprayable ink. This MWCNT ink fabrication process is described in detail by Wang and Loh [310].

The GNS-based ink was fabricated according to the process described by Lin et al. [311] and briefly reported herein. GNS, synthesized using water-assisted liquid-phase exfoliation [312], is added to ethyl cellulose (EC) solution and subjected to bath sonication to disperse the GNS properly. Then the mixer was heated to 60 °C and stirred for 12 min to make a sprayable ink.

The MWCNT-latex ink and GNS-EC ink were manually sprayed onto four 108×132 mm^2 PET substrates (two for each sensing material) using a Paasche airbrush. Each specimen was air-dried at room temperature for at least 12 h before use. After the thin film was completely dry, electrodes were attached along the boundaries of the specimen using copper tape strips. Colloidal silver paste (Ted Pella) was applied over copper tapes to reduce the contact impedance. 18 electrodes arranged in a 4×5 pattern were deployed. The fabrication procedure of the specimens is schematized in Figure 6.1.

Since PET sheets are flexible, the specimen and the electrodes were fixed on the table using electrical insulating tape. A razor blade was used to cut the specimen to simulate cracking of the substrate (representing a structural component coated by the sensing film).

For each specimen, a baseline voltage measurement $\mathbf{v}^{(0)}$ was taken before inducing the damage, when the specimen was intact. After each damage, a new voltage dataset $\mathbf{v}^{(c)}$ was then recorded and employed to calculate $\delta\overline{\mathbf{v}}^{(c)}$ according to Equation (6.8). ERT measurements were collected using a customized Data AcQuisition (DAQ) system consisting of a Keithley 6221 AC/DC generator (for

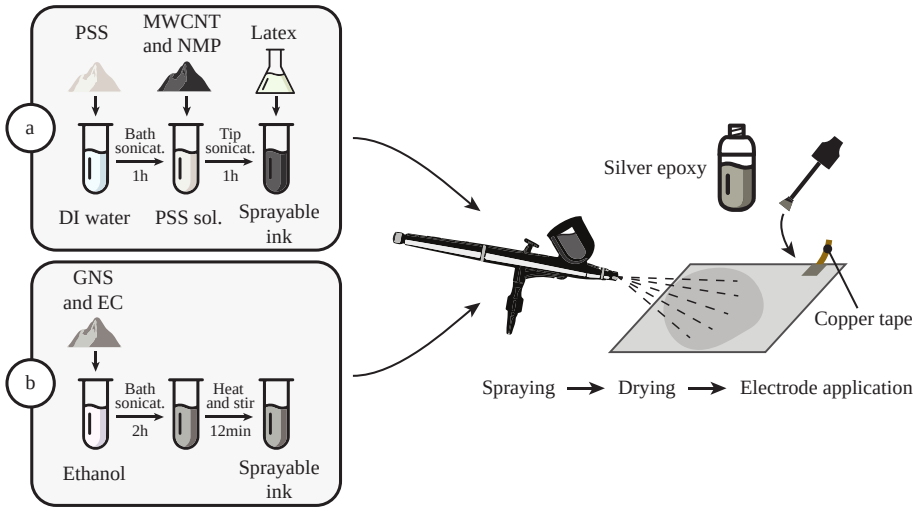

Figure 6.1: Fabrication process of the specimens: MWCNT-based (a) and GNS-based sensing surfaces (b)

boundary current excitations) and a Keysight 34980A multifunctional switch with an embedded digital multimeter (for switching and boundary voltage measurement). MATLAB was used to control the DAQ system using the adjacent interrogation pattern [183].

Following the procedure explained, two different synthetic datasets were generated to train the DNN employed for solving the inverse ERT problem in a defined region of interest of the interrogated body. Specifically, the first dataset was built by considering single and multiple polygonal areas, with random shape and position in the region of interest, where conductivity was reduced of a random factor. On the other hand, the second dataset was generated considering randomly-distributed line-shaped areas with zero conductivity in the sensing surface. These areas with reduced conductivity represent local defects in the monitored region. Two examples taken from these two datasets are reported in Figure 6.1, where the input (boundary voltage measurement) and output (related conductivity distribution in the region of interest) of the inverse problem are represented.

In an experimental campaign conducted using the four specimens described in Section 4.1, 16 difference voltage datasets were collected under different damage conditions, organized in column vectors $\delta\overline{\mathbf{v}}^{(c)}$ that constitute a real dataset $\delta\overline{\mathbf{V}}^{*}$. Two complete datasets $\delta\overline{\mathbf{V}}^{+}$

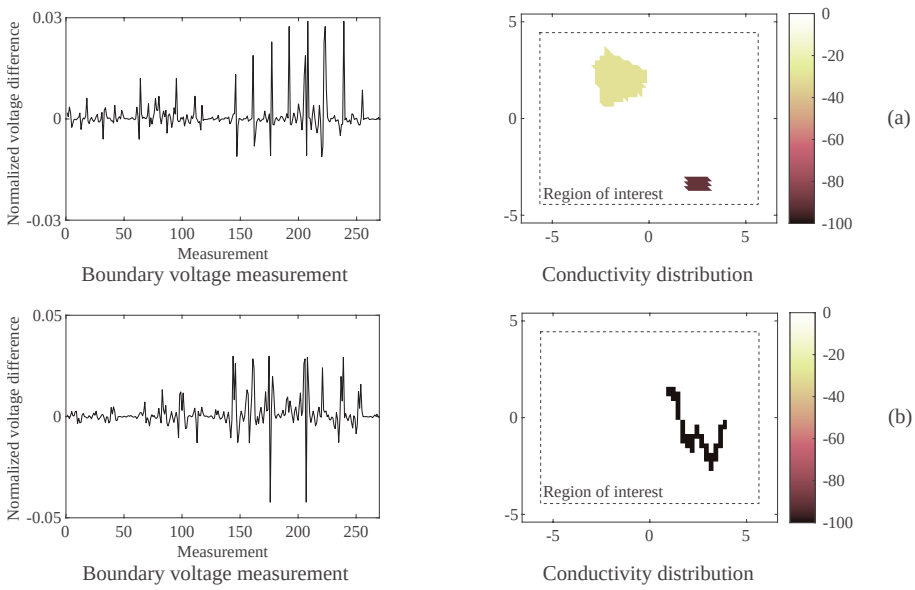

Figure 6.2: Two examples from the synthetic datasets built for training, consisting of pairs of conductivity distribution and related voltage measurement: polygonal defect (a) and crack-like defect (b)

were generated, the first including a synthetic dataset $\delta\overline{\mathbf{V}}$ containing 10000 instances representing polygonal defects, and the second including 10000 instances relevant to crack-like defects, in addition to the mentioned real dataset $\delta\overline{\mathbf{V}}^*$.

In order to understand which synthetic training dataset is the most appropriate for the application presented in this work, two sets of 100 SOMs were trained using the two complete datasets. More than a single SOM is considered in this study since training starts with a random selection of weights and may lead to slightly different results. Two examples of SOMs trained using the two complete datasets are reported in Figure 6.3a-b. The grey hexagons represent the neurons of the SOM, and the colors of the map are representative of the Euclidean distance between couples of neurons. Specifically, yellow indicates close neurons, while dark red denotes large inter-neuron distances. Thereby, yellow areas denote dense regions in the K-dimensional voltage space, while red areas signify remote regions. The black full hexagons in the gray grid represent the sample hits of the synthetic (top figures) and real (bottom figures) datasets obtained for the SOMs by classifying the synthetic and real

portion of the complete training datasets, respectively. Since the real dataset is much smaller than the synthetic one for lack of real recordings, some neurons are empty in the bottom figures, *i.e.*, they do not classify any real measurement. It should be noted that the real instances are the same for the two cases reported in Figure 6.3a-b. However, a different structure of the SOM can lead to a different sample hit map.

The sample hit distributions of the synthetic and real datasets, normalized with respect to their maximum values, can be compared by calculating the correlation coefficient reported in Equation (6.14). As aforementioned, the correlation coefficient measures the similarity between the synthetic and real space structure and is indicative of the suitability of a synthetic dataset to train a supervised machine learning tool able to predict the real instances. The average correlation coefficients λ calculated on 100 training procedures (*i.e.*, generating 100 different SOMs) are 0.7871 and 0.9245 for the datasets obtained for polygon and crack-like defects, respectively. These results indicate that the structure of the synthetic dataset representing

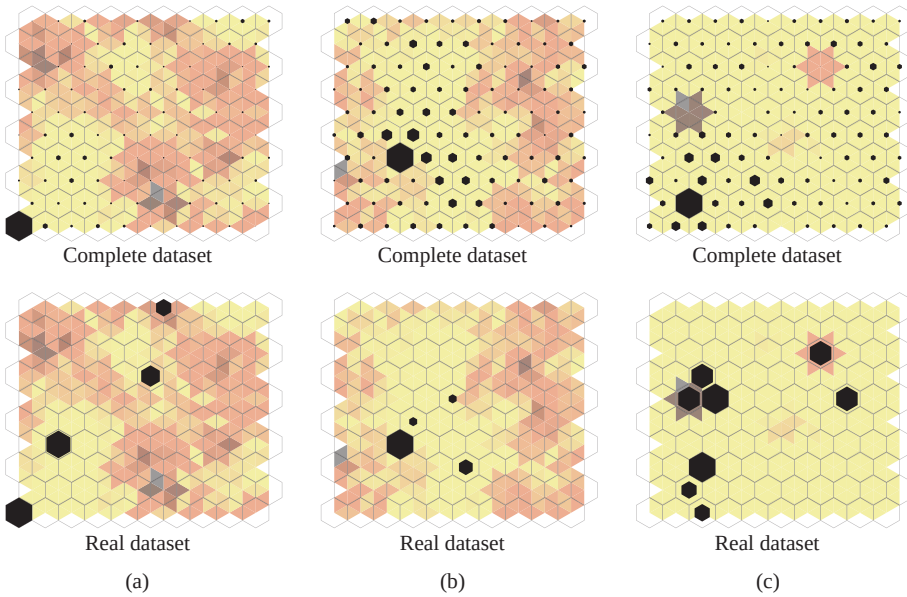

Figure 6.3: SOMs obtained for polygonal defects with normalized voltage data (a), crack-like defects with normalized voltage data (b), and crack-like defects with non-normalized voltage data (c); the size of full black hexagons is proportional to the sample hits of synthetic (top figures) and real (bottom figures) voltage data

crack-like defects is more similar to that of the collected voltage measurements.

It is worthy to note that the normalization performed in Equation (6.8) is of fundamental importance since training the SOM with non-normalized data would lead to the result reported in Figure 6.3c, where synthetic and real data populate different regions of the voltage space. Indeed, two remote spots in the SOM are clearly visible, which only include real instances. In the case of non-normalized data, the average correlation coefficient calculated on 100 training procedures would be only 0.1943, representing a training dataset that is poorly effective in predicting the real instances.

The normalized synthetic dataset representing crack-shaped defects is thus used to train a DNN employed to reconstruct the conductivity distributions associated with the real voltage measurements collected from the four specimens described above. Figure 6.4 and Figure 6.5 show the reconstructed conductivity distributions corresponding to the damage states induced by cutting the two MWCNT-based sensing specimens using the razor blade in the highlighted locations (red dashed lines). Specifically, Figure 6.4a and Figure 6.5a plot the results obtained using the presented ML-aided method. Here, the values in the color bar (0-100) are representative of a dimensionless conductivity reduction associated with the normalized voltage measurement. For comparison purpose, Figure 6.4b and Figure 6.5b show the results obtained with the TV method, using a weight α equal to 10^{-6} for the regularization matrix (see Equation (6.6)).

These two figures show that small cracks are generally correctly identified in both specimens. Concerning the ML-aided approach, as the crack size increases, a higher noise amount populates the reconstructed distribution. Also, the shape of multiple cracks cannot be properly recognized since the defect is reconstructed as a single connected region with low conductivity. Nevertheless, an approximate estimate of crack extension and location can always be identified. Besides, the magnitude of identified conductivity reduction is almost constant for the different damage cases, allowing easy identification of small defects. On the other hand, the shape of the damaged regions identified using the TV method is very similar

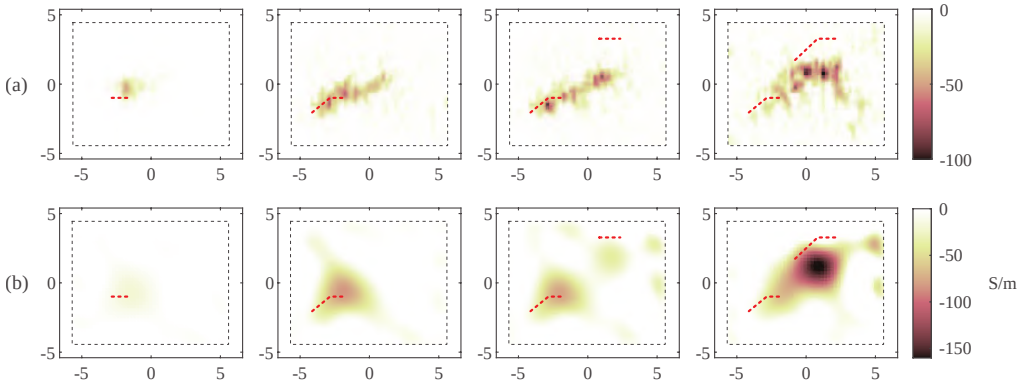

Figure 6.4: Conductivity distribution reconstructed for Specimen #1 through the TV method (a) and the ML-aided approach (b); reference cracks are reported as red dashed lines

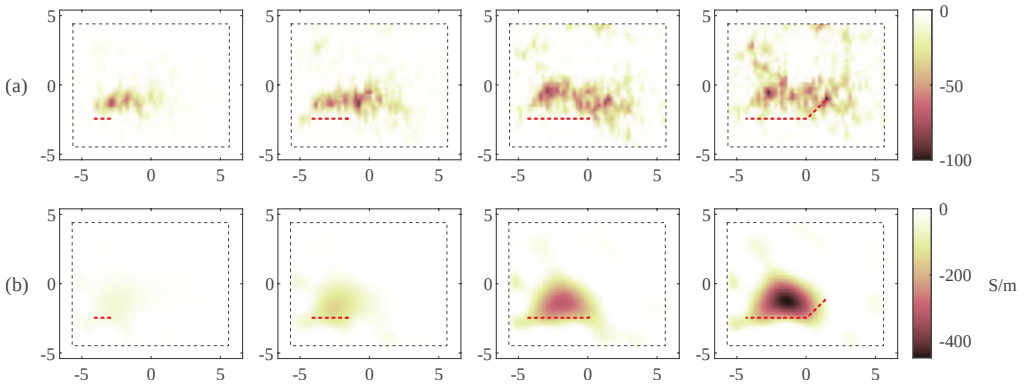

Figure 6.5: Conductivity distribution reconstructed for Specimen #2 through the TV method (a) and the ML-aided approach (b); reference cracks are reported as red dashed lines

between the different damage cases of the same specimen, changing in magnitude. This result makes understanding how damage is evolving particularly challenging.

As in the previous cases, Figure 6.6 and Figure 6.7 show the reconstructed conductivity distributions obtained using GNS-based specimens. In general, a less detailed reconstruction of the conductivity distribution is identified in this case. Considering Specimen #3, small defects are well localized and quantified (in terms of size) using the ML-aided approach. Besides, although the direction of the reconstructed crack is slightly different from that of the reference damage, the crack extension and location are well approximated. On the other hand, the results obtained using the TV method represent

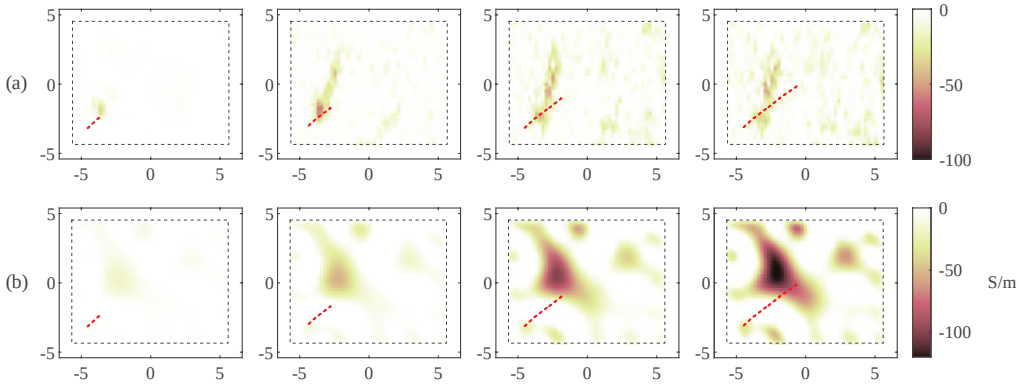

Figure 6.6: Conductivity distribution reconstructed for Specimen #3 through the TV method (a) and the ML-aided approach (b); reference cracks are reported as red dashed lines

the damage magnitude but do not provide accurate conductivity reconstruction. Considering Specimen #4, the small crack in the first damage state is not identified by any of the two methods. This result may be due to the selected interrogation pattern. Indeed, it is well known that the Sheffield measurement protocol is generally more sensitive to conductivity variations close to the boundary of the interrogated specimen [180]. On the other hand, an "opposite" [312] interrogation pattern would be more sensitive to conductivity variations in the central sensing region as the current travels more uniformly through the imaged body and is less sensitive close to the boundary [180]. The use of different interrogation patterns will be investigated in further research. Using the TV method, the second and third crack evolution in Specimen #4 are identified as a conductivity reduction that increases in magnitude as the crack size grows. The conductivity distribution reconstructed using the ML-based method in the last two scenarios also presents a wider low-conductivity region in the middle of the sensing area; however, the two cracks of the last damage case are not clearly distinguishable.

Strain sensing

This section reports the results obtained for strain sensing with the MWCNT-based paint in two different applications. First, the smart paint was applied to an elastic foam and the strain state was impressed by loading the specimen perpendicularly to the

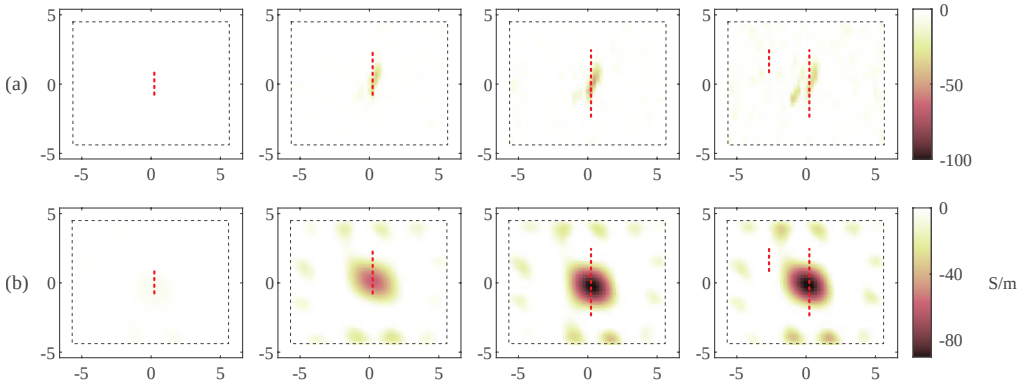

Figure 6.7: Conductivity distribution reconstructed for Specimen #4 through the TV method (a) and the ML-aided approach (b); reference cracks are reported as red dashed lines

sensing film. In this case, out-of-plane loads induced in-plane Poisson expansion of the coated sensing material. Second, the smart paint was spray-coated onto a patterned substrate to form a sensing mesh for distributed strain monitoring. In this case, the substrate is a plastic support subjected to three-point bending tests.

In the first application, the MWCNT-latex ink was manually spray-coated onto 214×230 mm^2 Smartfoam specimens (15DC-3G) produced by Nano Composite Products (NCP, Orem, UT) using a Paasche airbrush. Each specimen was then air-dried at room temperature for at least 12 h before use. After the thin film was completely dry, multi-strand wires were deployed along the boundaries of the specimen using copper tape and silver epoxy (provided by MG Chemicals) to form the electrodes. A total of 26 electrodes arranged in a 6×7 pattern was prepared as shown in Figure 6.8a. Since the foam was flexible and soft, the specimen was fixed to a rigid 3D-printed PLA support.

Prior to the start of any test, baseline ERT measurements of the unstrained nanocomposite-enhanced foam were obtained. ERT measurements were collected using a customized DAQ system consisting of a Keithley 6221 AC/DC generator (for boundary current excitations) coupled with a Keysight 34980A multifunctional switch with an embedded digital multimeter (for switching and boundary voltage measurement). MATLAB was used to control the DAQ system using the adjacent interrogation pattern. It should be mentioned

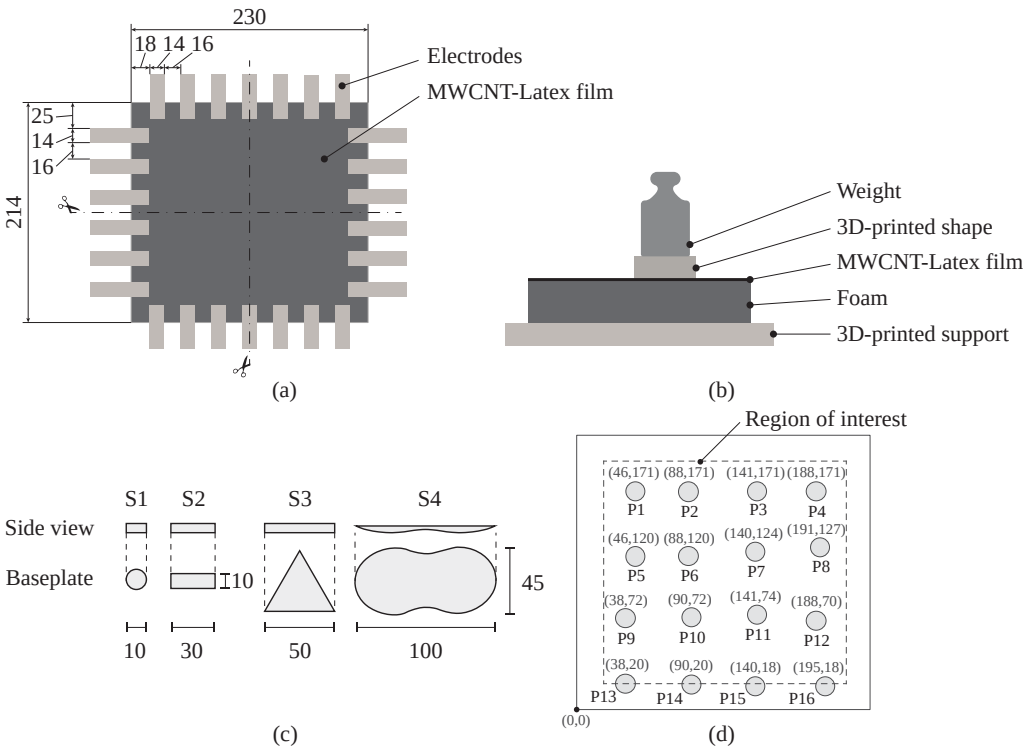

Figure 6.8: Schematic of the sensing specimen and ERT boundary electrodes (a); test setup for applying pressure hotspots (b); 3D-printed shapes to control contact area (c); and location of hotspots and coordinates of their centers (d). All dimensions are shown in millimeters

that DC was injected across a pair of boundary electrodes, while voltage magnitudes across all other adjacent pairs were recorded.

Two sets of pressure sensing tests were performed, both using the setup illustrated in Figure 6.8b. Test #1 was aimed at investigating whether the proposed sensing solution could accurately determine the location of pressure hotspots. In order to keep the contact area as constant as possible throughout the test, the S1 3D-printed PolyActic Acid (PLA) disc represented in Figure 6.8c with a diameter of 10 mm was inserted between a weight and the sensing specimen. A mass of 200 g was placed at 16 different positions on the nanocomposite-enhanced foam as shown in Figure 6.8d, and ERT measurements were obtained for each position. Test #2 aimed to characterize the accuracy of identifying different pressure shapes. In this case, three 3D-printed PLA shapes (*i.e.*, S2, S3, and S4 shown in Figure 6.8c) were placed at different positions on the sensing surface. Specifically,

a mass of 500 g was used for shape S2, 1 kg for shape S3, and 4 kg for shape S4. Similar to Test #1, ERT measurements were recorded after each pressure hotspot was introduced.

The nanocomposite-enhanced foam was modeled according to Figure 6.9a, with 9716 elements for the FE model and electrodes modeled as void areas. CEM conditions were imposed at the boundary of each electrode (*i.e.*, at the interface between the sensing film and the silver epoxy) as shown in Figure 6.9a. The experimental test setup is shown in Figure 6.9b, and the specimen resembles the FE model.

A training dataset was built following the algorithm by numerically solving the forward problem for polygonal conductivity variations shown in the previous sections. This dataset was then used to train a DNN and a RBFN. A set of $C = 15000$ random polygons within a rectangular region of interest of 3690 elements (see Figure 6.9a) were generated using the following parameters: $P = 4$, R_p=70 mm, and $K_p = 5$. The conductivity within the resulting area was reduced by a random value between 0% and 100% for each case. In order to improve the robustness of the training process, jitter was included in the training dataset with $\gamma = 0.01$ and $S = 5$.

The DNN used to solve the ERT inverse problem was designed as follows. After the input layer, which contains 598 neurons (*i.e.*, the size of voltage measurements for each inspection), four hidden fully-connected layers, each containing 2048 neurons and followed by exponential linear unit activation functions, were employed. At

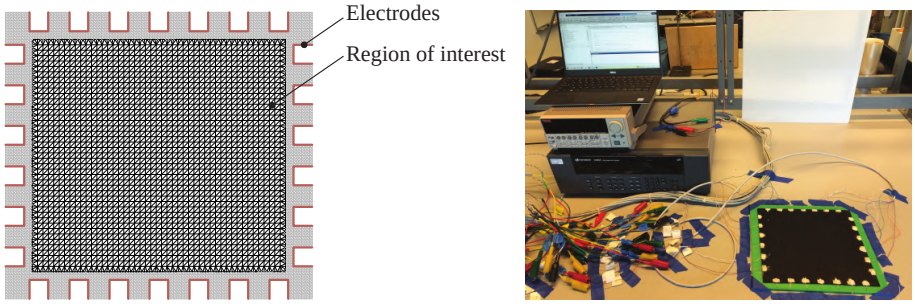

Figure 6.9: FE model of the specimen (a) and experimental setup (b)

the end of the network, a fully connected layer with 3690 neurons without activation functions was used, which has a size equal to the number of elements that constitute the region of interest in the FE mesh. The network was trained using the extended training set (*i.e.*, including jitter) that contains 75000 different cases, employing 30 epochs of the Adam optimization algorithm [313], with an initial learning rate equal to 0.001, which decreases every 10 epochs with a drop factor of 0.1. The denominator offset is 10^{-8}, and the decay rate of the gradient moving average is 0.9, while the batch size is 128.

On the other hand, the RBF network consists of a single fully connected layer containing 100 neurons activated by Gaussian RBFs. The centers of the kernel functions were selected as the centers of 100 clusters determined using the k-means algorithm on the jittered training dataset, while the spread parameter b was determined as explained in (6.18). The RBF network was trained by solving the least-squares problem of (6.20) while considering the full dataset containing 75000 cases.

First, Test #1 was performed, and the datasets were used for solving the ERT inverse problem using difference imaging and the TV method. Figure 6.10 plots the conductivity distribution changes between each applied pressure hotspot with respect to the baseline. Specifically, an α factor equal to 10^{-6} and a single iteration of the TV method were employed to generate these results. The location of the largest conductivity variation was, in general, correctly identified, as can be seen in Figure 6.10 (the reference locations of applied loads are represented as dashed red circles). However, the shape and size of the pressure hotspot (*i.e.*, using the S1 baseplate shown in Figure 6.8c) are not clearly visible due to the several artifacts present in the reconstructed change in conductivity distributions. It should also be noted that the magnitude of the conductivity changes (here expressed in S/m) were also inconsistent despite the applied pressure being the same. In fact, conductivity change is generally higher when the load was applied closer to the electrodes, which is consistent with previous reports of nonuniform sensitivity between the center and boundary regions [314]. Overall, the average computing time to solve the ERT inverse problem using the TV method was 0.65 s using MATLAB (R2020b version) running on

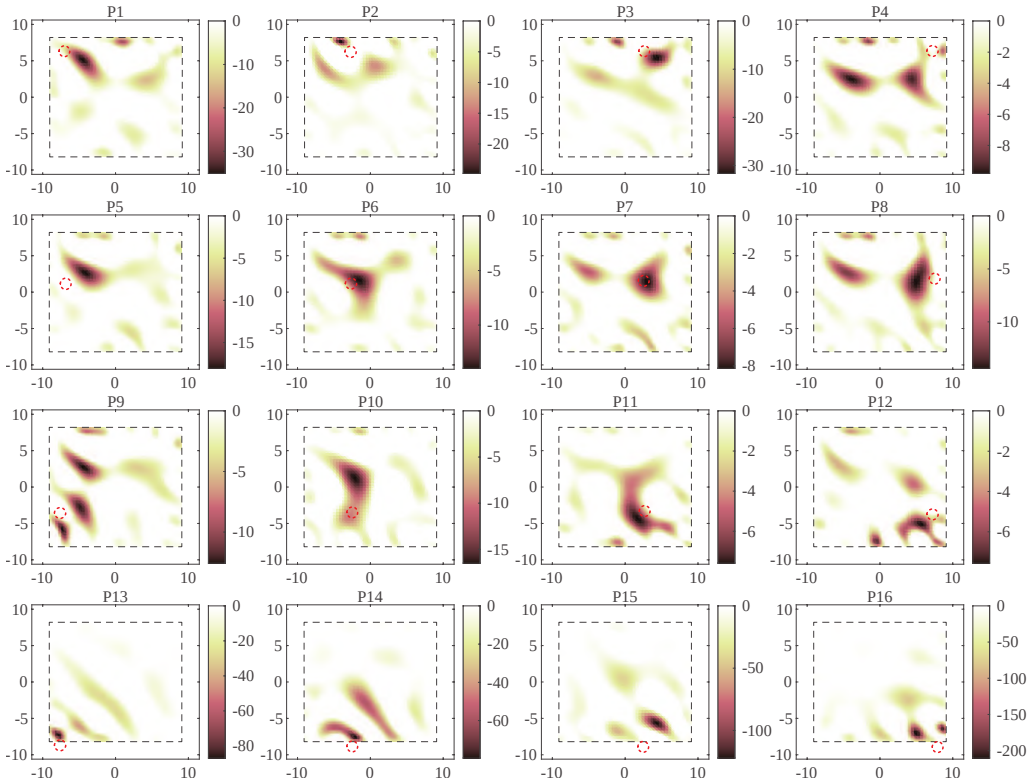

Figure 6.10: Conductivity distributions obtained using the TV method for Test #1

an Intel®Core™ i7-8700 6@3.20 GHz-processor CPU with 2GB NVIDIA Quadro P620 GPU, 32GB RAM, and Windows 10 operating system.

On the other hand, Figure 6.11 and Figure 6.12 show the results for Test #1 when the ERT datasets were processed using the DNN and the RBFN methods, respectively. Specifically, the elements in the output vector generated by the ML algorithms are represented on a 2D map corresponding to the respective mesh elements. Compared to the results of Figure 6.10, the DNN-based method provides a much higher resolution of detecting pressure hotspots, where the actual size and location of the footprint are generally accurately identified, while noise artifacts are minimized (Figure 6.11). The reconstruction process takes on average 0.005 s using the trained DNN running on the same hardware system (*i.e.*, less than two orders of magnitude as compared to the TV method). This considerable

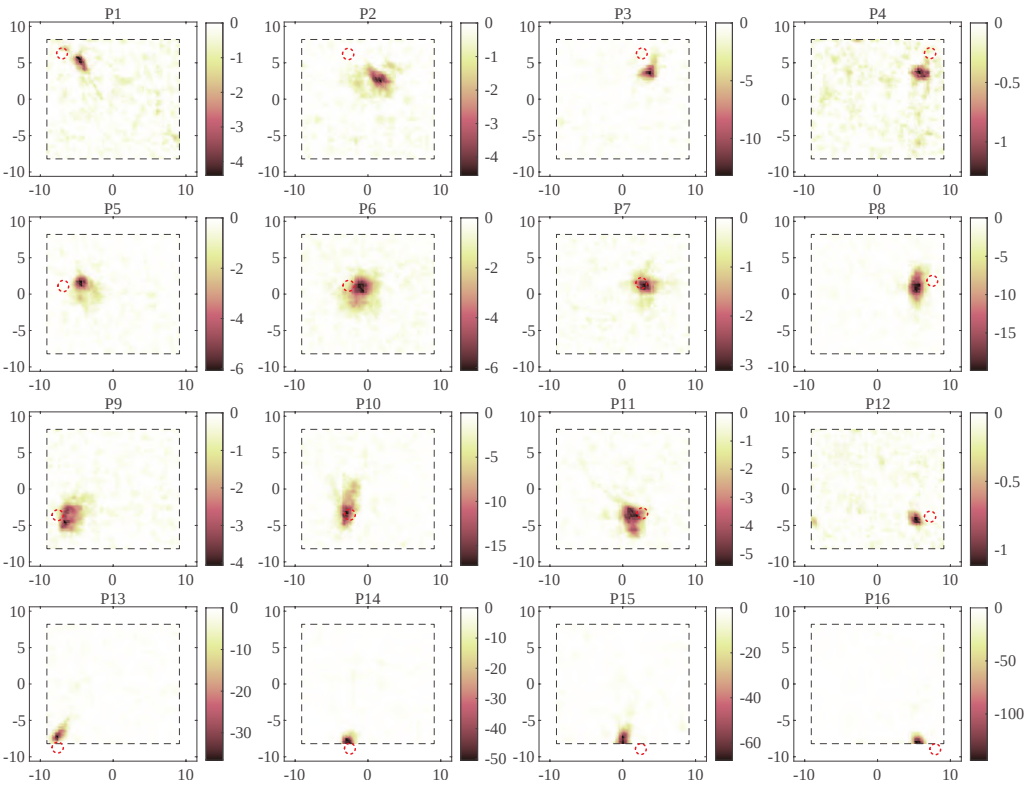

Figure 6.11: Conductivity distributions obtained using the DNN-based method for Test #1

improvement in computing performance is due to the nature of the feedforward process employed by DNN to solve the ERT inverse problem, which does not require performing demanding matrix inversion operations.

The results obtained using RBFN in Figure 6.12 have a visibly lower resolution as compared to DNN (Figure 6.11). Although hotspot location in each image is generally well estimated, noise artifacts are more regular as compared to the results of the TV method (Figure 6.10). The main advantage of the RBFN-based method is its computational time, which was significantly lower and was on average 0.003 s for each reconstruction. Moreover, due to the limited number of neurons employed in the network, the RBFN has 100 weights for each output value or 369000 weights in total. In contrast, DNN uses over 21 million weights and is difficult to track, especially when these algorithms are implemented and executed

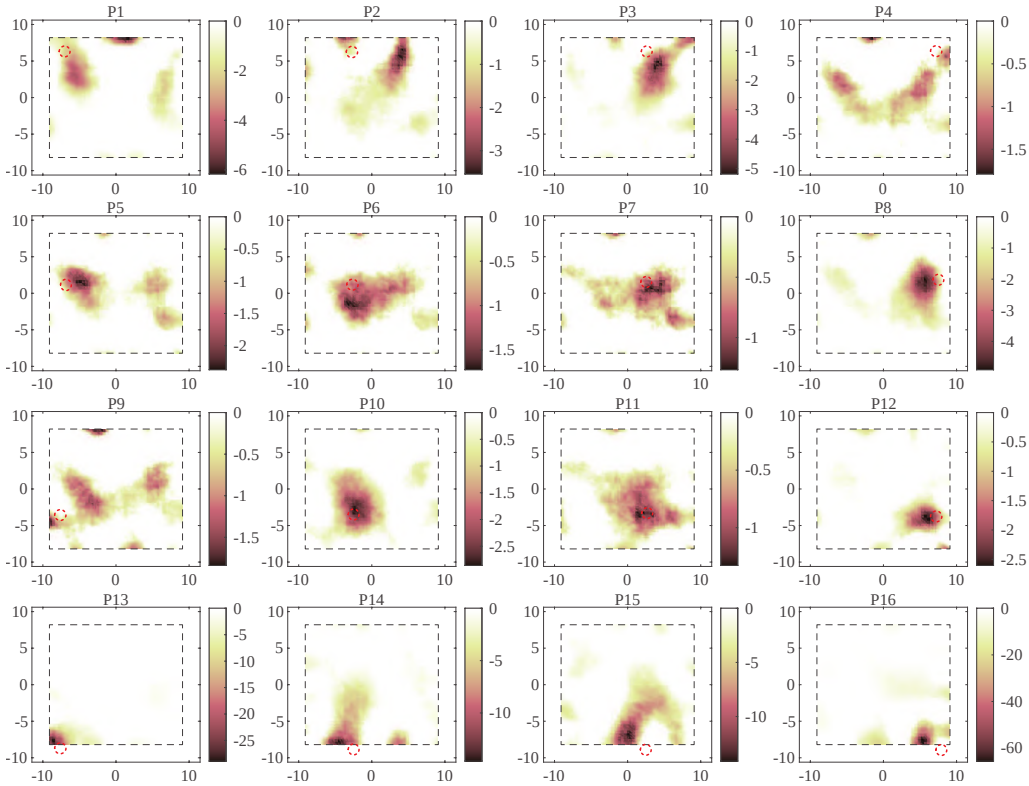

Figure 6.12: Conductivity distributions obtained using the RBFN-based method for Test #1

using portable computing nodes such as microcontrollers.

Overall, both ML methods provided conductivity reduction magnitudes that are almost proportional to those obtained by the TV method, which confirmed the efficacy of the adopted normalization process. However, the estimated magnitude was not only dependent on the load but also on the location on the sensing surface. This result could be due to the uneven thickness (and hence resistance) of the sensing specimen or local phenomena that affected areas close to the electrodes.

Second, the results for Test #2 are shown in Figure 6.13, where Test #2 corresponded to the case when different footprints or contact pressure patterns were applied to the nanocomposite-enhanced foam. Different weights were placed onto rectangular, triangular, and figure-eight baseplates and on the sensing specimens. Figure

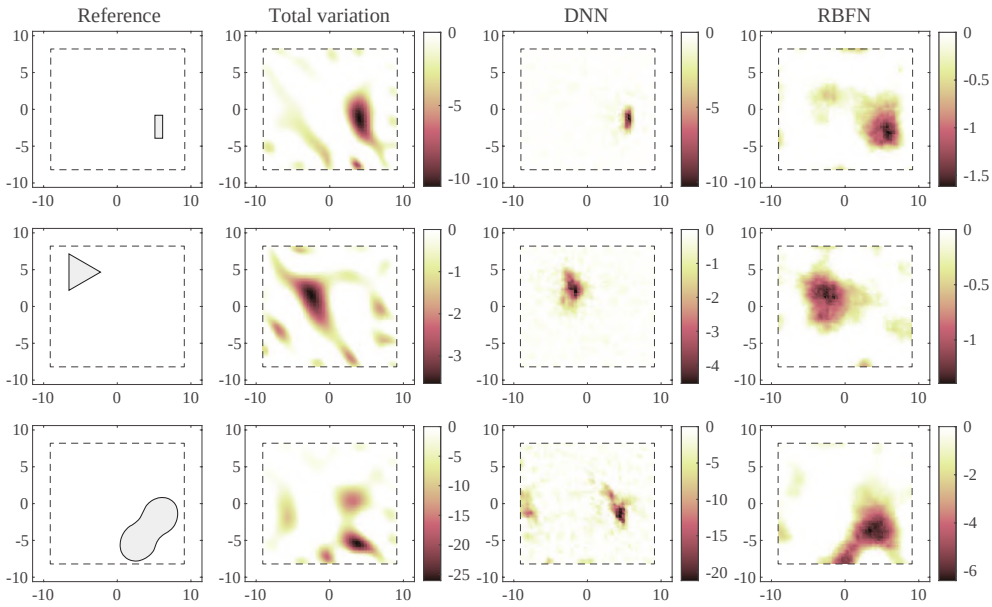

Figure 6.13: Conductivity distributions obtained for Test #2

6.13 shows that, although DNN generally provides a more accurate localization and shape reconstruction for small pressure hotspots, it behaves worse for distributed loads, as is visible from the results for the figure-eight baseplate. On the other hand, RBFN is more robust, although it did not accurately reconstruct the contact pressure shapes.

In the second strain sensing application, the nanocomposite paint was spray-coated onto the rough side of a thermoplastic polyurethane (TPU) sheet substrate, acquired from Wiman Corporation, using a Paasche airbrush. The substrate was then laser cut (using the Silhouette Cameo 3) into a grid-like pattern and applied to a PolyVinyl Chloride (PVC) support using epoxy. The total size of the sensing grid was 111×59 cm, with the geometric details shown in Figure 6.14. Ten electrodes were applied on the outer boundary of the sensing mesh at all the boundary intersections between vertical and horizontal sensing stripes.

The support was subjected to three-point bending tests, positioning the specimen in the test machine with the sensing mesh on the lower face, *i.e.*, the part subjected to tensile strain. Three increasing

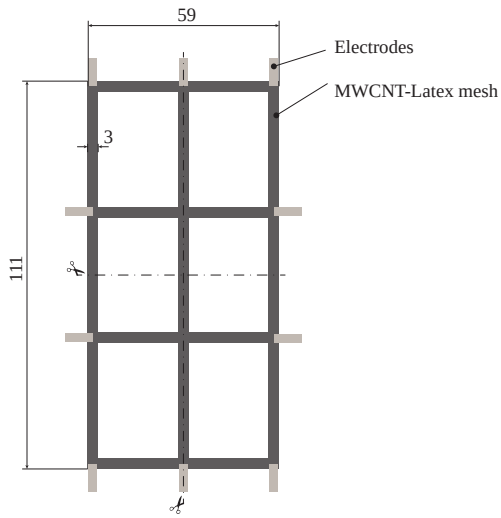

Figure 6.14: Geometry of the sensing mesh

displacement levels (1 mm,2 mm, and 3 mm) were induced at the load locations shown in Figure 6.15. The two contrasts at the extrema of the support make it behave as a simply-supported beam, as shown in Figure 6.16. In test #1 and test #2, the supports are perpendicular to the support axis. On the other hand, in test #3, the support is rotated, as shown in Figure 6.15 and Figure 6.16.

Before applying the load to the specimen, baseline voltage recordings are collected for each test. Then, a new voltage measurement is collected for each step of the increasing displacement.

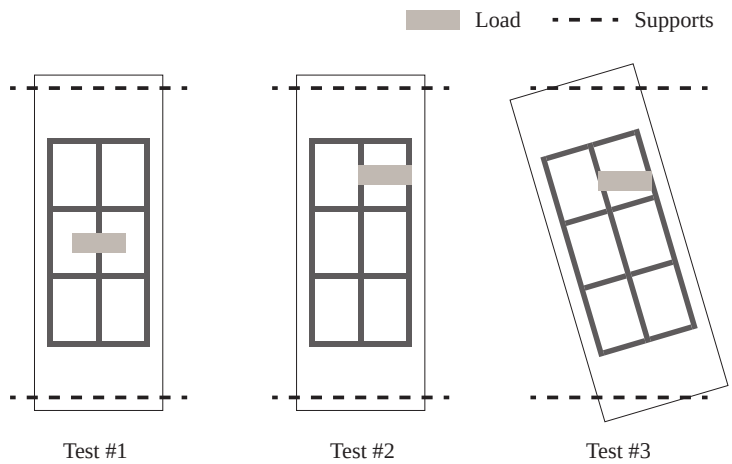

Figure 6.15: Schemes of the bending tests

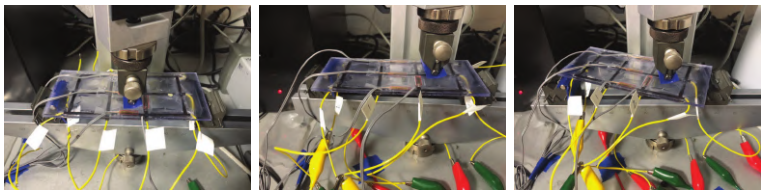

Figure 6.16: Experimental setups of the bending tests

An FE model was employed to generate a training dataset. The vertical and horizontal stripes of the mesh and their intersections were modeled using only two triangular elements each, thus considerably reducing the complexity of the model and limiting the degrees of freedom of the conductivity distribution. The training dataset consisted of 10000 instances, generated by assigning random conductivity variations to each stripe.

The RBFN described in the previous sections was employed to identify the strain distribution from collected voltage measurements. It should be noted that, since the model complexity is very low (each stripe can have just one conductivity value), the network layout can be simplified considerably compared to the other applications. Indeed, a RBFN with 10 nodes was employed, with centers and spread parameter determined in the same way as the previous application.

Figure 6.15 shows the results obtained for the three bending tests illustrated in Figure 6.14b. The longitudinal elements (represented with a vertical orientation in the reported schemes) present a conductivity reduction proportional to the strain state of the lower face fibers of the deflected specimen. On the other hand, due to the Poisson effect, the horizontal elements present a slight increment in the conductivity distribution. As in the last cases, the colormap is not representative of real measure units due to the normalization process.

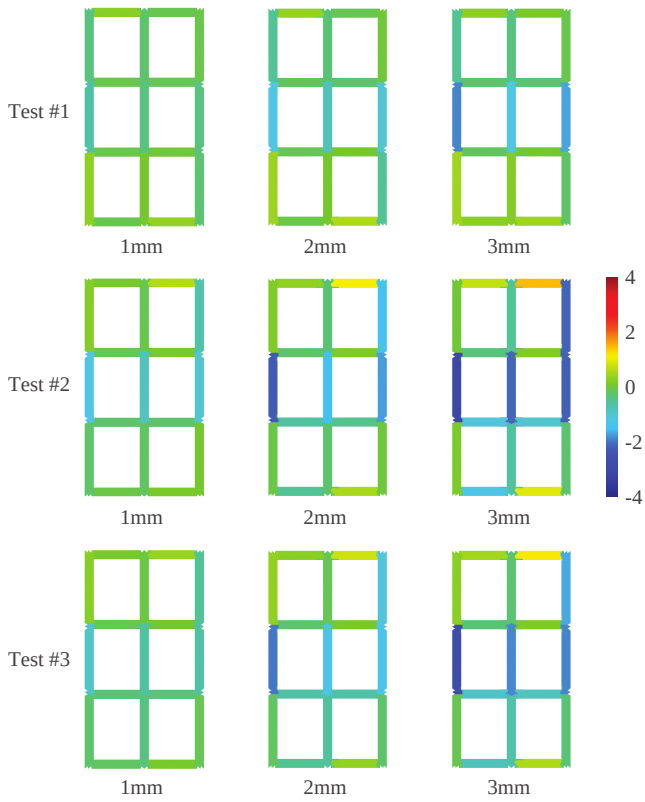

Figure 6.17: Conductivity distribution of the sensing mesh identified for different displacement levels in the three bending tests

7 Conclusions

The built environment is a complex system of structures, people, and nature, closely interconnected and interacting. This is the main reason why vibration-based structural health monitoring is particularly challenging in dense urban environments. Here, civil structures are not individual entities, and operators should consider several factors to assess their health state from a holistic perspective. Moreover, people make this picture even more complicated with their daily activities: vehicles induce quasi-static displacements on bridges, while individual or group activities, such as running and walking, can induce vibration with a narrow frequency band to urban infrastructure. Together with the phenomena related to natural and meteorological actions, such as earthquakes and wind, all these factors constitute a large and manifold set of excitation sources with particular properties rarely considered in traditional SHM methods.

It is also true that the structural vibration response induced by these effects contains valuable information which may help decision-makers in scheduling maintenance or managing emergencies.

Thanks to the recent advent of low-cost sensing systems, vibration-based SHM is increasingly used for minor structures and infrastructure. Moreover, smartphones are sensing devices widespread and always connected to the Internet, ready to transmit collected data.

This thesis mainly investigated three monitoring scenarios:

Scenario 1: Civil structures instrumented with dense low-cost sensor networks subjected to nonstationary excitation induced by nearby traffic, earthquakes, and weather-related sources.

Scenario 2: Bridges instrumented with sparse sensor networks subjected to direct vehicular traffic.

Scenario 3: Light bridges and footbridges, without any specific monitoring instrumentation, crossed by micromobility vehicles, such as bicycles, instrumented with smartphones that operate as moving sensors.

Although these scenarios consider everyday situations in the urban and extra-urban environment, several challenges still hamper vibration-based SHM methods due to particular phenomena related to excitation or data management. Besides, in some cases, vibration measurements are not enough to assess the structural state of health due to the complexity of the built environment.

This thesis presented original monitoring strategies, proposed novel signal processing algorithms, and tested innovative technologies to exploit the specific properties of the vibration response in the considered scenarios.

This final chapter reports the conclusions and open topics of this study.

7.1 Multivariate data and their inner relations

This thesis presented an original algorithm for the identification of instantaneous modal parameters suitable for time-varying linear and nonlinear systems. This method mainly consists of filtering and the filter construction is based on the inner relations between different recording channels.

In particular, the Modal Assurance Distribution was presented, a novel time-frequency representation for multivariate signals. In contrast to other signal processing methods, this distribution does not represent the energy density of the signal in the time-frequency

plane. On the other hand, it represents the similarity between instantaneous Operating Deflection Shapes computed for neighboring narrow-frequency band components. In the proposed algorithm, the decomposition into signal subbands is performed using the discrete wavelet packet transform (or its stationary variant), implemented into efficient algorithms for near-real-time applications. Two criteria are also presented to improve the readability of the MAD, which generally presents random similarities in non-modal ODSs. The first involves using a forgetting factor, while the second consists of a noise-assisted procedure, which does not corrupt the final results, as it happens instead in the ensemble empirical mode decomposition if the number of trials is low. Indeed, in the presented algorithm, noise is only used to create a mask to select signal components.

Moreover, an original decomposition algorithm based on Decomposition Algorithm based on Modal Assurance was presented to extract decoupled modal responses by applying a MAD-driven watershed segmentation and a clustering process. The MAD has shown to be particularly suitable for watershed segmentation, as the areas associated with different modes are well-separated by low values in the time-frequency distribution. However, using a forgetting factor may lead to local inaccuracies, which are limited to the intervals where structural dynamics vary abruptly. The two main hyperparameters of the DAMA were discussed, also proposing a selection criterion based upon the analyzed signal.

The analyses conducted on a first simulated case study demonstrate the potential of the method, showing low sensitivity to narrowband disturbances and performing well with vanishing modes and considerable variations of the dynamic features. Besides, the results of the second case study show the applicability of the identification method to signals collected on real structures, even under varying excitation with non-stationary amplitude. Accurate results are obtained, especially for the lower modes, both in instantaneous natural frequencies and mode shapes. The results obtained for the first case studies were compared to those obtained using the EMD and its multivariate variant, two of the most used algorithms to process nonstationary signals. These results showed clear mode mixing issues and the inability to identify vanishing modes.

An intuitive visualization criterion of multivariate datasets was also outlined, showing superior performances over well-known traditional time-frequency representations since it also enables the users to discern between different modal components and damage conditions using a particular color coding.

Clustered Filter Banks were also presented in this thesis as a variant of the MAD for distributed computing applications in wireless smart sensor networks. A new decentralized algorithm for online signal decomposition was proposed in this context. The algorithm consists of two steps: (1) initialization, in which a CFB is built based on a window of collected data, and (2) real-time analysis, in which the sensing nodes process the recorded signals and the monitoring station performs the instantaneous modal identification and post-processing operations. The study showed that a periodic refreshing of the CFB may be necessary to minimize errors and identify considerable variations in modal parameters. The *Fejér-Korovkin* wavelet function has shown particularly suitable for implementation in this algorithm since it allows the construction of perfect reconstruction filter banks of modest length, compared to other wavelet functions.

The Teager energy operator was used in the decentralized algorithm to identify natural frequencies, showing particularly fast and sufficiently accurate after applying a median filter. However, it involves an increase in the identification delay. In a "static" CFB implementation (*i.e.*, without refreshing), instantaneous natural frequencies and mode shapes of a full-scale bridge tested under ambient vibration were accurately estimated in early damage configurations. Specifically, modal parameters were correctly identified for the damage configurations that induced a percentage variation of the structural frequencies up to 10% with respect to the baseline condition (used to build the CFB). Refreshing the CFB , the accuracy increases considerably for all the considered damage configurations.

A simplified process to build the CFB considers only a few reference sensors. The results obtained from the case study showed that the efficacy of this method strongly depends on the choice of reference locations. However, good results with less computational

burden can be obtained by selecting the reference sensors not too close to the nodes of the main mode shapes.

An example of real-time damage identification was also studied using the deflection shape obtained by estimating the flexibility matrix as a damage-sensitive feature. For this purpose, the instantaneous uniform load lines were computed over time, and the percentage displacement variation was considered a damage index. Outlier analysis allowed detecting and locating the damage.

A variant to the DAMA was also proposed to identify the nonlinear normal modes of nonlinear structures during seismic excitation. In particular, the MAD was used to extract signal features, processed using a self-organizing map, and clustered through the k-means algorithm. The dimensionality reduction allows the user to select the number of clusters and automates the identification process. In this implementation, using the stationary wavelet packet transform to build the filter banks used for signal decomposition enables the application of the algorithm to short and strongly non-stationary recordings. Therefore, the procedure is suitable for seismic structural health monitoring applications. Indeed, accurate estimates of the instantaneous modal parameters are identified for numerical and real case studies. Nevertheless, the main advantages over literature techniques lie in the immunity to mode mixing issues (in contrast to EMD-based algorithms) and the ability to identify vanishing components prevalent during earthquakes. Moreover, compared to the traditional time-frequency representations, the MAD is not directly dependent on the amplitude of wavelet components, thus resulting in a distribution that is not generally dependent on the nature of the excitation. This aspect is of the utmost importance when dealing with seismic excitation.

The method proposed can be applied to identify instantaneous structural parameters during seismic events and investigate the condition of maximum excursion in the nonlinear field, which may provide valuable information about ongoing damage, such as disclosing the presence of breathing cracks.

For the considered case studies, the inter-story drifts and the curvature of the uniform load lines were analyzed to detect and

localize the damage, showing good agreement with the theoretical results, visual inspections, and displacement recordings.

As a further aspect of this study, a novel strategy is also proposed to compress collected data and update identified parameters online and efficiently. This process is particularly advantageous for dense or large line-topology sensor networks, very suitable for bridges. This study showed that no relevant information is lost due to data compression while reducing the weight of transmitted data considerably. The procedure is thus particularly promising for applications involving wireless technologies.

The proposed method was tested on a real case study, simulating a dense wireless sensor network in line topology. The results showed a considerable reduction in data weight by properly selecting the number of singular components used to factorize the collected data matrix. Moreover, power consumption is homogenized throughout the network, in the perspective of optimizing maintenance interventions. Moreover, the approximated data matrix reconstructed at the end of the linear network (*i.e.*, onboard a coordinator node or through cloud computing) is usable to identify accurate modal parameters, which are also sensitive to early damage.

The idea of measuring the similarity in neighboring ODSs, obtained through multivariate data, was already successfully used in the well-known enhanced frequency domain decomposition algorithm to identify modal parameters in the frequency domain. This concept was extended in this study to operate in the time-frequency domain, giving rise to a set of new signal processing algorithms with limited assumptions suitable for SHM applications in the complex built environment.

In all the proposed algorithms, the inner relations between different recording channels were exploited to mitigate the dependency on the input excitation and identify the modal parameters of the structure, avoiding common disturbances in the recorded signals.

Further studies need to be conducted to understand the applicability of the methods in other scenarios, such as railway bridges and bell towers, for which the excitation is periodic. Indeed, in the first case, the wheels of trains hit the rail joints at time intervals given by

the train speed and its geometry. On the other hand, bells induce low-frequency harmonic excitation to the towers.

7.2 Accelerometers measuring curvature

The second chapter of this thesis presented a novel approach for structural health monitoring of simply-supported RC viaducts, capable of identifying dynamic and quasi-static parameters in a simple and integrated fashion. The MAD was also shown to be suitable to extract sparse estimates of modal parameters from structures subjected to traffic excitation using clustered wavelet bandpass filters. Besides, quasi-static features enable a dense description of the structural behavior using few accelerometers. Relying on the relation between the recording time of the accelerometers and the space traveled by a moving vehicle with constant speed, it was demonstrated that the low-frequency component of acceleration is a direct representation of the curvature of the bridge subjected to a vertical force applied at the instrumented location. Therefore, accelerometers directly measure curvature in this application, which is one of the most used DSFs in SHM, removing the complex procedures (and thus approximations) which are generally necessary for traditional methods to calculate curvature from identified mode shapes. The curvature influence line can thus be obtained from low-frequency signal components through an additional lowpass wavelet filter compared to the modal identification algorithm presented before.

A damage index defined as the difference of the curvature influence lines showed the ability to localize damage with good accuracy using a sparse sensor network of accelerometers. Furthermore, the proposed index represents the damaged entity and does not require any knowledge about structural masses or the use of finite element models.

The results obtained from a numerical case study showed that damage can be detected, localized, and also quantified using a single acceleration recording in optimal conditions. However, there is a minimum spatial extension of the identifiable damaged portion that depends on the sampling frequency of the collected signal and the

vehicle speed. For local stiffness reductions with an extension shorter than the threshold, damage can still be detected and approximately localized. However, the information about damage magnitude is lost. In the real environment, noise could affect the outcome of the identification procedure, especially when using extremely sparse sensor networks. However, the cumulative difference function obtained by subtracting the inspection influence line from the baseline in multiple sensing locations considerably improves the accuracy of damage localization. Moreover, information obtained from modal features can help discard peaks of the damage index generated by dynamic effects and thus not related to actual damage. The proposed procedure provided promising results, proving particularly appealing for applications employing low-cost sparse sensing solutions for structural health monitoring at a territorial level.

More investigations need to be conducted to consider the dynamic vehicle-bridge interaction and road roughness in the problem formulation. Besides, the method needs to be tested on real datasets collected for case studies with induced damage conditions to assess the effectiveness of the damage identification algorithm.

7.3 Smart citizens and smart sensors

This thesis presented a pilot study to demonstrate the practicability of using drive-in smartphone data collected by citizens who drive micromobility light vehicles (*e.g.*, bicycles and kick scooters) to extract dynamic features of urban bridges, such as natural frequencies and modal amplitudes. Human-powered vehicles have never been considered for the health assessment of civil structures. This work constitutes a first step toward adopting light vehicles in indirect structural health monitoring applications. The main advantages of shared bicycles over other types of vehicles include the following aspects:

1. Relatively low speed of the micromobility vehicles allows the acquisition of longer datasets, minimizing vehicle vibration close to the expansion joints and reducing the effects of pavement roughness on the collected response.

2. High resonant frequencies of the bicycles (due to their low mass and high stiffness) are generally distant from the first fundamental frequencies of the inspected bridges, making the filtering procedure particularly effective for removing the vehicle dynamic effects from the collected response.
3. Shared bicycles, differently from private cars, are generally all identical. The effect of their dynamic characteristics on the response recorded by the smartphone can be studied and removed from the signal if needed.
4. Bicycles can access almost all the urban bridges, even those that are not accessible by cars.

This study proposed a novel automatic strategy based on the GPS and IMU measurements collected by regular smartphones. An extended Kalman filter and a simple band-pass filtering procedure are the only tools employed in the proposed strategy, making it particularly suitable for cloud processing.

The results obtained for a real footbridge situated in Bologna (Italy) show that, although single datasets collected by each vehicle can be particularly noisy, a crowdsensing-based strategy may provide features that can be potentially employed for monitoring urban infrastructures at a territorial scale. Data collected during different activities, such as standing, walking, and riding on the bridge, have shown the possibility of clearly identifying the first natural frequency of the bridge. Moreover, using the retrieved frequency value to design a suitable band-pass filter enables the identification of the absolute value of the modal amplitudes, enclosing information of the first two closely spaced modes. The results are in good accordance with the profile identified in previous studies. Since the presented method provides modal or operational shapes, all the damage detection techniques based on these parameters or their derivatives can be applied.

The proposed strategy can be particularly convenient for monitoring infrastructure in large areas since it does not require any deployments of traditional sensing systems and motivates citizens to take care of the urban environment, opening incredible possibilities for planning gamification and reward-based strategies in the monitoring process. However, further studies must be conducted

considering other vehicles, users, and pavements, simulating a robust crowdsensing application.

Dense estimates of mode shapes are helpful for identifying early civil infrastructure damage. However, dense sensor networks have relevant data management issues. The solutions presented in the second chapter exploit traffic to retrieve spatial information while using sparse sensor networks or individual sensing devices. Traffic is seen both as a source of excitation and a means for moving sensors.

7.4 A good trade-off between accuracy and complexity

PCM is a novel technology that has recently stepped into practical digital storage applications. However, the potential of this tool for signal processing makes it attractive for edge computing in structural health monitoring. The unified algorithm for identifying modal and quasi-static parameters presented in this thesis was adapted for implementation on PCM-based devices, which are thus proposed for the first time in the civil field.

This study shows that a recursive implementation of simple high-pass and low-pass filters on PCM-based nodes leads to a signal decomposition accuracy similar to that of the standard procedure based on ideal filters, reducing energy consumption and computational runtime. The challenges related to time-dependent nonidealities of PCMs, which could affect memory arrays programmed a long time before signal processing, are investigated. Structural parameters identified in two environments, one representative of a short-term implementation right after programming and one representative of a long-term PCM usage, resulted in comparable accuracy. In particular, the fundamental mode shape of a real case study is identified with excellent accuracy in both cases. This result demonstrates that the PCM does not necessarily need to be freshly programmed for SHM applications. Therefore, energy-consuming periodic reprogramming can be avoided.

The results reported in this study are affected by both identification uncertainties (mainly due to recording noise) and PCM nonidealities. This last effect, in particular, slightly affects identified parameters if the filter bank is implemented iteratively. Moreover, given the remarkable power saving of over 90% obtained in a first evaluation, the proposed procedure proves to be particularly convenient and worthy of future developments.

Further studies need to be conducted to optimize the current-to-voltage conversion between the different array layers representing different iterations of the recursive filtering. Besides, energy harvesting solutions should be coupled with the computing core to exploit vibrational energy and form fully self-powered devices.

7.5 Towards smart maintenance

This thesis presented the results obtained using two machine learning tools, namely a DNN and a RBFN, to solve the ERT inverse problem for crack identification and strain monitoring applications, employing two smart thin films fabricated using different formulations. The application of these coatings to ordinary structural elements enables self-sensing properties. Interrogating the smart paint through electrical pulses, the voltage measurements recorded on the boundary can be interpreted to reconstruct the electrical and mechanical properties of the structural substrate, this revealing cracks, the strain state, and the presence of dangerous chemical substances that may accelerate material degradation.

First, a deep neural network was trained using a synthetic dataset generated by solving the forward problem through a finite element mesh model. The suitability of the training set for practical applications involving real voltage measurements was proved using a novel procedure proposed in this work. In particular, a correlation coefficient that measures the similarity between the high-dimensional voltage space populated by real measurements and that populated by the generated synthetic data is calculated. Comparing this coefficient obtained by different synthetic training datasets allows deciding which one is more representative of the specific application

in which real data is collected. This coefficient is easy to calculate and does not necessitate any prior information on the damage location. Therefore, it can be calculated after collecting voltage measurements directly taken from the experimental campaign. Moreover, it enables a conscious evaluation of the suitability of the generated training dataset, which is generally a challenging aspect when applying supervised machine learning tools for real applications.

After training the network with the most suitable dataset, the conductivity distribution was reconstructed for different crack conditions induced in four rectangular sensing specimens tested in the laboratory environment. The results showed that, in general, early damage (consisting of small cracks) is accurately identified, both in terms of size and location. As the crack size increases, the reconstruction becomes noisier, still showing an approximate location and entity of the cracked area. Tests conducted on the carbon nanotubes-based specimen generally provide more accurate results than those based on graphene nanosheets. Moreover, damage conditions involving the boundary region are identified more accurately compared to those investing the central area of the sensing specimen, probably depending on the current injection pattern employed for interrogation.

The ability to reconstruct the strain state of the interrogated body was studied with two applications. First, pressure mapping was demonstrated using a nanocomposite-enhanced soft foam and the use of both the DNN and RBFN. The RBFN-based method provided accurate results for identifying small hotspots while also allowing precise shape reconstruction of the shape of the baseplate used to apply the load. Larger and more complex pressure regions are localized but without accurate shape information, confirming the results obtained for crack identification. On the other hand, although the RBFN did not accurately localize small pressure hotspots, it was more robust for identifying larger applied pressure regions. Both machine learning techniques performed better than the traditional total variation method, especially for computational efficiency, with a runtime two orders of magnitude lower than the traditional method. The RBFN required a much smaller physical memory and computational footprint than the RBFN since network weights are

58 times fewer. These results make RBFNs more suitable for portable applications and edge computing.

The RBFN proved to be particularly effective also for the second strain sensing application, employing a sensing mesh for distributed strain sensing in two orthogonal directions. In this case, due to the constraints introduced in the conductivity distribution of the sensing film, an RBFN with only 10 nodes demonstrated to be enough to reconstruct the strain state of a specimen subjected to a three-point bending test.

Further studies should be conducted to evaluate the efficacy of smart paint applied to real steel and reinforced concrete structural components. In the former case, however, particular attention should be paid to the interface between the metallic element and sensing skin since the 2D approach used in this study only assumes an electric flow through the sensing surface without considering any internal electric source or sink. Further investigations must be conducted considering a 3D propagation of the electrons within the body and effective insolation substrates.

Also, the techniques proposed in this thesis should be tested to detect the presence of humidity and dangerous chemical agents in the structural substrate. Indeed, information on this aspect is fundamental to understanding the sources of structural anomalies, *e.g.*, identified using vibration-based approaches and schedule targeted interventions in a smart maintenance perspective.

Appendixes

Decentralized identification algorithm

A

In this Appendix, the technical aspects of the decentralized identification algorithm presented in Section Section 3.4.

A.1 Computational complexity

Since the algorithm is organized in two individual steps, the complexity is estimated for the two steps separately.

Step 1

Since SWPT is performed through convolutions between a priori known sequences, the considered complexity is that of the fast convolution algorithm, which allows the computation of each convolution as:

$$y_k[\tau] = IDFT_M\{DFT_M\{x[\tau]\}DFT_M\{d_k[\tau]\}\} \tag{A.1}$$

where $DFT_M\{\bigcirc\}$ and $IDFT_M\{\bigcirc\}$ denote the discrete Fourier transform of length M and its inverse, respectively. In relation (A.1), in order to allow simple multiplications between the terms of DFTs, they have to be of the same length. To this aim, it is possible to extend $x[\tau]$ and $d_k[\tau]$ through zero-padding, in order to have a common length of $M = s + \overline{N} - 1$. Since the length of the analyzed signal is user-defined, it is also possible to choose s such that $s \geq \overline{N}$ and $M = 2^q$, with $q \in \mathbb{Z}^+$. In this case, the DFTs in Equation (A.1) can be computed through radix-2 FFT and the computational complexity of the SWPT can be expressed as reported in Table A.1, together with the complexity and storage space required by each process of Step 1. Here, the storage space is intended as the number of elements stored in memory for each process. Moreover, the values in $(\bigcirc)_{add}$, $(\bigcirc)_{mul}$, $(\bigcirc)_{div}$, $(\bigcirc)_{com}$, and $(\bigcirc)_{sqrt}$ denote the number

of additions/subtractions, multiplications, divisions, comparisons, and root square operations, respectively, r is the number of sensors, while c is the number of clusters identified before the energy-based selection.

In order to reduce the computational burden of Step 1, it is possible to limit the analysis to a selected frequency range, computing only a subset of the 2^n wavelet components, and therefore generating a CFB able to identify the vibration modes whose frequencies are contained in the considered range. Therefore, in Table A.1, $W \geq 2^n$ denotes the number of wavelet components considered in the initialization step.

In this evaluation, only the strictly necessary operations have been counted. In fact, the coefficients of a complete MAC matrix would be W^2 but, in this case, since only consecutive components can be grouped in the same cluster, the MAC coefficients necessary to verify the condition (3.27)of Section 3.4 are $W-1$, corresponding to the elements next to the main diagonal of the complete MAC matrix (*i.e.*, $MAC_{k,k+1}$, with $k = 1, \ldots, W-1$). At the end of Step 1, the CFB has to be built by summing the bandpass filters associated to the decomposition filters contained in each cluster. Therefore, if the b_k bandpass filters are already stored in the device memory (using WN storage space), up to $(WN-N)_{add}$ additional operations are necessary to obtain the CFB .

Table A.1: Computational complexity of each process of Step 1

Process	Complexity	Storage space
SWPT	$3Wr\left[\left(M\log_2 M\right)_{add} + \left(\frac{M}{2}\log_2 M - \frac{M}{6}\right)_{mul}\right]$	$W[\overline{N} + rM]$
ODS	$W(r-1)\left[(s-1)_{add} + (s)_{mul} + (1)_{div}\right]$	Wr
MAC	$(W-1)\left[3(r-1)_{add} + (3r+2)_{mul} + (1)_{div}\right]$	$W-1$
Clustering	$(W-1)_{com}$	—
RMS energy	$Wr\left[(s+r-1)_{add} + (s)_{mul} + (1)_{div} + (1)_{sqrt}\right] - (c)_{add}$	Wr
Energy-based selection	$(c)_{com}$	—

Step 2

Following the centralized initialization step, the monitoring system enters a decentralized processing phase. This section describes the computational complexity of the activities performed to obtain each instantaneous parameter, calculated as new data is recorded.

Assuming N the length of the generic filter b_{k_1,k_m} in the relation (3.25) of Section 3.4, the computational complexity of convolution for p identified modes is given by:

$$\mathscr{C}_c = [(N)_{mul} + (N-1)_{add}]p \tag{A.2}$$

per input sample. This procedure needs $N(p+1)+p$ elements stored in memory (*i.e.*, pN elements for the filter bank, N elements for the sliding window of collected data, and p output values). Since convolution is aimed at bandpass filtering, the rate at which it is performed can be reduced according to the frequency band of each filter [20], providing a smaller quantity of new samples for low-frequency components. In this way, the number of operations per second is reduced, making the procedure more efficient and reducing also the number of output values, that can be transferred to the monitoring station with a transfer rate which may even be lower than that of the simple transmission of the unfiltered signal.

Each new value obtained through convolution is then sent to the monitoring station, temporarily stored, and used to compute the instantaneous natural frequencies and modal shapes. In Table A.2, the computational complexity of DESA -1 is analyzed, indicating the number of mathematical operations needed to obtain each element of relations (3.30) and (3.31) of Section 3.4 for a given identified mode, computed by using the data collected at a given sensor position. Here, the value in $(\bigcirc)_{acos}$ denotes the number of arcocosines calculated. Since some values are used to compute the instantaneous frequency at different consecutive instants, the reported number of mathematical operations considers only the elements evaluated for each new sample of data, assuming that the previous values are stored rather than calculated each time. Also, the number of elements stored in memory is shown in Table A.2.

Table A.2: Computational complexity of each process of Step 1

Element	Usable from previous iterations	Computed for each new sample	Storage space	Complexity
y	$y[\tau-2]$, $y[\tau-1]$, $y[\tau]$, $y[\tau+1]$	$y[\tau+2]$	5	—
z	$z[\tau-1]$, $z[\tau]$, $z[\tau+1]$	$z[\tau+2]$	4	$(1)_{add}$
Ψ	$\Psi[z[\tau]]$	$\Psi[y[\tau]]$, $\Psi[z[\tau+1]]$	3	$(1)_{add} + (1)_{mul}$
Ω	—	$\Omega[\tau]$	1	$(2)_{add} + (1)_{mul}$ $+(1)_{div} + (1)_{acos}$

The computational complexity of the instantaneous frequency calculation does not depend on the filter length, but only depends on the number of identified modes p. It can be expressed as:

$$\mathscr{C}_f = [(5)_{add} + (5)_{mul} + (1)_{div} + (1)_{acos}]p \tag{A.3}$$

per input sample. The computational complexity of instantaneous shapes depends instead on the number of identified modes and on the number of sensors r:

$$\mathscr{C}_s = [(r-1)_{div}]p \tag{A.4}$$

In this last computation, no additional memory is needed, except for the $(r-1)p$ output elements, since the latest values obtained through convolution are directly used, as shown in Section 3.4. Considering also median filtering for denoising purposes, the complexity increases of:

$$\mathscr{C}_m = [(\mu-1)_{comp}]p \tag{A.5}$$

per input sample, for each quantity to which the filter is applied. It is observable that, in the decentralized configuration, a consistent part of the computational burden (αC_c per second) is carried out onboard each node, while $\alpha(\mathscr{C}_f + \mathscr{C}_s + 2\mathscr{C}_m)$ per second lies with the monitoring station, considering the median filter applied to both natural frequencies and modal shapes, where α is a coefficient that takes into account any downsampling ($\alpha \leq \overline{F}_s$, with $\overline{F}_s$ the sampling frequency of the original signal). Considering p and r modest with respect to N and μ, the computational complexity of the

instantaneous filtering process can be expressed in the order of $O(N)$ per input sample, while that related to the activities of the monitoring station is not dependent on N, and therefore assumable in the order of $O(\mu)$. On the other hand, using the proposed algorithm in a centralized topology would imply a computational burden of $\alpha(r\mathscr{C}_c + \mathscr{C}_f + \mathscr{C}_s + 2\mathscr{C}_m)$ per second on the monitoring station, which can be expressed in the order of $O(N)$ per input sample, assuming that N is proportional to μ.

A.2 Identification delay

Both due to the convolution and the application of DESA -1, a delay is introduced in the estimated modal parameters. In addition, by applying further post-processing operations to restrain the fluctuations of modal parameters, the delay increases further. In particular, for the proposed algorithm, the total delay δ is given by the sum of three contributions:

$$\delta = \delta_c + \delta_d + \delta_m \tag{A.6}$$

where δ_c is due to the convolution procedure ($\delta_c = (N-1)/2$) [224], δ_d is associated with the DESA -1 ($\delta_d = 2$), and δ_m is related to the smoothing technique: in case of median filtering, $\delta_m = \mu/2$, with the notations used in Equation (3.33) of Section 3.4.

Since the filter bank related to the SWPT is generated through convolutions between dyadic upsampled filters [202], the length of the obtained analysis and synthesis filters increases with the order of the wavelet function and with the level of decomposition. In particular, considering a wavelet with filters length λ, the length of the filters contained in the decomposition (or reconstruction) filter bank related to the n-th level is:

$$\overline{N} = \lambda(2^n - 1) - n + 1 \tag{A.7}$$

The length of the final filters used for online signal analysis is thus $N = 2\overline{N} - 1$, because of Equation (3.23) of Section 3.4. In Table A.3, the length of the decomposition and reconstruction filters associated with the wavelets already analyzed in Figure 3.1 are reported for different levels.

Table A.3: Length of the decomposition and reconstruction filters related to the wavelets *fk14*, *db14*, *sym14*, *db7*, *fk22*, and *db22*, at different decomposition levels

Level	*fk14* and *db7*	*db14* and *sym14*	*fk22*	*db22*
4	207	417	327	657
5	430	864	678	1360
6	877	1759	1381	2767
7	1722	3550	2788	5582

In general, filters with high order are suitable for applications in the civil field, where closely-spaced modes and high noise components are present. On the other hand, short filters are preferable for real-time identifications in other engineering fields (*e.g.*, flutter tests [244]).

Quasi-static contribution of the structural response

B

In this Appendix, the Fourier transform of the quasi-static structural response defined in Equation (4.14) is demonstrated.

Substituting $T = 2l/v$ in (4.10), it is possible to write $l_m(t)$ as

$$l_m(t) = \sin\left(\frac{m\pi v t}{l}\right)\Pi\left(\frac{t - T/4}{T/2}\right) \tag{B.1}$$

where T is the period of the sine function in the above equation when $m = 1$, *i.e.*, twice the time a passing car with a velocity equal to v takes to enter and leave the bridge span. Thanks to the frequency shift property, the Fourier transform of $l_m(t)$ can be written as

$$L_m(f) = \mathcal{F}\left[l_m(t)\right] = \mathcal{F}\left[l'_m(t)\right] e^{-j\frac{\pi l}{v}f} \tag{B.2}$$

where the shifted function $l'_m(t)$ reads:

$$l'_m(t) = \cos\left(\frac{m\pi v}{l}t + \frac{m-1}{2}\pi\right)\Pi\left(\frac{t}{T/2}\right) \tag{B.3}$$

The modulation theorem of Fourier transform can thus be employed, obtaining:

$$\begin{aligned}
&\mathcal{F}\left[l'_m(t)\right] = \\
&= \frac{l e^{j\frac{m-1}{2}\pi}}{2v}\operatorname{sinc}\left(\frac{l}{v}f - \frac{m}{2}\right) + \frac{l e^{-j\frac{m-1}{2}\pi}}{2v}\operatorname{sinc}\left(\frac{l}{v}f + \frac{m}{2}\right) = \\
&= \frac{l}{2v}\left[e^{j\frac{m-1}{2}\pi}\frac{\sin\left(\frac{\pi l}{v}f - \frac{m\pi}{2}\right)}{\frac{\pi l}{v}f - \frac{m\pi}{2}} + e^{-j\frac{m-1}{2}}\pi\frac{\sin\left(\frac{\pi l}{v}f + \frac{m\pi}{2}\right)}{\frac{\pi l}{v}f + \frac{m\pi}{2}}\right]
\end{aligned} \tag{B.4}$$

It should be noted that:

$$
\begin{aligned}
&e^{j\frac{m-1}{2}\pi}\sin\left(\frac{\pi l}{v}f-\frac{m\pi}{2}\right)+e^{-j\frac{m-1}{2}\pi}\sin\left(\frac{\pi l}{v}f+\frac{m\pi}{2}\right)=0 \quad \forall m\\
&e^{j\frac{m-1}{2}\pi}\sin\left(\frac{\pi l}{v}f-\frac{m\pi}{2}\right)-e^{-j\frac{m-1}{2}\pi}\sin\left(\frac{\pi l}{v}f+\frac{m\pi}{2}\right)= \\
&\qquad =2e^{j\frac{m-1}{2}\pi}\sin\left(\frac{\pi l}{v}f-\frac{m\pi}{2}\right) \quad \forall m
\end{aligned}
\tag{B.5}
$$

Therefore, Equation (B.4) simplifies in:

$$
\mathcal{F}\left[l'_m(t)\right]=\frac{le^{j\frac{m-1}{2}\pi}}{v\left(\frac{\pi^2 l^2}{v^2}f^2-\frac{m^2\pi^2}{4}\right)}\sin\left(\frac{\pi l}{v}f-\frac{m\pi}{2}\right) \tag{B.6}
$$

The result shown in Equation (4.14) can thus be obtained by substituting Equation (B.6) into (B.2).

Data fusion using smartphones

C

In this Appendix, the structure and the implementation of an extended Kalman filter is described to fuse asynchronous data collected by multiple sensors on a smartphone.

C.1 Structure of the extended Kalman filter

The state vector $\mathbf{x} \in \mathbb{R}^{28}$ and the state transition function $g(\mathbf{x})$ of the CD-EFK described in Section 4.3 have the following structure that depends on the geometrical and the physical relations between the measured variables [315]:

$$\mathbf{x} = \begin{bmatrix} \rho_0 & \\ \rho_1 & \vdots \\ \rho_2 & \eta_1 \\ \rho_3 & \eta_2 \\ \alpha_1 & \eta_3 \\ \alpha_2 & v_1 \\ \alpha_3 & v_2 \\ \theta_1 & v_3 \\ \theta_2 & \bar{\alpha}_1 \\ \theta_3 & \bar{\alpha}_2 \\ \sigma_1 & \bar{\alpha}_3 \\ \sigma_2 & \bar{\theta}_1 \\ \sigma_3 & \bar{\theta}_2 \\ \vdots & \bar{\theta}_3 \\ & \bar{\sigma}_1 \\ & \bar{\sigma}_2 \\ & \bar{\sigma}_3 \end{bmatrix}, \quad g(\mathbf{x}) = \begin{bmatrix} -\frac{\rho_1\theta_1+\rho_2\theta_2+\rho_3\theta_3}{2} & \\ -\frac{\rho_0\theta_1+\rho_3\theta_2+\rho_1\theta_3}{2} & \vdots \\ -\frac{\rho_3\theta_1+\rho_0\theta_2+\rho_1\theta_3}{2} & v_1 \\ -\frac{\rho_1\theta_1+\rho_2\theta_2+\rho_0\theta_3}{2} & v_2 \\ 0 & v_3 \\ 0 & \alpha_1 \\ 0 & \alpha_2 \\ 0 & \alpha_3 \\ 0 & 0 \\ 0 & 0 \\ 0 & 0 \\ 0 & 0 \\ 0 & 0 \\ \vdots & 0 \\ & 0 \\ & 0 \\ & 0 \end{bmatrix} \tag{C.1}$$

The meaning of the symbols used in these expressions is reported

Table C.1: Measurement symbols

Measurement	Symbol
Quaternion	$\rho_0, \rho_1, \rho_2, \rho_3$
Acceleration (IMU)	$\alpha_1, \alpha_2, \alpha_3$
Angular velocity (IMU)	$\theta_1, \theta_2, \theta_3$
Magnetic field (IMU)	$\sigma_1, \sigma_2, \sigma_3$
Position (GPS)	η_1, η_2, η_3
Velocity (GPS)	ν_1, ν_2, ν_3
Accelerometer bias	$\bar{\alpha}_1, \bar{\alpha}_2, \bar{\alpha}_3$
Gyroscope bias	$\bar{\theta}_1, \bar{\theta}_2, \bar{\theta}_3$
Magnetometer bias	$\bar{\sigma}_1, \bar{\sigma}_2, \bar{\sigma}_3$

in Table C.1, and the directions of measurement are illustrated in Figure C.1.

The function $g(\mathbf{x})$ describes the evolution of the state vector in time and computes, therefore, its derivative. It is noted that, in the model used in this study, the IMU measurements are expected to be constant while the vehicle moves. Therefore, the elements from the 5-th to the 13-th of the state transition function are taken as zero. Similarly, the model assumes all the biases constant over time, with a null derivative. On the other hand, the derivative of the GPS position is modeled as the measured GPS velocity, the derivative of which, in turn, is the acceleration measured by the MEMS accelerometer.

The observation function has a structure that depends on the quantities included in the measurement vector $\mathbf{z}_k$. Specifically, if a

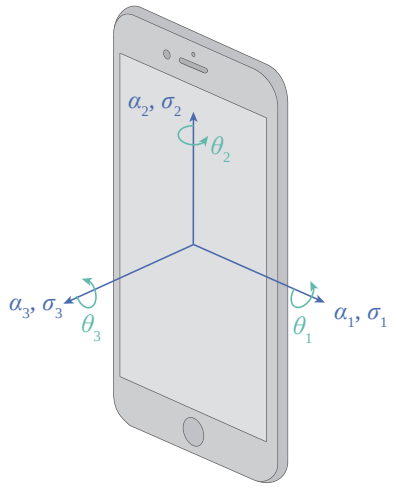

Figure C.1: Directions of measurement

new acceleration measurement is available ($\mathbf{z}_k = [\alpha_1, \alpha_2, \alpha_3]^T$), the observation function has the following form:

$$h_\alpha(\mathbf{x}) = \begin{bmatrix} \bar{\alpha}_1 - (\alpha_1 - \alpha_{r,1})\left(q_0^2 + q_1^2 - q_2^2 - q_3^2\right) \\ \qquad - 2\,(\alpha_2 - \alpha_{r,2})\left(q_0 q_3 + q_1 q_2\right) \\ \qquad + 2\,(\alpha_3 - \alpha_{r,3})\left(q_0 q_2 - q_1 q_3\right) \\ \bar{\alpha}_2 - (\alpha_2 - \alpha_{r,2})\left(q_0^2 - q_1^2 + q_2^2 - q_3^2\right) \\ \qquad + 2\,(\alpha_1 - \alpha_{r,1})\left(q_0 q_3 - q_1 q_2\right) \\ \qquad - 2\,(\alpha_3 - \alpha_{r,3})\left(q_0 q_1 + q_2 q_3\right) \\ \bar{\alpha}_3 - (\alpha_3 - \alpha_{r,3})\left(q_0^2 - q_1^2 - q_2^2 + q_3^2\right) \\ \qquad - 2\,(\alpha_1 - \alpha_{r,1})\left(q_0 q_2 + q_1 q_3\right) \\ \qquad + 2\,(\alpha_2 - \alpha_{r,2})\left(q_0 q_1 - q_2 q_3\right) \end{bmatrix} \tag{C.2}$$

with $\alpha_{r,1}$ being a reference acceleration measured by the mobile application at the beginning of the measurement process. Conversely, for angular velocity measurements ($\mathbf{z}_k = [\theta_1, \theta_2, \theta_3]^T$), the observation function becomes:

$$h_\theta(\mathbf{x}) = \begin{bmatrix} \bar{\theta}_1 + \theta_1 \\ \bar{\theta}_2 + \theta_2 \\ \bar{\theta}_3 + \theta_3 \end{bmatrix} \tag{C.3}$$

while for magnetic field measurements ($\mathbf{z}_k = [\sigma_1, \sigma_2, \sigma_3]^T$):

$$h_\sigma(\mathbf{x}) = \begin{bmatrix} \bar{\sigma}_1 + \sigma_1\left(q_0^2 + q_1^2 - q_2^2 - q_3^2\right) \\ \qquad + 2\sigma_2\left(q_0 q_3 + q_1 q_2\right) \\ \qquad - 2\sigma_3\left(q_0 q_2 - q_1 q_3\right) \\ \bar{\sigma}_2 + \sigma_2\left(q_0^2 - q_1^2 + q_2^2 - q_3^2\right) \\ \qquad - 2\sigma_1\left(q_0 q_3 - q_1 q_2\right) \\ \qquad + 2\sigma_3\left(q_0 q_1 + q_2 q_3\right) \\ \bar{\sigma}_3 + \sigma_3\left(q_0^2 - q_1^2 - q_2^2 + q_3^2\right) \\ \qquad + 2\sigma_1\left(q_0 q_2 + q_1 q_3\right) \\ \qquad - 2\sigma_2\left(q_0 q_1 - q_2 q_3\right) \end{bmatrix} \tag{C.4}$$

It should be noted that in the cases of acceleration and magnetic field, the measured components are projected onto the vehicle orientation. Besides, a bias is added to all the measurements. Concerning the GPS position data ($\mathbf{z}_k = [\eta_1, \eta_2, \eta_3]^T$), the observation function simply takes the measurement information:

$$h_\eta(\mathbf{x}) = \begin{bmatrix} \eta_1 \\ \eta_2 \\ \eta_3 \end{bmatrix} \tag{C.5}$$

C.2 Implementation with smartphone data

Let $\hat{\mathbf{x}}_{n|m}$ and $\mathbf{P}_{n|m}$ represent the estimate of $\mathbf{x}$ and of the state covariance matrix $\mathbf{P}$ at time t_n, respectively, given the observations up to the instant t_m. In general, the selection of $\hat{\mathbf{x}}_{0|0}$ and $\mathbf{P}_{0|0}$, that denote the initialization state and covariance, can be performed randomly or considering a priori information about the characteristics of the system at the instant t_0. In this study, the state vector elements are set as the measurements collected by the smartphone when the vehicle passes on the first expansion joint, *i.e.*, when it enters the bridge.

The prediction step consists of solving

$$\begin{cases} \dot{\hat{\mathbf{x}}}(t) = g(\hat{\mathbf{x}}(t)) \\ \dot{\mathbf{P}}(t) = \mathbf{G}(t)\mathbf{P}(t) + \mathbf{P}(t)\mathbf{G}(t)^T + \mathbf{Q}(t) \end{cases} \tag{C.6}$$

where $\dot{\hat{\mathbf{x}}}(t)$ and $\dot{\mathbf{P}}(t)$ indicate the time derivatives of the estimated state vector and state covariance matrix, respectively, and the state transition function is linearized as the Jacobian

$$\mathbf{G}(t) = \left.\frac{\partial g}{\partial \mathbf{x}}\right|_{\widehat{\mathbf{x}}(t)} \tag{C.7}$$

Equation (C.6) is solved considering the initial conditions $\hat{\mathbf{x}}(t_{k-1}) = \mathbf{x}_{k-1|k-1}$ and $\mathbf{P}(t_{k-1}) = \mathbf{P}_{k-1|k-1}$ evaluated at the time instant of the last measurement t_{k-1}, until the next measurement (at time t_k) is available. At this instant, the a priori estimate (*i.e.*, not including yet measurement information at time t) of the current state $\hat{\mathbf{x}}_{k|k-1}$ and

covariance $\mathbf{P}_{k|k-1}$ are defined as

$$\begin{cases} \hat{\mathbf{x}}_{k|k-1} = \mathbf{x}(t_k) \\ \mathbf{P}_{k|k-1} = \mathbf{P}(t_k) \end{cases} \tag{C.8}$$

As mentioned in Section 4.3, a constant frequency f_s, equal to the sampling frequency of the vertical acceleration, is selected to calculate the prediction step.

In the update step, the a priori prediction of the current state is combined with the measurement collected at time t_k to refine its estimate. This step consists of evaluating the near-optimal Kalman gain $\mathbf{K}_k$, which is employed in calculating the updated (a posteriori) state $\hat{\mathbf{x}}_{k|k}$ and covariance $\mathbf{P}_{k|k}$ estimates, as follows:

$$\mathbf{K}_k = \mathbf{P}_{k|k-1}\mathbf{H}_k^T \left(\mathbf{H}_k\mathbf{P}_{k|k-1}\mathbf{H}_k^T + \mathbf{R}_k\right)^{-1} \tag{C.9}$$

$$\hat{\mathbf{x}}_{k|k} = \hat{\mathbf{x}}_{k|k-1} + \mathbf{K}_k \left(\mathbf{z}_k - h\left(\hat{\mathbf{x}}_{k|k-1}\right)\right) \tag{C.10}$$

$$\mathbf{P}_{k|k} = \left(\mathbf{I} - \mathbf{K}_k\mathbf{H}_k\right)\mathbf{P}_{k|k-1} \tag{C.11}$$

where $\mathbf{I}$ indicates an identity matrix. In this case, the observation matrix $\mathbf{H}_k$ is defined as the Jacobian

$$\mathbf{H}_k = \left.\frac{\partial h}{\partial \mathbf{x}}\right|_{\hat{\mathbf{x}}_{k|k-1}} \tag{C.12}$$

Bibliography

[1] P. G. Bakir, E. Reynders, and G. De Roeck. 'Sensitivity-based finite element model updating using constrained optimization with a trust region algorithm'. In: *Journal of Sound and Vibration* 305.1-2 (2007), pp. 211–225. DOI: 10.1016/j.jsv.2007.03.044 (cited on pages 7, 138).

[2] E. Parloo, P. Verboven, P. Guillaume, and M. Van Overmeire. 'Sensitivity-based operational mode shape normalisation'. In: *Mechanical systems and signal processing* 16.5 (2002), pp. 757–767. DOI: 10.1006/mssp.2002.1498 (cited on pages 7, 138).

[3] W. Fan and P. Qiao. 'Vibration-based damage identification methods: a review and comparative study'. In: *Structural health monitoring* 10.1 (2011), pp. 83–111. DOI: 10.1177/1475921710365419 (cited on pages 11, 12, 177, 190).

[4] M. P. Limongelli, Z. I. Turksezer, and P. F. Giordano. 'Structural health monitoring for cultural heritage constructions: A resilience perspective'. In: *IABSE Symposium, Guimaraes 2019: Towards a Resilient Built Environment Risk and Asset Management - Report*. 2019, pp. 1552–1559. DOI: 10.2749/guimaraes.2019.1552 (cited on page 11).

[5] M. G. Masciotta, L. F. Ramos, and P. B. Lourenço. 'The importance of structural monitoring as a diagnosis and control tool in the restoration process of heritage structures: A case study in Portugal'. In: *Journal of Cultural Heritage* 27 (2017), pp. 36–47. DOI: 10.1016/j.culher.2017.04.003 (cited on page 11).

[6] W. Qiao and D. Lu. 'A Survey on Wind Turbine Condition Monitoring and Fault Diagnosis - Part II: Signals and Signal Processing Methods'. In: *IEEE Transactions on Industrial Electronics* 62.10 (2015), pp. 6546–6557. DOI: 10.1109/TIE.2015.2422394 (cited on page 11).

[7] R. Uma Maheswari and R. Umamaheswari. 'Trends in non-stationary signal processing techniques applied to vibration analysis of wind turbine drive train A contemporary survey'. In: *Mechanical Systems and Signal Processing* 85 (2017), pp. 296–311. DOI: 10.1016/j.ymssp.2016.07.046 (cited on page 11).

[8] S. D. Fassois and J. S. Sakellariou. 'Time-series methods for fault detection and identification in vibrating structures'. In: *Philosophical Transactions of the Royal Society A: Mathematical, Physical and Engineering Sciences* 365.1851 (2007), pp. 411–448. DOI: 10.1098/rsta.2006.1929 (cited on page 11).

[9] C. Smith, C. M. Akujuobi, P. Hamory, and K. Kloesel. 'An approach to vibration analysis using wavelets in an application of aircraft health monitoring'. In: *Mechanical Systems and Signal Processing* 21.3 (2007), pp. 1255–1272. DOI: 10.1016/j.ymssp.2006.06.008 (cited on page 11).

[10] M. P. Limongelli and M. Çelebi. 'Seismic Structural Health Monitoring'. In: *Springer Tracts in Civil Engineering* (2019), p. 447. DOI: 10.1007/978-3-030-13976-6 (cited on page 11).

[11] M. D. Spiridonakos and S. D. Fassois. 'Parametric identification of a time-varying structure based on vector vibration response measurements'. In: *Mechanical Systems and Signal Processing* 23.6 (2009), pp. 2029–2048. DOI: 10.1016/j.ymssp.2008.11.004 (cited on pages 11, 12).

[12] M. S. Allen, M. W. Sracic, S. Chauhan, and M. H. Hansen. 'Output-only modal analysis of linear time-periodic systems with application to wind turbine simulation data'. In: *Mechanical Systems and Signal Processing* 25.4 (2011), pp. 1174–1191. DOI: 10.1016/j.ymssp.2010.12.018 (cited on page 11).

[13] Z. Ni, R. Mu, G. Xun, and Z. Wu. 'Time-varying modal parameters identification of a spacecraft with rotating flexible appendage by recursive algorithm'. In: *Acta Astronautica* 118 (2016), pp. 49–61. DOI: 10.1016/j.actaastro.2015.10.001 (cited on page 12).

[14] A. Senba and H. Furuya. 'Implementation algorithms for self-identification of adaptive structures with variable geometric properties'. In: *Mechanical Systems and Signal Processing* 22.1 (2008), pp. 1–14. DOI: 10.1016/j.ymssp.2007.05.002 (cited on page 12).

[15] R. Ditommaso, M. Mucciarelli, S. Parolai, and M. Picozzi. 'Monitoring the structural dynamic response of a masonry tower: Comparing classical and time-frequency analyses'. In: *Bulletin of Earthquake Engineering* 10.4 (2012), pp. 1221–1235. DOI: 10.1007/s10518-012-9347-x (cited on pages 12, 14, 17).

[16] R. Ditommaso, F. C. Ponzo, and G. Auletta. 'Damage detection on framed structures: modal curvature evaluation using Stockwell Transform under seismic excitation'. In: *Earthquake Engineering and Engineering Vibration* 14.2 (2015), pp. 265–274. DOI: 10.1007/s11803-015-0022-5 (cited on pages 12, 16).

[17] C. Iacovino, R. Ditommaso, F. C. Ponzo, and M. P. Limongelli. 'The Interpolation Evolution Method for damage localization in structures under seismic excitation'. In: *Earthquake Engineering and Structural Dynamics* 47.10 (2018), pp. 2117–2136. DOI: 10.1002/eqe.3062 (cited on pages 12, 17).

[18] A. G. Poulimenos and S. D. Fassois. 'Parametric time-domain methods for non-stationary random vibration modelling and analysis - A critical survey and comparison'. In: *Mechanical Systems and Signal Processing* 20.4 (2006), pp. 763–816. DOI: 10.1016/j.ymssp.2005.10.003 (cited on page 12).

[19] M. D. Spiridonakos and S. D. Fassois. *Adaptable functional series TARMA models for non-stationary signal modelling*. Vol. 16. PART 1. IFAC, 2012, pp. 1276–1281 (cited on page 12).

[20] M. Vetterli and J. Kovaevi. *Wavelets and Subband Coding*. Prentice-hall, 1995, pp. 1–519 (cited on pages 12, 37, 38, 40, 74, 80, 195, 263).

[21] D. Gabor. 'Theory of communication. Part 1: The analysis of information'. In: *Journal of the Institution of Electrical Engineers - Part III: Radio and Communication Engineering* 93.26 (1946), pp. 429–441. DOI: 10.1049/ji-3-2.1946.0074 (cited on page 12).

[22] I. Daubechies. *Ten Lectures on Wavelets*. 1992 (cited on page 12).

[23] R. G. Stockwell. 'Localization of the complex spectrum: the s transform'. In: *IEEE Transactions on Signal Processing* 44.4 (1996), p. 993. DOI: 10.1109/78.492555 (cited on page 12).

[24] B. Boashash. *Theory of Quadratic TFDs*. 2003. DOI: 10.1016/B978-008044335-5/50024-3 (cited on page 13).

[25] B. Boashash. 'Time frequency analysis: A comprehensive reference'. In: *Time Frequency Analysis: A Comprehensive Reference* (2003), pp. 1–743. DOI: 10.1016/B978-0-08-044335-5.X5020-7 (cited on page 13).

[26] F. Auger, P. Flandrin, Y. T. Lin, S. McLaughlin, S. Meignen, T. Oberlin, and H. T. Wu. 'Time-frequency reassignment and synchrosqueezing: An overview'. In: *IEEE Signal Processing Magazine* 30.6 (2013), pp. 32–41. DOI: 10.1109/MSP.2013.2265316 (cited on page 13).

[27] I. Daubechies, J. Lu, and H. T. Wu. 'Synchrosqueezed wavelet transforms: An empirical mode decomposition-like tool'. In: *Applied and Computational Harmonic Analysis* 30.2 (2011), pp. 243–261. DOI: 10.1016/j.acha.2010.08.002 (cited on page 13).

[28] N. E. Huang, Z. Shen, S. R. Long, M. C. Wu, H. H. Snin, Q. Zheng, N. C. Yen, C. C. Tung, and H. H. Liu. 'The empirical mode decomposition and the Hubert spectrum for nonlinear and non-stationary time series analysis'. In: *Proceedings of the Royal Society A: Mathematical, Physical and Engineering Sciences* 454.1971 (1998), pp. 903–995. DOI: 10.1098/rspa.1998.0193 (cited on pages 13, 17).

[29] R. Ditommaso, M. Mucciarelli, and F. C. Ponzo. 'Analysis of non-stationary structural systems by using a band-variable filter'. In: *Bulletin of Earthquake Engineering* 10.3 (2012), pp. 895–911. DOI: 10.1007/s10518-012-9338-y (cited on page 13).

[30] Z. Wu and N. E. Huang. 'Ensemble empirical mode decomposition: A noise-assisted data analysis method'. In: *Advances in Adaptive Data Analysis* 1.1 (2009), pp. 1–41. DOI: 10.1142/S1793536909000047 (cited on page 14).

[31] J. M. Lilly and S. C. Olhede. 'Analysis of modulated multivariate oscillations'. In: *IEEE Transactions on Signal Processing* 60.2 (2012), pp. 600–612. DOI: 10.1109/TSP.2011.2173681 (cited on page 14).

[32] A. Omidvarnia, B. Boashash, G. Azemi, P. Colditz, and S. Vanhatalo. 'Generalised phase synchrony within multivariate signals: An emerging concept in time-frequency analysis'. In: *ICASSP, IEEE International Conference on Acoustics, Speech and Signal Processing - Proceedings*. 2012, pp. 3417–3420. DOI: 10.1109/ICASSP.2012.6288650 (cited on page 14).

[33] L. Stankovi, D. Mandi, M. Dakovi, and M. Brajovi. 'Time-frequency decomposition of multivariate multicomponent signals'. In: *Signal Processing* 142 (2018), pp. 468–479. DOI: 10.1016/j.sigpro.2017.08.001 (cited on page 14).

[34] A. Ahrabian, D. Looney, L. Stankovi, and D. P. Mandic. 'Synchrosqueezing-based time-frequency analysis of multivariate data'. In: *Signal Processing* 106 (2015), pp. 331–341. DOI: 10.1016/j.sigpro.2014.08.010 (cited on pages 14, 79).

[35] N. Rehman and D. P. Mandic. 'Multivariate empirical mode decomposition'. In: *Proceedings of the Royal Society A: Mathematical, Physical and Engineering Sciences* 466.2117 (2010), pp. 1291–1302. DOI: 10.1098/rspa.2009.0502 (cited on pages 14, 112).

[36] N. Ur Rehman and D. P. Mandic. 'Filter bank property of multivariate empirical mode decomposition'. In: *IEEE Transactions on Signal Processing* 59.5 (2011), pp. 2421–2426. DOI: 10.1109/TSP.2011.2106779 (cited on page 14).

[37] M. R. Thirumalaisamy and P. J. Ansell. 'Fast and adaptive empirical mode decomposition for multidimensional, multivariate signals'. In: *IEEE Signal Processing Letters* 25.10 (2018), pp. 1550–1554. DOI: 10.1109/LSP.2018.2867335 (cited on pages 14, 112).

[38] L. E. Avendaño, L. D. Avendaño-Valencia, and E. Delgado-Trejos. 'Diagonal time dependent state space models for modal decomposition of non-stationary signals'. In: *Signal Processing* 147 (2018), pp. 208–223. DOI: 10.1016/j.sigpro.2018.01.031 (cited on page 14).

[39] D. Iatsenko, P. V. McClintock, and A. Stefanovska. 'Extraction of instantaneous frequencies from ridges in time-frequency representations of signals'. In: *Signal Processing* 125 (2016), pp. 290–303. DOI: 10.1016/j.sigpro.2016.01.024 (cited on page 14).

[40] N. Delprat, P. Guillemain, B. Escudie, R. Kronland-Martinet, P. Tchamitchian, and B. Torresani. 'Asymptotic Wavelet and Gabor Analysis: Extraction of Instantaneous Frequencies'. In: *IEEE Transactions on Information Theory* 38.2 (1992), pp. 644–664. DOI: 10.1109/18.119728 (cited on page 14).

[41] L. Rankine, M. Mesbah, and B. Boashash. 'IF estimation for multicomponent signals using image processing techniques in the time-frequency domain'. In: *Signal Processing* 87.6 (2007), pp. 1234–1250. DOI: 10.1016/j.sigpro.2006.10.013 (cited on page 14).

[42] W. J. Staszewski. 'Identification of non-linear systems using multi-scale ridges and skeletons of the wavelet transform'. In: *Journal of Sound and Vibration* 214.4 (1998), pp. 639–658. DOI: 10.1006/jsvi.1998.1616 (cited on page 14).

[43] C. Wang, W. X. Ren, Z. C. Wang, and H. P. Zhu. 'Instantaneous frequency identification of time-varying structures by continuous wavelet transform'. In: *Engineering Structures* 52 (2013), pp. 17–25. DOI: 10.1016/j.engstruct.2013.02.006 (cited on page 14).

[44] T. P. Le and P. Paultre. 'Modal identification based on the time-frequency domain decomposition of unknown-input dynamic tests'. In: *International Journal of Mechanical Sciences* 71 (2013), pp. 41–50. DOI: 10.1016/j.ijmecsci.2013.03.005 (cited on page 14).

[45] N. Özkurt and F. A. Savaci. 'Determination of Wavelet Ridges of Nonstationary Signals by Singular Value Decomposition'. In: *IEEE Transactions on Circuits and Systems II: Express Briefs* 52.8 (2005), pp. 480–485. DOI: 10.1109/TCSII.2005.849041 (cited on page 14).

[46] W. Liu, V. R. Bastante, F. R. Rodriguez, N. Evans, and J. Mason. 'Morphological filtering of spectrograms for automatic speech recognition'. In: *Proceedings of Visualization, Imaging, and Image Processing*. 2004 (cited on page 15).

[47] S. Gómez, V. Naranjo, and R. Miralles. 'Removing interference components in time-frequency representations using morphological operators'. In: *Journal of Visual Communication and Image Representation* 22.5 (2011), pp. 401–410. DOI: 10.1016/j.jvcir.2011.03.007 (cited on page 15).

[48] Z. Zhang, K. Xu, D. Ta, and W. Wang. *Joint spectrogram segmentation and ridge-extraction method for separating multimodal guided waves in long bones*. Vol. 56. 7. Science China: Physics, Mechanics and Astronomy, 2013, pp. 1317–1323 (cited on page 15).

[49] L. Vincent, L. Vincent, and P. Soille. 'Watersheds in Digital Spaces: An Efficient Algorithm Based on Immersion Simulations'. In: *IEEE Transactions on Pattern Analysis and Machine Intelligence* 13.6 (1991), pp. 583–598. DOI: 10.1109/34.87344 (cited on page 15).

[50] A. Roueff, J. Chanussot, J. I. Mars, and M. Q. Nguyen. 'Unsupervised separation of seismic waves using the watershed algorithm on time-scale images'. In: *Geophysical Prospecting* 52.4 (2004), pp. 287–300. DOI: 10.1111/j.1365-2478.2004.00416.x (cited on page 15).

[51] W. Y. He, W. X. Ren, and S. Zhu. 'Damage detection of beam structures using quasi-static moving load induced displacement response'. In: *Engineering Structures* 145 (2017), pp. 70–82. DOI: 10.1016/j.engstruct.2017.05.009 (cited on pages 15, 23).

[52] H. Zhuang, B. S. Oh, D. Lin, K. A. Toh, and Z. Lin. 'Multicomponent Signal Decomposition Using Morphological Operations'. In: *International Conference on Digital Signal Processing, DSP*. Vol. 2018-November. 2019, pp. 1–5. DOI: 10.1109/ICDSP.2018.8631863 (cited on page 15).

[53] P. Soille. *Morphological Image Analysis*. Berlin, Heidelberg: Springer Berlin Heidelberg, 2004 (cited on page 15).

[54] G. Kerschen, M. Peeters, J.-C. Golinval, and A. F. Vakakis. 'Nonlinear normal modes, Part I: A useful framework for the structural dynamicist'. In: *Mechanical systems and signal processing* 23.1 (2009), pp. 170–194. DOI: 10.1016/j.ymssp.2008.04.002 (cited on pages 15, 98).

[55] S. F. Ghahari, F. Abazarsa, and E. Taciroglu. 'Identification of soil-structure systems'. In: *Springer Tracts in Civil Engineering* (2019), pp. 139–167. DOI: 10.1007/978-3-030-13976-6_6 (cited on page 15).

[56] G. Kerschen, K. Worden, A. F. Vakakis, and J.-C. Golinval. 'Past, present and future of nonlinear system identification in structural dynamics'. In: *Mechanical systems and signal processing* 20.3 (2006), pp. 505–592. DOI: 10.1016/j.ymssp.2005.04.008 (cited on pages 15–17, 139).

[57] R. M. Lin and T. Y. Ng. 'Applications of higher-order frequency response functions to the detection and damage assessment of general structural systems with breathing cracks'. In: *International Journal of Mechanical Sciences* 148 (2018), pp. 652–666. DOI: 10.1016/j.ijmecsci.2018.08.027 (cited on pages 15, 17).

[58] R. Brincker and C. Ventura. *Introduction to operational modal analysis*. John Wiley & Sons, 2015, pp. 1–360 (cited on pages 15, 22, 36, 99, 209).

[59] M. P. Limongelli, M. Dolce, D. Spina, P. Guéguen, M. Langlais, D. Wolinieck, E. Maufroy, C. Z. Karakostas, V. A. Lekidis, K. Morfidis, T. Salonikios, E. Rovithis, K. Makra, M. G. Masciotta, and P. B. Lourenço. 'S 2 HM in some European countries'. In: *Springer Tracts in Civil Engineering* (2019), pp. 303–343. DOI: 10.1007/978-3-030-13976-6_13 (cited on page 16).

[60] Y. Fu, T. Hoang, K. Mechitov, J. R. Kim, D. Zhang, and B. F. Spencer. 'Sudden event monitoring of civil infrastructure using demand-based wireless smart sensors'. In: *Sensors (Switzerland)* 18.12 (2018). DOI: 10.3390/s18124480 (cited on page 16).

[61] J. P. Noël and G. Kerschen. 'Nonlinear system identification in structural dynamics: 10 more years of progress'. In: *Mechanical Systems and Signal Processing* 83 (2017), pp. 2–35. DOI: 10.1016/j.ymssp.2016.07.020 (cited on page 16).

[62] R. M. Rosenberg. 'On Nonlinear Vibrations of Systems with Many Degrees of Freedom'. In: *Advances in Applied Mechanics* 9.C (1966), pp. 155–242. DOI: 10.1016/S0065-2156(08)70008-5 (cited on pages 16, 98, 100).

[63] G. Kerschen, A. F. Vakakis, Y. S. Lee, D. M. McFarland, and L. A. Bergman. 'Toward a fundamental understanding of the Hilbert-Huang transform in nonlinear structural dynamics'. In: *JVC/Journal of Vibration and Control* 14.1-2 (2008), pp. 77–105. DOI: 10.1177/1077546307079381 (cited on page 17).

[64] P. F. Pai and A. N. Palazotto. 'Detection and identification of nonlinearities by amplitude and frequency modulation analysis'. In: *Mechanical Systems and Signal Processing* 22.5 (2008), pp. 1107–1132. DOI: 10.1016/j.ymssp.2007.11.006 (cited on page 17).

[65] W. J. Staszewski. 'Analysis of non-linear systems using wavelets'. In: *Proceedings of the Institution of Mechanical Engineers, Part C: Journal of Mechanical Engineering Science* 214.11 (2000), pp. 1339–1353. DOI: 10.1243/0954406001523317 (cited on page 17).

[66] H. Ebrahimian, R. Astroza, J. P. Conte, and C. Papadimitriou. 'Bayesian optimal estimation for output-only nonlinear system and damage identification of civil structures'. In: *Structural Control and Health Monitoring* 25.4 (Apr. 2018), e2128. DOI: 10.1002/stc.2128 (cited on page 17).

[67] G. De Roeck. 'Modelbased methods of damage identification of structures under seismic excitation'. In: *Springer Tracts in Civil Engineering* (2019), pp. 237–259. DOI: 10.1007/978-3-030-13976-6_10 (cited on page 17).

[68] C. C. Huang and C. H. Loh. 'Nonlinear identification of dynamic systems using neural networks'. In: *Computer-Aided Civil and Infrastructure Engineering* 16.1 (2001), pp. 28–41. DOI: 10.1111/0885-9507.00211 (cited on page 17).

[69] C. H. Loh and H. M. Lin. 'Application of off-line and on-line identification techniques to building seismic response data'. In: *Earthquake Engineering and Structural Dynamics* 25.3 (Mar. 1996), pp. 269–290. DOI: 10.1002/(SICI)1096-9845(199603)25:3<269::AID-EQE554>3.0.CO;2-J (cited on page 17).

[70] B. Bhowmik, T. Tripura, B. Hazra, and V. Pakrashi. 'Real time structural modal identification using recursive canonical correlation analysis and application towards online structural damage detection'. In: *Journal of Sound and Vibration* 468 (2020), p. 115101. DOI: 10.1016/j.jsv.2019.115101 (cited on pages 17, 80).

[71] M. W. Sracic and M. S. Allen. 'Identifying parameters of multi-degree-of-freedom nonlinear structural dynamic systems using linear time periodic approximations'. In: *Mechanical Systems and Signal Processing* 46.2 (2014), pp. 325–343. DOI: 10.1016/j.ymssp.2014.01.014 (cited on pages 17, 112).

[72] H. S. Park, Y. Shin, S. W. Choi, and Y. Kim. 'An integrative structural health monitoring system for the local/global responses of a large-scale irregular building under construction.' In: *Sensors (Basel, Switzerland)* 13.7 (July 2013), pp. 9085–9103. DOI: 10.3390/s130709085 (cited on page 18).

[73] A. C. Tokognon, B. Gao, G. Y. Tian, and Y. Yan. 'Structural Health Monitoring Framework Based on Internet of Things: A Survey'. In: *IEEE Internet of Things Journal* 4.3 (2017), pp. 619–635. DOI: 10.1109/JIOT.2017.2664072 (cited on page 18).

[74] J. P. Lynch and K. J. Loh. 'A summary review of wireless sensors and sensor networks for structural health monitoring'. In: *Shock and Vibration Digest* 38.2 (2006), pp. 91–130. DOI: 10.1177/0583102406061499 (cited on pages 18, 89).

[75] A. B. Noel, A. Abdaoui, T. Elfouly, M. H. Ahmed, A. Badawy, and M. S. Shehata. 'Structural health monitoring using wireless sensor networks: A comprehensive survey'. In: *IEEE Communications Surveys & Tutorials* 19.3 (2017), pp. 1403–1423. DOI: 10.1109/COMST.2017.2691551 (cited on pages 18, 90).

[76] G. Hackmann, F. Sun, N. Castaneda, C. Lu, and S. Dyke. 'A holistic approach to decentralized structural damage localization using wireless sensor networks'. In: *Proceedings - Real-Time Systems Symposium*. IEEE, Nov. 2008, pp. 35–46. DOI: 10.1109/RTSS.2008.40 (cited on page 18).

[77] A. Jindal and M. Liu. 'Networked computing in wireless sensor networks for structural health monitoring'. In: *IEEE/ACM Transactions on Networking* 20.4 (2012), pp. 1203–1216. DOI: 10.1109/TNET.2011.2175450 (cited on page 18).

[78] J. Long and O. Büyüköztürk. 'A power optimised and reprogrammable system for smart wireless vibration monitoring'. In: *Structural Control and Health Monitoring* 27.2 (2020). DOI: 10.1002/stc.2468 (cited on pages 18, 19).

[79] H. Jo, S.-H. Sim, T. Nagayama, and B. Spencer Jr. 'Development and application of high-sensitivity wireless smart sensors for decentralized stochastic modal identification'. In: *Journal of Engineering Mechanics* 138.6 (June 2012), pp. 683–694. DOI: 10.1061/(asce)em.1943-7889.0000352 (cited on pages 18, 20, 89).

[80] L. E. Linderman, K. A. Mechitov, and B. F. Spencer. 'TinyOS-based real-time wireless data acquisition framework for structural health monitoring and control'. In: *Structural Control and Health Monitoring* 20.6 (June 2013), pp. 1007–1020. DOI: 10.1002/stc.1514 (cited on page 18).

[81] J. A. Rice, K. A. Mechitov, S. H. Sim, B. F. Spencer, and G. A. Agha. 'Enabling framework for structural health monitoring using smart sensors'. In: *Structural Control and Health Monitoring* 18.5 (Aug. 2011), pp. 574–587. DOI: 10.1002/stc.386 (cited on page 18).

[82] S. H. Sim, J. F. Carbonell-Mrquez, B. F. Spencer, and H. Jo. 'Decentralized random decrement technique for efficient data aggregation and system identification in wireless smart sensor networks'. In: *Probabilistic Engineering Mechanics* 26.1 (Jan. 2011), pp. 81–91. DOI: 10.1016/j.probengmech.2010.07.002 (cited on page 18).

[83] G. J. Yun, S. G. Lee, J. Carletta, and T. Nagayama. 'Decentralized damage identification using wavelet signal analysis embedded on wireless smart sensors'. In: *Engineering Structures* 33.7 (2011), pp. 2162–2172. DOI: 10.1016/j.engstruct.2011.03.007 (cited on page 18).

[84] A. Sadhu and S. Narasimhan. 'A decentralized blind source separation algorithm for ambient modal identification in the presence of narrowband disturbances'. In: *Structural Control and Health Monitoring* 21.3 (Mar. 2014), pp. 282–302. DOI: 10.1002/stc.1558 (cited on page 19).

[85] D. Vakman. 'On the analytic signal the teager-kaiser energy algorithm and other methods for defining amplitude and frequency'. In: *IEEE Transactions on Signal Processing* 44.4 (Apr. 1996), pp. 791–797. DOI: 10.1109/78.492532 (cited on page 19).

[86] Z. Wang and G. Chen. 'Recursive Hilbert-Huang transform method for time-varying property identification of linear shear-type buildings under base excitations'. In: *Journal of engineering mechanics* 138.6 (June 2012), pp. 631–639. DOI: 10.1061/(asce)em.1943-7889.0000357 (cited on pages 19, 90).

[87] C. Bao, H. Hao, and Z.-X. Li. 'Multi-stage identification scheme for detecting damage in structures under ambient excitations'. In: *Smart materials and structures* 22.4 (Apr. 2013), p. 045006. DOI: 10.1088/0964-1726/22/4/045006 (cited on pages 19, 80, 90).

[88] F. Magalhães, A. Cunha, and E. Caetano. 'Vibration based structural health monitoring of an arch bridge: From automated OMA to damage detection'. In: *Mechanical Systems and Signal Processing* 28 (Apr. 2012), pp. 212–228. DOI: 10.1016/j.ymssp.2011.06.011 (cited on page 19).

[89] J. A. Goulet and I. F. C. Smith. 'Performance-Driven Measurement System Design for Structural Identification'. In: *Journal of Computing in Civil Engineering* 27.4 (July 2013), pp. 427–436. DOI: 10.1061/(asce)cp.1943-5487.0000250 (cited on page 19).

[90] K. Zhou, Z. Y. Wu, X. H. Yi, D. P. Zhu, R. Narayan, and J. Zhao. 'Generic Framework of Sensor Placement Optimization for Structural Health Modeling'. In: *Journal of Computing in Civil Engineering* 31.4 (July 2017), p. 04017018. DOI: 10.1061/(asce)cp.1943-5487.0000662 (cited on page 19).

[91] K. Dragos, M. Theiler, F. Magalhães, C. Moutinho, and K. Smarsly. 'On-board data synchronization in wireless structural health monitoring systems based on phase locking'. In: *Structural Control and Health Monitoring* 25.11 (2018). DOI: 10.1002/stc.2248 (cited on page 19).

[92] Y. Fu, K. Mechitov, T. Hoang, J. R. Kim, S. A. Memon, and B. F. Spencer. 'Efficient and high-precision time synchronization for wireless monitoring of civil infrastructure subjected to sudden events'. In: *Structural Control and Health Monitoring* 28.1 (2021). DOI: 10.1002/stc.2643 (cited on page 19).

[93] S. N. Pakzad, G. L. Fenves, S. Kim, and D. E. Culler. 'Design and Implementation of Scalable Wireless Sensor Network for Structural Monitoring'. In: *Journal of Infrastructure Systems* 14.1 (2008), pp. 89–101. DOI: 10.1061/(asce)1076-0342(2008)14:1(89) (cited on pages 19, 20).

[94] S. Jang, H. Jo, S. Cho, K. Mechitov, J. A. Rice, S.-H. Sim, H.-J. Jung, C.-B. Yun, B. F. Spencer Jr, and G. Agha. 'Structural health monitoring of a cable-stayed bridge using smart sensor technology: deployment and evaluation'. In: *Smart Structures and Systems* 6.5-6 (2010), pp. 439–459. DOI: 10.12989/sss.2010.6.5_6.439 (cited on pages 19, 20, 89).

[95] M. J. Whelan, M. V. Gangone, K. D. Janoyan, and R. Jha. 'Real-time wireless vibration monitoring for operational modal analysis of an integral abutment highway bridge'. In: *Engineering Structures* 31.10 (2009), pp. 2224–2235. DOI: 10.1016/j.engstruct.2009.03.022 (cited on page 19).

[96] S. Yuan, X. Lai, X. Zhao, X. Xu, and L. Zhang. 'Distributed structural health monitoring system based on smart wireless sensor and multi-agent technology'. In: *Smart Materials and Structures* 15.1 (2006), pp. 1–8. DOI: 10.1088/0964-1726/15/1/029 (cited on page 20).

[97] S. Kim, S. Pakzad, D. Culler, J. Demmel, G. Fenves, S. Glaser, and M. Turon. 'Health monitoring of civil infrastructures using wireless sensor networks'. In: *IPSN 2007: Proceedings of the Sixth International Symposium on Information Processing in Sensor Networks* (2007), pp. 254–263. DOI: 10.1145/1236360.1236395 (cited on page 20).

[98] J. A. Rice, K. Mechitov, S. H. Sim, T. Nagayama, S. Jang, R. Kim, B. F. Spencer, G. Agha, and Y. Fujino. 'Flexible smart sensor framework for autonomous structural health monitoring'. In: *Smart Structures and Systems* 6.5-6 (2010), pp. 423–438. DOI: 10.12989/sss.2010.6.5_6.423 (cited on page 20).

[99] B. F. Spencer, H. Jo, K. A. Mechitov, J. Li, S. H. Sim, R. E. Kim, S. Cho, L. E. Linderman, P. Moinzadeh, R. K. Giles, and G. Agha. 'Recent advances in wireless smart sensors for multi-scale monitoring and control of civil infrastructure'. In: *Journal of Civil Structural Health Monitoring* 6.1 (2016), pp. 17–41. DOI: 10.1007/s13349-015-0111-1 (cited on page 20).

[100] J. A. Rice and B. F. Spencer, Jr. *Structural health monitoring sensor development for the Imote2 platform*. Ed. by M. Tomizuka. 2008. DOI: 10.1117/12.776695 (cited on page 20).

[101] B. F. Spencer, J. W. Park, K. A. Mechitov, H. Jo, and G. Agha. 'Next Generation Wireless Smart Sensors Toward Sustainable Civil Infrastructure'. In: *Procedia Engineering* 171 (2017), pp. 5–13. DOI: 10.1016/j.proeng.2017.01.304 (cited on page 20).

[102] A. Sabato, M. Q. Feng, Y. Fukuda, D. L. Carni, and G. Fortino. 'A Novel Wireless Accelerometer Board for Measuring Low-Frequency and Low-Amplitude Structural Vibration'. In: *IEEE Sensors Journal* 16.9 (May 2016), pp. 2942–2949. DOI: 10.1109/JSEN.2016.2522940 (cited on page 21).

[103] L. Liu and F. G. Yuan. 'Wireless sensors with dual-controller architecture for active diagnosis in structural health monitoring'. In: *Smart Materials and Structures* 17.2 (Apr. 2008), p. 025016. DOI: 10.1088/0964-1726/17/2/025016 (cited on page 21).

[104] A. Cigada, G. Moschioni, M. Vanali, and A. Caprioli. 'The measurement network of the san siro meazza stadium in milan: Origin and implementation of a new data acquisition strategy for structural health monitoring: Dynamic testing of civil engineering structures series'. In: *Experimental Techniques* 34.1 (Jan. 2010), pp. 70–81. DOI: 10.1111/j.1747-1567.2009.00536.x (cited on page 21).

[105] V. K. Varadan. 'Wireless microsensors for health monitoring of structures'. In: *Smart Structures, Devices, and Systems*. Ed. by E. C. Harvey, D. Abbott, and V. K. Varadan. Vol. 4935. Nov. 2002, p. 526. DOI: 10.1117/12.473337 (cited on page 21).

[106] D. Ielmini and H. S. Wong. 'In-memory computing with resistive switching devices'. In: *Nature Electronics* 1.6 (June 2018), pp. 333–343. DOI: 10.1038/s41928-018-0092-2 (cited on page 21).

[107] F. Arnaud, P. Zuliani, J. P. Reynard, A. Gandolfo, F. Disegni, P. Mattavelli, E. Gomiero, G. Samanni, C. Jahan, R. Berthelon, O. Weber, E. Richard, V. Barral, A. Villaret, S. Kohler, J. C. Grenier, R. Ranica, C. Gallon, A. Souhaite, D. Ristoiu, L. Favennec, V. Caubet, S. Delmedico, N. Cherault, R. Beneyton, S. Chouteau, P. O. Sassoulas, A. Vernhet, Y. Le Friec, F. Domengie, L. Scotti, D. Pacelli, J. L. Ogier, F. Boucard, S. Lagrasta, D. Benoit, L. Clement, P. Boivin, P. Ferreira, R. Annunziata, and P. Cappelletti. 'Truly Innovative 28nm FDSOI Technology for Automotive Micro-Controller Applications embedding 16MB Phase Change Memory'. In: *Technical Digest - International Electron Devices Meeting, IEDM*. Vol. 2018-December. IEEE, Dec. 2019, pp. 18.4.1–18.4.4. DOI: 10.1109/IEDM.2018.8614595 (cited on page 21).

[108] D. Ielmini and S. Ambrogio. 'Emerging neuromorphic devices'. In: *Nanotechnology* 31.9 (Feb. 2020), p. 092001. DOI: 10.1088/1361-6528/ab554b (cited on page 21).

[109] Q. F. Ou, B. S. Xiong, L. Yu, J. Wen, L. Wang, and Y. Tong. 'In-memory logic operations and neuromorphic computing in non-volatile random access memory'. In: *Materials* 13.16 (2020). DOI: 10.3390/MA13163532 (cited on page 21).

[110] A. Pirovano, A. L. Lacaita, F. Pellizzer, S. A. Kostylev, A. Benvenuti, and R. Bez. 'Low-field amorphous state resistance and threshold voltage drift in chalcogenide materials'. In: *IEEE Transactions on Electron Devices* 51.5 (2004), pp. 714–719. DOI: 10.1109/TED.2004.825805 (cited on page 21).

[111] G. W. Burr, R. M. Shelby, C. Di Nolfo, J. W. Jang, R. S. Shenoy, P. Narayanan, K. Virwani, E. U. Giacometti, B. Kurdi, and H. Hwang. 'Experimental demonstration and tolerancing of a large-scale neural network (165,000 synapses), using phase-change memory as the synaptic weight element'. In: *Technical Digest - International Electron Devices Meeting, IEDM*. Vol. 2015-February. February. IEEE, Dec. 2015, pp. 29.5.1–29.5.4. DOI: 10.1109/IEDM.2014.7047135 (cited on page 21).

[112] V. Joshi, M. Le Gallo, S. Haefeli, I. Boybat, S. R. Nandakumar, C. Piveteau, M. Dazzi, B. Rajendran, A. Sebastian, and E. Eleftheriou. 'Accurate deep neural network inference using computational phase-change memory'. In: *Nature communications* 11.1 (2020), pp. 1–13. DOI: 10.1038/s41467-020-16108-9 (cited on pages 21, 200).

[113] T. Tuma, A. Pantazi, M. Le Gallo, A. Sebastian, and E. Eleftheriou. 'Stochastic phase-change neurons'. In: *Nature Nanotechnology* 11.8 (Aug. 2016), pp. 693–699. DOI: 10.1038/nnano.2016.70 (cited on page 21).

[114] S. K. Yoon, J. Yun, J. G. Kim, and S. D. Kim. 'Self-Adaptive Filtering Algorithm with PCM-Based Memory Storage System'. In: *ACM Transactions on Embedded Computing Systems* 17.3 (June 2018), pp. 1–23. DOI: 10.1145/3190856 (cited on page 21).

[115] P. Narayanan, S. Ambrogio, A. Okazaki, K. Hosokawa, H. Tsai, A. Nomura, T. Yasuda, C. Mackin, S. C. Lewis, A. Friz, M. Ishii, Y. Kohda, H. Mori, K. Spoon, R. Khaddam-Aljameh, N. Saulnier, M. Bergendahl, J. Demarest, K. W. Brew, V. Chan, S. Choi, I. Ok, I. Ahsan, F. L. Lie, W. Haensch, V. Narayanan, and G. W. Burr. 'Fully On-Chip MAC at 14 nm Enabled by Accurate Row-Wise Programming of PCM-Based Weights and Parallel Vector-Transport in Duration-Format'. In: *IEEE Transactions on Electron Devices* 68.12 (2021), pp. 6629–6636. DOI: 10.1109/TED.2021.3115993 (cited on page 22).

[116] R. Schlaifer and H. Raiffa. *Applied statistical decision theory*. 1961 (cited on page 22).

[117] P. F. Giordano, L. J. Prendergast, and M. P. Limongelli. 'A framework for assessing the value of information for health monitoring of scoured bridges'. In: *Journal of Civil Structural Health Monitoring* 10.3 (2020), pp. 485–496. DOI: 10.1007/s13349-020-00398-0 (cited on pages 22, 24).

[118] A. Aloisio, R. Alaggio, and M. Fragiacomo. 'Time-domain identification of the elastic modulus of simply supported box girders under moving loads: Method and full-scale validation'. In: *Engineering Structures* 215 (2020), p. 110619. DOI: 10.1016/j.engstruct.2020.110619 (cited on pages 23, 138, 155, 207).

[119] M. A. Khan, D. P. McCrum, L. J. Prendergast, E. J. OBrien, P. C. Fitzgerald, and C. W. Kim. 'Laboratory investigation of a bridge scour monitoring method using decentralized modal analysis'. In: *Structural Health Monitoring* 20.6 (2021), pp. 3327–3341. DOI: 10.1177/1475921720985122 (cited on page 23).

[120] F. Cavadas, I. F. Smith, and J. Figueiras. 'Damage detection using data-driven methods applied to moving-load responses'. In: *Mechanical Systems and Signal Processing* 39.1-2 (2013), pp. 409–425. DOI: 10.1016/j.ymssp.2013.02.019 (cited on page 23).

[121] G. T. Frøseth, A. Rønnquist, D. Cantero, and O. Øiseth. 'Influence line extraction by deconvolution in the frequency domain'. In: *Computers and Structures* 189 (2017), pp. 21–30. DOI: 10.1016/j.compstruc.2017.04.014 (cited on pages 23, 146).

[122] X. Zheng, D. H. Yang, T. H. Yi, and H. N. Li. 'Development of bridge influence line identification methods based on direct measurement data: A comprehensive review and comparison'. In: *Engineering Structures* 198 (2019). DOI: 10.1016/j.engstruct.2019.109539 (cited on page 23).

[123] X. Zheng, D.-H. Yang, T.-H. Yi, H.-N. Li, and Z.-W. Chen. 'Bridge Influence Line Identification Based on Regularized Least-Squares QR Decomposition Method'. In: *Journal of Bridge Engineering* 24.8 (2019), p. 06019004. DOI: 10.1061/(asce)be.1943-5592.0001458 (cited on page 23).

[124] D. Hester, J. Brownjohn, F. Huseynov, E. Obrien, A. Gonzalez, and M. Casero. 'Identifying damage in a bridge by analysing rotation response to a moving load'. In: *Structure and Infrastructure Engineering* 16.7 (2020), pp. 1050–1065. DOI: 10.1080/15732479.2019.1680710 (cited on page 23).

[125] Z.-W. Chen, S. Zhu, Y.-L. Xu, Q. Li, and Q.-L. Cai. 'Damage Detection in Long Suspension Bridges Using Stress Influence Lines'. In: *Journal of Bridge Engineering* 20.3 (Mar. 2015), p. 05014013. DOI: 10.1061/(asce)be.1943-5592.0000681 (cited on page 23).

[126] B. Heitner, F. Schoefs, E. J. OBrien, A. nidari, and T. Yalamas. 'Using the unit influence line of a bridge to track changes in its condition'. In: *Journal of Civil Structural Health Monitoring* 10.4 (2020), pp. 667–678. DOI: 10.1007/s13349-020-00410-7 (cited on page 23).

[127] A. nidari and J. Kalin. 'Using bridge weigh-in-motion systems to monitor single-span bridge influence lines'. In: *Journal of Civil Structural Health Monitoring* 10.5 (Nov. 2020), pp. 743–756. DOI: 10.1007/s13349-020-00407-2 (cited on page 23).

[128] D. Zonta, B. Glisic, and S. Adriaenssens. 'Value of information: Impact of monitoring on decision-making'. In: *Structural Control and Health Monitoring* 21.7 (July 2014), pp. 1043–1056. DOI: 10.1002/stc.1631 (cited on page 24).

[129] Y. B. Yang, C. W. Lin, and J. D. Yau. 'Extracting bridge frequencies from the dynamic response of a passing vehicle'. In: *Journal of Sound and Vibration* 272.3-5 (2004), pp. 471–493. DOI: 10.1016/S0022-460X(03)00378-X (cited on page 24).

[130] C. Lin and Y. Yang. 'Use of a passing vehicle to scan the fundamental bridge frequencies: An experimental verification'. In: *Engineering Structures* 27.13 (2005), pp. 1865–1878. DOI: 10.1016/j.engstruct.2005.06.016 (cited on pages 24, 25, 183).

[131] C. W. Kim and M. Kawatani. 'Challenge for a drive-by bridge inspection'. In: *Safety, Reliability and Risk of Structures, Infrastructures and Engineering Systems*. Ed. by H. Furuta, D. Frangopol, and M. Shinozuka. Osaka, Japan: Taylor & Francis, 2010, pp. 758–765 (cited on page 24).

[132] A. González, E. J. Obrien, and P. J. McGetrick. 'Identification of damping in a bridge using a moving instrumented vehicle'. In: *Journal of Sound and Vibration* 331.18 (2012), pp. 4115–4131. DOI: 10.1016/j.jsv.2012.04.019 (cited on pages 24, 25).

[133] F. Cerda, J. Garrett, J. Bielak, J. Barrera, Z. Zhuang, S. Chen, M. McCann, J. Kovaevi, and P. Rizzo. 'Indirect structural health monitoring in bridges: Scale experiments'. In: *Bridge Maintenance, Safety, Management, Resilience and Sustainability - Proceedings of the Sixth International Conference on Bridge Maintenance, Safety and Management* (2012), pp. 346–353 (cited on page 24).

[134] R. Zaurin and F. N. Catbas. 'Structural health monitoring using video stream, influence lines, and statistical analysis'. In: *Structural Health Monitoring* 10.3 (2011), pp. 309–332. DOI: 10.1177/1475921710373290 (cited on page 25).

[135] B. Chen, X. Wang, D. Sun, and X. Xie. 'Integrated system of structural health monitoring and intelligent management for a cable-stayed bridge'. In: *Scientific World Journal* 2014 (2014). DOI: 10.1155/2014/689471 (cited on page 25).

[136] J. Kim, J. P. Lynch, J. J. Lee, and C. G. Lee. 'Truck-based mobile wireless sensor networks for the experimental observation of vehicle-bridge interaction'. In: *Smart Materials and Structures* 20.6 (2011). DOI: 10.1088/0964-1726/20/6/065009 (cited on page 25).

[137] C. W. Kim, S. Inoue, K. Sugiura, P. J. McGetrick, and M. Kawatani. 'Extracting bridge frequencies from dynamic responses of two passing vehicles'. In: *Insights and Innovations in Structural Engineering, Mechanics and Computation - Proceedings of the 6th International Conference on Structural Engineering, Mechanics and Computation, SEMC 2016*. 2016, pp. 1858–1864. DOI: 10.1201/9781315641645-307 (cited on page 25).

[138] J. Li, X. Zhu, S. seong Law, and B. Samali. 'Indirect bridge modal parameters identification with one stationary and one moving sensors and stochastic subspace identification'. In: *Journal of Sound and Vibration* 446 (2019), pp. 1–21. DOI: 10.1016/j.jsv.2019.01.024 (cited on page 25).

[139] J. Kim and J. P. Lynch. 'Experimental analysis of vehicle-bridge interaction using a wireless monitoring system and a two-stage system identification technique'. In: *Mechanical Systems and Signal Processing* 28 (2012), pp. 3–19. DOI: 10.1016/j.ymssp.2011.12.008 (cited on page 25).

[140] S. Sadeghi Eshkevari, T. J. Matarazzo, and S. N. Pakzad. 'Bridge modal identification using acceleration measurements within moving vehicles'. In: *Mechanical Systems and Signal Processing* 141 (2020), p. 106733. DOI: 10.1016/j.ymssp.2020.106733 (cited on page 25).

[141] S. Ercolessi, G. Fabbrocino, and C. Rainieri. 'Indirect measurements of bridge vibrations as an experimental tool supporting periodic inspections'. In: *Infrastructures* 6.3 (Mar. 2021), p. 39. DOI: 10.3390/infrastructures6030039 (cited on page 25).

[142] Y. Oshima, K. Yamamoto, and K. Sugiura. 'Damage assessment of a bridge based on mode shapes estimated by responses of passing vehicles'. In: *Smart Structures and Systems* 13.5 (May 2014), pp. 731–753. DOI: 10.12989/sss.2014.13.5.731 (cited on page 25).

[143] C. W. Kim, K. C. Chang, P. J. McGetrick, S. Inoue, and S. Hasegawa. 'Utilizing moving vehicles as sensors for bridge condition screening-A laboratory verification'. In: *Sensors and Materials* 29.2 (2017), pp. 153–163. DOI: 10.18494/SAM.2017.1433 (cited on page 25).

[144] G. Lederman, Z. Wang, J. Bielak, H. Noh, J. H. Garrett, S. Chen, J. Kovaevi, F. Cerda, and P. Rizzo. 'Damage quantification and localization algorithms for indirect SHM of bridges'. In: *Bridge Maintenance, Safety, Management and Life Extension - Proceedings of the 7th International Conference of Bridge Maintenance, Safety and Management, IABMAS 2014*. 2014, pp. 640–647. DOI: 10.1201/b17063-93 (cited on page 25).

[145] J. Liu, S. Chen, M. Bergés, J. Bielak, J. H. Garrett, J. Kovaevi, and H. Y. Noh. 'Diagnosis algorithms for indirect structural health monitoring of a bridge model via dimensionality reduction'. In: *Mechanical Systems and Signal Processing* 136 (2020). DOI: 10.1016/j.ymssp.2019.106454 (cited on page 25).

[146] Y. Yang, K. Chang, and Y. Li. 'Filtering techniques for extracting bridge frequencies from a test vehicle moving over the bridge'. In: *Engineering Structures* 48 (Mar. 2013), pp. 353–362. DOI: 10.1016/j.engstruct.2012.09.025 (cited on pages 25, 187).

[147] H. Wang, T. Nagayama, J. Nakasuka, B. Zhao, and D. Su. 'Extraction of bridge fundamental frequency from estimated vehicle excitation through a particle filter approach'. In: *Journal of Sound and Vibration* 428 (2018), pp. 44–58. DOI: 10.1016/j.jsv.2018.04.030 (cited on page 25).

[148] P. J. McGetrick and C. W. Kim. 'An indirect bridge inspection method incorporating a wavelet-based damage indicator and pattern recognition'. In: *Proceedings of the International Conference on Structural Dynamic , EURODYN*. Vol. 2014-January. 2014, pp. 2605–2612 (cited on page 25).

[149] A. Aloisio, R. Alaggio, and M. Fragiacomo. 'Bending Stiffness Identification of Simply Supported Girders using an Instrumented Vehicle: Full Scale Tests, Sensitivity Analysis, and Discussion'. In: *Journal of Bridge Engineering* 26.1 (2021), p. 04020115. DOI: 10.1061/(asce)be.1943-5592.0001654 (cited on pages 25, 138, 207).

[150] D. M. Siringoringo and Y. Fujino. 'Estimating bridge fundamental frequency from vibration response of instrumented passing vehicle: analytical and experimental study'. In: *Advances in Structural Engineering* 15.3 (Mar. 2012), pp. 417–433. DOI: 10.1260/1369-4332.15.3.417 (cited on pages 25, 188).

[151] A. Miyamoto and A. Yabe. 'Development of practical health monitoring system for short- and medium-span bridges based on vibration responses of city bus'. In: *Journal of Civil Structural Health Monitoring* 2.1 (2012), pp. 47–63. DOI: 10.1007/s13349-012-0017-0 (cited on page 25).

[152] A. Malekjafarian, P. J. McGetrick, and E. J. OBrien. 'A review of indirect bridge monitoring using passing vehicles'. In: *Shock and vibration* 2015 (2015). DOI: 10.1155/2015/286139 (cited on pages 25, 183).

[153] H. Shokravi, H. Shokravi, N. Bakhary, M. Heidarrezaei, S. S. R. Koloor, and M. Petr. 'Vehicle-assisted techniques for health monitoring of bridges'. In: *Sensors (Switzerland)* 20.12 (June 2020), pp. 1–29. DOI: 10.3390/s20123460 (cited on page 25).

[154] X. Q. Zhu and S. S. Law. 'Structural health monitoring based on vehicle-bridge interaction: Accomplishments and challenges'. In: *Advances in Structural Engineering* 18.12 (2015), pp. 1999–2015. DOI: 10.1260/1369-4332.18.12.1999 (cited on page 25).

[155] M. Feng, Y. Fukuda, M. Mizuta, and E. Ozer. 'Citizen sensors for SHM: Use of accelerometer data from smartphones'. In: *Sensors (Switzerland)* 15.2 (2015), pp. 2980–2998. DOI: 10.3390/s150202980 (cited on pages 26, 27).

[156] P. McGetrick, D. Hester, and S. Taylor. 'Implementation of a drive-by monitoring system for transport infrastructure utilising smartphone technology and GNSS'. In: *Journal of Civil Structural Health Monitoring* 7.2 (2017), pp. 175–189. DOI: 10.1007/s13349-017-0218-7 (cited on pages 26, 188).

[157] A. Elhattab, N. Uddin, and E. OBrien. 'Drive-by bridge damage monitoring using Bridge Displacement Profile Difference'. In: *Journal of Civil Structural Health Monitoring* 6.5 (2016), pp. 839–850. DOI: 10.1007/s13349-016-0203-6 (cited on page 26).

[158] E. Ozer, R. Purasinghe, and M. Q. Feng. 'Multi-output modal identification of landmark suspension bridges with distributed smartphone data: Golden Gate Bridge'. In: *Structural Control and Health Monitoring* 27.10 (2020), pp. 1–29. DOI: 10.1002/stc.2576 (cited on page 26).

[159] T. J. Matarazzo, P. Santi, S. N. Pakzad, K. Carter, C. Ratti, B. Moaveni, C. Osgood, and N. Jacob. 'Crowdsensing Framework for Monitoring Bridge Vibrations Using Moving Smartphones'. In: *Proceedings of the IEEE* 106.4 (2018), pp. 577–593. DOI: 10.1109/JPROC.2018.2808759 (cited on page 26).

[160] Q. Mei and M. Gül. 'A crowdsourcing-based methodology using smartphones for bridge health monitoring'. In: *Structural Health Monitoring* 18.5-6 (2019), pp. 1602–1619. DOI: 10.1177/1475921718815457 (cited on page 26).

[161] E. Ozer, M. Q. Feng, and D. Feng. 'Citizen sensors for SHM: Towards a crowdsourcing platform'. In: *Sensors (Switzerland)* 15.6 (2015), pp. 14591–14614. DOI: 10.3390/s150614591 (cited on page 26).

[162] E. Ozer and M. Q. Feng. 'Direction-sensitive smart monitoring of structures using heterogeneous smartphone sensor data and coordinate system transformation'. In: *Smart Materials and Structures* 26.4 (2017). DOI: 10.1088/1361-665X/aa6298 (cited on page 26).

[163] E. Ozer and M. Q. Feng. 'Structural reliability estimation with participatory sensing and mobile cyber-physical structural health monitoring systems'. In: *Applied Sciences (Switzerland)* 9.14 (July 2019), p. 2840. DOI: 10.3390/app9142840 (cited on page 26).

[164] T. J. Matarazzo, D. Kondor, P. Santi, S. Milardo, S. S. Eshkevari, S. N. Pakzad, and C. Ratti. *Crowdsourcing Bridge Vital Signs with Smartphone Vehicle Trips*. 2020. URL: http://arxiv.org/abs/2010.07026 (cited on page 26).

[165] S. Cho, R. K. Giles, and B. F. Spencer. 'System identification of a historic swing truss bridge using a wireless sensor network employing orientation correction'. In: *Structural Control and Health Monitoring* 22.2 (Feb. 2015), pp. 255–272. DOI: 10.1002/stc.1672 (cited on page 27).

[166] H. Sun and O. Büyüköztürk. 'Identification of traffic-induced nodal excitations of truss bridges through heterogeneous data fusion'. In: *Smart Materials and Structures* 24.7 (2015). DOI: 10.1088/0964-1726/24/7/075032 (cited on page 27).

[167] E. Ozer and M. Q. Feng. 'Biomechanically influenced mobile and participatory pedestrian data for bridge monitoring'. In: *International Journal of Distributed Sensor Networks* 13.4 (Apr. 2017), p. 1550147717705240. DOI: 10.1177/1550147717705240 (cited on pages 27, 187).

[168] F. Seraj, B. J. Van Der Zwaag, A. Dilo, T. Luarasi, and P. Havinga. 'Roads: A road pavement monitoring system for anomaly detection using smart phones'. In: *Lecture Notes in Computer Science (including subseries Lecture Notes in Artificial Intelligence and Lecture Notes in Bioinformatics)*. Vol. 9546. 2016, pp. 128–146. DOI: 10.1007/978-3-319-29009-6_7 (cited on page 27).

[169] T.-Y. Chuang, N.-H. Perng, and J.-Y. Han. 'Pavement performance monitoring and anomaly recognition based on crowdsourcing spatiotemporal data'. In: *Automation in construction* 106 (Oct. 2019), p. 102882. DOI: 10.1016/j.autcon.2019.102882 (cited on pages 27, 168).

[170] S. Mustapha, A. Kassir, K. Hassoun, Z. Dawy, and H. Abi-Rached. 'Estimation of crowd flow and load on pedestrian bridges using machine learning with sensor fusion'. In: *Automation in Construction* 112 (Apr. 2020), p. 103092. DOI: 10.1016/j.autcon.2020.103092 (cited on page 27).

[171] S. Shokouhyar, S. Shokoohyar, A. Sobhani, and A. J. Gorizi. 'Shared mobility in post-COVID era: New challenges and opportunities'. In: *Sustainable Cities and Society* 67 (2021). DOI: 10.1016/j.scs.2021.102714 (cited on page 27).

[172] A. Hosseinzadeh, M. Algomaiah, R. Kluger, and Z. Li. 'E-scooters and sustainability: Investigating the relationship between the density of E-scooter trips and characteristics of sustainable urban development'. In: *Sustainable Cities and Society* 66 (2021). DOI: 10.1016/j.scs.2020.102624 (cited on page 27).

[173] A. Seppänen, M. Hallaji, and M. Pour-Ghaz. 'A functionally layered sensing skin for the detection of corrosive elements and cracking'. In: *Structural Health Monitoring* 16.2 (2017), pp. 215–224. DOI: 10.1177/1475921716670574 (cited on pages 28, 30).

[174] D. Smyl, M. Hallaji, A. Seppänen, and M. Pour-Ghaz. 'Three-Dimensional Electrical Impedance Tomography to Monitor Unsaturated Moisture Ingress in Cement-Based Materials'. In: *Transport in Porous Media* 115.1 (Oct. 2016), pp. 101–124. DOI: 10.1007/s11242-016-0756-1 (cited on page 28).

[175] S. Gupta, J. G. Gonzalez, and K. J. Loh. 'Self-sensing concrete enabled by nano-engineered cement-aggregate interfaces'. In: *Structural Health Monitoring* 16.3 (2017), pp. 309–323. DOI: 10.1177/1475921716643867 (cited on pages 28, 29, 215).

[176] B. Han, S. Ding, and X. Yu. 'Intrinsic self-sensing concrete and structures: A review'. In: *Measurement: Journal of the International Measurement Confederation* 59 (Jan. 2015), pp. 110–128. DOI: 10.1016/j.measurement.2014.09.048 (cited on pages 28, 29).

[177] S. Rana, P. Subramani, R. Fangueiro, and A. G. Correia. 'A review on smart self-sensing composite materials for civil engineering applications'. In: *AIMS Materials Science* 3.2 (2016), pp. 357–379. DOI: 10.3934/matersci.2016.2.357 (cited on pages 28, 29).

[178] R. Ranade, J. Zhang, J. P. Lynch, and V. C. Li. 'Influence of micro-cracking on the composite resistivity of Engineered Cementitious Composites'. In: *Cement and Concrete Research* 58 (Apr. 2014), pp. 1–12. DOI: 10.1016/j.cemconres.2014.01.002 (cited on page 28).

[179] A. D'Alessandro, M. Rallini, F. Ubertini, A. L. Materazzi, and J. M. Kenny. 'Investigations on scalable fabrication procedures for self-sensing carbon nanotube cement-matrix composites for SHM applications'. In: *Cement and Concrete Composites* 65 (2016), pp. 200–213. DOI: 10.1016/j.cemconcomp.2015.11.001 (cited on page 29).

[180] D. S. Holder. *Electrical impedance tomography: methods, history and applications*. CRC Press, 2004 (cited on pages 29, 215–217, 233).

[181] T. C. Hou, K. J. Loh, and J. P. Lynch. 'Spatial conductivity mapping of carbon nanotube composite thin films by electrical impedance tomography for sensing applications'. In: *Nanotechnology* 18.31 (Aug. 2007), p. 315501. DOI: 10.1088/0957-4484/18/31/315501 (cited on page 29).

[182] K. J. Loh, T. C. Hou, J. P. Lynch, and N. A. Kotov. 'Carbon nanotube sensing skins for spatial strain and impact damage identification'. In: *Journal of Nondestructive Evaluation* 28.1 (Mar. 2009), pp. 9–25. DOI: 10.1007/s10921-009-0043-y (cited on page 29).

[183] B. R. Loyola, V. L. Saponara, K. J. Loh, T. M. Briggs, G. O'Bryan, and J. L. Skinner. 'Spatial sensing using electrical impedance tomography'. In: *IEEE Sensors Journal* 13.6 (2013), pp. 2357–2367. DOI: 10.1109/JSEN.2013.2253456 (cited on pages 29, 224, 228).

[184] M. Hallaji, A. Seppänen, and M. Pour-Ghaz. 'Electrical impedance tomography-based sensing skin for quantitative imaging of damage in concrete'. In: *Smart Materials and Structures* 23.8 (2014). DOI: 10.1088/0964-1726/23/8/085001 (cited on page 30).

[185] S. Gupta, G. Vella, I. N. Yu, C. H. Loh, W. H. Chiang, and K. J. Loh. 'Graphene sensing meshes for densely distributed strain field monitoring'. In: *Structural Health Monitoring* 19.5 (2020), pp. 1323–1339. DOI: 10.1177/1475921719877418 (cited on page 30).

[186] J. Guo and X. Zhu. 'The factorization method for cracks in electrical impedance tomography'. In: *Computational and Applied Mathematics* 40.3 (2021), pp. 1–20. DOI: 10.1007/s40314-021-01468-9 (cited on page 30).

[187] T. C. Hou and J. P. Lynch. 'Electrical impedance tomographic methods for sensing strain fields and crack damage in cementitious structures'. In: *Journal of Intelligent Material Systems and Structures* 20.11 (July 2009), pp. 1363–1379. DOI: 10.1177/1045389X08096052 (cited on page 30).

[188] Z. Lin, R. Guo, K. Zhang, M. Li, F. Yang, S. Xu And, and A. Abubakar. 'Neural network-based supervised descent method for 2D electrical impedance tomography'. In: *Physiological Measurement* 41.7 (2020). DOI: 10.1088/1361-6579/ab9871 (cited on page 30).

[189] Z. Chen, Y. Yang, and P. O. Bagnaninchi. 'Hybrid Learning-Based Cell Aggregate Imaging with Miniature Electrical Impedance Tomography'. In: *IEEE Transactions on Instrumentation and Measurement* 70 (2021), p. 70. DOI: 10.1109/TIM.2020.3035384 (cited on page 30).

[190] M. Capps and J. L. Mueller. 'Reconstruction of Organ Boundaries with Deep Learning in the D-Bar Method for Electrical Impedance Tomography'. In: *IEEE Transactions on Biomedical Engineering* 68.3 (2021), pp. 826–833. DOI: 10.1109/TBME.2020.3006175 (cited on page 30).

[191] S. Ren, K. Sun, C. Tan, and F. Dong. 'A Two-Stage Deep Learning Method for Robust Shape Reconstruction with Electrical Impedance Tomography'. In: *IEEE Transactions on Instrumentation and Measurement* 69.7 (2020), pp. 4887–4897. DOI: 10.1109/TIM.2019.2954722 (cited on page 30).

[192] R. J. Allemang. 'The modal assurance criterion - Twenty years of use and abuse'. In: *Sound and Vibration* 37.8 (2003), pp. 14–21 (cited on pages 33, 209).

[193] E. Reynders, R. Pintelon, and G. De Roeck. 'Uncertainty bounds on modal parameters obtained from stochastic subspace identification'. In: *Mechanical Systems and Signal Processing* 22.4 (2008), pp. 948–969. DOI: 10.1016/j.ymssp.2007.10.009 (cited on page 33).

[194] N.-J. Jacobsen, P. Andersen, and R. Brincker. 'Using enhanced frequency domain decomposition as a robust technique to harmonic excitation in operational modal analysis'. In: *Proceedings of ISMA2006: International Conference on Noise and Vibration Engineering*. Vol. 6. 2006, pp. 3129–3140 (cited on page 33).

[195] A. K. Chopra. *Dynamics of Structures: Theory and Applications to Earthquake Engineering*. Fourth Ed. Vol. 17. 3. Pearson, 2017, p. 960 (cited on page 34).

[196] S. Sarangi, M. Sahidullah, and G. Saha. 'Optimization of data-driven filterbank for automatic speaker verification'. In: *Digital Signal Processing* 104 (Sept. 2020), p. 102795. DOI: 10.1016/j.dsp.2020.102795 (cited on page 36).

[197] S. Nagarajaiah and B. Basu. 'Output only modal identification and structural damage detection using time frequency & wavelet techniques'. In: *Earthquake Engineering and Engineering Vibration* 8.4 (2009), pp. 583–605. DOI: 10.1007/s11803-009-9120-6 (cited on page 36).

[198] T. Kijewski and A. Kareem. 'Wavelet transforms for system identification in civil engineering'. In: *Computer-Aided Civil and Infrastructure Engineering* 18.5 (2003), pp. 339–355. DOI: 10.1111/1467-8667.t01-1-00312 (cited on page 36).

[199] C. Wang, W. Guan, J. Wang, B. Zhong, X. Lai, Y. Chen, and L. Xiang. 'Adaptive operational modal identification for slow linear time-varying structures based on frozen-in coefficient method and limited memory recursive principal component analysis'. In: *Mechanical Systems and Signal Processing* 100 (2018), pp. 899–925. DOI: 10.1016/j.ymssp.2017.06.018 (cited on page 36).

[200] T.-P. Le and P. Paultre. 'Modal identification based on continuous wavelet transform and ambient excitation tests'. In: *Journal of Sound and Vibration* 331.9 (2012), pp. 2023–2037. DOI: 10.1016/j.jsv.2012.01.018 (cited on page 36).

[201] T. Uhl and A. Klepka. 'Application of wavelet transform to identification of modal parameters of nonstationary systems'. In: *Journal of theoretical and applied mechanics* 43.2 (2005), pp. 277–296 (cited on page 36).

[202] G. P. Nason and B. W. Silverman. 'The stationary wavelet transform and some statistical applications'. In: *Wavelets and statistics*. Springer, 1995, pp. 281–299. DOI: 10.1007/978-1-4612-2544-7_17 (cited on pages 36, 265).

[203] A. P. Bradley. 'Shift-invariance in the discrete wavelet transform'. In: *Proceedings of VIIth Digital Image Computing: Techniques and Applications. Sydney* (2003), pp. 10–12 (cited on page 37).

[204] D. K. Alves, F. B. Costa, R. L. de Araujo Ribeiro, C. M. de Sousa Neto, and T. d. O. A. Rocha. 'Real-time power measurement using the maximal overlap discrete wavelet-packet transform'. In: *IEEE Transactions on Industrial Electronics* 64.4 (2016), pp. 3177–3187. DOI: 10.1109/TIE.2016.2637304 (cited on page 37).

[205] S. Mallat. 'A theory for multiresolution signal decomposition: the wavelet representation'. In: *IEEE Transactions on Pattern Analysis and Machine Intelligence* 11.7 (1989), pp. 674–693. DOI: 10.1109/34.192463 (cited on page 37).

[206] S. A. Ravanfar, H. A. Razak, Z. Ismail, and H. Monajemi. 'An improved method of parameter identification and damage detection in beam structures under flexural vibration using wavelet multi-resolution analysis'. In: *Sensors* 15.9 (2015), pp. 22750–22775. DOI: 10.3390/s150922750 (cited on page 37).

[207] C.-S. Huang, S.-L. Hung, C. Lin, and W. Su. 'A wavelet-based approach to identifying structural modal parameters from seismic response and free vibration data'. In: *Computer-Aided Civil and Infrastructure Engineering* 20.6 (2005), pp. 408–423. DOI: 10.1111/j.1467-8667.2005.00406.x (cited on page 37).

[208] W. Su, C.-S. Huang, C. Chen, C. Liu, H. Huang, and Q. Le. 'Identifying the modal parameters of a structure from ambient vibration data via the stationary wavelet packet'. In: *Computer-Aided Civil and Infrastructure Engineering* 29.10 (2014), pp. 738–757. DOI: 10.1111/mice.12115 (cited on page 37).

[209] M. Nielsen. 'On the construction and frequency localization of finite orthogonal quadrature filters'. In: *Journal of Approximation Theory* 108.1 (2001), pp. 36–52. DOI: 10.1006/jath.2000.3514 (cited on page 38).

[210] M. Varanis and R. Pederiva. 'The influence of the wavelet filter in the parameters extraction for signal classification: An experimental study.' In: *Proceeding Series of the Brazilian Society of Computational and Applied Mathematics* 5.1 (2017). DOI: 10.5540/03.2017.005.01.0501 (cited on page 38).

[211] S. G. Mallat. *A wavelet tour of signal processing*. Third edit. Academic Press, 2009 (cited on pages 38, 40, 45, 194).

[212] G. Strang and T. Nguyen. *Wavelets and Filter Banks*. SIAM, 1996, p. 490 (cited on pages 40, 195).

[213] H. Abdi and L. J. Williams. 'Principal component analysis'. In: *Wiley Interdisciplinary Reviews: Computational Statistics* 2.4 (2010), pp. 433–459. DOI: 10.1002/wics.101 (cited on page 47).

[214] B. Moaveni, X. He, J. P. Conte, and J. I. Restrepo. 'Damage identification study of a seven-story full-scale building slice tested on the UCSD-NEES shake table'. In: *Structural Safety* 32.5 (2010), pp. 347–356. DOI: 10.1016/j.strusafe.2010.03.006 (cited on pages 55, 56, 129, 135).

[215] B. Moaveni, X. He, J. P. Conte, J. I. Restrepo, and M. Panagiotou. 'System identification study of a 7-story full-scale building slice tested on the UCSD-NEES shake table'. In: *Journal of Structural Engineering* 137.6 (June 2011), pp. 705–717. DOI: 10.1061/(ASCE)ST.1943-541X.0000300 (cited on pages 55–57, 59, 61, 129, 132, 135).

[216] P. Martinelli and F. C. Filippou. 'Simulation of the shaking table test of a seven-story shear wall building'. In: *Earthquake Engineering and Structural Dynamics* 38.5 (2009), pp. 587–607. DOI: 10.1002/eqe.897 (cited on pages 55, 56, 128).

[217] J. Conte, J. Restrepo, and M. Panagiotou. *Shake Table Test of 7-story RC Bearing Wall Building*. 2006. DOI: 10.4231/D35T3G04T (cited on page 56).

[218] V. C. E. VCE. *Progressive damage test S101 - Flyover reibersdorf*. Tech. rep. 08. 2009, Report nr. 08/2308 (cited on pages 63–67, 88, 89, 93).

[219] D. M. Siringoringo, Y. Fujino, and T. Nagayama. 'Dynamic characteristics of an overpass bridge in a full-scale destructive test'. In: *Journal of Engineering Mechanics* 139.6 (2013), pp. 691–701. DOI: 10.1061/(ASCE)EM.1943-7889.0000280 (cited on page 63).

[220] M. Döhler, F. Hille, L. Mevel, and W. Rücker. 'Structural health monitoring with statistical methods during progressive damage test of S101 Bridge'. In: *Engineering Structures* 69 (2014), pp. 183–193. DOI: 10.1016/j.engstruct.2014.03.010 (cited on pages 63, 65, 92).

[221] H. Wenzel and D. Pichler. *Ambient vibration monitoring*. John Wiley & Sons, 2005, pp. 1–291 (cited on pages 65, 66).

[222] M. Ester, H.-P. Kriegel, J. Sander, and X. Xu. 'Density-Connected Sets and their Application for Trend Detection in Spatial Databases.' In: *KDD*. Vol. 97. 1997, pp. 10–15 (cited on pages 67, 111).

[223] G. Bernagozzi, S. Mukhopadhyay, R. Betti, L. Landi, and P. P. Diotallevi. 'Output-only damage detection in buildings using proportional modal flexibility-based deflections in unknown mass scenarios'. In: *Engineering Structures* 167 (2018), pp. 549–566. DOI: https://doi.org/10.1016/j.engstruct.2018.04.036 (cited on page 69).

[224] P. Prandoni and M. Vetterli. *Signal processing for communications*. Collection le savoir suisse, 2008 (cited on pages 74, 265).

[225] R. Brincker, P. Andersen, and N. Møller. 'An indicator for separation of structural and harmonic modes in output-only modal testing'. In: *Proceedings of the European COST F3 Conference on System Identification & Structural Health Monitoring, 6-9 June, 2000, Universidad Politécnica de Madrid, Spain*. Vol. 2. Universidad Politécnica de Madrid. 2000, pp. 265–272 (cited on page 77).

[226] J. F. Kaiser. 'On a simple algorithm to calculate the'energy'of a signal'. In: *International conference on acoustics, speech, and signal processing*. Vol. 1. IEEE. 1990, pp. 381–384. DOI: 10.1109/icassp.1990.115702 (cited on pages 78, 151).

[227] P. Maragos, J. F. Kaiser, and T. F. Quatieri. 'Energy separation in signal modulations with application to speech analysis'. In: *IEEE transactions on signal processing* 41.10 (1993), pp. 3024–3051. DOI: 10.1109/78.277799 (cited on pages 78, 79).

[228] M. Cao, G. Sha, Y. Gao, and W. Ostachowicz. 'Structural damage identification using damping: a compendium of uses and features'. In: *Smart Materials and structures* 26.4 (2017), p. 043001. DOI: 10.1088/1361-665X/aa550a (cited on page 79).

[229] Y.-H. Wang, C.-H. Yeh, H.-W. V. Young, K. Hu, and M.-T. Lo. 'On the computational complexity of the empirical mode decomposition algorithm'. In: *Physica A: Statistical Mechanics and its Applications* 400 (2014), pp. 159–167. DOI: 10.1016/j.physa.2014.01.020 (cited on pages 80, 90).

[230] F. Amini and V. Ghasemi. 'Adaptive modal identification of structures with equivariant adaptive separation via independence approach'. In: *Journal of Sound and Vibration* 413 (2018), pp. 66–78. DOI: 10.1016/j.jsv.2017.09.033 (cited on page 80).

[231] V. Zarzoso and A. K. Nandi. 'Adaptive blind source separation for virtually any source probability density function'. In: *IEEE Transactions on signal processing* 48.2 (2000), pp. 477–488. DOI: 10.1109/78.823974 (cited on page 80).

[232] L. D. Avendano-Valencia and S. D. Fassois. 'Gaussian Mixture Random Coefficient model based framework for SHM in structures with time–dependent dynamics under uncertainty'. In: *Mechanical Systems and Signal Processing* 97 (2017), pp. 59–83. DOI: 10.1016/j.ymssp.2017.04.016 (cited on page 81).

[233] L. D. Avendaño-Valencia, E. N. Chatzi, K. Y. Koo, and J. M. Brownjohn. 'Gaussian process time-series models for structures under operational variability'. In: *Frontiers in Built Environment* 3 (2017), p. 69. DOI: 10.3389/fbuil.2017.00069 (cited on page 81).

[234] M. P. Limongelli. 'Seismic health monitoring of an instrumented multistory building using the interpolation method'. In: *Earthquake engineering & structural dynamics* 43.11 (2014), pp. 1581–1602. DOI: 10.1002/eqe.2411 (cited on page 81).

[235] A. Cabboi, C. Gentile, and A. Saisi. 'From continuous vibration monitoring to FEM-based damage assessment: application on a stone-masonry tower'. In: *Construction and Building Materials* 156 (2017), pp. 252–265. DOI: 10.1016/j.conbuildmat.2017.08.160 (cited on page 81).

[236] A. Saisi, C. Gentile, and A. Ruccolo. 'Continuous monitoring of a challenging heritage tower in Monza, Italy'. In: *Journal of Civil Structural Health Monitoring* 8.1 (2018), pp. 77–90. DOI: 10.1007/s13349-017-0260-5 (cited on page 81).

[237] G. Zonno, R. Aguilar, R. Boroschek, and P. B. Lourenço. 'Analysis of the long and short-term effects of temperature and humidity on the structural properties of adobe buildings using continuous monitoring'. In: *Engineering Structures* 196 (2019), p. 109299. DOI: 10.1016/j.engstruct.2019.109299 (cited on page 81).

[238] Z. Chen, X. Zhou, X. Wang, L. Dong, and Y. Qian. 'Deployment of a smart structural health monitoring system for long-span arch bridges: A review and a case study'. In: *Sensors* 17.9 (2017), p. 2151. DOI: 10.3390/s17092151 (cited on page 81).

[239] A. BÂRLEANU, V. BITOIU, and A. STAN. 'FIR filtering on ARM Cortex-M3'. In: *Proceedings of the 6th WSEAS European Computing Conference, 9, WSEAS*. 2012, pp. 490–494 (cited on pages 89, 90).

[240] A. Sloss, D. Symes, and C. Wright. *ARM system developer's guide: designing and optimizing system software*. Elsevier, 2004, p. 703 (cited on page 90).

[241] Intel. *Intel PXA27x Processor Family: Optimization guide*. 2004, pp. 1–1242 (cited on page 90).

[242] L. Wang, M. I. Vai, P. U. Mak, and C. I. Ieong. 'Hardware-accelerated implementation of EMD'. In: *2010 3rd International Conference on Biomedical Engineering and Informatics*. Vol. 2. IEEE. 2010, pp. 912–915. DOI: 10.1109/BMEI.2010.5639875 (cited on page 90).

[243] G. Rilling, P. Flandrin, P. Goncalves, et al. 'On empirical mode decomposition and its algorithms'. In: *IEEE-EURASIP workshop on nonlinear signal and image processing*. Vol. 3. 3. Citeseer. 2003, pp. 8–11 (cited on page 90).

[244] A. Klepka and T. Uhl. 'Identification of modal parameters of non-stationary systems with the use of wavelet based adaptive filtering'. In: *Mechanical Systems and Signal Processing* 47.1-2 (2014), pp. 21–34. DOI: 10.1016/j.ymssp.2013.09.001 (cited on pages 91, 266).

[245] Z. Zhang and A. Aktan. 'Application of modal flexibility and its derivatives in structural identification'. In: *Journal of Research in Nondestructive Evaluation* 10.1 (1998), pp. 43–61. DOI: 10.1007/pl00003899 (cited on page 96).

[246] J. Serra. *Image Analysis and Mathematical Morphology*. USA: Academic Press, Inc., 1983 (cited on page 103).

[247] A. K. Jain. 'Data clustering: 50 years beyond K-means'. In: *Pattern recognition letters* 31.8 (2010), pp. 651–666. DOI: 10.1016/j.patrec.2009.09.011 (cited on page 103).

[248] T. Kohonen. 'Self-organized formation of topologically correct feature maps'. In: *Biological cybernetics* 43.1 (1982), pp. 59–69. DOI: 10.1007/BF00337288 (cited on pages 103, 109, 221).

[249] J. Vesanto and E. Alhoniemi. 'Clustering of the self-organizing map'. In: *IEEE Transactions on neural networks* 11.3 (2000), pp. 586–600. DOI: 10.1109/72.846731 (cited on page 110).

[250] M. Chen, E. Pantoli, X. Wang, R. Astroza, H. Ebrahimian, S. Mintz, T. Hutchinson, J. P. Conte, J. Restrepo, B. Meacham, et al. 'Full-scale structural and nonstructural building system performance during earthquakes and post-earthquake fire-specimen design, construction and test protocol (BNCS Report# 1)'. In: (2013) (cited on pages 115, 116).

[251] E. Pantoli, M. Chen, X. Wang, R. Astroza, S. Mintz, H. Ebrahimian, T. Hutchinson, J. P. Conte, J. Restrepo, J. Kim, et al. 'Full-scale structural and nonstructural building system performance during earthquakes and post-earthquake fire-Test results (BNCS Report# 2)'. In: (2013) (cited on pages 115, 119).

[252] E. Pantoli, M. Chen, T. Hutchinson, and J. Restrepo. 'Full-scale structural and non-structural building system performance during earthquakes and post-earthquake fire - camera and analog sensor details (BNCS Report# 3)'. In: (2013), pp. 1–338 (cited on page 115).

[253] M. Chen, E. Pantoli, X. Wang, T. Hutchinson, and J. Restrepo. 'Full-scale structural and nonstructural building system performance during earthquakes and post-earthquake fire - construction details and technical specifications of specific subsystems (BNCS Report# 4)'. In: (2013), pp. 1–338 (cited on page 115).

[254] S. Quqa, L. Landi, and P. P. Diotallevi. 'Instantaneous modal identification under varying structural characteristics: A decentralized algorithm'. In: *Mechanical Systems and Signal Processing* 142 (Aug. 2020), p. 106750. DOI: 10.1016/j.ymssp.2020.106750 (cited on page 122).

[255] M. Gavish and D. L. Donoho. 'The optimal hard threshold for singular values is $4/\sqrt{3}$'. In: *IEEE Transactions on Information Theory* 60.8 (2014), pp. 5040–5053. DOI: 10.1109/TIT.2014.2323359 (cited on pages 122, 125, 129).

[256] M. Brand. 'Fast low-rank modifications of the thin singular value decomposition'. In: *Linear algebra and its applications* 415.1 (2006), pp. 20–30. DOI: 10.1016/j.laa.2005.07.021 (cited on pages 123, 125).

[257] M. K. Singh and S. I. Amin. 'Energy-efficient data transmission technique for wireless sensor networks based on DSC and virtual MIMO'. In: *ETRI Journal* 42.3 (June 2020), pp. 341–350. DOI: 10.4218/etrij.2018-0632 (cited on page 125).

[258] M. M.-T. Chiang and B. Mirkin. 'Intelligent choice of the number of clusters in k-means clustering: an experimental study with different cluster spreads'. In: *Journal of classification* 27.1 (2010), pp. 3–40. DOI: 10.1007/s00357-010-9049-5 (cited on page 126).

[259] R. Brincker, L. Zhang, and P. Andersen. 'Modal identification of output-only systems using frequency domain decomposition'. In: *Smart materials and structures* 10.3 (2001), p. 441. DOI: 10.1088/0964-1726/10/3/303 (cited on pages 132, 157, 207).

[260] F. Catbas, M. Gul, and J. Burkett. 'Damage assessment using flexibility and flexibility-based curvature for structural health monitoring'. In: *Smart materials and structures* 17.1 (2007), p. 015024. DOI: 10.1088/0964-1726/17/01/015024 (cited on page 134).

[261] S.-H. Sung, H. Jung, and H. Jung. 'Damage detection for beam-like structures using the normalized curvature of a uniform load surface'. In: *Journal of Sound and Vibration* 332.6 (2013), pp. 1501–1519. DOI: 10.1016/j.jsv.2012.11.016 (cited on page 134).

[262] P. F. Giordano and M. P. Limongelli. 'Response-based time-invariant methods for damage localization on a concrete bridge'. In: *Structural Concrete* 21.4 (2020), pp. 1254–1271. DOI: 10.1002/suco.202000013 (cited on pages 134, 175, 190).

[263] G. Bernagozzi, C. E. Ventura, S. Allahdadian, Y. Kaya, L. Landi, and P. P. Diotallevi. 'Output-only damage diagnosis for plan-symmetric buildings with asymmetric damage using modal flexibility-based deflections'. In: *Engineering Structures* 207 (2020), p. 110015. DOI: 10.1016/j.engstruct.2019.110015 (cited on page 134).

[264] A. Aloisio, R. Alaggio, and M. Fragiacomo. 'Dynamic identification and model updating of full-scale concrete box girders based on the experimental torsional response'. In: *Construction and Building Materials* 264 (2020), p. 120146. DOI: 10.1016/j.conbuildmat.2020.120146 (cited on pages 138, 207).

[265] A. Aloisio, D. P. Pasca, R. Alaggio, and M. Fragiacomo. 'Bayesian estimate of the elastic modulus of concrete box girders from dynamic identification: A statistical framework for the A24 motorway in Italy'. In: *Structure and infrastructure engineering* 17.12 (2021), pp. 1626–1638. DOI: 10.1080/15732479.2020.1819343 (cited on pages 138, 207).

[266] C. R. Farrar and K. Worden. *Structural health monitoring: a machine learning perspective*. John Wiley & Sons, 2012 (cited on page 139).

[267] L. Fryba. *Vibration of solids and structures under moving loads*. Vol. 1. Springer Science & Business Media, 2013 (cited on page 141).

[268] X. Zheng, D.-H. Yang, T.-H. Yi, and H.-N. Li. 'Bridge influence line identification from structural dynamic responses induced by a high-speed vehicle'. In: *Structural Control and Health Monitoring* 27.7 (2020), e2544. DOI: 10.1002/stc.2544 (cited on page 146).

[269] N. E. Huang. *Hilbert-Huang transform and its applications*. Vol. 16. World Scientific, 2014 (cited on page 151).

[270] T. H. Silva, C. Celes, J. Neto, V. Mota, F. Cunha, A. Ferreira, A. Ribeiro, P. Vaz de Melo, J. Almeida, and A. Loureiro. 'Users in the urban sensing process: Challenges and research opportunities'. In: *Pervasive Computing: Next Generation Platforms for Intelligent Data Collection* (2016), pp. 45–95. DOI: 10.1016/B978-0-12-803663-1.00003-6 (cited on page 167).

[271] S. Shaheen, A. Cohen, N. Chan, and A. Bansal. 'Sharing strategies: carsharing, shared micromobility (bikesharing and scooter sharing), transportation network companies, microtransit, and other innovative mobility modes'. In: *Transportation, land use, and environmental planning*. Elsevier, 2020, pp. 237–262. DOI: 10.1016/B978-0-12-815167-9.00013-X (cited on page 167).

[272] S. Di Dio, M. La Gennusa, G. Peri, G. Rizzo, and I. Vinci. 'Involving people in the building up of smart and sustainable cities: How to influence commuters behaviors through a mobile app game'. In: *Sustainable Cities and Society* 42 (Oct. 2018), pp. 325–336. DOI: 10.1016/j.scs.2018.07.021 (cited on page 167).

[273] S. J. Julier and J. K. Uhlmann. 'Unscented filtering and nonlinear estimation'. In: *Proceedings of the IEEE* 92.3 (2004), pp. 401–422. DOI: 10.1109/JPROC.2003.823141 (cited on page 171).

[274] G. Y. Kulikov and M. V. Kulikova. 'Accurate numerical implementation of the continuous-discrete extended Kalman filter'. In: *IEEE Transactions on Automatic Control* 59.1 (2013), pp. 273–279. DOI: 10.1109/TAC.2013.2272136 (cited on page 172).

[275] N. E. Huang, Z. Wu, S. R. Long, K. C. Arnold, X. Chen, and K. Blank. 'On instantaneous frequency'. In: *Advances in adaptive data analysis* 1.02 (Apr. 2009), pp. 177–229. DOI: 10.1142/S1793536909000096 (cited on page 175).

[276] M. P. Limongelli. 'Frequency response function interpolation for damage detection under changing environment'. In: *Mechanical Systems and Signal Processing* 24.8 (2010), pp. 2898–2913. DOI: 10.1016/j.ymssp.2010.03.004 (cited on pages 175, 177).

[277] M. Dilena, M. P. Limongelli, and A. Morassi. 'Damage localization in bridges via the FRF interpolation method'. In: *Mechanical Systems and Signal Processing* 52.1 (2015), pp. 162–180. DOI: 10.1016/j.ymssp.2014.08.014 (cited on pages 177, 190).

[278] M. MAJOWIECKI. 'Three footbridges'. In: *Proceedings of the 2nd Int. Conf. on Footbridges*. Venice, 2005 (cited on page 177).

[279] M. MAJOWIECKI and N. COSENTINO. 'Experiences on footbridge conceptual design vs. dynamic performances'. In: *4th International Conference Footbridge 2011, Wroclaw, Poland, July 6-8*. Wroclaw, 2011, pp. 325–332 (cited on pages 179, 183).

[280] K. Katevas. 'Analysing Crowd Behaviours using Mobile Sensing'. PhD thesis. Queen Mary University of London, 2018, p. 120 (cited on page 180).

[281] H. Nandan and M. P. Singh. 'Effects of thermal environment on structural frequencies: Part I–A simulation study'. In: *Engineering Structures* 81 (Dec. 2014), pp. 480–490. DOI: 10.1016/j.engstruct.2014.06.046 (cited on page 183).

[282] Y. Champoux, S. Richard, and J.-M. Drouet. 'Bicycle structural dynamics'. In: *Sound and vibration* 41.7 (2007), pp. 16–25 (cited on page 187).

[283] C. R. Farrar and K. Worden. 'An introduction to structural health monitoring'. In: *Philosophical Transactions of the Royal Society A: Mathematical, Physical and Engineering Sciences* 365.1851 (2007), pp. 303–315. DOI: 10.1098/rsta.2006.1928 (cited on page 190).

[284] W. Haensch, T. Gokmen, and R. Puri. 'The next generation of deep learning hardware: Analog computing'. In: *Proceedings of the IEEE* 107.1 (2018), pp. 108–122. DOI: 10.1109/JPROC.2018.2871057 (cited on page 197).

[285] G. W. Burr, B. N. Kurdi, J. C. Scott, C. H. Lam, K. Gopalakrishnan, and R. S. Shenoy. 'Overview of candidate device technologies for storage-class memory'. In: *IBM Journal of Research and Development* 52.4.5 (2008), pp. 449–464. DOI: 10.1147/rd.524.0449 (cited on page 197).

[286] M. Pasotti, R. Zurla, M. Carissimi, C. Auricchio, D. Brambilla, E. Calvetti, L. Capecchi, L. Croce, D. Gallinari, C. Mazzaglia, et al. 'A 32-KB ePCM for real-time data processing in automotive and smart power applications'. In: *IEEE Journal of Solid-State Circuits* 53.7 (2018), pp. 2114–2125. DOI: 10.1109/JSSC.2018.2828805 (cited on page 197).

[287] A. Cabrini, S. Braga, A. Manetto, and G. Torelli. 'Voltage-driven multilevel programming in phase change memories'. In: *2009 IEEE International Workshop on Memory Technology, Design, and Testing*. IEEE. 2009, pp. 3–6. DOI: 10.1109/MTDT.2009.11 (cited on pages 198, 200).

[288] D. Ielmini and G. Pedretti. 'Device and Circuit Architectures for In-Memory Computing'. In: *Advanced Intelligent Systems* 2.7 (2020), p. 2000040. DOI: 10.1002/aisy.202000040 (cited on pages 198, 201, 202).

[289] Z. Sun, G. Pedretti, E. Ambrosi, A. Bricalli, W. Wang, and D. Ielmini. 'Solving matrix equations in one step with cross-point resistive arrays'. In: *Proceedings of the National Academy of Sciences* 116.10 (2019), pp. 4123–4128. DOI: 10.1073/pnas.1815682116 (cited on page 198).

[290] R. L. Bruce, S. G. Sarwat, I. Boybat, C.-W. Cheng, W. Kim, S. Nandakumar, C. Mackin, T. Philip, Z. Liu, K. Brew, et al. 'Mushroom-Type phase change memory with projection liner: An array-level demonstration of conductance drift and noise mitigation'. In: *2021 IEEE International Reliability Physics Symposium (IRPS)*. Vol. 2021-March. IEEE. 2021, pp. 1–6. DOI: 10.1109/IRPS46558.2021.9405191 (cited on page 200).

[291] B. Kersting, V. Ovuka, V. P. Jonnalagadda, M. Sousa, V. Bragaglia, S. G. Sarwat, M. Le Gallo, M. Salinga, and A. Sebastian. 'State dependence and temporal evolution of resistance in projected phase change memory'. In: *Scientific reports* 10.1 (2020), pp. 1–11. DOI: 10.1038/s41598-020-64826-3 (cited on page 200).

[292] A. Antolini, E. Franchi Scarselli, A. Gnudi, M. Carissimi, M. Pasotti, P. Romele, and R. Canegallo. 'Characterization and Programming Algorithm of Phase Change Memory Cells for Analog In-Memory Computing'. In: *Materials* 14.7 (2021), p. 1624. DOI: 10.3390/ma14071624 (cited on page 200).

[293] S. Braga, A. Sanasi, A. Cabrini, and G. Torelli. 'Voltage-driven partial-RESET multilevel programming in phase-change memories'. In: *IEEE Transactions on Electron Devices* 57.10 (2010), pp. 2556–2563. DOI: 10.1109/TED.2010.2062185 (cited on page 200).

[294] C. Paolino, A. Antolini, F. Pareschi, M. Mangia, R. Rovatti, E. F. Scarselli, A. Gnudi, G. Setti, R. Canegallo, M. Carissimi, et al. 'Compressed Sensing by Phase Change Memories: coping with encoder non-linearities'. In: *2021 IEEE International Symposium on Circuits and Systems (ISCAS)*. Vol. 2021-May. IEEE. 2021, pp. 1–5. DOI: 10.1109/ISCAS51556.2021.9401176 (cited on page 200).

[295] M. Carissimi, R. Zurla, C. Auricchio, E. Calvetti, L. Capecchi, L. Croce, S. Zanchi, V. Rana, P. Mishra, R. Mukherjee, et al. '2-Mb embedded phase change memory with 16-ns read access time and 5-Mb/s write throughput in 90-nm BCD technology for automotive applications'. In: *ESSCIRC 2019-IEEE 45th European Solid State Circuits Conference (ESSCIRC)*. IEEE. 2019, pp. 135–138. DOI: 10.1109/ESSCIRC.2019.8902656 (cited on page 200).

[296] Y. Zhang, J. Feng, Y. Zhang, Z. Zhang, Y. Lin, T. Tang, B. Cai, and B. Chen. 'Multi-bit storage in reset process of Phase Change Access Memory (PRAM)'. In: *physica status solidi (RRL)–Rapid Research Letters* 1.1 (2007), R28–R30 (cited on page 200).

[297] F. Bedeschi, R. Fackenthal, C. Resta, E. M. Donze, M. Jagasivamani, E. C. Buda, F. Pellizzer, D. W. Chow, A. Cabrini, G. M. A. Calvi, et al. 'A bipolar-selected phase change memory featuring multi-level cell storage'. In: *IEEE Journal of Solid-State Circuits* 44.1 (2008), pp. 217–227. DOI: 10.1109/JSSC.2008.2006439 (cited on page 200).

[298] F. G. Volpe, A. Cabrini, M. Pasotti, and G. Torelli. 'Drift induced rigid current shift in Ge-Rich GST Phase Change Memories in Low Resistance State'. In: *2019 26th IEEE International Conference on Electronics, Circuits and Systems (ICECS)*. IEEE. 2019, pp. 418–421. DOI: 10.1109/ICECS46596.2019.8964986 (cited on page 201).

[299] A. P. Calderón. 'On an inverse boundary value problem'. In: *Computational & Applied Mathematics* 25 (2006), pp. 133–138. DOI: 10.1590/S0101-82052006000200002 (cited on page 215).

[300] T. N. Tallman and D. J. Smyl. 'Structural health and condition monitoring via electrical impedance tomography in self-sensing materials: a review'. In: *Smart Materials and Structures* 29.12 (2020), p. 123001. DOI: 10.1088/1361-665X/abb352 (cited on page 217).

[301] R. Reed and R. J. MarksII. *Neural smithing: supervised learning in feedforward artificial neural networks*. Mit Press, 1999 (cited on page 220).

[302] C. M. Bishop. 'Training with noise is equivalent to Tikhonov regularization'. In: *Neural computation* 7.1 (1995), pp. 108–116. DOI: 10.1162/neco.1995.7.1.108 (cited on page 220).

[303] G. An. 'The effects of adding noise during backpropagation training on a generalization performance'. In: *Neural computation* 8.3 (1996), pp. 643–674. DOI: 10.1162/neco.1996.8.3.643 (cited on page 220).

[304] D. E. Rumelhart and D. Zipser. 'Feature discovery by competitive learning'. In: *Cognitive science* 9.1 (1985), pp. 75–112. DOI: 10.1016/S0364-0213(85)80010-0 (cited on page 222).

[305] T. Kohonen. *Self-Organizing Maps*. Third edit. Springer Berlin Heidelberg, 2001 (cited on pages 222, 223).

[306] V. Chaudhary, R. S. Bhatia, and A. K. Ahlawat. 'A novel Self-Organizing Map (SOM) learning algorithm with nearest and farthest neurons'. In: *Alexandria Engineering Journal* 53.4 (2014), pp. 827–831. DOI: 10.1016/j.aej.2014.09.007 (cited on page 222).

[307] G. Spanakis and G. Weiss. 'AMSOM: Adaptive Moving Self-Organizing Map for clustering and visualization'. In: *ICAART 2016 - Proceedings of the 8th International Conference on Agents and Artificial Intelligence* 2 (2016), pp. 129–140. DOI: 10.5220/0005704801290140 (cited on page 222).

[308] E. Alhoniemi, J. Hollmén, O. Simula, and J. Vesanto. 'Process monitoring and modeling using the Self-Organizing Map'. In: *Integrated Computer-Aided Engineering* 6.1 (1999), pp. 3–14. DOI: 10.3233/ica-1999-6102 (cited on page 223).

[309] Y. M. Cheung and L. T. Law. 'Rival-model penalized self-organizing map'. In: *IEEE Transactions on Neural Networks* 18.1 (2007), pp. 289–295. DOI: 10.1109/TNN.2006.885039 (cited on page 223).

[310] L. Wang and K. J. Loh. 'Spray-coated carbon nanotube-latex strain sensors'. In: *Science Letters Journal* 5 (2016), p. 234 (cited on page 227).

[311] Y.-A. Lin, Y. Zhao, L. Wang, Y. Park, Y.-J. Yeh, W.-H. Chiang, and K. J. Loh. 'Graphene KTape Meshes for Densely Distributed Human Motion Monitoring'. In: *Advanced Materials Technologies* 6.1 (Jan. 2021), p. 2000861. DOI: 10.1002/admt.202000861 (cited on page 227).

[312] N. J. Avis and D. C. Barber. 'Image reconstruction using non-adjacent drive configurations (electric impedance tomography)'. In: *Physiological Measurement* 15.2A (May 1994), A153–A160. DOI: 10.1088/0967-3334/15/2A/020 (cited on pages 227, 233).

[313] D. P. Kingma and J. L. Ba. 'Adam: A method for stochastic optimization'. In: *3rd International Conference on Learning Representations, ICLR 2015 - Conference Track Proceedings*. 2015 (cited on page 237).

[314] A. Baltopoulos, N. Polydorides, L. Pambaguian, A. Vavouliotis, and V. Kostopoulos. 'Damage identification in carbon fiber reinforced polymer plates using electrical resistance tomography mapping'. In: *Journal of Composite Materials* 47.26 (Dec. 2013), pp. 3285–3301. DOI: 10.1177/0021998312464079 (cited on page 237).

[315] MathWorks. *Navigation Toolbox Reference*. 2021. URL: https://www.mathworks.com/help/pdf_doc/nav/nav_ref.pdf (visited on 07/09/2021) (cited on page 269).

List of Acronyms

AC Alternating Current

ADC Analog-to-Digital Converter

ANN Artificial Neural Network

ASIC Application-Specific Integrated Circuit

BL BitLine

CEM Complete Electrode Model

CFB Clustered Filter Bank

CMOS Complementary Metal-Oxide Semiconductor

CNN Convolutional Neural Network

CNT Carbon NanoTube

DAMA Decomposition Algorithm based on Modal Assurance

DAQ Data AcQuisition

DBSCAN Debsity-Based Spatial Clustering of Applications with Noise

DC Direct Current

DESA Discrete-time Energy Separation Algorithm

DMOS Double-diffused Metal-Oxide-Semiconductor

DNN Deep Neural Network

DOF Degree Of Freedom

DSF Damage-Sensitive Feature

DtN Dirichlet to Neumann

DWT Discrete Wavelet Transform

EASI Equivalent Adaptive Separation Algorithm

ECC Engineered Cementitious Composite

ECG ElectroCardioGraphy

EEMD Ensemble Empirical Mode Decomposition

EFDD Enhanced Frequency Domain Decomposition

EIT Electrical Impedance Tomography

EKF Extended Kalman Filter

EMD Empirical Mode Decomposition

ERT Electrical Resistance Tomography

FBA Force-Balance Accelerometers

FDD Frequency Domain Decomposition

FE Finite Element

FFT Fast Fourier Transform

FPGA Field Programmable Gate Array

FRF Frequency Response Function

FWT Fast Wavelet Transform

GFRP Glass FiberReinforced Polymer

GNS Graphene NanoSheet

GPS Global Positioning System

HHT Hilbert-Huang Transform

HPV Human-Powered Vehicle

HT Hilbert Transform

IMF Intrinsic Mode Function

IMU Inertial Measurement Unit

ISD Inter-Story Drift

ISHM Indirect Structural Health Monitoring

IWPT Inverse Wavelet Packet Transform

KF Kalman Filter

MAC Modal Assurance Criterion

MAD Modal Assurance Distribution

MARG Magnetic, Angular Rate, Gravity

MEMD Multivariate Empirical Mode Decomposition

MEMS Micro-ElectroMechanical System

ML Machine Learning

MVM Matrix-Vector Multiplication

MWCNT Multi-Walled Carbon NanoTube

NMP N-Methyl-2-Pyrrolidinone

NMR Nonlinear Modal Response

NNM Nonlinear Normal Mode

NtD Neumann to Dirichlet

ODS Operating Deflection Shapes

OMA Operational Modal Analysis

PC Principal Component

PCA Principal Component Analysis

PCM Phase Change Memory

PET PolyEthylene Terephthalate

PLA PolyLactic Acid

PSS Poly-(Sodium 4-Styrenesulfonate)

PVC PolyVinyl Chloride

RBF Radial Basis Function

RBFN Radial Basis Function Network

RC Reinforced Concrete

RMS Root Mean Square

RTOS Real-Time Operating System

S^2HM Seismic Structural Health Monitoring

SBC Single-Board Computer

SDOF Single Degree Of Freedom

SHM Structural Health Monitoring

SMLAL Signed Long Multiply with Accumulate

SMU Source Meter Unit

SNR Signal-to-Noise Ratio

SOM Self-Organizing Map

SST SynchroSqueezed Transform

STFT Short-Time Fourier Transform

SV Singular Value

SVD Singular Value Decomposition

SWPT Stationary Wavelet Packet Transform

TEO Teager Energy Operator

TFR Time-Frequency Representation

TV Total Variation

ULL Uniform Load Line

ULS Uniform Load Surface

WL WordLine

WPT Wavelet Packet Transform

WSN Wireless Sensor Network

WSSN Wireless Smart Sensor Network

WT Wavelet Transform

WVD Wigner-Ville Decomposition